Spring 2015

# Distributed real-time hybrid simulation: Modeling, development and experimental validation

Ali Irmak Ozdagli
*Purdue University*

*Graduate School Form 30*
*Updated 1/15/2015*

**PURDUE UNIVERSITY**
**GRADUATE SCHOOL**
**Thesis/Dissertation Acceptance**

This is to certify that the thesis/dissertation prepared

By Ali Irmak Ozdagli

Entitled

Distributed Real-time Hybrid Simulation: Modeling, Development and Experimental Validation

For the degree of Doctor of Philosophy

Is approved by the final examining committee:

| | |
|---|---|
| Shirley J. Dyke<br>Chair | Jian Zhang |
| Ayhan Irfanoglu | |
| Arun Prakash | |
| Douglas E. Adams | |

To the best of my knowledge and as understood by the student in the Thesis/Dissertation Agreement, Publication Delay, and Certification Disclaimer (Graduate School Form 32), this thesis/dissertation adheres to the provisions of Purdue University's "Policy of Integrity in Research" and the use of copyright material.

Approved by Major Professor(s): Shirley J. Dyke

Approved by: Dulcy M. Abraham 4/14/2015

Head of the Departmental Graduate Program Date

# DISTRIBUTED REAL-TIME HYBRID SIMULATION: MODELING, DEVELOPMENT AND EXPERIMENTAL VALIDATION

A Dissertation

Submitted to the Faculty

of

Purdue University

by

Ali Irmak Ozdagli

In Partial Fulfillment of the

Requirements for the Degree

of

Doctor of Philosophy

May 2015

Purdue University

West Lafayette, Indiana

To my family

# ACKNOWLEDGMENTS

Firstly, my sincere gratitude and appreciation goes to my advisor, Dr. Shirley Dyke for I all I have learned from her and for her continuous guidance, support and patience. Without her advice in all stages of my studies, this thesis would not have been a reality. I feel grateful and indebted forever for being her student. I also want to thank my committee members, Dr. Jian Zhang, Dr. Arun Prakash, Dr. Ayhan Irfanoglu and Dr. Douglas Adams for their valuable input to this dissertation.

I want to acknowledge my fellow graduate students, Gaby for her knowledge and insights, Amin for keeping my motivation up, Charlie for always feeling me happy, Christian for his support in developing the MR damper loading frame for RTHS tests, and other members of Infrastructure Systems Laboratory (IISL) whom I didn't mention their names here. Their company made my life always full of happiness and fun. In addition, I want to specifically mention former IISL members, Dr. Tony Friedman, Dr. Xiuyu Gao, Dr. Nestor Castaneda, and Dr. Wei Song for their constant support. I also would like to express my deep gratitude to Dr. Wang Xi for his true friendship. Our technical and casual discussions will never be forgotten.

Special thanks and recognition go to Dr. Guoshan Xu, Dr. Ding Yong and Bo Li for their assistance in the development of shake table experiments performed at Structural and Seismic Test Center at Harbin Institute of Technology, as well as Dr. Bill Spencer and Dr. Nicholas Wierschem for their generous help in the configuration of distributed real-time hybrid simulation platform in the Smart Structure Technology Laboratory at the University of Illinois in Urbana-Champaign.

Finally, I would like to thank my parents for their love and support during my graduate work. I would also like to thank my brother, 'Big' Ali. I am proud to say that he will be always my role model.

The financial support of this research is provided in part by the U.S. National Science Foundation under Grant CMMI-1011534 (NEESR), and ACI-1148255, CMMI-0927178, Purdue University, the National Natural Science Foundation of China under Grant-90715036 and Purdue International Programs under the Sohmen Fund.

TABLE OF CONTENTS

Page

# LIST OF TABLES

# LIST OF FIGURES

Figure Page

Figure Page

Figure Page

# ABSTRACT

Ozdagli, Ali Irmak Ph.D., Purdue University, May 2015. Distributed Real-time Hybrid Simulation: Modeling, Development and Experimental Validation.
Major Professor: Shirley J. Dyke.

Real-time hybrid simulation (RTHS) has become a recognized methodology for isolating and evaluating performance of critical structural components under potentially catastrophic events such as earthquakes. Although RTHS is efficient in its utilization of equipment and space compared to traditional testing methods such as shake table testing, laboratory resources may not always be available in one location to conduct appropriate large-scale experiments. Consequently, distributed systems, capable of connecting multiple RTHS setups located at numerous geographically distributed facilities through information exchange, become essential. This dissertation focuses on the development, evaluation and validation of a new distributed RTHS (dRTHS) platform enabling integration of physical and numerical components of RTHS in geographically distributed locations over the Internet.

One significant challenge for conducting successful dRTHS over the Internet is sustaining real-time communication between test sites. The network is not consistent and variations in the Quality of Service (QoS) are expected. Since dRTHS is delay-sensitive by nature, a fixed transmission rate with minimum jitter and latency in the network traffic should be maintained during an experiment. A Smith predictor can compensate network delays, but requires use of a known dead time for optimal operation. The platform proposed herein is developed to mitigate the aforementioned challenge. An easily programmable environment is provided based on MATLAB/xPC. In this method, (i) a buffer is added to the simulation loop to minimize network jitter and stabilize the transmission rate, and (ii) a routine is implemented to estimate the network time delay on-the-fly for the optimal operation of the Smith predictor.

The performance of the proposed platform is investigated through a series of numerical and experimental studies. An illustrative demonstration is conducted using a three story structure equipped with an MR damper. The structure is tested on the shake table and its global responses are compared to RTHS and dRTHS configurations where the physical MR damper and numerical structural model are tested in local and geographically distributed laboratories.

The main contributions of this research are twofold: (1) dRTHS is validated as a feasible testing methodology, alternative to traditional and modern testing techniques such as shake table testing and RTHS, and (ii) the proposed platform serves as a viable environment for researchers to develop, evaluate and validate their own tools, investigate new methods to conduct dRTHS and advance the research in this area to the limits.

# CHAPTER 1
# INTRODUCTION

With recent advances in technology and science, engineering research has evolved into a new form, in which collaboration and distribution of knowledge across communities are promoted using cybersystems (Atkins et al., 2003). Innovations in computing diversified academic activities to discover new approaches to replace certain testing facilities with virtual laboratories at national and international scale (Oden et al., 2006; Cyberinfrastructure Council, 2007). The earliest attempt to overcome challenges associated with traditional testing in the area of earthquake engineering is made by combining computers with actuators in an online environment (Takanashi et al., 1975; Mahin and Shing, 1985). Basically, this concept, also known as hybrid simulation (HS), partitions an experimental setup into physical and numerical substructures, and couples them via a transfer system, usually a hydraulic actuator (Nakata et al., 2014).

In the last few decades, HS has drawn a lot of interest from the engineering community due the fact that it provides relatively more flexibility in terms of time, cost and workmanship, compared to classical testing methodologies such as shake table test (Nakashima et al., 1992; Saouma and Sivaselvan, 2008). Furthermore, hardware and software enhancements to facilitate hard real-time computing leveraged capabilities of HS to explore more realistic simulation cases of rate-dependent structural systems (Christenson et al., 2008). Finally, in 2011, NEES took initiative to promote HS and RTHS (real-time hybrid simulation) among earthquake engineering community to accelerate research and education (Deierlein et al., 2011).

Although HS, whether it is real-time or not, is efficient in utilization of equipment and space, laboratory resources may not always be optimized to employ more complex testing plans involving multiple apparatus and large-scale systems. Consequently, distributed systems, capable of connecting multiple HS setups located at numerous

geographically dispersed facilities through information exchange, become essential. Typically, such systems refer to a medium of integrated networks which are coordinated by message passing (Coulouris et al., 2005) and operate on the Internet infrastructure.

Utilization of geographically distributed RTHS (dRTHS) does not only require execution of equations of motions (EOM) within a strict time step, which is also a necessity for conducting RTHS, but also transmission of the data in real-time between distributed facilities running essential HS components such as numerical and physical subsystems. Today, the Internet is accessed by millions of people for various purposes including email, social interactions and access to the information. The Internet is heterogeneous in the sense that Internet service providers (ISP) may not accommodate best Quality of Service (QoS) all the time to all clients for all types of services. Degradation in QoS due to regular traffic and/or cyber-attacks is expected and may disrupt data exchange among users. QoS issues often manifest themselves as (i) network time delay, (ii) jitter, or even (iii) packet loss (Morton and Claise, 2009; Verma et al., 1991; Koodli and Ravikanth, 2009). In the event of such disruptions, maintaining successful dRTHS becomes a major challenge. Fortunately, loss of data is minimized with the improvements of the current infrastructure. On the other hand, transmission protocols, by design, cannot afford to deliver data in real-time to the destination, robustly due network delay and jittering.

To overcome the aforementioned challenges, in this dissertation, a platform to enable dRTHS is proposed. The goal of this platform is twofold: (1) to provide a transparent recipe based on MATLAB/xPC (MATLAB, 2011) to interconnect facilities, thus the possibility of a natural evolution of the platform into more complex applications; (2) to establish methodologies to avoid jitter during transmission, and to estimate and compensate the network time delay between communication nodes on-the-fly. Specifically, research efforts are focused on developing and validating the proposed platform by comparing shake table test responses with dRTHS results. To realize this research task, an experimental study is conducted in three phases. In the first phase of this study, a large-scale prototype test structure with a magneto-

rheological (MR) damper attached to its first floor is assembled at Harbin Institute of Technology (HIT) in China and excited on the shake table at HIT under various ground motion inputs. In the second phase, RTHS tests are conducted at Purdue University where the whole system is partitioned into analytical model of the structure as the numerical substructure and MR damper as the physical substructure. In the final phase, the proposed platform is tested by distributing the numerical substructure to University of Illinois at Urbana-Champaign (UIUC) and physical substructure to Purdue University. Responses from dRTHS is compared to RTHS and shake table tests to demonstrate the performance of the proposed platform.

## 1.1 Literature Review

The most prominent development towards multi-site testing has first started within NEESGrid ecosystem (NEESgrid, 2003). To support reliable transmission between facilities using Internet, a protocol named NEESGrid Teleoperation Control Protocol (NTCP) has been standardized (Pearlman et al., 2004). With the help of this protocol, simulation and testing computers within the grid could exchange data with each other over the NTCP back-end servers.

An initial distributed HS (dHS) implementation based on this frame was Multi-Site Online Simulation Testbed (MOST), where two physical substructures located at UIUC and University of Colorado, Boulder (CU) were linked to the numerical model simulated by National Center for Supercomputing Applications (NCSA), also located at UIUC (NEESgrid, 2004; Spencer et al., 2004). Later, a low-cost and mobile version of MOST, known as MiniMOST was developed to conduct MOST experiments in small scale (Nakata et al., 2004).

Since the original NTCP had large overhead that compromised the robustness of data exchange, protocol was not effective in utilization network resources, causing decrease in speed of test. To improve the testing rate, Mosqueda et al. (2008) proposed Fast-MOST by modifying NTCP handshake method and parallelizing communication

procedures of coordinator with other sites. In addition, an event-driven distributed controller developed by Stojadinovic et al. (2006) was adopted to satisfy command continuity minimize the force relaxations which is common problem for slow rate HS.

A drawback of MOST framework is the support for interconnection of multiple types of simulation programs with physical systems. Kwon et al. (2005) developed UI-SIMCOR, a universal middleware that establishes a coordinator between multiple sites and numerical simulation software for dHS, built on the MOST. As the demonstration example, Multi-site Soil-Structure Interaction Test (MISST) was conducted where UI-SIMCOR coupled a physical specimen with ZEUS-NL finite element program (FEM).

Concurrently, alternative testing protocols were also developed. For instance, NTCP has been evolved to NEES Hybrid Communications Protocol (NHCP) to enable soft RTHS by handling some design bottlenecks such as transmission rate, data packing, security and parallel processing (Cowart et al., 2007). Later, this protocol was adopted by UI-SIMCOR's new versions (Kwon et al., 2007). Takahashi and Fenves (2006) exploited an early release candidate of OpenFresco to connect OpenSees FEM to a physical substructure and a HS was performed with this framework between Kyoto University and University of California, Berkeley. Following, Schellenberg et al. (2009) realased full version of OpenFresco and extended its capabilities to support many varieties of numerical simulation programs and UI-SIMCOR, as well as NHCP.

Another notable application was studied by Park et al. (2005) by connecting test laboratories with Wireless Application Protocol (WAP). SAMBA software suite over TCP/IP was chosen as the main communication scheme in the instance when computers controlling actuators and running analysis engine operated on different operating systems. Xiao et al. (2004) implemented Networked Structural Laboratories (NetSLab) network platform built on XML application layer. Internet-based Simulation for Earthquake Engineering (ISEE) was developed by Yang et al. (2007) and Wang et al. (2007), where a shared database is used via Structured Query Language (SQL) to remove the need for coordinator communication. Last, but not least, Pan et al. (2006)

designed a peer-to-peer (P2P) hybrid simulation system, similar to coordinator–client type scheme.

Compared to HS based distributed tests, there is limited research on dRTHS. The first significant attempt was made by Kim et al. (2012) by using QUARC Real-time Control Software developed by Quanser. The distributed tests were conducted at a rate of 500 Hz between University of Connecticut (UCONN) and UIUC. For the transport layer, to ensure real-time uninterrupted data streaming, Transmission Control Protocol (TCP) embedded into QUARC was used. In addition, to compensate network delays in the feedback, a Smith predictor was introduced to numerical component. The system was designed to be stable up to 100 msec delay.

As an alternative to TCP, Ojaghi et al. (2014) developed a full-fledged framework named as Interdependent Channel – Distributed Hybrid Testing (IC-DHT) that acts as a middleware between facilities carrying numerical simulations and physical substructure testing. IC-DHT operates in soft real-time over a new high level protocol, Data Handling Protocol (DHP) built on User Datagram Protocol (UDP). Additionally, the network delays were treated by compensating the command input with polynomial extrapolation before sending to the actuator site. The example tests were conducted between Oxford and Bristol Universities at a rate of 50 Hz.

## 1.2 Remaining Challenges

The methods used for dHS are fairly mature. On the other hand, dRTHS is still in the development phase. Although encouraging results have been acquired to date, several challenges still remain before dRTHS will be actively used by the community.

First of all, outside hard real-time restrictions, currently available platforms are formed based on individual requirement. Following that, there is a lack of standardization specifying minimum requirements to conduct a successful test (Christenson et al., 2014). Community efforts should focus on development of new open-source transparent protocols, hardware and software components for dRTHS. Likewise, pri-

orities given by the researchers to sampling frequencies, transmission rates, data loss, delays and jitters according to operational needs should be well assessed through standards. Ultimately, the resulting framework should be flexible in satisfying all types of research demanding this technology.

In order to improve testing conditions, Internet infrastructure should be allocated. For example, to provide the fastest transmission speed available between sites, related privileges to control over local and wide area traffic should be given to IT team of facilities at the time of testing. For that matter, software-defined networks should be offered for elastic resource allocation. In addition, the security of the connection should be ensured with existing or alternately new tools.

Last but not least, there is a growing interest in cloud computing. As a part of the efficient utilization of distributed system towards virtual labs, with more numerically complex models are tested in real-time, high power computing resources within the cloud should be dedicated to real-time simulation. Yet, as the biggest challenge, the collected data through dRTHS should be instantly available to the community either during or after the testing for further analysis. Eventually, ready-to-use data in the cloud will be evaluated to accelerate and push research to its limit in this area of earthquake engineering.

## 1.3 Objective and Scope

The need for development and verification of a new dRTHS platform proposed here arises from the following requirements and objectives listed below:

1. Previous attempts to employ dRTHS often integrate a middleware into the transmission loop between sites. The complex control mechanisms implemented within the middleware prohibit dRTHS from running at high rates. The platform proposed here builds directly on UDP which provides only the essential control elements required for packet exchange. Thus, faster transmission rates are undertaken.

2. Available dRTHS middleware is either proprietary or closed-source. Evidently, advancement of the research in this area calls for open-source applications. The MATLAB/xPC framework selected for this platform provides an easily programmable environment. This study demonstrates a method for researchers to design their own platforms based on the specifications provided here.

3. To avoid performance reductions and even instabilities in dRTHS, network delays between testing sites should be quantified and compensated. Using programmable xPC environment, a Simulink block is implemented to estimate nondeterministic network time delay on-the-fly, by inspecting sent and received data packages between dRTHS nodes. Network delay estimation is especially helpful for Smith predictor-based time delay compensation scheme, which expects a known constant delay for optimal operation.

The performance of the proposed dRTHS platform is validated by comparing results to RTHS and shake table responses of a three story test structure equipped with MR damper. The primary scope of the comparisons are selected as in-plane displacements and accelerations of each floor, and the force at the MR damper level. RMS and peak errors are presented to demonstrate that dRTHS is a reliable and robust option among the many choices of testing methodologies.

## 1.4 Overview

This work focuses on the development, evaluation and validation of dRTHS setup employed between Purdue and UIUC. dRTHS results are compared with global responses of a three story, large-scale test structure excited with a shake table at HIT. Flow of information in this work can be summarized with the schematic given in Figure 1.1.

Chapter 2 presents an overview and purpose of the test configurations towards verification of the dRTHS. Configurations described in this chapter include: (i) system

identification, (ii) shake table configuration, (iii) RTHS setup at HIT, and (iv) RTHS setup at Purdue.

In Chapter 3, an improved system identification and model updating process towards structural control and model response estimation is proposed. First, a theoretical background on system identification and model updating is presented. Next, the motivation behind the proposed model updating technique along with the derivation of the methodology is explained. Finally, verification tests are conducted on the uncontrolled test structure when excited with various ground motions using the shake table.

Chapter 4 discusses modeling of MR dampers at Purdue and at HIT through characterization. Since shake table and RTHS tests have been performed at HIT and Purdue on different damper types, for the sake of a fair comparison, equivalent voltages for Purdue damper to generate force levels of HIT damper at passive-off and -on modes are provided in this chapter. In addition, fundamentals of control theory and design approaches for passive and semi-active control of MR dampers are discussed.

In Chapter 5, analytical simulations using an integrated model containing numerical models of the test structure and MR damper are compared to shake table results. The errors tabulated in this chapter are considered as the baseline for dRTHS comparisons.

Chapter 6 presents experimental verification by comparing shake table response of the test structure to RTHS results. In the first part of this section, $H_\infty$ type controller to compensate actuator dynamics is introduced and tracking performance of the controller is validated through a series of tests. In the second part, implementation of RTHS at Purdue University is discussed in detail and several experiments are conducted with the proposed setup. Finally, results from RTHS are compared to shake table responses. An in-depth analysis of the comparisons is given and possible sources of errors are discussed to justify the results.

In Chapter 7, concepts on the Internet network and proposed dRTHS architecture and network configurations are introduced. In addition, the basics of the method and implementation through the network time delay estimation block is discussed. Finally, a virtual distributed RTHS (vdRTHS) example test is conducted at different communication rates where all substructures including MR damper and a prototype structure is simulated at real-time at Purdue and UIUC, respectively and physical Internet infrastructure is used for data exchange between test sites. To verify the architecture and delay estimation block, vdRTHS results are compared to responses from virtual RTHS (vRTHS), where all RTHS components are numerically simulated in real-time.

Chapter 8 investigates adaptation of the proposed architecture to simulate the controlled HIT test structure using dRTHS. The performance of the dRTHS platform is evaluated by comparing results to RTHS and shake table test responses.

Finally, Chapter 9 summarizes the important research findings through this study and draws general conclusions from the study presented here. Moreover, future work on this research area is presented.

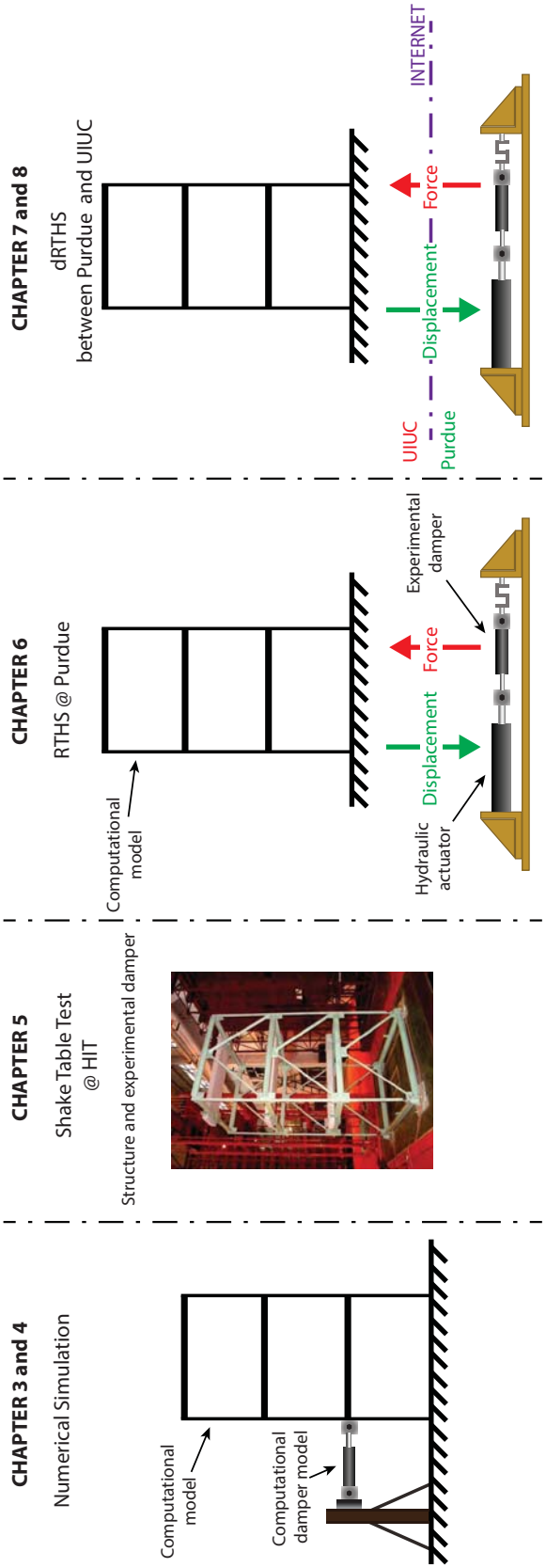


Figure 1.1: Schematic of validation scenarios

# CHAPTER 2
# EXPERIMENTAL SETUP FOR SHAKE TABLE AND RTHS TESTS

In this chapter, an overview of experimental configurations built at Intelligent Infrastructure Systems Lab (IISL) at Purdue University and Structural Engineering Laboratory at HIT towards realizing the objectives of this dissertation is given. Section 2.1 focuses on the three story test structure and structural modifications performed on the structure. In Sections 2.2 and 2.3, configurations for system identification and shake table tests are described including instrumentation setup. Introductory information on the dampers used for shake table and RTHS/dRTHS tests is also provided in this section. In Section 2.4, the loading frame designed at HIT for actuator tracking evaluation, and in Section 2.5, RTHS setup developed at IISL are discussed in details. Finally, a summary of the chapter is given in Section 2.6.

## 2.1 HIT Test Structure

The original prototype test structure (PS) is a three-dimensional, three story frame located at Harbin Institute of Technology (HIT), China, shown in Figure 2.1a. The structure has a base plan with dimensions 1.84 m by 2.04 m. Each story is 1.2 m tall and the total height is 3.6 m (See Figure 2.1b). The columns, beams and girders are made of structural steel with an elastic modulus estimated to be 220 GPa. Each joint, where column and beam members are connected to each other, is welded and does not allow free rotation. The structure is braced in one direction with v-type braces such that the system is weak in the y-axis and strong along the x-axis (See Figure 2.1c). At each story, a concrete slab weight approximately 250 kg is attached as seismic mass. The total mass of the structure including the self-weight of the members is calculated

to be 1066 kg. Section properties of the members used in the design of the PS is summarized in Table 2.1.

(a) Experimental structure

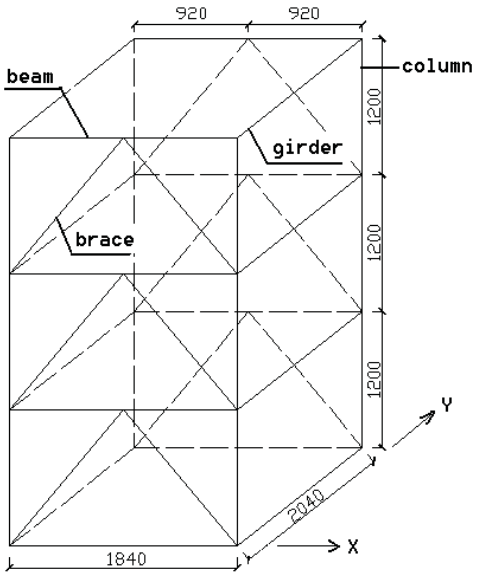


(b) Stick figure representation

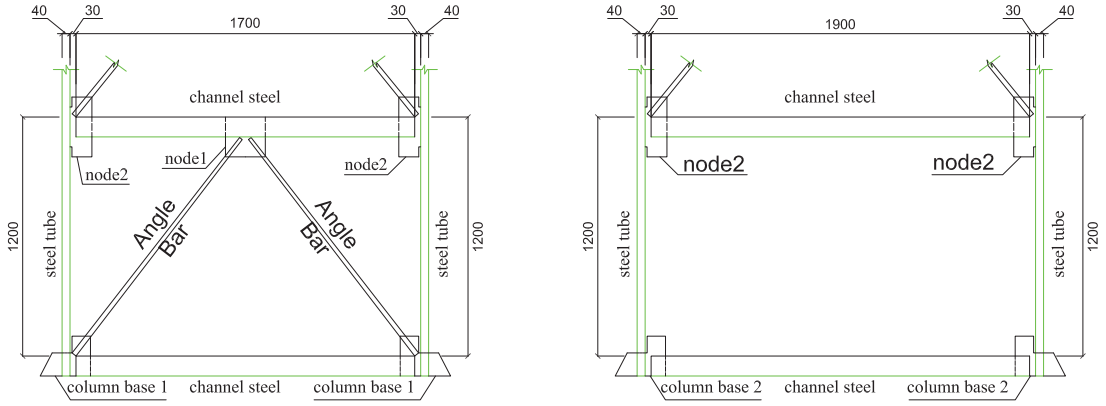


(c) CAD drawings of floor plan details

Figure 2.1: Original experimental structure

For passive-off, passive-on and semi-active vibration control tests, an MR damper is attached to the structure at first floor. To connect the MR damper to the first floor, a slight modification is performed at the first floor by adding a horizontal v-brace in the plan of the floor. Thus, the beam, where the MR damper is attached, will have

Table 2.1: Section properties of the prototype structure

| Beam and Girder | | | | | Column | | | | | Brace | | | | |
|---|---|---|---|---|---|---|---|---|---|---|---|---|---|---|
| 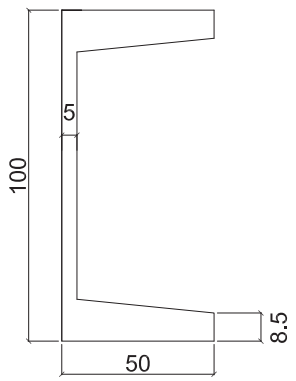 | | | | | 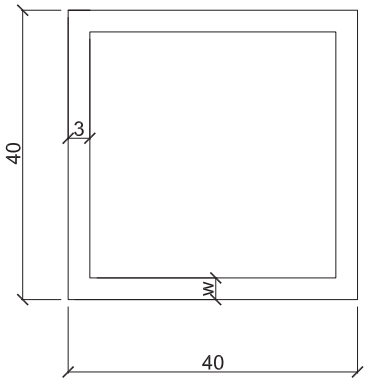 | | | | | 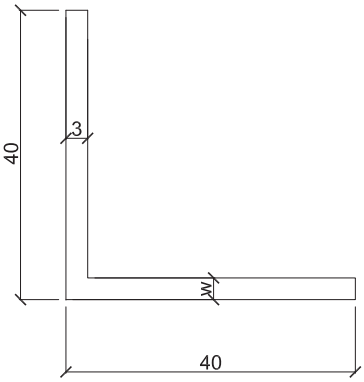 | | | | |
| $A$ | $I_{X-X}$ | $I_{Y-Y}$ | $J$ | $\rho$ | $A$ | $I_{X-X}$ | $I_{Y-Y}$ | $J$ | $\rho$ | $A$ | $I_{X-X}$ | $I_{Y-Y}$ | $J$ | $\rho$ |
| $cm^2$ | $cm^4$ | $cm^4$ | $cm^4$ | $Kg/m$ | $cm^2$ | $cm^4$ | $cm^4$ | $cm^4$ | $Kg/m$ | $cm^2$ | $cm^4$ | $cm^4$ | $cm^4$ | $Kg/m$ |
| 12.74 | 198.3 | 25.6 | 223.9 | 10.0 | 4.44 | 10.2 | 10.2 | 20.4 | 3.487 | 2.31 | 3.59 | 3.59 | 7.2 | 1.814 |



additional stiffness against deflection caused by damper force. A stick figure of the modified structure is shown in Figure 2.2a. Top and side views of the MR damper attachment joint are presented in Figures 2.2b and 2.2c. In addition, a detail where v-brace is welded to the beam-column joint is given in Figure 2.2d. The cross-sectional properties of the v-braces are same as the girders/beams, shown in Table 2.1. The additional first floor mass contribution to the v-braces is about 45 kg which makes the total mass of the structure about 1110 kg.

## 2.2 System Identification Test Equipment

Development of high fidelity mathematical models of the test structure is undertaken by choosing appropriate testing equipment. This section describes test instrumentation including DAQ system used for system identification.

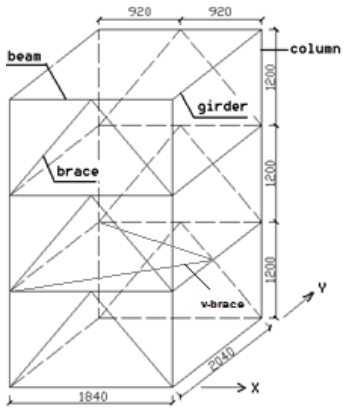


(a) Modified stick figure representation

(b) Top view of MR damper attachment joint

(c) Side view of MR damper attachment joint

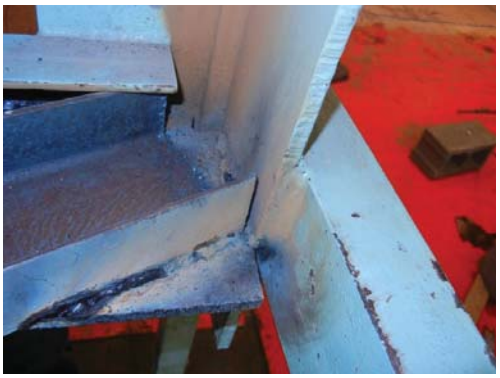

(d) Corner detail

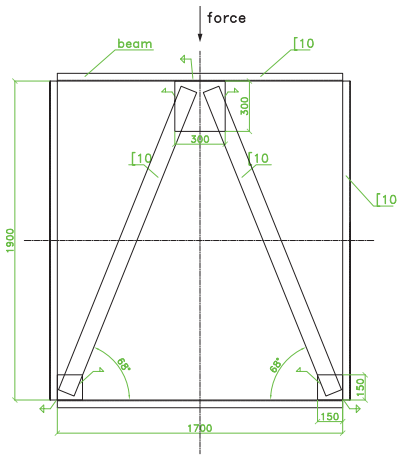


(e) CAD drawings of floor plan details

Figure 2.2: Additional details for modified test structure

## DAQ System

To acquire system identification data of the test structure, NI USB-6259, a multi-functional data acquisition system box made by National Instruments is employed (see Figure 2.3). The DAQ system has the capability to sample data upto 1.25 MHz rate from 16 differential analog input channels at 16 bit analog-to-digital conversion resolution. The data acquired online from DAQ system is transmitted over USB 2.0 to a Dell Inspiron 1720 notebook to be processed by DeweSoft Dynamic Signal Analyzer v6.6 developed by DeweSoft (see Figure 2.4) The raw data is later exported **.mat* to be processed in MATLAB (2011).

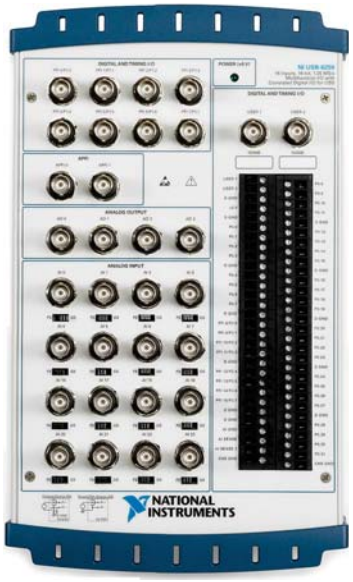


Figure 2.3: NI USB-6259

## Instrumentation

Charge-type acceloremeters produced by Brüel & Kjær model #4368 with a flat frequency response between 0.2 Hz and 4800 Hz are used to measure acceleration response of the structure (see Figure 2.5). The one-hand operable modally tuned impact hammer used in the tests is made by Jiangsu Lianneng Electronic Technology


Figure 2.4: DeweSoft start-up screen

Limited Corporation with a model #LC-01A from Sinocera Piezotronics branch (see Figure 2.6). The hammer is equipped with a charge type load cell with model #CL-YD-303 and a rubber tip on the load cell. All together, hammer is rated to generate maximum thrust of 2 kN. The acceleration sensors and impact hammer are powered with signal conditioners capable of producing velocity and displacement by integration, belonging to Sinocera Piezotronics branch with modepl #YE5858A, which is based on Brüel & Kjær's model #2635 charge amplifier (see Figure 2.7). The amplifier has selectable dial gains, high-pass filter ranging from 0.3 Hz to 10 Hz for acceleration measurements and a low pass filter from 300 Hz to 100 000 Hz (wide-band). All filters attenuate maximum 3 dB at the cutoff frequency during normal operation conditions. The decay rate for low and high pass filters are 12 dB and 6 dB per octave, respectively.

## 2.3 Shake Table Test Configuration

This section introduces the test structure used in the validation of dRTHS, along with the shake table and other test equipment including DAQs and instrumentation. Shake table test results are provided in Chapter 5.

Figure 2.5: Brüel & Kjær model #4368 with its base magnet

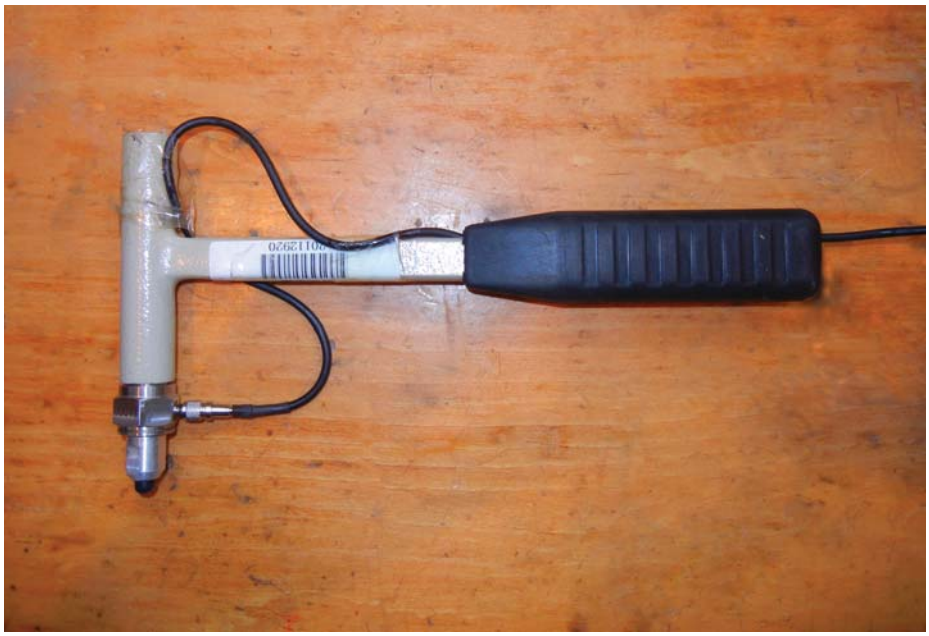

Figure 2.6: Jiangsu Lianneng made impact hammer

### 2.3.1 Shake Table

The testing facility located in HIT is a unidirectional shake table and is 3 meters wide and 4 meters long in shaking direction. A photograph of the shake table is given in Figure 2.8. The actuator attached to the shake table is manufactured by Schenck, shown in Figure 2.9. The two column servo-hydraulic actuator with model


Figure 2.7: Sinocera signal conditioners

#PM250R is rated up to 250 kN static loading or 200 kN dynamic loading and can drive the bare shake table (no payload) with a peak acceleration of ±1.33 g, peak velocity of ±600 mm/sec at a stroke restricted to ±125 mm. The maximum payload and maximum overturning moment of the shake table is limited to 12 tonne and 30 tonne · m, respectively. The hydraulic oil to the actuator is supplied by the hydraulic power unit produced by Schenck. The frequency of the excitation input is bounded between 0 Hz and 30 Hz. An #493.10 MTS FlexTest GT #100 Controller, shown in Figure 2.10 is used to provide the control input to the shake table. The controller is capable of controlling of 8 servo-valves at the same time while sampling at a maximum rate of 6000 Hz using 16 bit resolution.

MTS #793.00 TestSuite Multipurpose software is used to drive the controller. A screenshot of the software is given in Figure 2.11.

Figure 2.8: Shake table located at HIT

Figure 2.9: 250 kN capacity Schenck actuator


Figure 2.10: MTS FlexTest GT controller

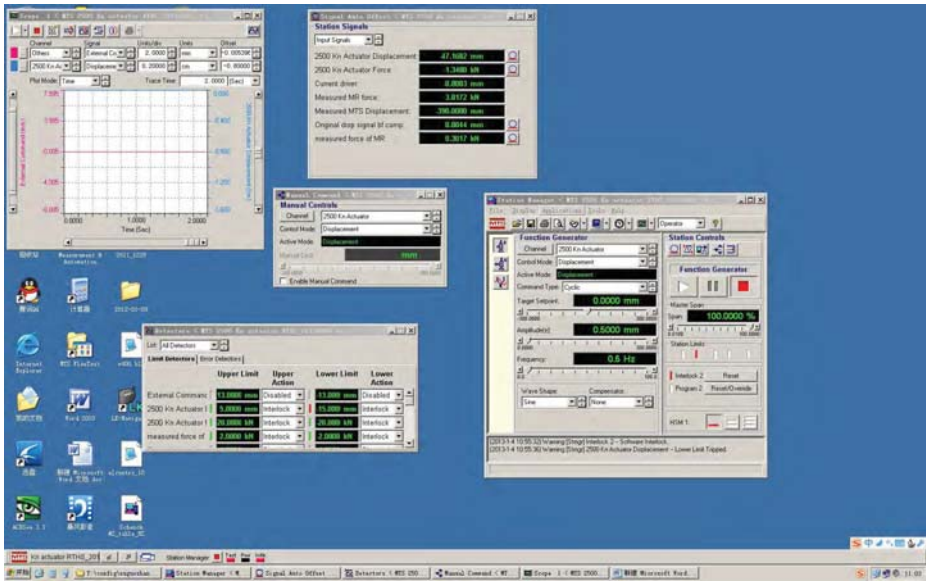

Figure 2.11: TestSuite Multipurpose Software layout

### 2.3.2 Test Equipment

Equipment to measure shake table responses of the structure is categorized in two following subsections.

DAQ System

For data acquisition, Dong-Hua Universal Dynamic Signal Test System #DH5922 made by Jiangsu Donghua Testing Technology, that is capable of sampling 16 channels simultaneously up to 200 kHz at 24 bit conversion is used (see Figure 2.12). The system is controlled with DHDAS dynamic signal test and analysis software v4.3.55 over IEEE 1394 interface also known as Firewire, and driven by Dell Inspiron 1720.


Figure 2.12: Dong-Hua Universal Dynamic Signal Test System

To acquire structural responses and to control equipments such as MR damper or current driver, DS1104 along with the terminal board CP1104 from dSPACE GmbH is selected as real-time control development platform (see Figure 2.13). DS1104 is essentially a PCI board and can sample data at up to 250 MHz using 4 ADC input multiplex setting with 16 bit resolution and 4 ADC input sampling in parallel setting with 12 bit resolution. The system can also produce analog output using 8 DAC units with 16 bit resolution. ControlDesk Developer Version Release 6.3 software running on Dell Dimension 5150 desktop computer, which is also hosting DS1104, is used as the user interface to program and control real-time simulation that is compiled and downloaded via Simulink/Real-Time Workshop (see Figure 2.14). Brüel & Kjær accelerometers are paired with charge amplifier, Ke Dong KD #5018 made by Yangzhou Dynamic Electronics. KD #5018 has a configurable gain varying from

1 and 1000, high-pass filter ranging from 0.1 Hz to 10 Hz and a low pass filter from 300 Hz to 100 000 Hz (wide-band).

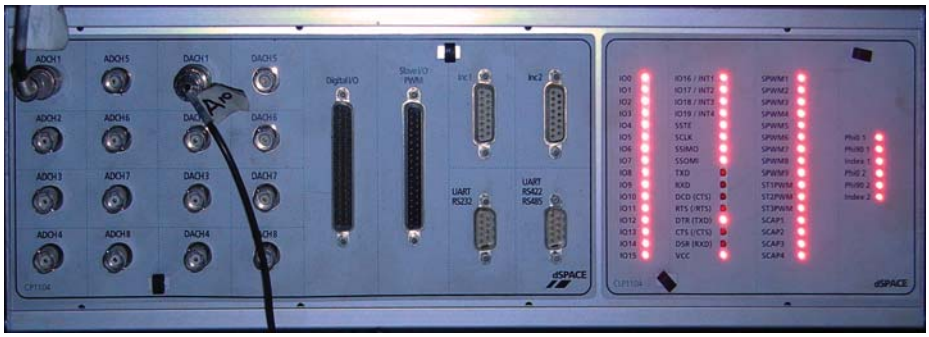

Figure 2.13: dSpace DS1104 system terminal board

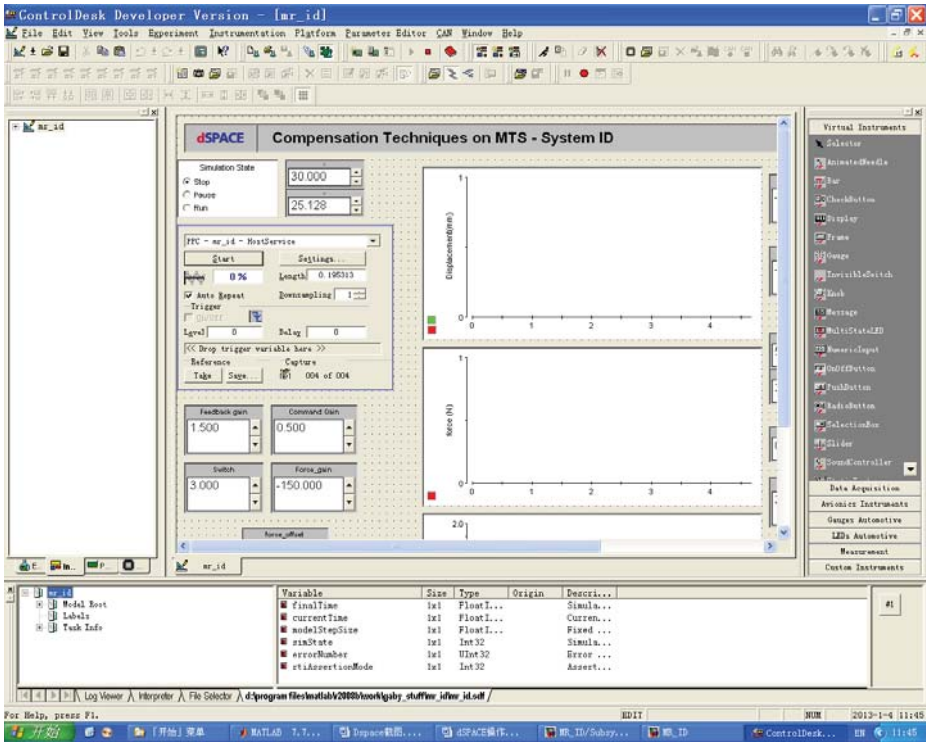


Figure 2.14: dSpace ControlDesk Software layout

Figure 2.15: Ke Dong KD 5018 signal conditioner

Instrumentation

Charge-type acceloremeters from Brüel & Kjær explained in Section 2.2 are used to measure structural acceleration responses and ground acceleration of the shake table. For displacement measurements, LVDT and Laser sensors are used. The laser sensors made by Keyence with model LK-400 and LK-405 have ±100 mm measurement range with extremely low linearity, ±0.05% over full scale (see Figure 2.16a). The laser sensors are powered up by a LK-G3001V Controller (see Figure 2.16b) that allows sampling rates reaching up to 50 000 Hz. In addition, Beijing Haiquan Sensor Technology made DC-type LVDTs with model #DA-50 (reengaging spring type) and #DA-150 (non-spring type) having respective strokes of ±50 mm and ±150 mm are used (see Figure 2.17).

MR Damper

For passive-on/off and semi-active control tests, MR damper with model #RD-1005-3 made by LORD is used. The damper is capable of producing forces up to 2500 N when powered with an input current of 1 A. To power the damper, a voltage controllable current driver that can provide current up to 0 A to 3 A is used (see Figure 2.18). The current driver is controlled via dSpace DS1104. To measure force generated by MR damper, force transducer #661.19F-03 produced by MTS with a


(a) LK-400 (b) LK-G3001

Figure 2.16: Keyence laser displacement sensor and controller

Figure 2.17: BHST #DA-50 LVDT

load capacity of ±15 kN is used (see Figure 2.19). The force transducer is powered by MTS Flex GT Controller. To attach the MR damper to the first floor of the structure, a fixture rigid enough not to deflect more than ±0.1 mm under maximum MR damper load is designed (see Figure 2.20). For additional stiffness, tension-compression bars are welded to the rigid fixture.


Figure 2.18: MR damper amplifier


Figure 2.19: MTS load cell

### 2.3.3 Ground Excitation

Generally, any actuator has physical limitations in terms of realizing the desired input. The limitations can often manifest as time delay or amplitude loss. For this reason, a delay and amplitude compensation scheme needs to be implemented if the reproduction of the excitation input is a must. The actuator of the shake table at

(a) Top View

(b) Full Setup including MR Damper and Load Cell

Figure 2.20: MR damper fixture

HIT is controlled on the software-hardware level with internal PID control. Since displacement is used as the feedback to the PID loop, acceleration records are double integrated with trapezoidal integration rule in MATLAB. Excitation input is selected as *(i)* historical El Centro earthquake recorded at El Centro Terminal Substation Buildings concrete floor during Imperial Valley, CA earthquake on May 18, 1940, *(ii)* Kobe earthquake recorded at station Takarazuka, Japan on January 16, 1995 and *(iii)* Morgan Hill, CA earthquake recorded at station Gilroy Array #6 on April 24, 1984. Since the existence of the MR damper fixture is limiting maximum allowable stroke of the shake table to nearly $\pm 75\,\mathrm{mm}$, El Centro and Kobe earthquakes are scaled to 50 % and 35 % of their recorded peak ground displacement, respectively. No time scaling is applied to any of the ground excitations. Tracking performance of the shake table with payload while simulating earthquakes is given in Figure 2.21 for El Centro, in Figure 2.22 for Kobe and in Figure 2.23 for Morgan Hill earthquakes. The relative error calculated as $RMS_{Error}/RMS_{Reference}$, where $RMS_{Reference}$ is historical data, is found [86.8, 1.16] % for El Centro Earthquake acceleration and displacement, [80.5, 7.90] % for Kobe Earthquake acceleration and displacement and [81.0, 5.23] %

for Morgan Hill Earthquake acceleration and displacement, respectively. Although reported errors on accelerations are relatively high, the shake table showed good performance in tracking of the intended displacement.

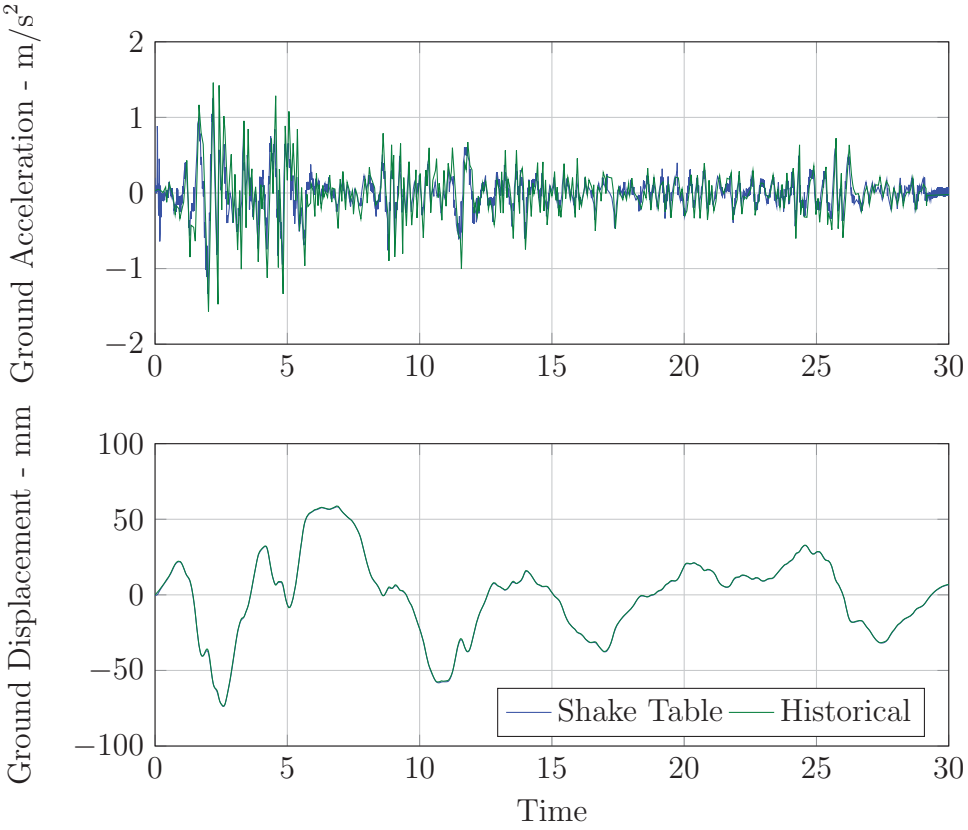


Figure 2.21: El Centro ground motion comparison

## 2.4 Loading Frame at HIT

This section introduces the test equipment including DAQs required to conduct tracking performance tests of actuator compensation algorithms at HIT. Results are provided in Section 6.1.3.

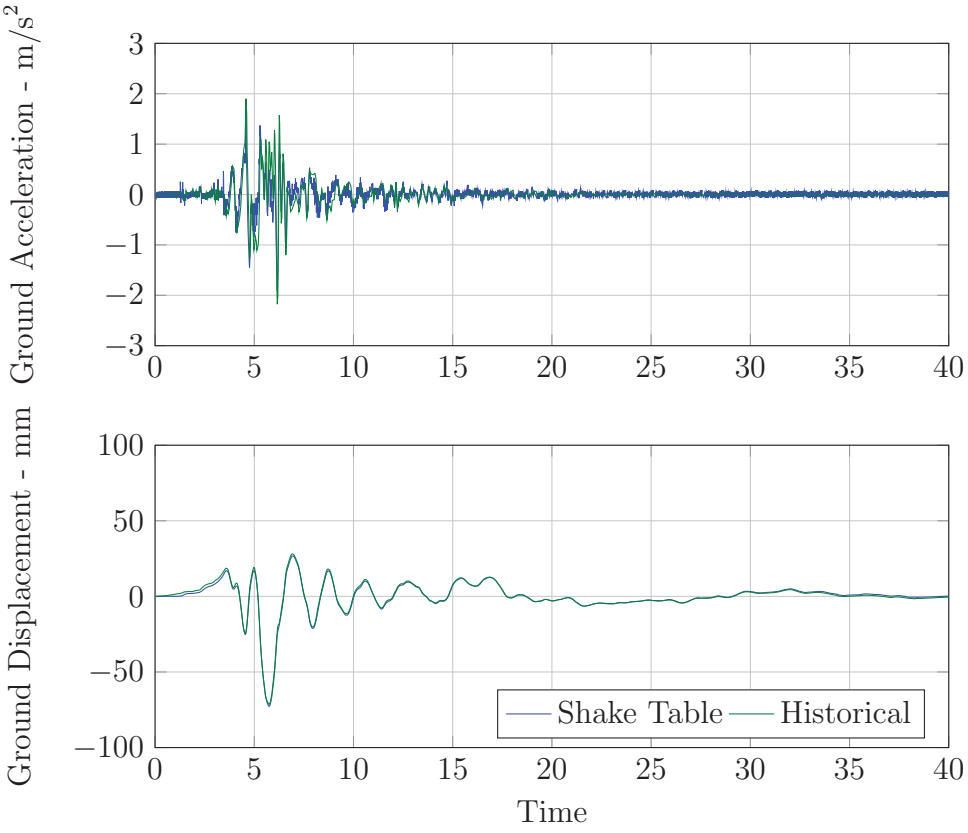


Figure 2.22: Kobe ground motion comparison

### 2.4.1 Test Equipment

Tracking tests conducted at HIT are performed with MR damper #RD-1005-3 attached to an uniaxial servohydraulic load frame with a model #311.41 from MTS and a capacity of ±2500 kN (see Figure 2.24). The hydraulic system has a saturation velocity limit of ±90 mm/sec when six pump units are running on Model #505.180 MTS SilentFlo Hydraulic Power Unit providing up to 160 gal/min hydraulic oil flow with a pressure of 3000 psi. The force transducer and MR damper is attached to the actuator with hydraulically controlled wedge grips #641.39 that requires #685 hydraulic grip supply unit, both made by MTS. For inner-loop and outer-loop control, Flex GT Controller and DS1104 are used, respectively.

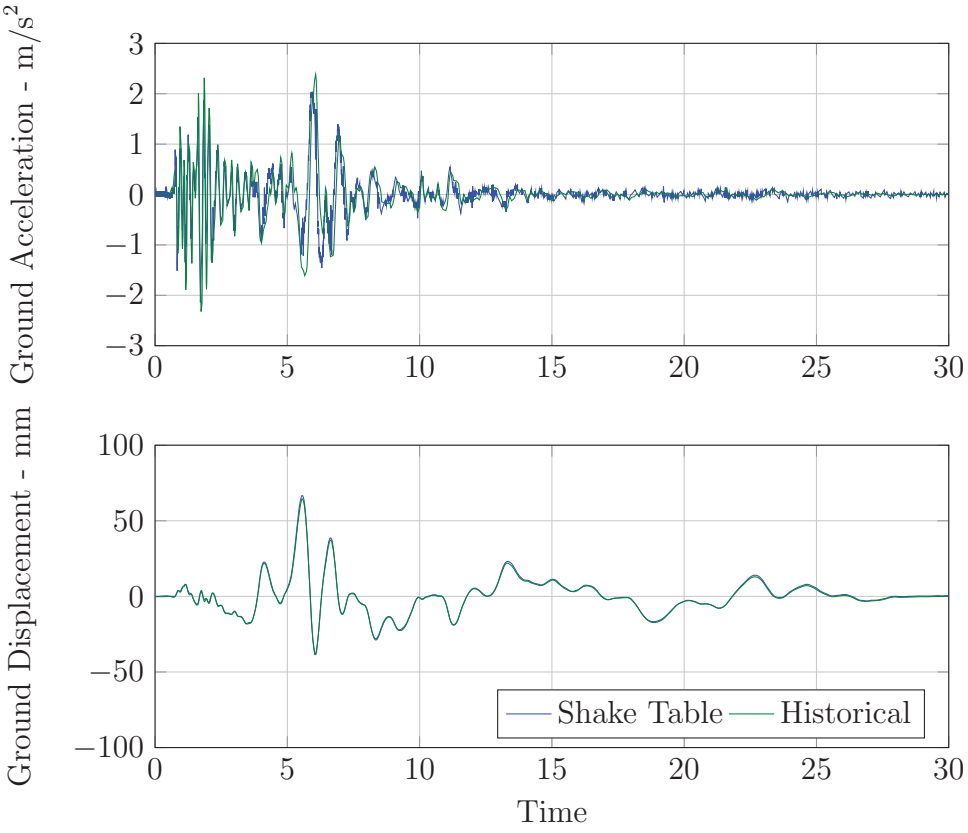


Figure 2.23: Morgan Hill ground motion comparison

## 2.5 Real-time Hybrid Simulation Setup at Purdue

This section introduces the test equipment including DAQs required to conduct RTHS at IISL. The results of RTHS conducted on this frame are provided in Chapter 6.

### 2.5.1 Test Equipment

RTHS tests conducted at IISL are performed with MR damper #RD-8041-1 made by LORD. Current in the MR damper is controlled by LORD Wonder Box Device Controller Kit with model #RD-3002-03 via external command. The force of MR damper is measured by Omega made model #LC101-2K S-type force transducer with a capacity of ±9000 N (±2000 lb). An Omega made model #DMD-465WB wide

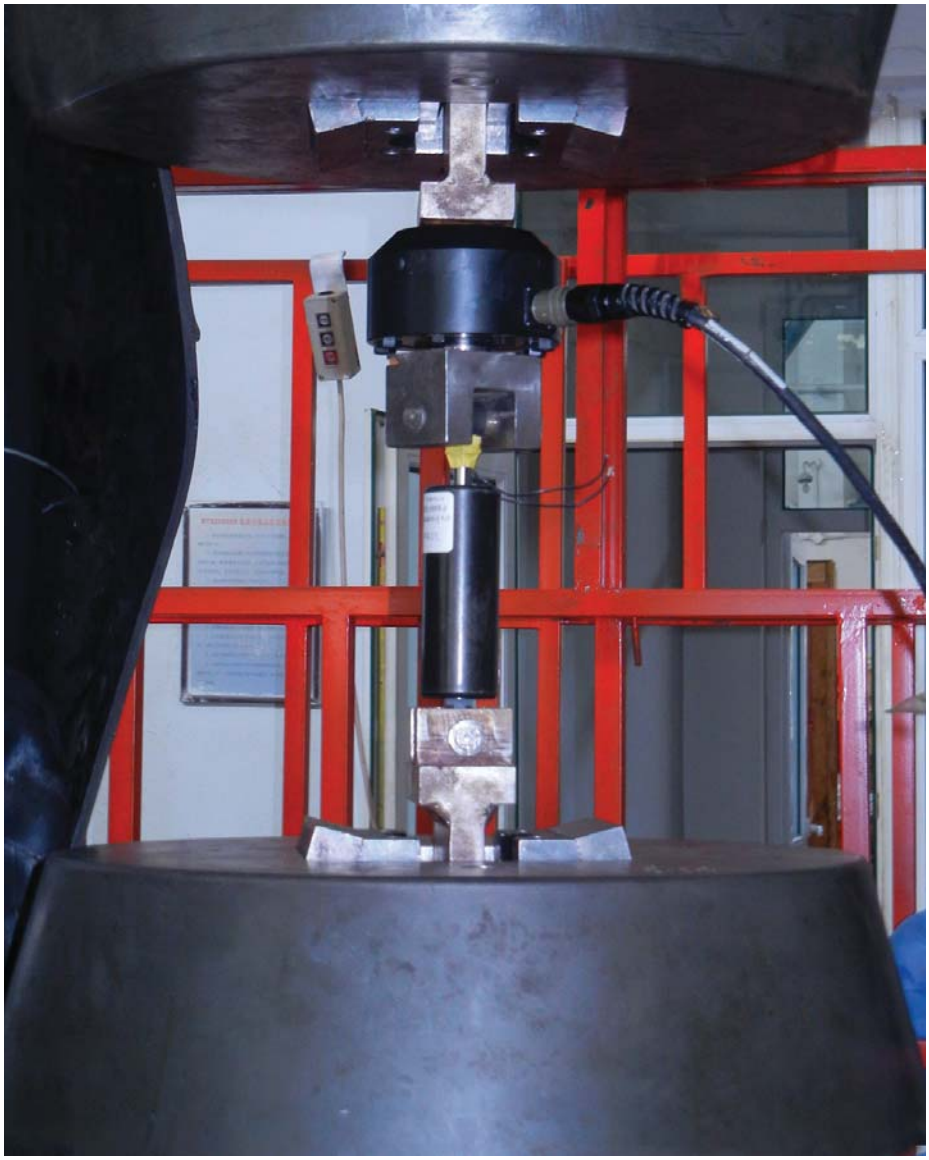

Figure 2.24: MTS loading frame with MR damper and load cell attached at HIT

bandwidth signal conditioner module with a frequency response up to 2 kHz is used to power up the force transducer. Both damper and load cell are attached to a loading frame also containing Shore Western made actuator model #910D rated with ±5000 N force capacity (Figure 2.25). A MOOG made #G761-3004B controllable servo-valve that provides a flow rate of 10 gal/min at 1000 psi valve pressure drop is used to operate actuator. The oil supply is provided by a model #505.120 MTS SilentFlo

Hydraulic Power Unit providing up to 120 gal/min hydraulic oil flow with a pressure of 3000 psi, when four motor pumps are running.

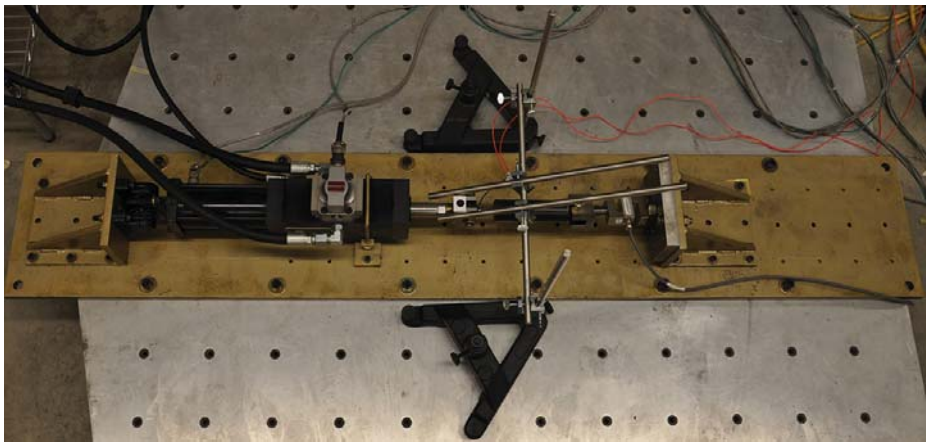

Figure 2.25: Shore Western Actuator, MR damper and load cell attached to loading frame at Purdue

For the inner-loop control of the actuator, a Shore Western SC6000 analog servo-hydraulic control system is used (see Figure 2.26). The actuator is operated through Shore Western MDOF Control System software running on a PC, embedded in SC6000.

For the outer-loop control, a performance real-time target machine made by Speedgoat is used (see Figure 2.27). RT system has a software-level RT-kernel that is configurable using MATLAB/Simulink/xPC. High-resolution, high accuracy A/D board model #IO112 supporting up to 32 differential simultaneous A/D channels with 18-bit resolution and D/A board model #IO113 supporting up to 8 differential D/A channels with 18-bit resolution are integrated into this digital control system. In addition, it contains an Intel 8255X series #IO702 Ethernet controller providing two Fast Ethernet ports for real-time communication.

## 2.6 Summary

In this chapter, the experimental setup for system identification and shake table tests including sensors, DAQ and actuator systems are described. Furthermore,


Figure 2.26: Shore Western SC6000 controller


Figure 2.27: Speedgoat Performance Real-time Target Machine

earthquake excitations to be used for the validation of RTHS and also shake table performance for the given ground motions are briefly discussed. In addition, loading frame located at HIT and RTHS setup located at IISL are explained in detail.

# CHAPTER 3
# MODELING, SYSTEM IDENTIFICATION AND MODEL UPDATING OF THE TEST STRUCTURE

A proper mathematical description of the test structure is crucial for the comparisons to be performed using RTHS/dRTHS. Development of the system model must take the dynamic characteristics of the structure into account. Nevertheless, success of control design strategies benefits from an appropriate model.

In essence, system identification is the process of establishing a model that reproduces the input/output behavior of the target structure. By selecting a system identification procedure suitable for the experimental objectives, one can develop reliable predictions and explain system behavior (Catbas et al., 2013). As explained by Aktan and Moon (2005), to fully achieve potential outcomes of system identification, six steps should be followed. Those are: (i) conceptualization of the structure based on the needs; (ii) a-priori modeling; (iii) experimentation and collection of data; (iv) feature extraction; (v) model calibration and (vi) model evaluation.

In this chapter, an overview of system modeling, identification and model updating to develop an appropriate mathematical description of the test structure is given. Section 3.1 presents a baseline model of the test structure along with the mathematical formulations in state-space representations for the numerical and dRTHS evaluations. Next, Section 3.2 introduces a commonly used system identification methodology, Eigensystem Realization Algorithm (ERA) along with its theory and modification of the method for real world application. In Section 3.3, a new model updating process aggregating identified system characteristic with physical mass-damping-stiffness properties is presented with verification tests. In Section 3.4, the limitations of the proposed method are discussed. Evaluation criteria used for performance assessment of the developed model is given in Section 3.5. Section 3.6 presents the initial model

based on the baseline modeling assumptions, identified results of the system, transfer function comparisons between different models and lastly comparison of simulated results of the model to experimental shake table tests of the uncontrolled structure. Finally, a summary of the chapter is given in Section 3.7

## 3.1 Baseline Model

For the development of the model, the structure is assumed to be a linear system and remains linear throughout the entire test plan. Thus, based on the description presented in Section 2.1, a simple mass-damper-spring system equivalent to a shear model of the structure is developed as follows:

$$M\ddot{x} + C\dot{x} + Kx = -M\ddot{x}_g + F \tag{3.1}$$

where $M$, $C$ and $K$ are the mass, damping and stiffness matrices respectively. The right-hand-side of the equation represents earthquake excitation, $\ddot{x}_g$ and force input, $F$ to the structure.

The system is established to have three degrees of freedom (DOF), where each node represents a floor of the test structure. Seismic concrete masses and structural weight are lumped at floor level for each degree of freedom, as shown in Figure 3.1. $m_1$ and $m_3$ represent first floor and top floor, respectively. This system model has the following structural properties:

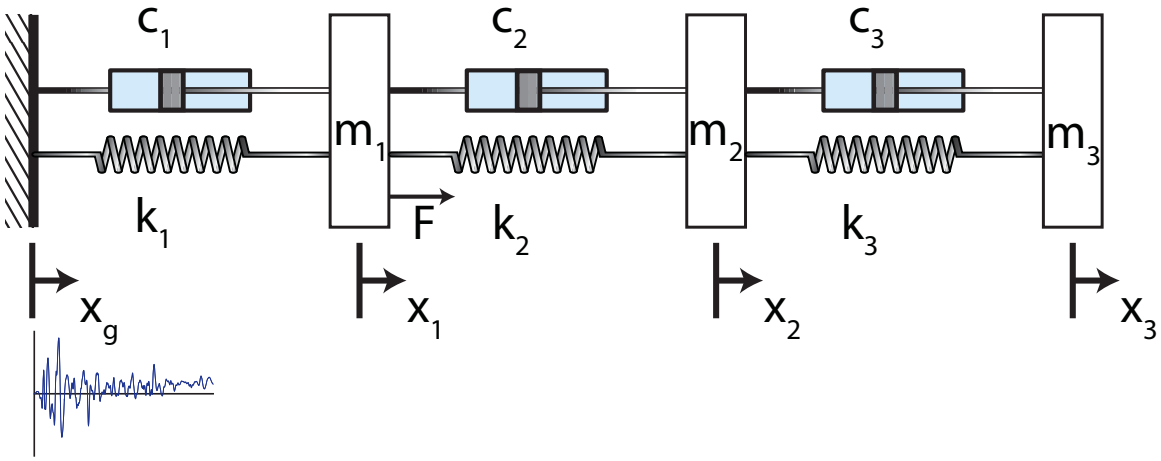


Figure 3.1: Lumped mass model idealization of the test structure

$$[M] = \begin{bmatrix} m_1 & 0 & 0 \\ 0 & m_2 & 0 \\ 0 & 0 & m_3 \end{bmatrix} \tag{3.2a}$$

$$[C] = \begin{bmatrix} c_1 + c_2 & -c_2 & 0 \\ -c_2 & c_2 + c_3 & -c_3 \\ 0 & -c_3 & c_3 \end{bmatrix} \tag{3.2b}$$

$$[K] = \begin{bmatrix} k_1 + k_2 & -k_2 & 0 \\ -k_2 & k_2 + k_3 & -k_3 \\ 0 & -k_3 & k_3 \end{bmatrix} \tag{3.2c}$$

$$[F] = \begin{bmatrix} f \\ 0 \\ 0 \end{bmatrix} \tag{3.2d}$$

The model described herein is designed to reproduce only horizontal responses in the weak axis when a disturbance is applied as means of ground motion or external force in the weak axis. Torsional and out-of-plane responses are omitted in the modeling assumptions.

Given $M$ and $K$, as an alternative to the proportional damping matrix, a non-proportional type can be formed based on a specific set of damping ratios:

$$[C] = [M]\Phi(2\xi[2\pi f])\Phi^T \tag{3.3}$$

where $\Phi$ is mode shape of the system, $f$ and $\xi$ represent diagonal matrix of natural frequencies in Hertz and damping ratios, respectively.

***State-space Formulation***

For continuous linear time invariant (LTI) systems, the standard state-space representation derived either from physical properties or experimental data of the baseline model is introduced below:

$$\dot{x} = Ax + Bf + E\ddot{x}_g \tag{3.4}$$

$$y = Cx + Df + F\ddot{x}_g \tag{3.5}$$

where, $x$ is the internal state vector, $y$ is system response vector, $f$ is the input force and $\ddot{x}_g$ is the ground acceleration. The state matrix, $A$ and input-to-state matrix, $B$ and $E$ of the system in Equation (3.4) can be written as:

$$[A] = \begin{bmatrix} 0 & I \\ -M^{-1}K & -M^{-1}C \end{bmatrix}, [B] = \begin{bmatrix} 0 \\ M^{-1}P \end{bmatrix}, [E] = \begin{bmatrix} 0 \\ -I \end{bmatrix} \tag{3.6}$$

where $P$ and $G$ are influence matrices of applied external force and ground motion excitation. $[C]$, $[D]$ and $[F]$ matrices depend on the chosen output vectors. For a system that produces displacement and velocity responses relative to the ground and absolute acceleration responses, the state-to-output and feedthrough matrices are given as:

$$[C] = \begin{bmatrix} 1 & 0 \\ 0 & 1 \\ -M^{-1}K & -M^{-1}C \end{bmatrix}, [D] = \begin{bmatrix} 0 \\ 0 \\ M^{-1}P \end{bmatrix}, [F] = \begin{bmatrix} 0 \\ 0 \\ 0 \end{bmatrix} \tag{3.7}$$

Given the above state-space representations, $P$ is formulated as:

$$[P] = \begin{bmatrix} 1 \\ 0 \\ 0 \end{bmatrix} \tag{3.8}$$

## 3.2 System Identification

To construct the state-space matrices given in Equations (3.4) and (3.5), $M$, $C$ and $K$ matrices can either be approximated from the lumped 3-DOF model presented in Section 3.1 or can be estimated from experimental data. Considering the fact that deficiencies and discrepancies between the estimations and experimental data are often evident, implementing a system identification method tool that reveals dynamic properties of the structure is needed.

For this study, a commonly used time-domain approach, ERA is selected. Juang and Pappa (1985) proposed ERA to extract modal parameter and create a minimal realization model that replicates the output response of a linear dynamical system when it is subjected to a unit impulse. The success of this algorithm has been verified in multiple studies (Caicedo et al., 2004; Giraldo et al., 2004; Caicedo, 2011). The workflow for ERA can be summarized in five steps. Those are (i) Hankel matrix assembly, (ii) singular value decomposition, (iii) state-space realization, (iv) eigenvalue extraction and (v) model assurance.

### 3.2.1 Procedure

A discrete-time representation of Equation (3.4) with $n$-dimensional state vector, $x$; $m$-dimensional control input, $u$ and $p$-dimensional output vector, $y$ can be written as:

$$x(k+1) = Ax(k) + Bu(k) \tag{3.9a}$$

$$y(k) = Cx(k) \tag{3.9b}$$

where $A$ is $n \times n$ matrix, $B$ is $n \times m$ matrix and $C$ is $p \times n$ matrix. The matrix impulse response, known as Markov parameter sequence, can be derived from Equations (3.9a) and (3.9b):

$$Y(k) = CA^{k-1}B \tag{3.10}$$

where $Y(k)$ is $p \times m$ matrix. $Y_{ij}(k)$ is $i$th output to $j$th input at time step $k$.

***(i) Hankel matrix assembly***

As the first step of the ERA algorithm, Hankel matrix for a time step $k$ is formed:

$$H(k-1) = \begin{bmatrix} Y(k) & Y(k+1) & \cdots & Y(k+s) \\ Y(k+1) & Y(k+2) & \cdots & Y(k+s+1) \\ \vdots & \vdots & \ddots & \vdots \\ Y(k+r) & Y(k+r+1) & \cdots & Y(k+r+s) \end{bmatrix} \tag{3.11}$$

For a typical application, as a rule of thumb, $r$, row of $H(k-1)$ matrix should be at least 10 times the modes to be identified and $s$, column of $H(k-1)$ should be 2-3 times of $r$.

***(ii) Singular value decomposition***

A singular value decomposition is performed using $H(0)$:

$$H(0) = PDQ^T \tag{3.12}$$

where $P$ is $rp \times n$, $Q$ is $ms \times n$ and $D$ is $n \times n$ diagonal matrix.

***(iii) State-space realization***

By integrating $P$, $D$, $Q$ and $H(k)$, a minimum realization of the identified system in Equations (3.9a) and (3.9b) can be derived in state-space form:

$$A = D^{-1/2} P^T H(1) Q D^{-1/2} \tag{3.13a}$$

$$B = D^{1/2} Q^T E_m \tag{3.13b}$$

$$C = E_p^T P D^{1/2} \tag{3.13c}$$

where $E_p^T = [I_p \ 0]$ and $E_m^T = [I_m \ 0]$.

***(iv) Eigenvalue extraction***

Natural frequencies, damping ratios and mode shapes can be obtained by applying eigen-decomposition on the state matrix, $A$, as given in Equation (3.13a). A typical way to obtain the identified parameters is prescribed below:

$$[v, \lambda] = eig(A) \tag{3.14a}$$

$$s = \ln(\lambda) f_s \tag{3.14b}$$

$$f_{dE} = \frac{\Im(s)}{2\pi} \tag{3.14c}$$

$$\zeta_E = \frac{\Re(s)}{|s|} \tag{3.14d}$$

$$\Phi_E = E_P^T P D^{1/2} v \tag{3.14e}$$

where $v$ and $\lambda$ are eigenvectors and eigenvalues of the system in $z$-plane since state $A$ is in discrete-time form, $f_s$ is the sampling rate of the system in $Hz$, $s$ is the Laplace root of the system converted from the $z$-plane, $f_{dE}$, $\zeta_E$ and $\Phi_E$ are experimental damped frequency in $Hz$, damping ratio and complex mode shape, respectively. The experimental natural frequency of the system can be obtained as following:

$$f_{nE} = \frac{f_{dE}}{\sqrt{1 - \zeta_E}} \tag{3.15}$$

where $f_{dE}$ and $f_{nE}$ are experimentally obtained damped and natural frequencies, respectively.

Most of these operations are automated through *damp* function in MATLAB (2011).

Although for typical ERA applications mode shapes will be complex-valued, as it will be shown later in Section 3.3, model updating process requires a real mode shape. It is expected that a transformation from real to complex mode shape should maintain the original information of the identified complex mode shape to conserve dynamic characteristic of the test structure as much as possible (Panichacarn, 2006). Thus, a rotation transformation is applied to reduce the error between real and complex mode shapes:

$$\phi_{iEr} = \phi_{iE}/\phi_{1iE} \tag{3.16a}$$

$$\phi_{iEreal} = sgn\left(\Re(\phi_{iEr})\right) \odot \|\phi_{iEr}\| \tag{3.16b}$$

where $\phi_{iE}$ is the $ith$ column of $\Phi_E$, $\phi_{1iE}$ is the first element of $\phi_{iE}$, $\phi_{iEr}$ is rotated $\phi_{iE}$, $\|\phi_{iEr}\|$ is absolute value of $\phi_{iEr}$, $sgn(x)$ is the *signum* operator for $x$, $\odot$ is the element-by-element vector multiplication operator, and finally $\phi_{iEreal}$ is real mode shape of the $ith$ column of $\Phi_E$. Right hand side of Equation (3.16a) is basically a rotation transformation where $\phi_{iE}$ is normalized with respect to its first element. The procedure minimizes the imaginary part of the complex mode shape such that Equation (3.16b) is able to produce real values with a minimal error.

To understand the effect of Equation (3.16a) better, an example is presented. For a 3-DOF model as described in Equations (3.2a) to (3.2c), where system parameters are $[m_1, m_2, m_3] = [1, 1, 1]$ kg, $[c_1, c_2, c_3] = [10, 10, 10]$ N sec/m and $[k_1, k_2, k_3] = [1000, 1000, 1000]$ N/m, initial and rotated values of the first mode shape are shown in Figure 3.2. The reduction in the imaginary part should be noted.

### *(v) Model Assurance*

Quality of the identified modal parameters is estimated through model assurance indicators. A model assurance criteria introduced by Juang and Pappa (1985), known as the Model Amplitude Coherence (MAC) indicator does not always deliver the most

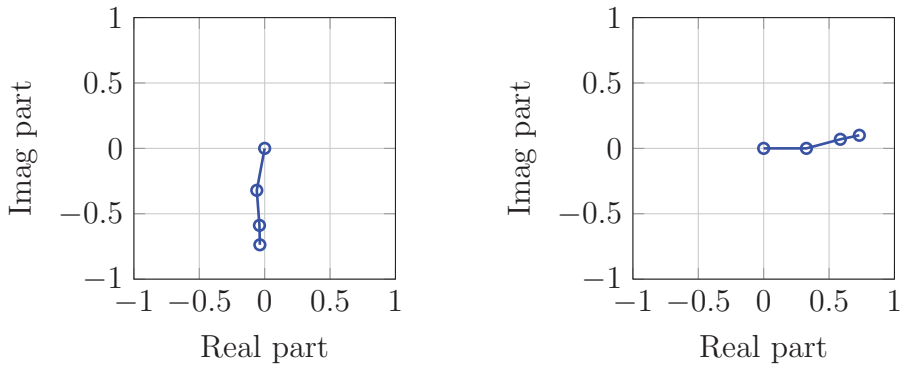


(a) Before rotation - normalized (b) After rotation - normalized

Figure 3.2: Effect of rotation transformation on the complex mode shapes

reliable values. The flaws of MAC are resolved with Extended Modal Amplitude (EMAC). EMAC is explained in detail by (Pappa, 1994).

### 3.2.2 Application

Theory behind the ERA for system identification has been explained in the previous section. In this section, (i) collection, (ii) preparation, (iii) pre-processing, and regeneration of the data is explained.

#### *(i) Collection*

ERA is effective for identifying structural characteristics, and is intended to be applied to impulse response functions. An impulse response function can be retrieved either from any type of transfer function by applying inverse Fourier transformation or directly from structural responses to an impulse. For this study, impact hammer testing is selected as the most appropriate testing methodology.

In concept, a hammer impact, which is equipped with a load cell at its tip, can produce a broadband signal at contact time and excite each mode of the structure with equal energy. For proper testing, the structure should be instrumented at several

points based on the available sensors, data channels on data acquisition system and testing plan (Trethewey and Cafeo, 1992). In typical applications, system responses are captured with accelerometers placed at critical points.

Theoretically, a single hit would suffice for ERA to capture system dynamics. However, with colored or colorless noise present, and small-scale local and global nonlinearities in the structure, some performance degradation during parametric estimations such as erroneous minimum realization or fictitious natural frequencies is expected. Performing a large number of impacts will manage the issues stated above to some extent, as it will provide more averaging for frequency domain pre-process and thus will result in higher quality data.

Lastly, between each hammer hit, system should be left in free-vibration until impact energy dies in the system substantially through structural damping.

### *(ii) Preparation*

Data gathering of an impact test should take the least effort and time, especially if the system will be excited at multiple locations. Since setting DAQ system for each hit is time consuming, all of the impact data and system response generated for a single contact point should be collected at one single run. After data collection, each hit and associated outputs can be manually parsed. To automize parsing with a minimal user-software interaction, a MATLAB script has been developed. Features such as automatic parsing and windowing has been added to align with project goals.

Essentially, script described herein manipulates and parses the impact and response data in `*.mat` file format based on user selections. These selections include: (i) minimum peak threshold for the impact force to be identified, (ii) order number of successful impacts, (iii) impact length, (iv) exponential decay window parameters for system response; and (v) pre- and post-impact boxcar window parameters for the impact force data. The procedure is summarized in the flow diagram given in Figure 3.3.

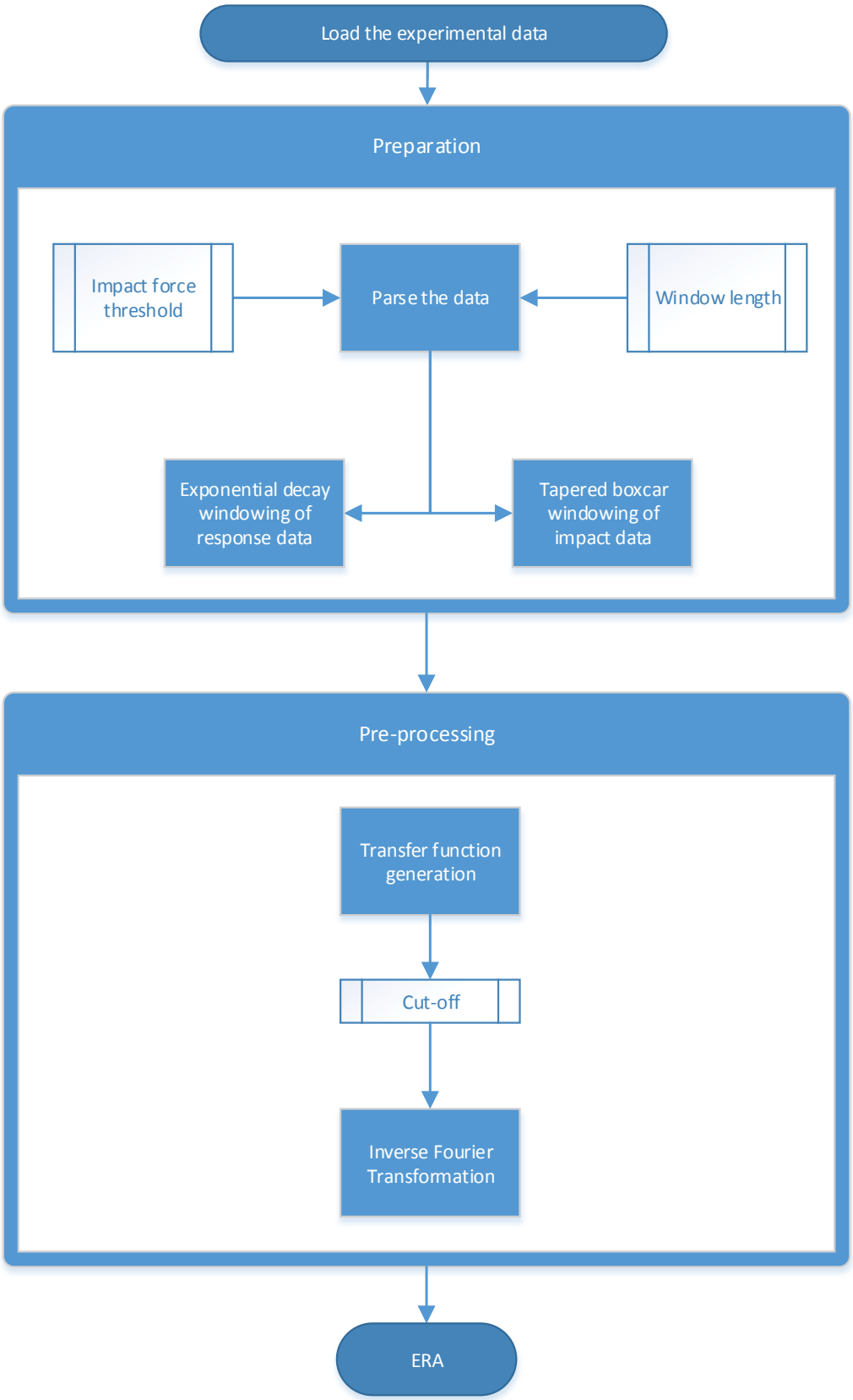


Figure 3.3: Impact data parser script workflow

As the first step, the script identifies the peaks in the impact data according to the threshold. After user manually rejects unsuccessful hits, the remaining response data is parsed based on the window length parameter.

The second step is windowing. During impact testing, the tester should wait for some amount of time between each hammer hit until system damps out completely. For lightly damped systems, waiting time can take more than a minute. In cases where structure needs to be excited, for instance, thirty times, test may take over thirty minutes. Thus, tester may choose to shorten the impact period and hit the system before it dies out. However, when a discontinued measurement is converted to frequency domain through discrete Fourier transformation (DFT), the boxcar window applied by default is going to create spectral leakage. Although spectral leakage cannot be completely prevented, the effect of it in the measurement can be minimized by the use of exponential decay window or so-called damping window for freely vibrating systems. An exponential decay window can be represented as given by Trethewey and Cafeo (1992):

$$w_{exp}(t) = \begin{cases} e^{\frac{-t}{\tau_w}} & 0 \leq t \leq T \\ 0 & T < t \end{cases} \tag{3.17}$$

where $\tau_w$ is time constant and $T$ is length of window. $\tau_w$ is chosen based on desired decay ratio:

$$\tau_w = -\frac{T}{\ln(r_{decay})} \tag{3.18}$$

where $r_{decay}$ is decay ratio in percentage. A windowed response, $y_{iw}$ should be formulated as:

$$y_{iw} = w_{exp} y_i \tag{3.19}$$

To reject the noise in the impact force, a boxcar window is applied. A boxcar function can be described as:

$$w_{box}(t) = \begin{cases} 1 & T_{prehit} < t < T_{posthit} \\ 0 & otherwise \end{cases} \tag{3.20}$$

where $T_{prehit}$ is the point of time before the impact, $T_{posthit}$ is the point of time after the impact that contains ringing of the sensor. Often, to minimize the spectral leakage, tapered half-sin is concatenated with box car function. A half-sin function is given below:

$$w_{sin-pre}(t) = sin(k_{sin} * t) \tag{3.21a}$$

$$w_{cos-post}(t) = cos(k_{cos} * t) \tag{3.21b}$$

where $k$ is a shape modifier. Finally, the tapered boxcar window becomes:

$$w_{taper}(t) = \begin{cases} 0 & t \leq T_{start} \\ sin(k_{sin} * t - T_{start}) & T_{start} < t \leq T_{prehit} \\ 1 & T_{prehit} < t < T_{posthit} \\ cos(k_{cos} * t - T_{posthit}) & t \leq T_{posthit} + T_{end} \\ 0 & t > T_{posthit} + T_{end} \end{cases} \tag{3.22}$$

where $T_{start}$ and $T_{end}$ are the start and end of the taper window, respectively. $k_{sin}$ and $k_{cos}$ should be selected in such a way that $sin(k_{sin} * t)$ and $cos(k_{cos} * t - T_{posthit})$ should yield 1 at $T_{prehit}$ and at $T_{cos}$, respectively. Tapered boxcar window based on Equation (3.22) is shown in Figure 3.4.

In conclusion, a windowed response, $y_{iw}$ should be formulated as:

$$y_{iw} = w_{taper} y_i \tag{3.23}$$

After the windowing is performed, parsed data is ready to be pre-processed in frequency domain.

Although exponential and force window functions can reduce the leakage phenomenon, it introduces bias error on the estimated frequency response functions, hence, natural frequencies and damping ratios to be identified. Therefore, it is always a good practice to compare model estimations with experimental data after system identification and model updating. The effect of windowing has been discussed in depth by Halvorsen and Brown (1977) and McConnell and Varoto (1995).

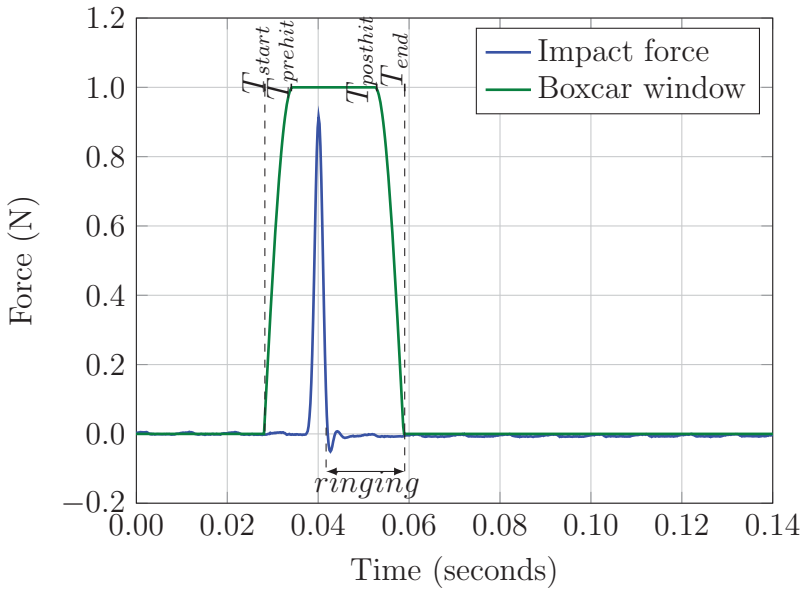


Figure 3.4: Tapered boxcar window

### *(iii) Pre-processing*

As stated before, frequency domain pre-processing of data can minimize effect of nonlinearities and noise when multiple transfer functions are averaged. Here, production and averaging of transfer functions, and reconstruction of the impulse response function (IRF) by Inverse Fourier Transformation are explained before the resulting IRF is used for ERA. Procedures involving pre-processing is summarized in Figure 3.4.

A system can be idealized as in Figure 3.5, where $h(t)$ is IRF, $x(t)$ and $y(t)$ are system inputs and outputs, respectively (Craig and Kurdila, 2006; Chopra, 1995). The impulse function can be defined as:

$$h(t) = \frac{y(t)}{x(t)} \tag{3.24}$$

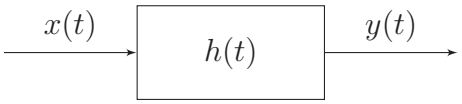


Figure 3.5: An idealization of a linear system in time domain

A linear relationship of the system output to its input can be described in the complex Laplace domain. Frequency response function, also known as, transfer function, $H(s)$ is defined as such:

$$H(s) = \frac{Y(s)}{X(s)} \tag{3.25}$$

where $Y(s)$ and $X(s)$ are the input and output in Laplace domain. Equation (3.25) can be rewritten in frequency domain:

$$H(f) = \frac{Y(f)}{X(f)} \tag{3.26}$$

or

$$H(f) = \frac{S_y(f)}{S_x(f)} \tag{3.27}$$

where $S_x$ and $S_y$ are Fourier spectrum of $x(t)$ and $y(t)$. $S_y$ and $S_x$ can be easily obtained by applying Fast Fourier Transformation to input and outputs of the system. Although Equation (3.27) is sufficient to generate a unit impulse frequency response function, for impact hammer test, system response to hammer input is more prone to noise compared to the input. To reduce the effect of noise, the frequency response function is redefined by multiplying right hand side nominator and denominator of $H(f)$ with complex conjugate of $S_y$:

$$\begin{aligned} H(f) &= \frac{S_y(f)}{S_x(f)} \\ &= \frac{S_y(f) \cdot S_y^T(f)}{S_x(f) \cdot S_y^T(f)} \\ &= \frac{G_{yy}(f)}{G_{xy}(f)} \end{aligned} \tag{3.28}$$

where $S_y^T$ is complex conjugate of $S_y$, $Gyy$ is the cross-spectral density of $x(y)$ and $y(x)$ and $Gxy$ are auto-spectral density of $x(y)$. For each impact, a new transfer function

can be constructed using the method explained above. Yet, transfer functions are affected by the noise and nonlinearities. Assuming the test structure is linear and noise is Gaussian, as many as observations necessary in transfer function form need to be arithmetically averaged as shown:

$$\begin{aligned} H_{avg}(f) &= \frac{1}{n}\sum_{i=1}^{n}\big(H_i(f)\big) \\ &= \frac{1}{n}\big(H_1(f) + H_2(f) + \ldots + H_n(f)\big) \end{aligned} \tag{3.29}$$

where $H_i$ is the transfer function from $i$th impact test and $H_{avg}$ is the averaged transfer function. At this point, optionally, to increase performance of ERA in obtaining minimum realization, higher frequencies of the transfer function can be rejected by simply narrowing down the bandwidth. Consequently, the resulting transfer function will have less information, however with no more high frequency content noise and uninterested modes. Finally, a noiseless IRF based on $H_{avg}$ can be regenerated by Inverse Fast Fourier Transformation (IFFT).

## 3.3 Model Updating

As explained before, using ERA, a state-space model of the structure can be generated based on measured quantities. This state-space representation also contains dynamic characteristic of the identified structure, i.e. natural frequencies, damping ratios and mode shapes. On the other hand, the ERA-obtained states do not contain any physical information of the structure that is not measured. Consequently, a feedback control algorithm relying on unmeasured structural responses cannot be developed since those remain unobservable. To overcome this disadvantage of the ERA, Giraldo et al. (2004) proposed a model updating method where experimental results are combined with an analytical model. According to this approach, the

stiffness and damping matrices are modified using identified natural frequencies and damping ratios as given below:

$$[K_E] = M_A \Phi_A [2\pi f_E] \Phi_A^T \tag{3.30a}$$

$$[C_E] = M_A \Phi_A (2\xi_E [2\pi f_E]) \Phi_A^T \tag{3.30b}$$

where $M_A$, $K_E$ and $C_E$ are analytical mass matrix, experimentally-modified stiffness and damping matrices, respectively. $f_E$ and $\xi_E$ represents diagonal matrix of ERA identified natural frequencies in Hertz and damping ratios, respectively. Analytical modal matrix, $\Phi_A$ is taken as $M_A$-mass normalized eigenvectors of $M_A^{-1} K_A$ where $K_A$ is the analytical stiffness matrix. Although this method produces accurate model for control design purposes, resulting model may not always accurately capture the zeros of the experimental transfer functions. A clear reason for the poor zero tracking is because the model updating method uses eigenvectors of the analytical model. If the real eigenvectors of the structure deviate from eigenvectors $\Phi_A$ of the analytical model, the modeling error may lead to low quality models, thus, semi-active controllers with lowered performance or even unstable active controllers. To overcome this problem, a new model-updating methodology promising better zeros-tracking is necessary. The proposed method herein uses mode shapes identified by ERA process. A straightforward application of modal updating based on the use of identified mode shapes can be written as below:

$$[K_E] = M_A \Phi_E [2\pi f_E]^2 \Phi_E^T \tag{3.31a}$$

$$[C_E] = M_A \Phi_E (2\xi_E [2\pi f_E]) \Phi_E^T \tag{3.31b}$$

where $\Phi_E$ is ERA identified eigenvector matrix of the structure.

However, in most cases, since eigenvector $\Phi_E$ will not be $M_A$-orthogonal (i.e. $\Phi_{E_i}^T M_A \Phi_{E_i} = 1$ where $\Phi_{E_i}$ is the $i$th column of $\Phi_E$), the resulting matrices will not be symmetric. Although $K_E$ and $C_E$ trace zeros very successfully, their asymmetry does not reconcile with the Maxwell's Reciprocal Theorem. In order to symmetrize $K_E$ and $C_E$, $M_A$ needs to be modified in such a way that, $\Phi_E$ will be $M_E$-orthogonal,

where $M_E$ is the updated mass matrix of the system. At the same time, for the sake of the problem, $M_E$ needs to be as similar as possible to $M_A$, so that $M_E$ will still comply with initial modeling assumptions. Then, the objective function is minimizing the quadratic error between $M_A$ and $M_E$ as given below:

$$min[vec(M_E - M_A)^T W vec(M_E - M_A)] \tag{3.32}$$

subject to

$$M_E = Z_E^T D_E Z_E \tag{3.33}$$

$$Z_E = \Phi_E^{-1} \tag{3.34}$$

where $vec$ is the vectorization operation, $Z_E$ is the inverse of $\Phi_E$ as given in Equation (3.34), $W$ is the weighting matrix and $D_E$ is a diagonal matrix to be found as a solution to the minimization problem given in Equation (3.32). Weighting vector $W$ can be adjusted to give more weight to the elements that need to be minimized.

Note that, Equations (3.33) and (3.34) also lead us to the flowing formula:

$$\Phi_E^T M_E \Phi_E = D_E \tag{3.35}$$

After finding $D_E$, the mass matrix, $M_E$ can be produced from Equation (3.33). Finally, by rewriting Equations (3.31a) and (3.31b), updated stiffness and damping matrices, $K_E$ and $C_E$ can be obtained as follows:

$$[K_E] = M_E \Phi_E [2\pi f_E]^2 \Phi_E^T \tag{3.36a}$$

$$[C_E] = M_E \Phi_E (2\xi_E [2\pi f_E]) \Phi_E^T \tag{3.36b}$$

It should be noted that Equation (3.36) allows fine-tuning of mode shapes, as well as natural frequencies and damping ratios, in case those parameters are not accurately identified using ERA.

The model updating methodology explained above is implemented and automated in MATLAB. To solve the minimization problem, $fminunc$, unconstrained nonlinear optimization function already implemented in MATLAB is used.

## 3.4 Limitations of the Proposed Method

Although this method supersedes the previous model updating method in various ways, it has some incompetencies either inherited from its predecessor or due to implications regarding implementation.

It has been observed that the model updating methodology may introduce small off-diagonal terms in the lumped mass matrix up to 1% of the diagonal terms. Since the updated mass matrix is not diagonal anymore, the inverse of mass matrix is not going to be diagonal. Eventually, off-diagonal terms of $M^{-1}$ will leak in $B$, $D$ and $E$ vectors. Although the leakage does not impose any problem, it should be noted that for a system presented in Equations (3.4) to (3.8), force applied at first floor will affect all internal states related to its relative accelerations, even if initial conditions are zero. A similar behavior is observed also for the systems modeled with consistent mass matrix.

The proposed method can yield symmetric matrices that comply with direct stiffness method, albeit, the results will not be in band matrix form with a bandwidth of three like shown in Equations (3.2b) and (3.2c). Thus, stiffness and damping of individual floors cannot be extracted. One potential impact of this issue is not being able to calculate exact shear force at floor level.

## 3.5 Evaluation Criteria

A set of criteria is developed to understand:

- the effectiveness of numerical model in simulating reference structure responses on the shake table
- the performance of RTHS/dRTHS conducted at Purdue to simulate reference structure responses

Focusing on global structural performance, evaluation criteria are concentrated on peak, root mean square (RMS) responses and moving RMS responses. Relative

displacement and absolute acceleration responses are selected as the basis of comparison for two cases mentioned above. The performance indices are prepared such that smaller values indicate better performance. A summary of these criteria is presented in Table 3.1. Here, $x_i$ and $\ddot{x}_i$ represent displacement relative to the ground and absolute acceleration at $i$th floor. Definition for $RMS$ of an arbitrary discrete signal, $x$ is given as:

$$RMS(x) = \sqrt{\frac{1}{n}\sum_{i=1}^{n}(x_i - \bar{x})^2} \tag{3.37}$$

Likewise, RMS error between two arbitrary signals, $x$ and $y$, is calculated as:

$$RMS(x-y) = \sqrt{\frac{1}{n}\sum_{i=1}^{n}(x_i - y_i)^2} \tag{3.38}$$

To calculate moving RMS error, a window of length $\tau$ is slid until the end of the signal. Therefore, this index is a function of time. Since RMS with sliding window is computationally demanding when implemented in loop form, convolution is used to compute the moving average of the squared signal.

## 3.6 Results

To perform model verification, the structure is identified experimentally at HIT and the results of the model updating technique are compared to the shake table response.

### 3.6.1 Initial Model

An initial model of the test structure based on the information provided in Sections 2.1 and 3.1 is established as the baseline model.

The following assumptions are made for the baseline model:

- Each column is assumed to have fixed-fixed connection with identical stiffness of $12EI/L^3$.

Table 3.1: List of evaluation criteria

| Index # | Equation | Description |
|---|---|---|
| J1 | $\frac{RMS(x_{i,\text{ actual}}(t) - x_{i,\text{ reference}}(t))}{RMS(x_{i,\text{ reference}}(t))}$ | Normalized RMS Floor Displacement Error<br>Ratio of RMS error between actual and reference value to the RMS reference value |
| J2 | $\left\lvert \frac{x^{max}_{i,\text{ actual}} - x^{max}_{i,\text{ reference}}}{x^{max}_{i,\text{ reference}}} \right\rvert$ | Peak Floor Displacement Error<br>Ratio of error between peak actual and peak reference value to the peak reference value |
| J3 | $\frac{RMS(\ddot{x}_{i,\text{ actual}}(t) - \ddot{x}_{i,\text{ reference}}(t))}{RMS(\ddot{x}_{i,\text{ reference}}(t))}$ | Normalized RMS Floor Acceleration Error<br>Ratio of RMS error between actual and reference value to the RMS reference value |
| J4 | $\left\lvert \frac{\ddot{x}^{max}_{i,\text{ actual}} - \ddot{x}^{max}_{i,\text{ reference}}}{\ddot{x}^{max}_{i,\text{ reference}}} \right\rvert$ | Peak Floor Acceleration Error<br>Ratio of error between peak actual and peak reference value to the peak reference value |
| J5 | $\frac{RMS(x_{i,\text{ actual}}(t) - x_{i,\text{ reference}}(t))}{x^{max}_{i,\text{ reference}} - x^{min}_{i,\text{ reference}}}$ | RMS Floor Displacement Error divided by the range<br>Ratio of RMS error between actual and reference value to the difference of the maximum and minimum value |
| J6 | $\frac{RMS(\ddot{x}_{i,\text{ actual}}(t) - \ddot{x}_{i,\text{ reference}}(t))}{\ddot{x}^{max}_{i,\text{ reference}} - \ddot{x}^{min}_{i,\text{ reference}}}$ | RMS Floor Acceleration Error divided by the range<br>Ratio of RMS error between actual and reference value to the difference of the maximum and minimum value |
| J7 | $\left[\frac{RMS(x_{i,\text{ actual}}(t) - x_{i,\text{ reference}}(t))}{RMS(x_{i,\text{ reference}}(t))}\right]_\tau$ | Moving RMS Floor Displacement Error<br>Ratio of RMS error between actual and reference value to the RMS reference value in a time window |
| J8 | $\left[\frac{RMS(\ddot{x}_{i,\text{ actual}}(t) - \ddot{x}_{i,\text{ reference}}(t))}{RMS(\ddot{x}_{i,\text{ reference}}(t))}\right]_\tau$ | Moving RMS Floor Acceleration Error<br>Ratio of RMS error between actual and reference value to the RMS reference value in a time window |

- $E$, Young's modulus of structural steel is equal to 220 GPa.
- $I$, moment of inertia of a single column in weak-axis is equal to 10.2 $\text{cm}^4$.
- $L$, length of the column is equal to 1.2 m.
- Damping ratio, $\xi$ for all of the structural modes is assumed to be 0.5 %.
- Each story is supported by four columns.
- Structural masses and concrete slabs are lumped to the nodes.

Using the assumptions stated above, the baseline model can be formed as:

$$[M] = \begin{bmatrix} 400.1 & 0 & 0 \\ 0 & 355.3 & 0 \\ 0 & 0 & 355.3 \end{bmatrix} \text{kg} \tag{3.39a}$$

$$[C] = \begin{bmatrix} 211.1 & -60.5 & -13.6 \\ -60.5 & 187.4 & -71.1 \\ -13.6 & -71.1 & 128.5 \end{bmatrix} \text{N sec/m} \tag{3.39b}$$

$$[K] = \begin{bmatrix} 1222.2 & -611.1 & 0 \\ -611.1 & 1222.2 & -611.1 \\ 0 & -611.1 & 611.1 \end{bmatrix} 10^3 \text{ N/m} \tag{3.39c}$$

The estimated natural frequencies are calculated 2.92 Hz, 7.96 Hz and 11.62 Hz.

### 3.6.2 System Identification: Identified Parameters

A general block diagram of the structure to be identified is shown in Figure 3.6. Here, $\ddot{x}_g$ is the disturbance as the ground motion to the system, $f_1$ is the input force applied at the first floor, also where the MR damper device will be connected, and $x_i$, $\dot{x}_i$, $\ddot{x}_i$ are the relative displacement to the ground, relative velocity to the ground, and absolute acceleration of $i^{th}$ floor, respectively.

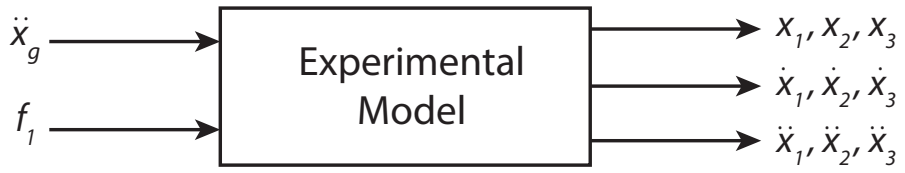


Figure 3.6: Block diagram of the structure to be identified

Structure is identified with an impact hammer by hitting to its first floor and recording the resulting acceleration responses. Due to the limited number of sensors available, multiple tests were performed. Thus, three sensors are used in each test to measure the accelerations at various locations in the weak direction. The tests are categorized based on the sensor placements at north side, mid point and south side as given in Figure 3.7. At each trial, 25 hits, each having up to 60 sec time window, are performed on the mid point of the girder at the first floor. For each set of data, including the hammer force, 4 channels are sampled at 3000 Hz. For all acceleration and hammer force sensors, 0.3 Hz and 300 Hz are selected as low pass filter and high pass filter, respectively. Interested readers can access the impact test data from the NEES Project Warehouse (Ozdagli et al., 2013a,b).

After the data are collected, post-processing is conducted involving dividing each impact response into individual time history associated with the hammer force response. A decaying exponential window of 1% to the structural responses is applied to the structural responses. Transfer functions are generated from force to acceleration for all successful hits and averaging is performed in order to increase signal to noise ratio and eliminate structural nonlinearities. Using the averaged transfer functions, impulse response functions are developed. After impulse functions are bounded to 0 Hz to 40 Hz, ERA procedure has been applied on each trial individually. 500 columns and 1500 rows with a singular value of 25 are selected as the input parameters to ERA. Finally, 11 modes are identified in the system. However, only first three modes are used since higher modes are mainly associated with the torsional movement of the structure. The identified modes and damping ratios are determined as 2.88 Hz,

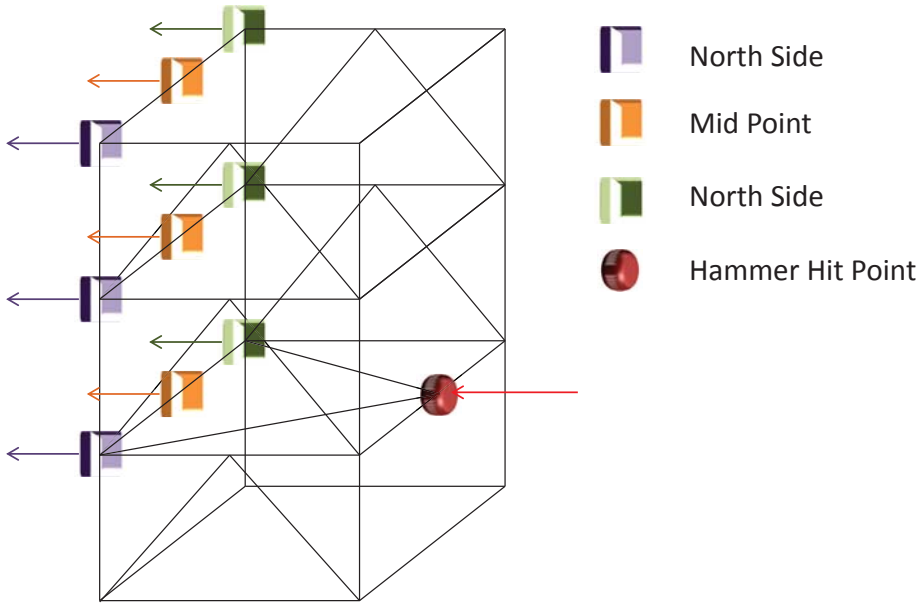


Figure 3.7: Sensor and hit location layout

8.10 Hz and 12.34 Hz; 0.57 %, 0.21 % and 0.15 %, respectively. For each ERA application, EMAC numbers yielded over 95 %. Transfer functions and phase diagrams of experimental data are compared to those generated with ERA in Figures 3.8 and 3.9. The identified mode shapes for each identified mode are represented in Figure 3.10.

As seen from comparisons and identified mode shapes, there is no significant difference between results. However, since ERA results of mid-point accelerations have better estimations on the zeros, it is decided to place the accelerometers to the mid-point for further shake table tests.

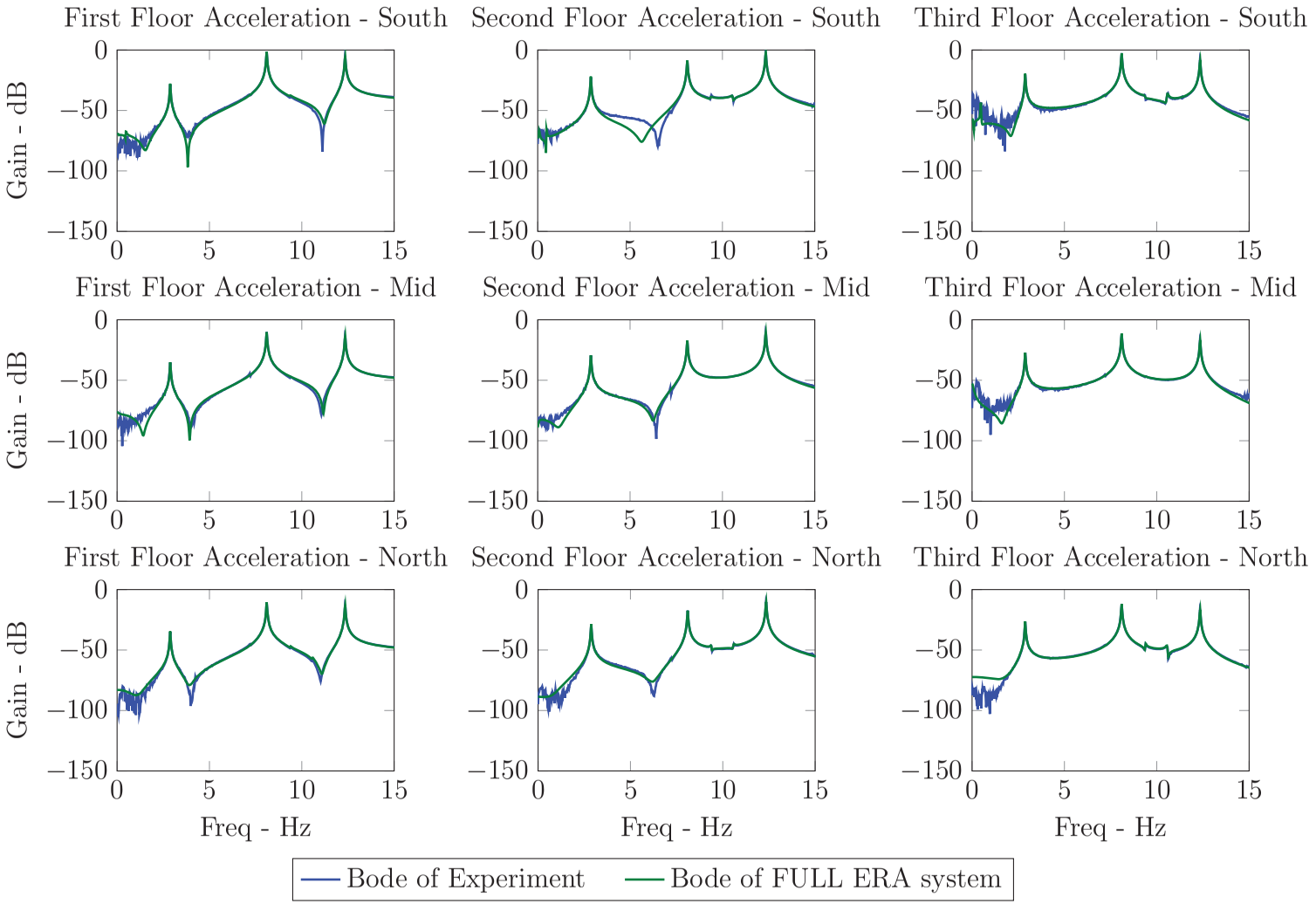


Figure 3.8: Transfer function comparison between experimental data vs ERA data

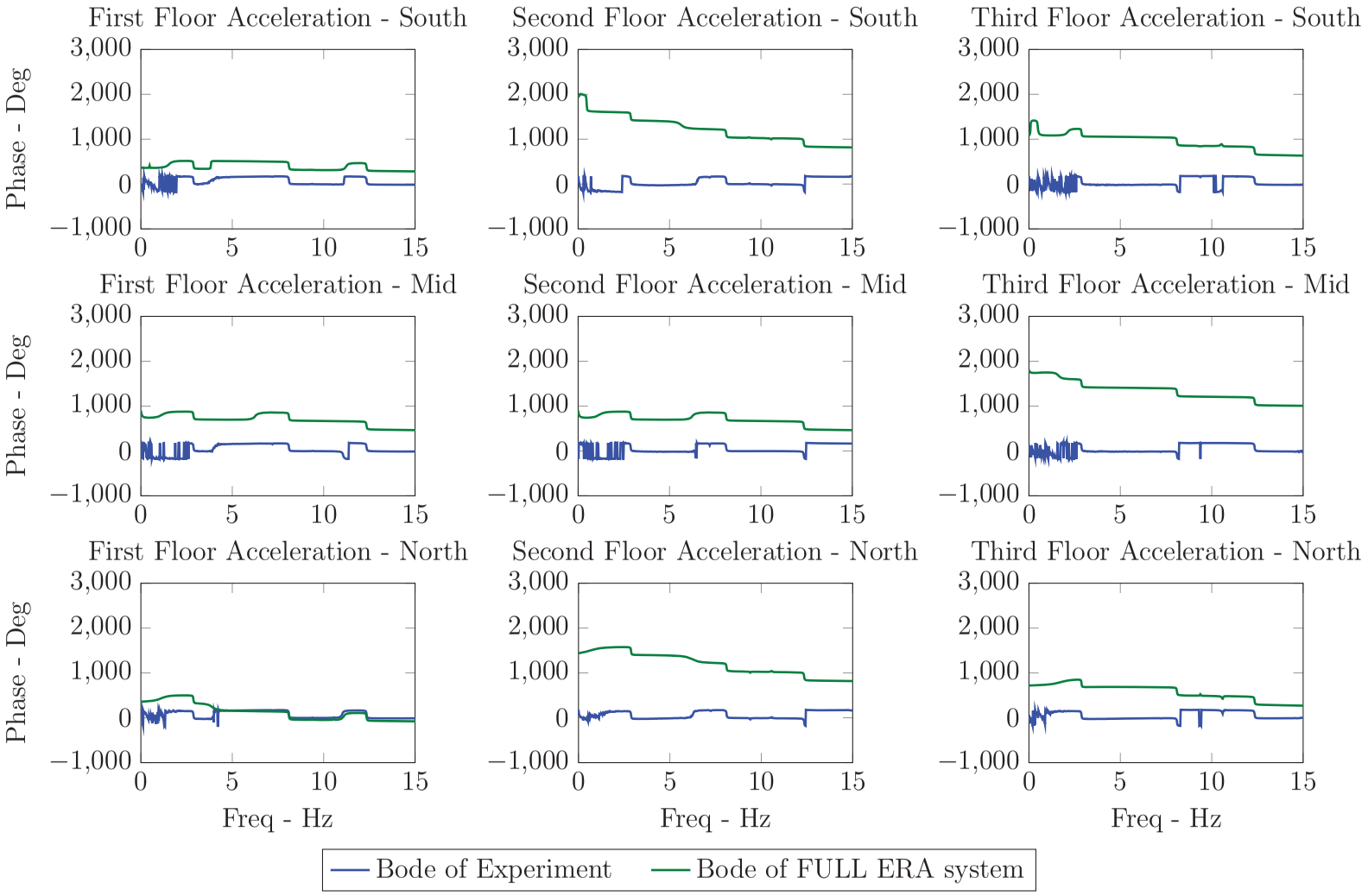


Figure 3.9: Phase diagram comparison between experimental data vs ERA data

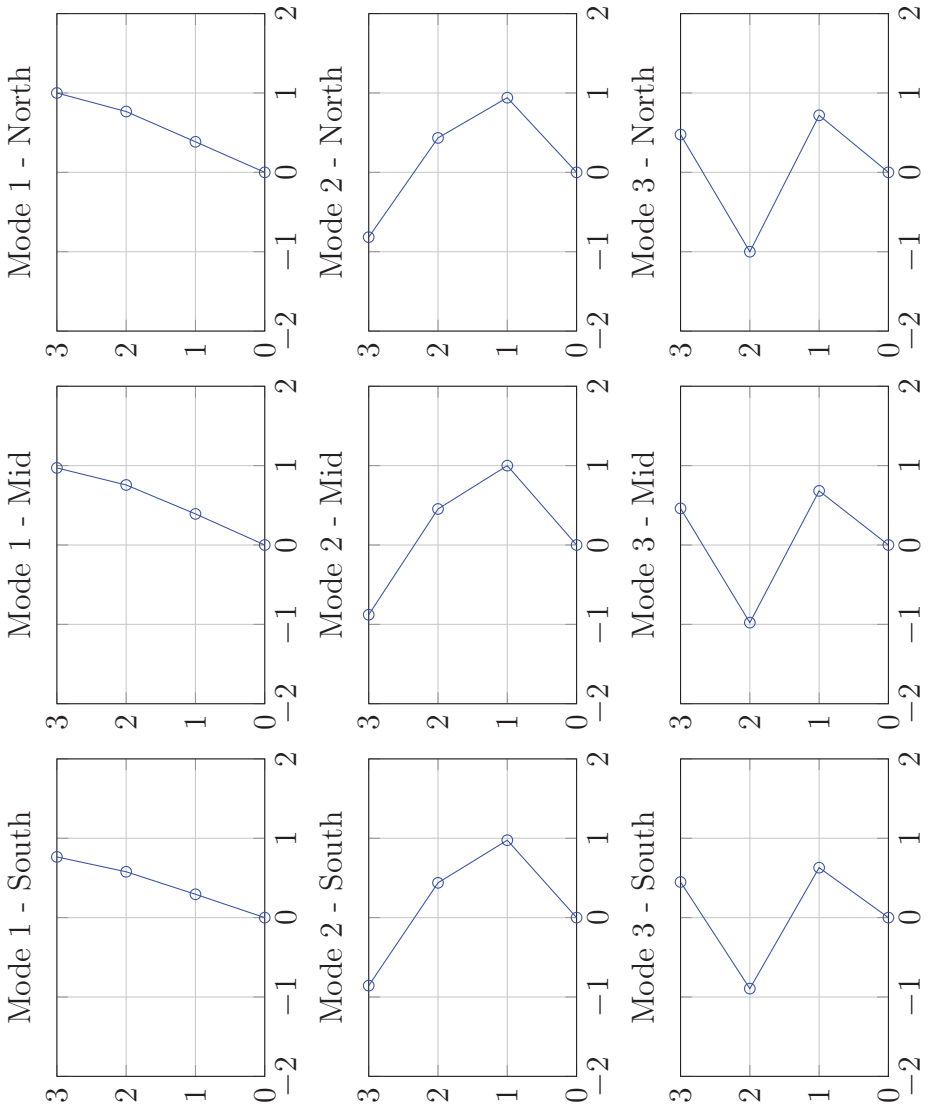


Figure 3.10: Identified mode shapes of the first three identified modes

### 3.6.3 Comparison of Model Updating Methods

Two model updating methodologies have been discussed previously in Section 3.3. According $CK$ updating method (Equation (3.30)), the following matrices are formed:

$$[M] = \begin{bmatrix} 400.1 & 0 & 0 \\ 0 & 355.3 & 0 \\ 0 & 0 & 355.3 \end{bmatrix} \text{kg} \tag{3.40a}$$

$$[C] = \begin{bmatrix} 101.6 & 3.3 & 3.8 \\ 3.3 & 93.3 & 6.2 \\ 3.8 & 6.2 & 96.2 \end{bmatrix} \text{N sec/m} \tag{3.40b}$$

$$[K] = \begin{bmatrix} 1316.4 & -703.8 & 30.5 \\ -703.8 & 1357.1 & -680.2 \\ 30.5 & -680.2 & 649.8 \end{bmatrix} 10^3 \text{ N/m} \tag{3.40c}$$

For the $MCK$ update method (Equation (3.36)), there are 9 components, each corresponding to an element in $M$ matrix. Given a weighting vector, $W$ in the form of $I_9$, the identified $MCK$ system based on the identified parameters is given as:

$$[M] = \begin{bmatrix} 419.1 & 2.6 & 2.4 \\ 2.6 & 359.1 & 10.1 \\ 2.4 & 1.1 & 325.9 \end{bmatrix} \text{kg} \tag{3.41a}$$

$$[C] = \begin{bmatrix} 91.4 & -1.7 & 0.3 \\ -1.7 & 75.23 & -0.1 \\ -0.1 & -0.1 & 69.0 \end{bmatrix} \text{N sec/m} \tag{3.41b}$$

$$[K] = \begin{bmatrix} 1446.7 & -726.0 & 44.7 \\ -726.0 & 1299.6 & -615.9 \\ 44.72 & -609.3 & 552.3 \end{bmatrix} 10^3 \text{ N/m} \tag{3.41c}$$

Readers should note that all matrices from $CK$ and $MCK$ methods are symmetric but have small off-diagonal terms that are not larger than 10 % of diagonal elements.

Transfer functions of experimental data collected from mid-point accelerometers upon impact, initial analytical model estimation and updated models are compared in Figure 3.11.

As seen from the figures, it is evident that the proposed $MCK$ updating method is superior not only in capturing zeros but also peaks, compared to $CK$ updating method.

### 3.6.4 Model Verification

For the validation of the model, structural responses of the seismically excited, uncontrolled system are compared to updated model. El Centro, Kobe and Morgan Hill earthquakes explained in Section 2.3.3 are chosen as the disturbance (Figure 3.6). The simulated earthquake motion measured on the shake table (ST) by accelerometers is used as the input to the analytical simulation (AS) of the model given in Equation (3.41). For the basis of the comparisons, the experimental displacement and acceleration records are compared to analytical simulation responses. Experiments and simulations, both are conducted at a rate of 5000 Hz.

The comparison plots are given in Figures 3.12 to 3.14. RMS and peak response errors are tabulated in Table 3.2. Only the first 25 seconds of data is processed to calculate the given errors. All values are given as percentages.

From Table 3.2, it is reported that average peak error of floor accelerations and displacements are ranging from 6 % to 8 %. For the RMS response categories, the average error is varying from 10 % to 14 %. The overall criteria average yields about 10 % error for all three earthquakes.

Among three earthquakes, largest RMS error has occured during Kobe earthquake both for displacement and accelerations. Similarly, largest peak displacement and acceleration errors are reported for the Morgan Hill earthquake.

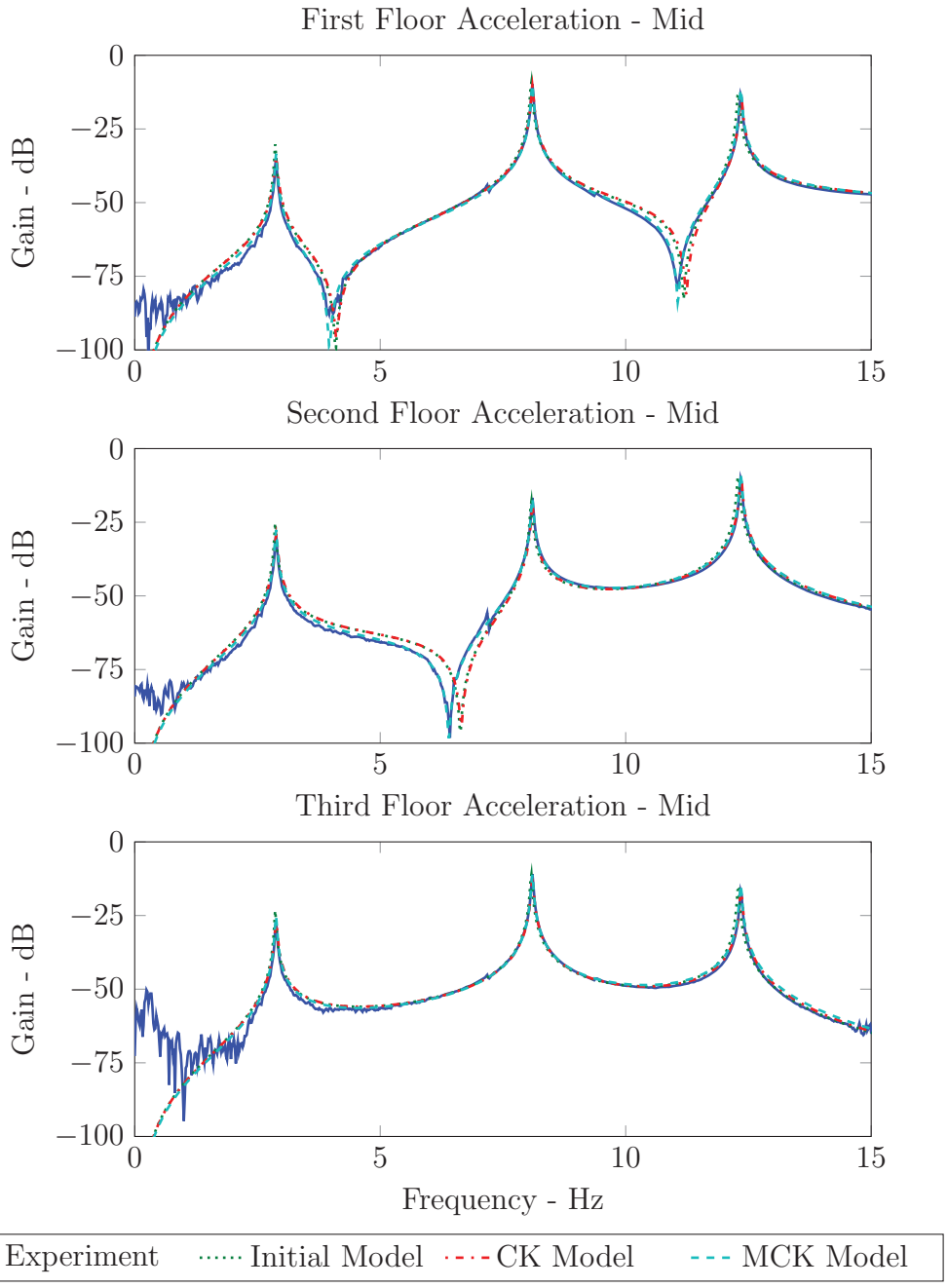


Figure 3.11: Transfer function comparison between experimental data and updated models

It is natural that systems having been identified based on impact testing parameters may behave differently when excitation input used for the model validation is a

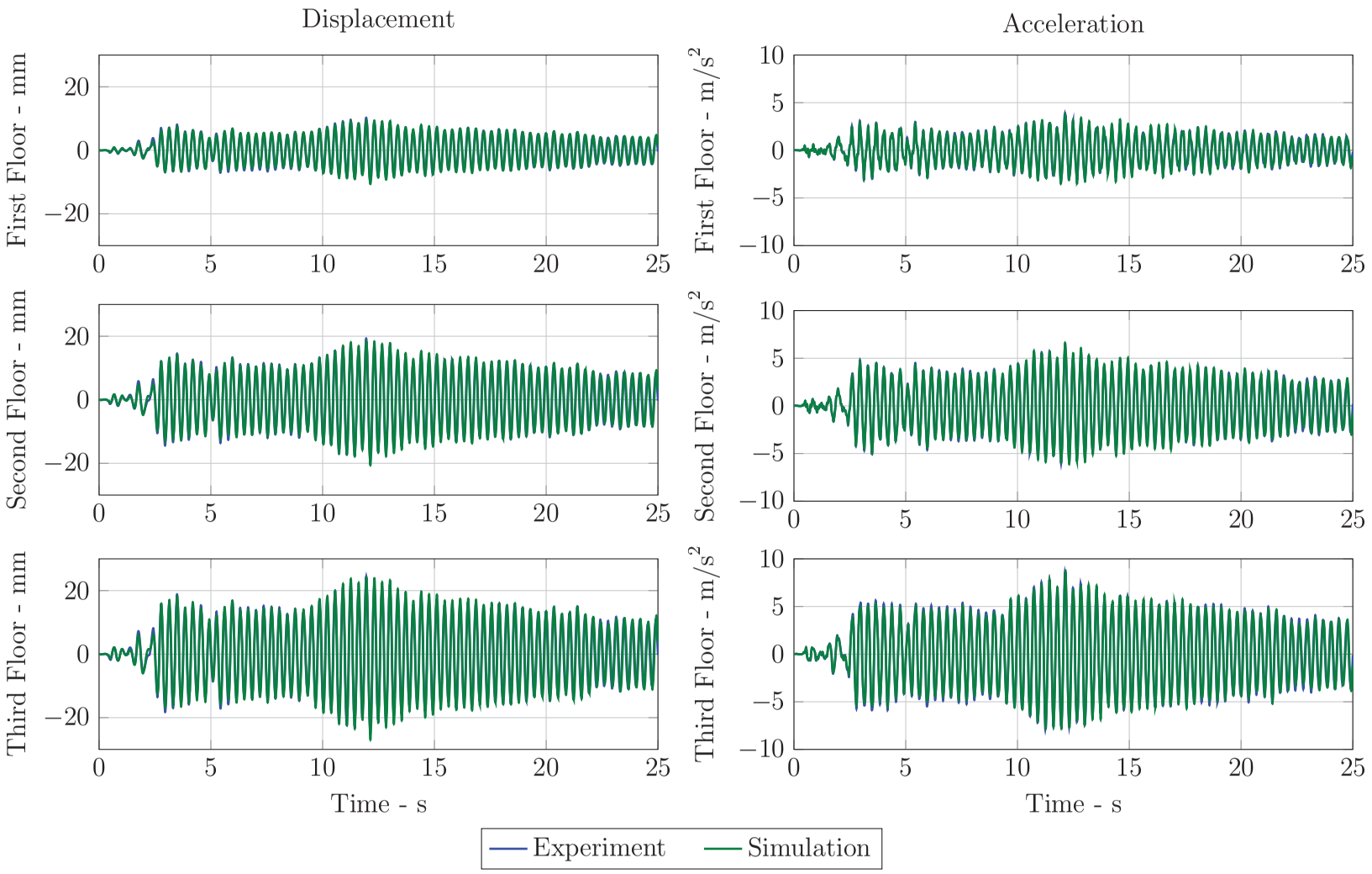


Figure 3.12: El Centro earthquake response comparison in time domain for ST–AS

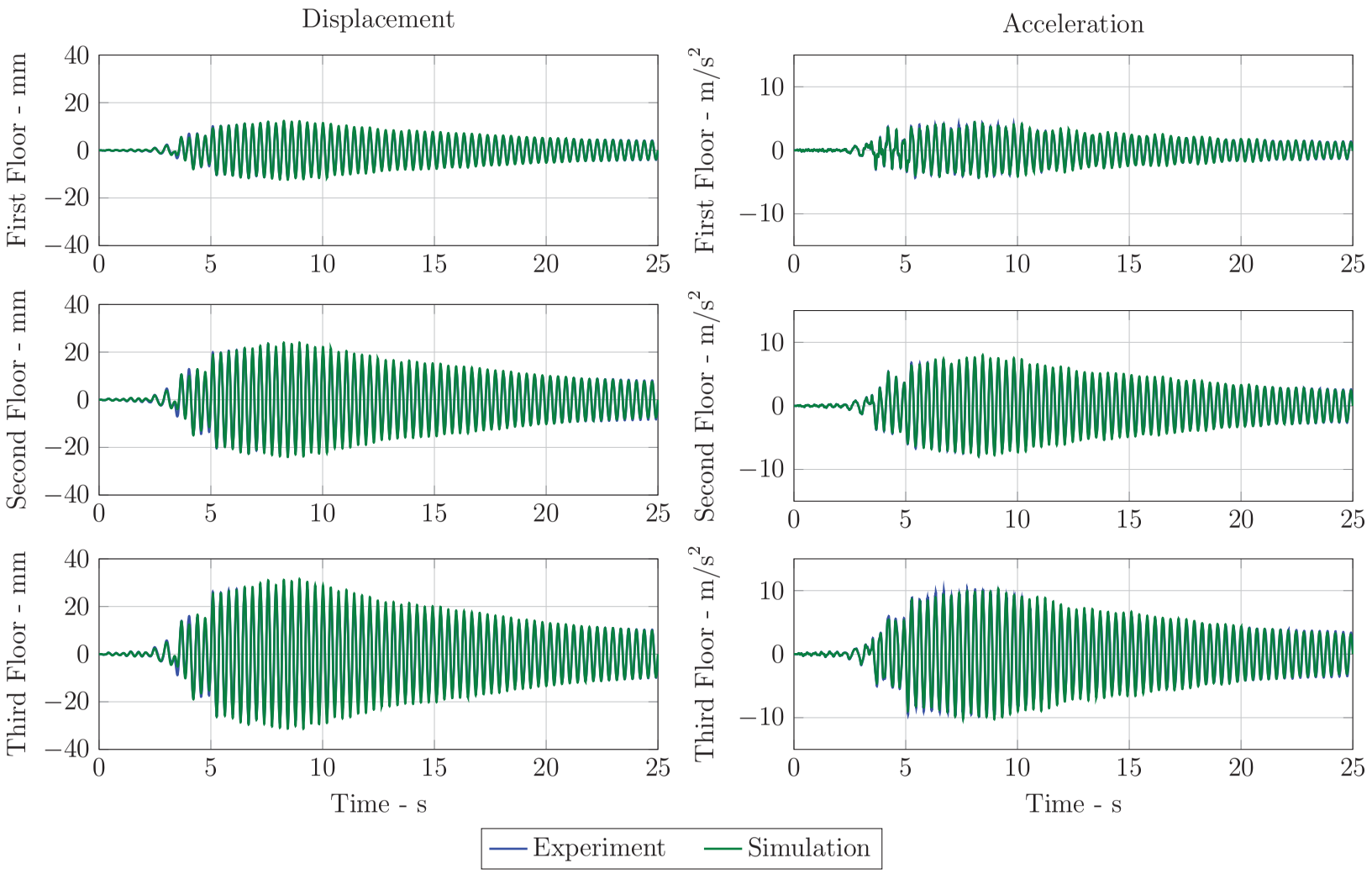


Figure 3.13: Kobe earthquake response comparison in time domain for ST–AS

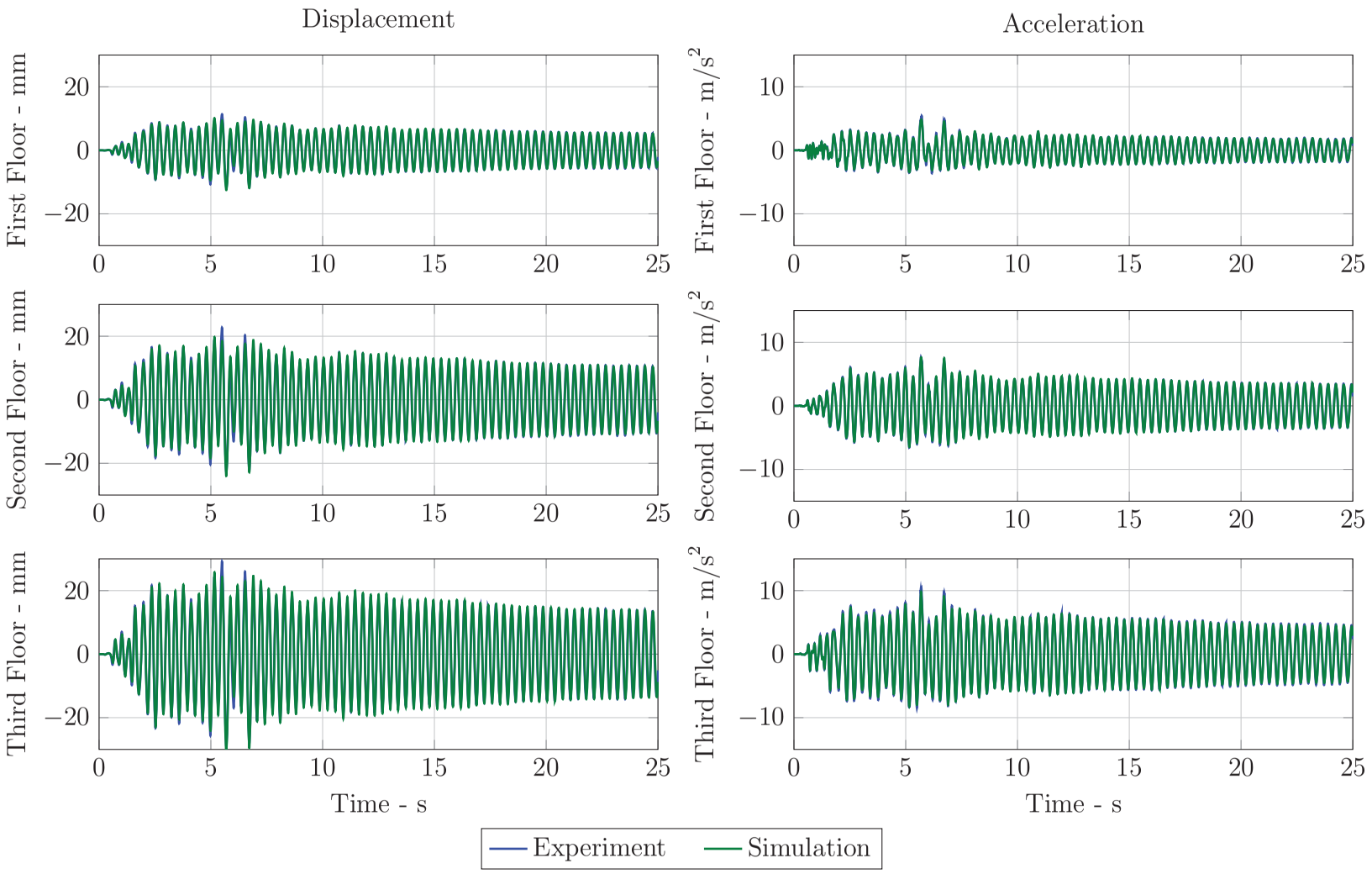


Figure 3.14: Morgan Hill earthquake response comparison in time domain for ST–AS

different source, e.g. ground motion. Dynamic characteristic of the system in time domain is often ignored while frequency domain processes linearize the system that contains small local nonlinearities and other dynamic impurities such as out-of-plane movements or torsion.

After all, a model is a mathematical explanation of the system it represents. User requirements define a basis for the assumptions made to eliminate discretizations at the expense of modeling inaccuracies. Development of a computationally inexpensive model due to time constraints of hard real-time simulation is a major requirement for this study.

Table 3.2: Evaluation criteria for model verification

| Ground Motion | Location | Evaluation Criteria | | | | Criteria |
|---|---|---|---|---|---|---|
| | | J1 | J2 | J3 | J4 | Average |
| El Centro | First Floor | 8.17 | 12.08 | 0.65 | 15.25 | 9.04 |
| | Second Floor | 4.81 | 10.92 | 1.22 | 10.21 | 6.79 |
| | Third Floor | 1.54 | 11.46 | 1.56 | 10.07 | 6.16 |
| Kobe | First Floor | 5.14 | 13.85 | 4.09 | 17.31 | 10.10 |
| | Second Floor | 2.71 | 14.80 | 10.16 | 14.45 | 10.53 |
| | Third Floor | 4.82 | 16.23 | 1.58 | 12.98 | 8.91 |
| Morgan Hill | First Floor | 10.95 | 10.70 | 10.68 | 9.28 | 10.40 |
| | Second Floor | 13.19 | 11.07 | 0.20 | 7.41 | 7.97 |
| | Third Floor | 11.84 | 11.24 | 5.96 | 7.79 | 9.21 |
| EQ Average | First Floor | 8.09 | 12.21 | 5.14 | 13.95 | 9.85 |
| | Second Floor | 6.90 | 12.26 | 3.86 | 10.69 | 8.43 |
| | Third Floor | 6.07 | 12.98 | 3.03 | 10.28 | 8.09 |

## 3.7 Conclusion

To validate dRTHS with experimental data, an accurate model of the test structure is necessary. In this chapter, theoretical background on system identification via dynamic impact hammer testing and novel MCK model updating methodology based on identified structural parameters are described. To verify the proposed updating method, the test structure is excited using shake table when no MR damper device is attached and the global responses of the system to several ground motions were compared to those of pure numerical model.

Overall, the new model updating method has proven to be superior compared to its predecessors for estimating non-observable states while relying completely on identified structural characteristics.

# CHAPTER 4
# MAGNETO-RHEOLOGICAL DAMPER CHARACTERIZATION AND SEMI-ACTIVE VIBRATION CONTROL DESIGN

Both RTHS and dRTHS setups at IISL use a magneto-rheological damper as the physical substructure for the validation tests. However, the damper utilized during the shake table tests conducted at HIT is different from the one that is used for Purdue tests. For the sake of a fair comparison between shake table and dRTHS results, the main differences between two damper should be understood. This chapter focuses on the working principle, modeling and semi-active control of MR damping devices. Section 4.1 presents a brief background on vibration control and the development idea behind semi-actively controllable devices. Section 4.2 explains behavior characterization and modeling procedure of the MR dampers used at HIT and IISL for this study. In addition, this chapter discusses the main differences of physics in HIT and Purdue damper and prescribes a method to describe one damper in terms of the other one, mathematically. In Section 4.3, the theory behind a common semi-active controller, clipped-optimal control algorithm is introduced, including its implementation. Finally, a summary of this chapter is presented.

## 4.1 Introduction

The seismic performance of a building is related to the damage and loss its structural and non-structural elements can take during an earthquake (Deierlein et al., 2010). Although aseismic design practices improve perseverance of civil structures and reduce life loss significantly by sacrificing non-structural elements, severe economic losses may be still inevitable considering dynamic nature of ground motions (Constantinou et al., 1998). ASCE (2007) provides a guideline on three performance

levels: Immediate Occupancy; Life Safety; and Collapse Prevention. By separating structural frame from energy dissipative structural elements and adding vibration control devices, an improvement in the safety level of buildings can be achieved.

Roots of vibration control reach back to 1972 with the conceptual introduction by Yao (1972). From this date forward, the evolution of the civil engineering field in structural control has been rapid, attracting many researchers for decades and the topic still continues to mature (Housner et al., 1997). Among vibration control devices currently available on the market, passive damping devices are often considered as the first solution to control structural vibration since they can dissipate energy directly by increasing the damping of the structure. As an example to this device category, passive base isolation systems for seismic protection have become an accepted design strategy in low- and medium-rise buildings, in US and worldwide (Kelly and Konstantinidis, 2011). Even though those devices are commonly used in the practice, they may not be, in fact, effective for every type of excitation, especially where stochastic nature of the input governs its overall behavior (Chang et al., 2009). To overcome the limitations of passive devices, active control strategies have been developed. Essentially, active devices can adapt themselves to the excitation and structural responses by imposing external forces supplied by actuators (Spencer and Nagarajaiah, 2003). For successful operation of those devices, uninterrupted power source for actuation and computer systems, that monitor structural responses and enforce command to these devices based on a predefined control strategy, are needed. An extensive study on the effectiveness of this device type is explored by Dyke (1996) and Loh et al. (2007).

As a major drawback, the active control device may be ineffective or at risk of becoming unstable in such cases where uncertainties and disturbances in the system affect structural integrity. To ensure a fail safe operation of control system and still to minimize the structural vibration, a new generation of control devices have been developed. Namely, semi-active devices that combine best features of passive and active control system offers a great range of adaptability and reliability (Soong and Spencer,

2002). By nature, a semi-active device is a controllable passive device. By using small amount of external power of ≈100 W, system stiffness and damping characteristics can be modified via control signal tuned according to structural responses, and system can *consume* the motion of the structure to develop control forces. The device does not increase mechanical energy in the structure and bounded input - bounded output stability is guaranteed during its operation. Moreover, in the event of loss of power due to impact loads caused by earthquakes, the system can still rely on its passive damping features.

Vibration control using semi-active force generators dates back to 1974 (Karnopp et al., 1974). Among many semi-active devices developed so far, MR fluid dampers have received a lot of attention due to their reliability and adaptability, in the last decade. A typical MR damper contains a special type of fluid called MR fluid that consists of a suspension of micron-sized magnetic iron particles that can be controlled with the help of magnetic field. By exposing to the magnetic field, the viscous MR fluid can turn into a semi-solid state instantly and generate large amount of resisting forces, as shown in Figure 4.1. Since an appropriate magnetic field can be imposed with a very small amount of electrical current, MR dampers are counted as sustainable devices. Combining high reliability with meager power consumption, the MR damper becomes a strong candidate for vibration control applications. An illustration of MR damper is provided in Figure 4.2.

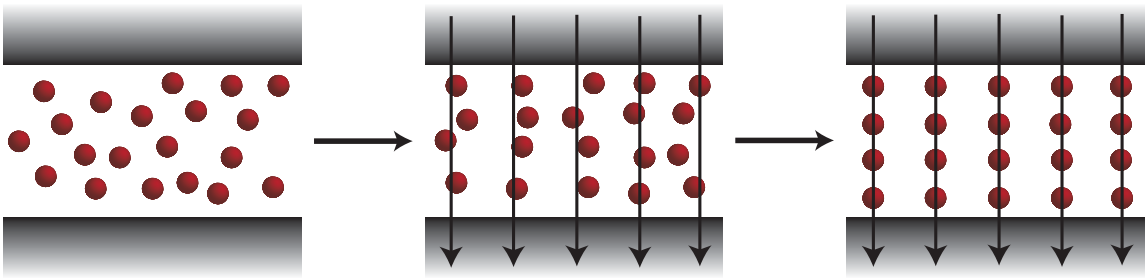

Figure 4.1: Particulate alignment in MR fluid

Pilot studies conducted by Dyke et al. (1996b) and Johnson et al. (1998) demonstrated through laboratory experiments that MR damper can reduce seismic response of structures compared to passive configurations. In addition, the success of this novel technology has been proven in small-scale mechanical systems such as vehicular suspension by Karkoub and Zribi (2006) and large-scale civil engineering structures as in Dongting Lake Cable-stayed Bridge, China by Chen et al. (2003) and National Museum of Emerging Science and Innovation, Tokyo. To persuade contractors, especially in US, hesitant to apply MR damper technology on current structures and future designs, many research projects nationwide are focused on investigation of the effectiveness of MR dampers and development of appropriate design procedures (Friedman et al., 2010; Jiang and Christenson, 2011; Phillips and Spencer, 2013).

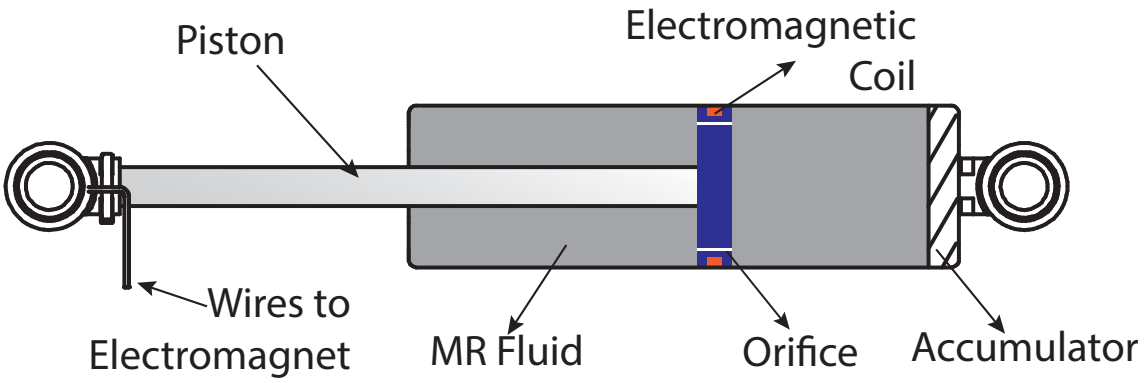


Figure 4.2: MR damper internals

## 4.2 Damper Identification and Modeling

MR dampers are highly nonlinear devices and their force-velocity relationship shows a hysteretic behavior that cannot be easily represented using simple mathematical relationships (Zapateiro de la Hoz, 2009). There has been serious effort on modeling of MR damper hysteresis to ease the implementation and performance evaluation of new controllers and to simulate the behavior in numerical analyses and real-time hybrid simulations where experimentation in full-scale is not possible. As for

damper models, there exists two mainstream models: parametric and non-parametric. While parametric models are developed loosely based on mechanical properties of the damper, non-parametric models do not have a physical ground (Sahin et al., 2010). A tree of known models are listed in Figure 4.3. This dissertation will focus on a member of parametric model family, the phenomenological Bouc-Wen model introduced by Dyke et al. (1996b) and Spencer et al. (1997).

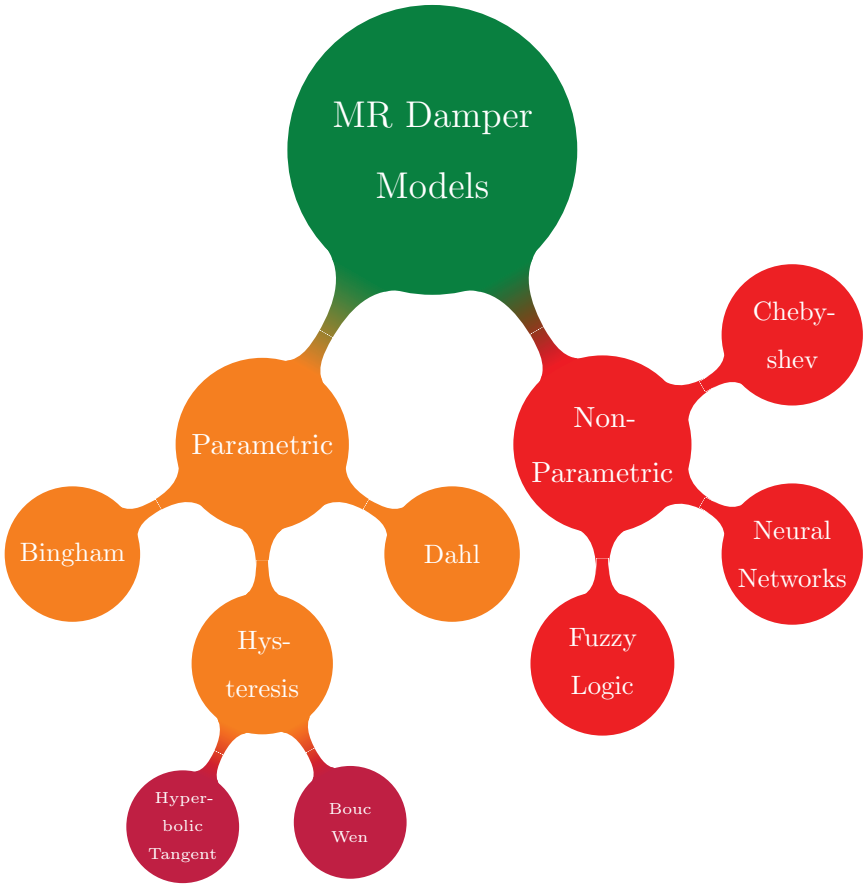


Figure 4.3: MR damper models

### 4.2.1 Modeling of the MR Damper

A phenomenological MR damper was proposed by Spencer et al. (1997). This model, which combines Bouc-Wen equations proposed by Bouc (1971) and Wen (1976)

with a series of springs and dashpots in parallel, was sufficient in simulating dynamics of prototype dampers by Lord Corp. A mathematical idealization of this model is shown in Figure 4.4. In addition, a simplified version of Bouc-Wen model was developed by Dyke et al. (1996b) with the aim to portray force-velocity characteristics of a specific MR damper family more accurately. This dissertation will focus on the complex MR damper model.

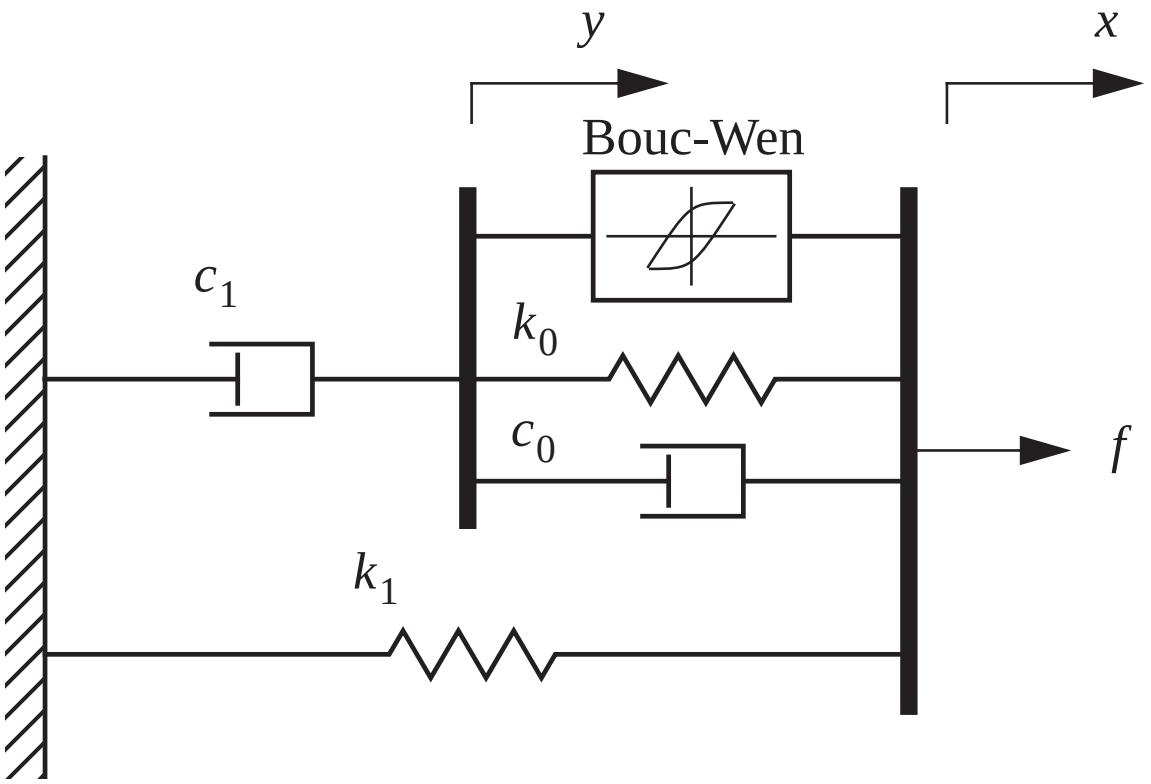


Figure 4.4: Phenomenological Bouc-Wen hysteresis model of the MR damper

According to phenomenological Bouc-Wen model, an MR damper can be characterized by the following equations:

$$c_1\dot{y} = \alpha z + k_0(x - y) + c_0(\dot{x} - \dot{y}) \tag{4.1a}$$

$$\dot{z} = -\gamma|\dot{x}_d - \dot{y}|z|z|^{n-1} - \beta(\dot{x}_d - \dot{y})|z|^n + A(\dot{x}_d - \dot{y}) \tag{4.1b}$$

$$F = \alpha z + c_0(\dot{x} - \dot{y}) + k_0(x - y) + k_1(x - x_0) \tag{4.1c}$$

where $F$ represents the total damper force, $k_1$ represents the accumulator stiffness, $c_0$ represents the viscous damping observed at larger velocities, $c_1$ produces roll-off at low velocities, $k_0$ controls the stiffness at large velocities and $x_0$ is the initial displacement of spring, $k_1$.

For a passive damper system, where voltage kept constant, identifying the parameters mentioned above is adequate. However, for achieving optimal performance, a semi-active control scheme needs to be implemented through commanding voltage signal using a current driver. In view of that, any change in voltage will create a fluctuation in the magnetic field. In other words, damping constants given in Equation (4.1) will vary virtually linearly with the applied voltage. The equations given below reveal this relationship:

$$\alpha(u) = \alpha_a + \alpha_b u \tag{4.2a}$$

$$c_0(u) = c_{0a} + c_{0b} u \tag{4.2b}$$

$$c_1(u) = c_{1a} + c_{1b} u \tag{4.2c}$$

$$\dot{u} = -\eta(u - v) \tag{4.2d}$$

where $v$ and $u$ are the command voltage sent to current driver and filtered voltage, respectively, and $\eta$ is the lag constant. Equation (4.2d) can be recognized as a filter that defines a basic model of the current driver and dynamics of MR fluid reaching rheological equilibrium.

Equations (4.1) and (4.2) can be implemented as an input-output block or hard-coded inside embedded function block in MATLAB/Simulink (MATLAB, 2011).

### 4.2.2 Identification Process

The damper parameters mentioned in the Equation (4.1) are determined based on characterization tests. In a typical parameter identification process, for each supply voltage level, the damper attached to an actuator is excited with a sinusoidal displacement and damper reaction force is measured. Since MR damper is a nonlinear

device, its behavior may change with respect to the frequency and amplitude for the given displacement. Thus, for the sake of best performance in characterization, the frequency and amplitude of the sine wave should be adjusted according to the characteristic dynamics of the test structure, to which damper is going to be attached.

To obtain the parameters related to each voltage supplied to the damper, *lsqcurvefit*, nonlinear curve-fitting algorithm is used, which has already been implemented in MATLAB. The identification process should be set up in such a way that different voltage levels should yield same values for $k_0$, $k_1$, $\gamma$, $\beta$ and $A$, while varying $\alpha$, $c_0$ and $c_1$. Since the parameters $n$, $\eta$ and $x_0$ are pre-defined based on damper properties, they are not required to be part of the curve-fit algorithm. Finally, using characterization results and Equation (4.2), $\alpha_a$, $\alpha_b$, $c_{0a}$, $c_{0b}$, $c_{1a}$ and $c_{1b}$ are calculated.

### 4.2.3 Damper Characterization Results

In this section, the identification process explained above are applied to MR dampers located at HIT and IISL/Purdue. The characterization results of those dampers, as well as representation of Purdue damper with HIT damper equations are also given in subsequent sections.

#### *(i) HIT Damper*

Characterization tests conducted at HIT are performed with MR damper #RD-1005-3 attached to the uniaxial servohydraulic load frame (see Section 2.4). A sinusoidal displacement input with a magnitude of 5 mm at a frequency close to the first mode of the test structure, 2.9 Hz is tested, when the damper is subjected to constant voltage levels of passive-off (0 V) and -on (1.7 V). Since damper characteristics are different between pushing and pulling state, load response is detrended to remove the offset.

The force-time history, force-displacement and force-velocity relationships are given in Figure 4.5. In Figure 4.6, comparison between the experimentally obtained

responses and the identified Bouc-Wen model is presented. It is observed that the Bouc-Wen model is effective at capturing the dampers behavior. Optimization routine yielding Bouc-Wen model parameters are listed in Table 4.1. A relative standard deviation error of 15 % to 18 % is found between experimental data and model.

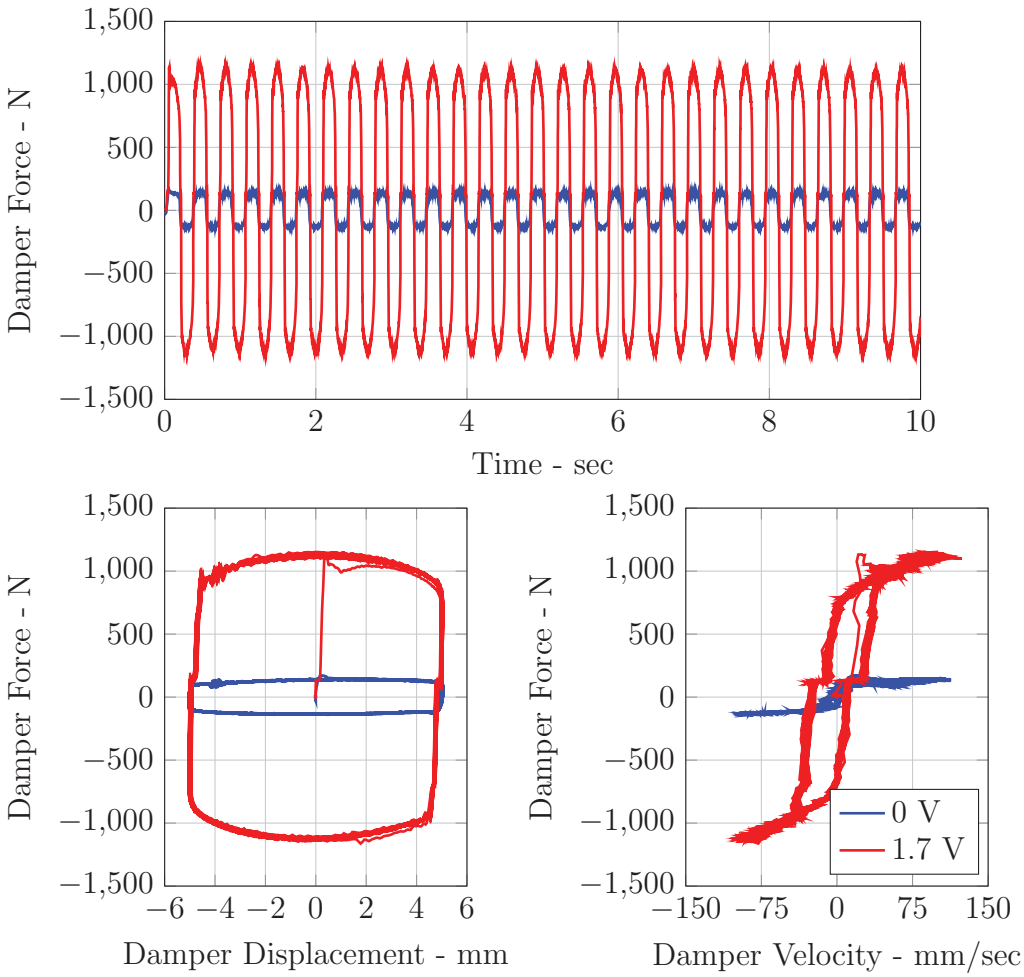


Figure 4.5: HIT MR damper experimental data for 0 V and 1.7 V constant voltage levels

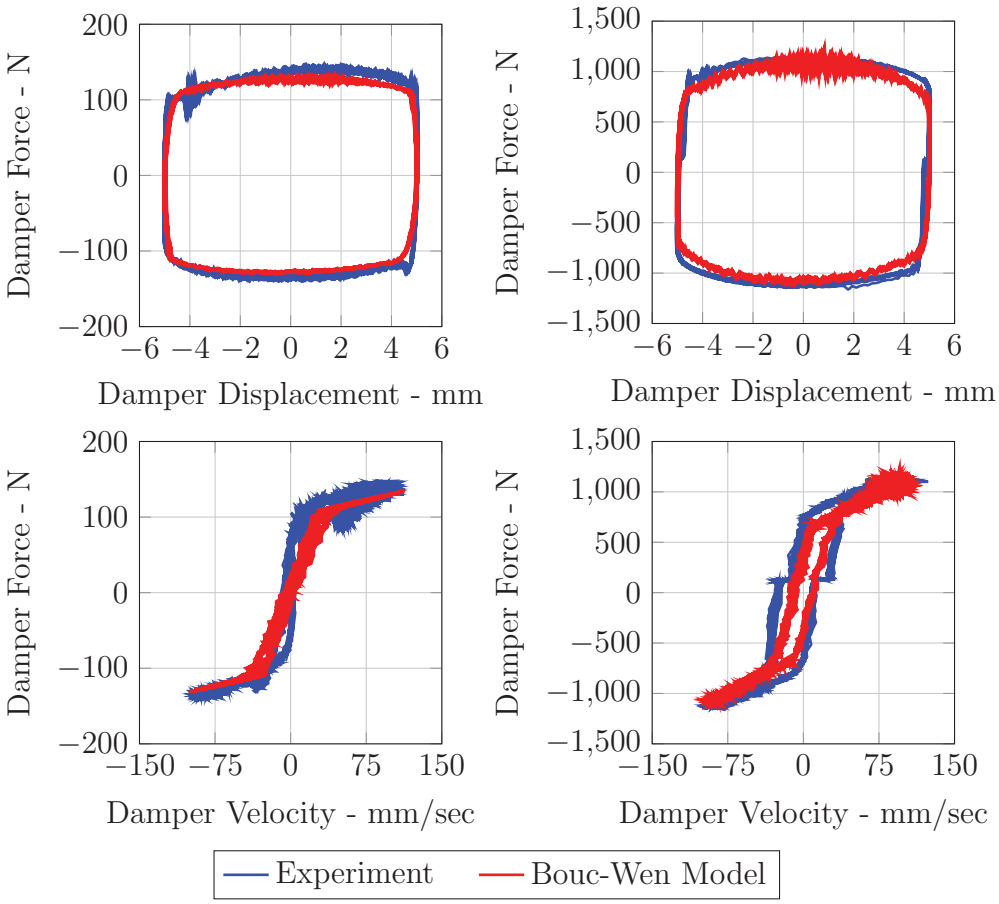


Figure 4.6: Comparisons for HIT MR damper experimental data vs identified model

### *(ii) Representation of Purdue Damper with HIT Damper Behavior*

Since MR damper and current driver used at HIT are different from the devices used at IISL, it is expected the change in mechanical properties of these devices will affect the damper behavior.

Therefore, to perform successful dRTHS tests and understand sources of experimental errors due to the use of physical substructures, it is imperative that a comparison between their mechanical behaviors should be employed. For this reason, both dampers are subjected to constant voltage levels in passive-off and -on modes while driven by a sinusoidal displacement input damper with a magnitude of 5 mm at 2.9 Hz. The comparison results are presented in Figure 4.7.

Table 4.1: Identified Bouc-Wen model parameters for HIT damper

| Parameter | Value | Unit |
|---|---|---|
| $\alpha_a$ | 2740.734 | $\mathrm{N\,m^{-1}}$ |
| $\alpha_b$ | 10010.25 | $\mathrm{N\,m^{-1}\,V^{-1}}$ |
| $c_{0a}$ | 175.13 | $\mathrm{N\,sec\,m^{-1}}$ |
| $c_{0b}$ | 1709.24 | $\mathrm{N\,sec\,m^{-1}\,V^{-1}}$ |
| $c_{1a}$ | 3353.68 | $\mathrm{N\,sec\,m^{-1}}$ |
| $c_{1b}$ | 175.13 | $\mathrm{N\,sec\,m^{-1}\,V^{-1}}$ |
| $k_0$ | 1940.41 | $\mathrm{N\,m^{-1}}$ |
| $k_1$ | 1.58 | $\mathrm{N\,m^{-1}}$ |
| $\gamma$ | 36332.07 | $\mathrm{m^{-2}}$ |
| $\beta$ | 36332.07 | $\mathrm{m^{-2}}$ |
| $A$ | 155.32 | - |
| $x_0$ | 0 | m |
| $n$ | 2 | - |
| $\eta$ | 60 | sec |

It is observed that two dampers show similar passive-off (0 V) behavior before the saturation occurs, both in force-displacement and force-velocity relationships. On the other hand, at peak saturation level, Purdue damper is generating 80 N more force than HIT damper. As for the passive-on mode, the force generated at 1.7 V for HIT damper is equivalent to the behavior of Purdue damper at 2.1 V. The two dampers show similar force-displacement and force-velocity relationships.

Based on the observations, to simulate HIT damper on the shake table on a RTHS/dRTHS platform at IISL/Purdue, the Purdue damper should be driven at constant 0 V and 2.1 V for passive-off and -on modes, respectively.

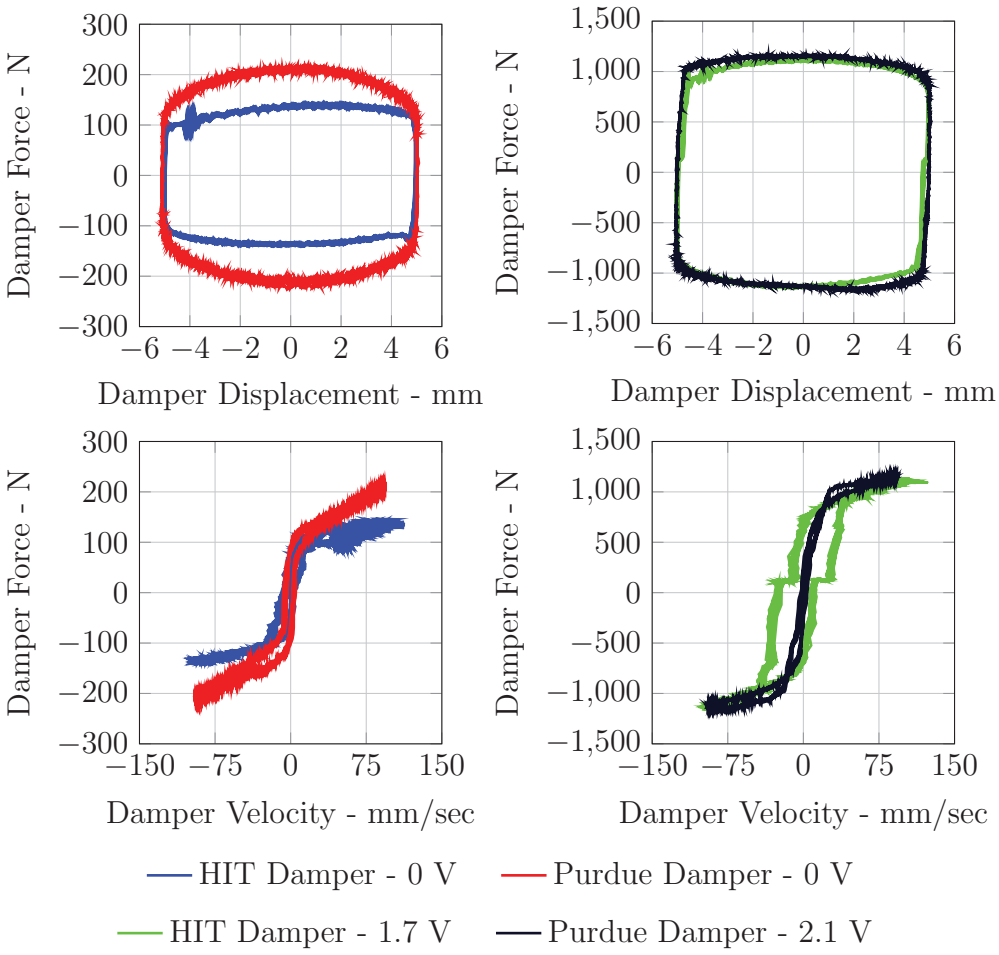


Figure 4.7: Comparisons for HIT vs Purdue dampers

### 4.3 Semi-active Control Algorithm

Essentially, MR dampers represent a class of controllable devices where the shear force of the fluid is controlled by a magnetic field (Carlson et al., 1996; Carlson and Spencer, 1996). The effectiveness of an MR damper in controlling vibration highly depends on developing a proper control strategy. However, for designers, generating control algorithms for MR damper is often a challenge due to nonlinear nature of the fluid. To overcome the difficulty in controlling MR damper, Dyke (1996); Dyke et al. (1996a,b) proposed a Linear Quadratic Gaussian (LQG) regulator based clipped optimal controller that uses acceleration feedback while eliminating the need for states

of velocities and displacements, which are difficult to measure for real civil structures. Although the clipped optimal control ignores dynamics of the MR damper, LQG control block attempts to linearize the nonlinear plant, herein, MR damper, with a bang-bang control. Thus, the optimal controller has still the ability to track the control force.

### 4.3.1 Implementation of Clipped-optimal Control Algorithm

A structure controlled with an MR damper can be idealized as in Figure 4.8. The structure produces structural responses, $y_m$, when seismically excited with $\ddot{x}_g$. Reactively, MR damper develops force, $f_m$ that is feedback to the structure. The system has already been formulated in Section 3.1. The force generated by the MR damper cannot be controlled directly, however, by varying the voltage input, the magnetic field can be adjusted such that a desired force history can be induced. Nevertheless, a control algorithm needs to be implemented to achieve an optimal control force while reducing structural responses. Determination of the desired force, $f_c$ is determined with a linear optimal controller gain, $K_c$ as:

$$f_c = \mathcal{L}^{-1}\left\{-K_c(s)\mathcal{L}\left(\begin{bmatrix} y_m \\ f_m \end{bmatrix}\right)\right\} \tag{4.3}$$

where $\mathcal{L}$ is the Laplace transform, $y_m$ is the measured system response, and $f_m$ is the measured force. To utilize desired force, $f_c$, clipped optimal control (COC) proposed by Dyke et al. (1996b) is used. Essentially, COC compares the sign of the desired force and the measured force of the damper and applies maximum voltage if the signs match, otherwise zero voltage using a bang-bang controller, as given in Equation (4.4):

$$v = V_{max}H\big((f_c - f_m)f_m\big) \tag{4.4}$$

where $f_c$ represents selected optimal control force, $f_m$ represents measured damper force and $H(x)$ is the Heaviside step function.

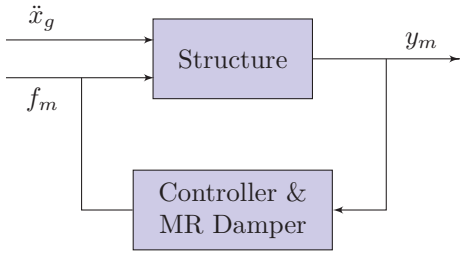


Figure 4.8: An idealization of structural control with MR damper

### 4.3.2 Implementation of $H_2$/LQG Control

Assuming earthquake is a stochastic process, an optimal control problem to estimate $K_c$ with the aim towards optimal minimization of structural responses can be constructed using $H_2$/LQG. Fundamentally, LQG is the combination of a linear-quadratic estimator (LQE) with a linear-quadratic regulator (LQR). In general, LQR is sufficient to estimate the control force only with the internal states, such as velocity and displacement responses of a structure. In reality, it is hard to measure such states without fixed reference points. Fortunately, many accelerometer forms are classified as inertial sensors, have their reference frame inside the sensor mechanism and allow measuring acceleration without any issues. Later, unobserved internal states can be restored with the help of observed states with LQE and are feed-forward to LQR (Kalman, 1960). A typical LQG regulator can be described such as:

$$\dot{\hat{x}} = (A - LC)\hat{x} + Ly_m + (B - LD)f_m \tag{4.5}$$

where $\hat{x}$ is estimated unobserved states and $L$ is quadratic estimator gain. With the help of Equation (4.5), Equation (4.3) can be simplified to:

$$f_c = K\dot{\hat{x}} \tag{4.6}$$

where $K$ is quadratic regulator gain.

Computation of LQR Gain

For a continuous-time state-space model with state-feedback presented in Equation (4.6), infinite horizon performance index or cost function, J to be minimized can be formulated:

$$J(f_m) = \int_0^\infty y_o^T Q_{LQR} y_o + f_m^T R_{LQR} f_m \, \mathrm{d}x \tag{4.7}$$

where $y_o$ is the system responses to be optimized, $Q_{LQR}$ and $R_{LQR}$ are weighting matrices determining the relative importance of state variables and control forces. A Riccatti equation can be formed using $Q_{LQR}$, $R_{LQR}$ and state space of the system.

$$A^T S + SA - (SB) R_{LQR}^{-1} (B^T S) + Q_{LQE} = 0 \tag{4.8}$$

Finally, regulator gain, $K$ can be derived as:

$$K = R_{LQR}^{-1} BS \tag{4.9}$$

Computation of LQE Gain

LQE, i.e. Kalman state estimator filter provides an optimal solution of unobserved states for a given system with process and measurement noise. A system described in Equations (3.4) and (3.5) can be rewritten including such noises:

$$\dot{x} = Ax + Bu + G\mathrm{w} \tag{4.10}$$

$$y = Cx + Du + H\mathrm{w} + \mathrm{v} \tag{4.11}$$

where w and v are white process and white measurement noises with the following definitions:

$$E(\mathrm{w}) = E(v) = E(\mathrm{w}\mathrm{v}^T) = 0 \tag{4.12a}$$

$$E(\mathrm{w}\mathrm{w}^T) = Q_{LQE} \tag{4.12b}$$

$$E(\mathrm{v}\mathrm{v}^T) = R_{LQE} \tag{4.12c}$$

Here, $G$ and $H$ correspond to $E$ and $F$ in Equations (3.4) and (3.5). Equation (4.12) implies that ground excitation is a process noise and both process and measurement noises are Gaussian stationary white noise with zero mean. Estimated state, $\hat{x}$ can be obtained by minimizing error covariance such as:

$$P = \lim_{t \to \infty} \left( \{x - \hat{x}\} \{x - \hat{x}\}^T \right) \tag{4.13}$$

A Ricatti equation can be assembled to solve $P$:

$$A^T P + PA - (PC^T) R^{-1} (CP) + Q_{LQR} = 0 \tag{4.14}$$

which leads to the computation of the estimator gain, $L$:

$$L = \left( PC^T + GQ_{LGE} H^T \right) \left( R_{LGE} + HQH^T \right)^{-1} \tag{4.15}$$

For typical implementations of COC, first, regulator and estimator gains are determined from built-in *lqry.m* and *lqew.m* MATLAB scripts. Later, Equations (4.4) and (4.5) are formulated as block diagrams in Simulink.

## 4.4 Summary

In this chapter, a general way to characterize and model MR dampers are discussed. Following that, a parametric model of the MR damper located at HIT is developed. In addition, force-displacement and force-velocity relationships of the Purdue damper are tried against HIT damper at passive-off and -on modes. The motivation and concepts of semi-active control strategies, particularly, LQG control and its implementation are discussed for its use in shake table tests, RTHS and dRTHS. In the following chapters, the control algorithm introduced here will be employed in several numerical simulations, experiments and hybrid simulations.

# CHAPTER 5
# VALIDATION OF ANALYTICAL SIMULATIONS WITH SHAKE TABLE TESTS

In this chapter, a description of the experimental study is given to validate the model of the three story structure equipped with MR damper by comparing the responses with those of shake table tests. First, Section 5.1 discusses the selection and design of MR damper controllers aimed towards effective structural control. Next, Section 5.2 illustrates post-processing procedure of the structural responses yielding from shake table tests and simulations for comparison purposes. In Section 5.3, performance of the structural model introduced in Chapter 3 is evaluated using a variety of earthquake inputs through both numerical simulation and shake table tests under different damper control strategies. For all cases, error in relative displacement, absolute acceleration in the global sense of the structure is examined including other evaluation criteria discussed in Section 3.5. Finally, a summary of the chapter, that interprets and concludes main findings in the comparisons, is given in Section 5.4.

In order to perform a successful comparison between shake table experiments and pure analytical simulations, several steps must be taken, including (i) modeling of the existing test structure, (ii) characterization of the MR damper which will be used in analytical simulations, and (iii) design of MR damper semi-active control algorithms.

Step (i) was already explained in Chapter 3 in detail. Furthermore, steps (ii) and (iii) were discussed in Chapter 4. In the following sections of this chapter, design of the MR damper controllers is also discussed.

## 5.1 Design of MR Damper Controllers

For pure simulations, the damper model based on HIT damper is utilized. Three cases are considered for structural control problem based on this damper. Those are

(i) passive-off case where a constant 0 V is sent to the current driver; (ii) passive-on case where damper is fed with a constant 1.7 V; and finally (iii) semi-active control case where clipped-optimal control strategy is implemented. The principle of semi-active control has already been discussed in Chapter 4. For semi-active control, displacement responses are estimated from three floor accelerations and first floor relative MR damper displacement. To ensure effectiveness of the structural control in reducing accelerations, R matrix is selected to be the identity matrix with proper order, whereas a wide range of Q matrices were tested using a variety of earthquakes. Finally, Q matrix is selected to be 23000 with equal weighting on all floor accelerations of the structure, for shake table tests and pure simulations.

## 5.2 Post-processing of Data

Each shake table test record lasts 60-200 seconds or longer. For the initial 10–60 seconds of the recorded data, shake table is kept at zero position. After stand-by time, the actual earthquake input is initiated which takes 50–60 seconds. Finally, another 10–60 seconds of data is recorded until the structural responses fully decay and test setup is ready for a new test.

The recorded data are long and also contains noise due to the test apparatus used during the experiments. Therefore, post-processing is required to make it presentable for further analysis. It should be noted that the results of the shake table tests and simulation results are similarly post-processed as explained in the following sections.

### 5.2.1 Time Windowing

To employ a robust visual comparison between records, a boxcar function is applied to isolate structural responses in time domain where ground motion is dominant. An example is illustrated in Figure 5.1, where first floor displacement response from Morgan Hill semi-active control case is windowed for the time range of 13–28 sec. After windowing, the start of the response is assumed as $t = 0$.

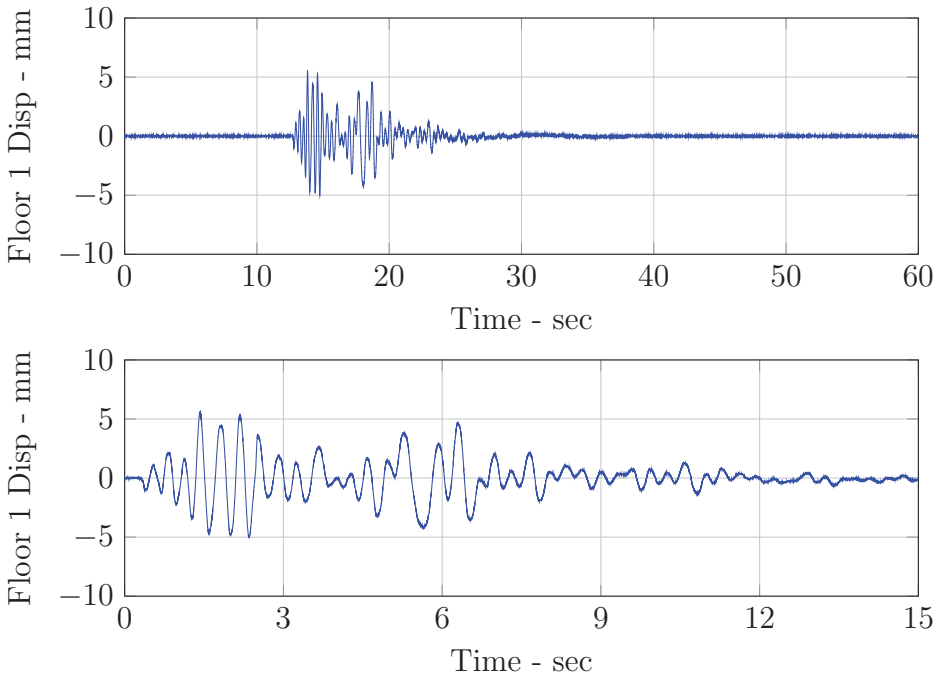


Figure 5.1: Application of rectangular window function to first floor displacement response for Morgan Hill semi-active control case

For relative RMS and peak error calculations, the responses are windowed even further, where the earthquake is strongest. For already windowed responses, this range is 2–5 sec for El Centro, 3–6 sec for Kobe, and 1.5–4 sec for Morgan Hill.

### 5.2.2 Filtering

The structural responses obtained experimentally from shake table tests may contain some artifacts that can affect comparisons of simulations results. Mostly, such artifacts are comprised of measurement errors due to (a) unwanted forced vibrations caused by the actuator driving the shake table and (b) amplification of the forced vibration by the structure, and (c) strong ground motion affecting off-plane dynamics of the test structure.

Since hydraulic fluid is compressible, it has a finite stiffness. When a hydraulic actuator system is coupled with mass, the fluid resonates with mass. This phenomenon, often called oil-column resonance, tend to cause vibration issues. Eventually, if the coupled mass is large enough, the resonance can leak into frequency content of the structure. Considering the fact that shake table represents a very large mass, oil-column resonance frequency is low enough to affect the structural responses (Nakata, 2013).

The proposed modeling approach discussed in Chapter 3 discretizes the *continuous-time system* test structure into 3-DOF model. Although the applied ground motion is unidirectional along the weak-plane of the structure, the test setup is not perfect and therefore, it is inevitable that higher modes including torsional and off-plane modes of the system will be induced.

Those artifact can be reduced substantially by filtering responses of the system. A $5^{\text{th}}$ order Butterworth filter with a cut-off frequency of 50 Hz is used to eliminate such responses. The same filter is also applied to the pure simulation results. An example is illustrated in Figure 5.2 to demonstrate the effectiveness of the filter. It should be noted that the acceleration response is smoothed.

### 5.2.3 Frequency-Domain Calculations

In addition to time-domain post-processing, results were also evaluated in frequency domain. In the course, power spectral density (PSD) of the strong motion response are calculated using *pwelch* command in MATLAB. PSD estimates are determined as one-sided with no window-averaging and overlapping using windowed responses of 2–6 seconds for all three earthquakes.

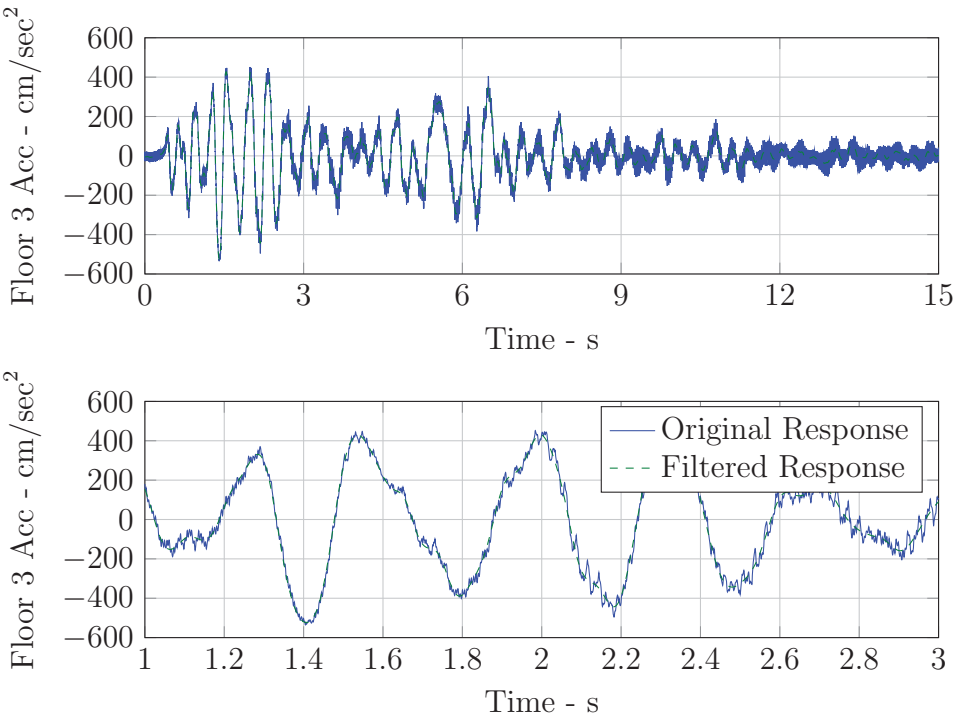


Figure 5.2: Effect of Butterworth filtering to third floor acceleration response for Morgan Hill semi-active control case

## 5.3 Comparison of Shake Table Test Responses with Pure Simulation Results

To employ a proper comparison between simulation and experimental results, a good understanding of the test structure is required. The test structure used in the shake tables tests was explained in detail in Chapter 2. Development of the accurate model of the structure in *MCK* format was provided in Chapter 3. To simulate the behavior of MR Damper under various control voltages, a model was proposed in Chapter 4. Excitation input to the structure is selected as El Centro, Kobe and Morgan Hill earthquakes. The ground motion in displacement form calculated by double integrating each earthquake is fed to the shake table actuator controller. More detail on the selected earthquakes and tracking performance of the shake table are given in Section 2.3.3. All floor accelerations for the shake tables tests are

sampled at 5000 Hz. The ground acceleration of the shake table is captured with two accelerometers and the response is averaged. For each structural control case, the averaged ground acceleration recorded during the specific test is applied as the excitation input to the numerical model, as-is without further modifications. As the shake table tests, numerical simulations are also conducted at a rate of 5000 Hz. An illustration of the Simulink diagram containing numerical structure and MR damper model is given in Figure 5.3.

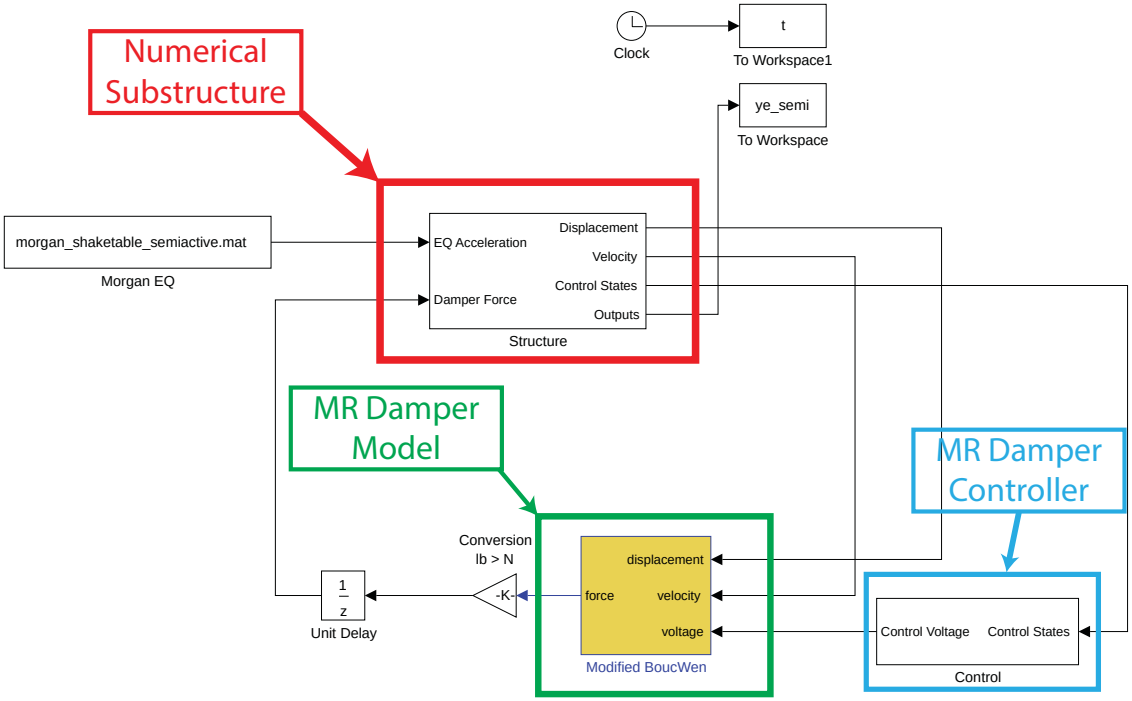


Figure 5.3: A representative Simulink model of the analytical simulation

The experimental plan for evaluation and validation of the integrated model is focused on replicating the dynamic response of the seismically-excited three story structure equipped with damper device at passive on/off and semi-active control modes. To assess accuracy of the proposed model, the shake table responses are compared to simulation results using the evaluation criteria proposed in Chapter 3. Particularly, RMS, peak and sliding RMS errors are utilized for recorded displacements and accelerations. To sum up, nine individual comparisons, containing three

earthquake cases each with three control modes, are conducted to achieve the study goals.

### 5.3.1 El Centro

In this section, results between shake table and pure simulations are compared for El Centro earthquake. Passive-off (POFF), -on (PON) and semi-active (SA) cases are considered for the comparisons.

#### Passive-off

Displacement and acceleration comparisons are given in Figures 5.4 and 5.5. RMS and peak response errors are tabulated in Table 5.1 in percentage. Likewise, in Figure 5.6, moving RMS errors are illustrated.

While the reported peak error of floor accelerations and displacements are ranging from 4 % to 15 %, the normalized RMS errors are trending from 15 % to 20 %. In addition, range-normalized RMS errors are no more than 15 %. Both time- and frequency-domain responses are in correlation.

#### Passive-on

For PON case, related comparisons and error tables are given in Figures 5.7 to 5.9 and table 5.1. Although time-domain displacement responses are not in an ideal correlation, the power spectrum demonstrates that the frequency contents still agree. There is a deviation observed in the first floor displacement time-domain responses around 3–9 seconds. This same trend is also observed in moving RMS error plot. Considering the fact that the first floor acceleration responses are very similar, the aforementioned discrepancy does not indicate a modeling error, but LVDT failure. By inspecting the results, one can conclude that MR damper LVDT might have been stuck due to friction when cyclic displacements are small enough ($\pm 0.5$ mm).

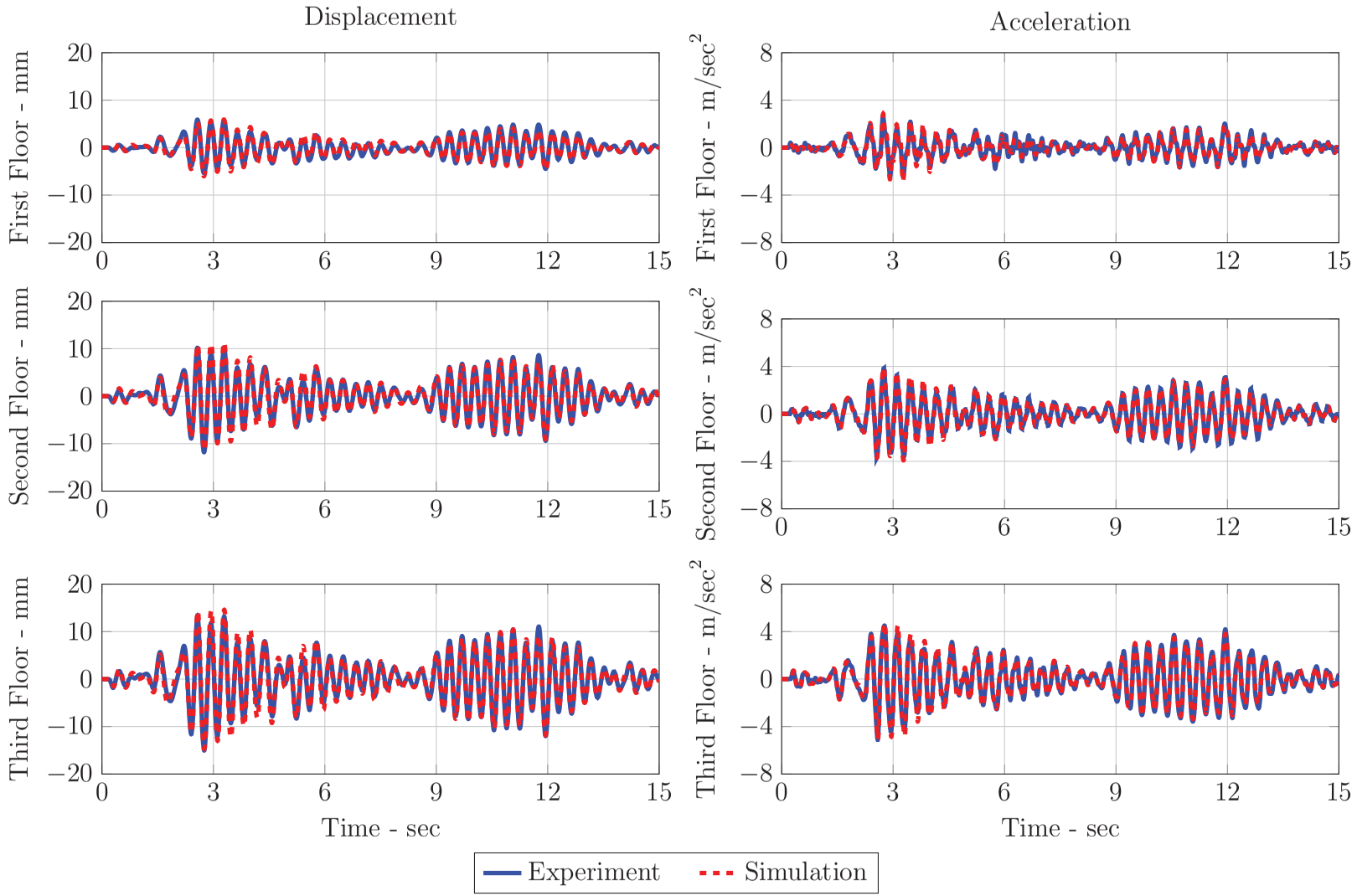


Figure 5.4: El Centro earthquake response comparison in time domain for ST–AS POFF case

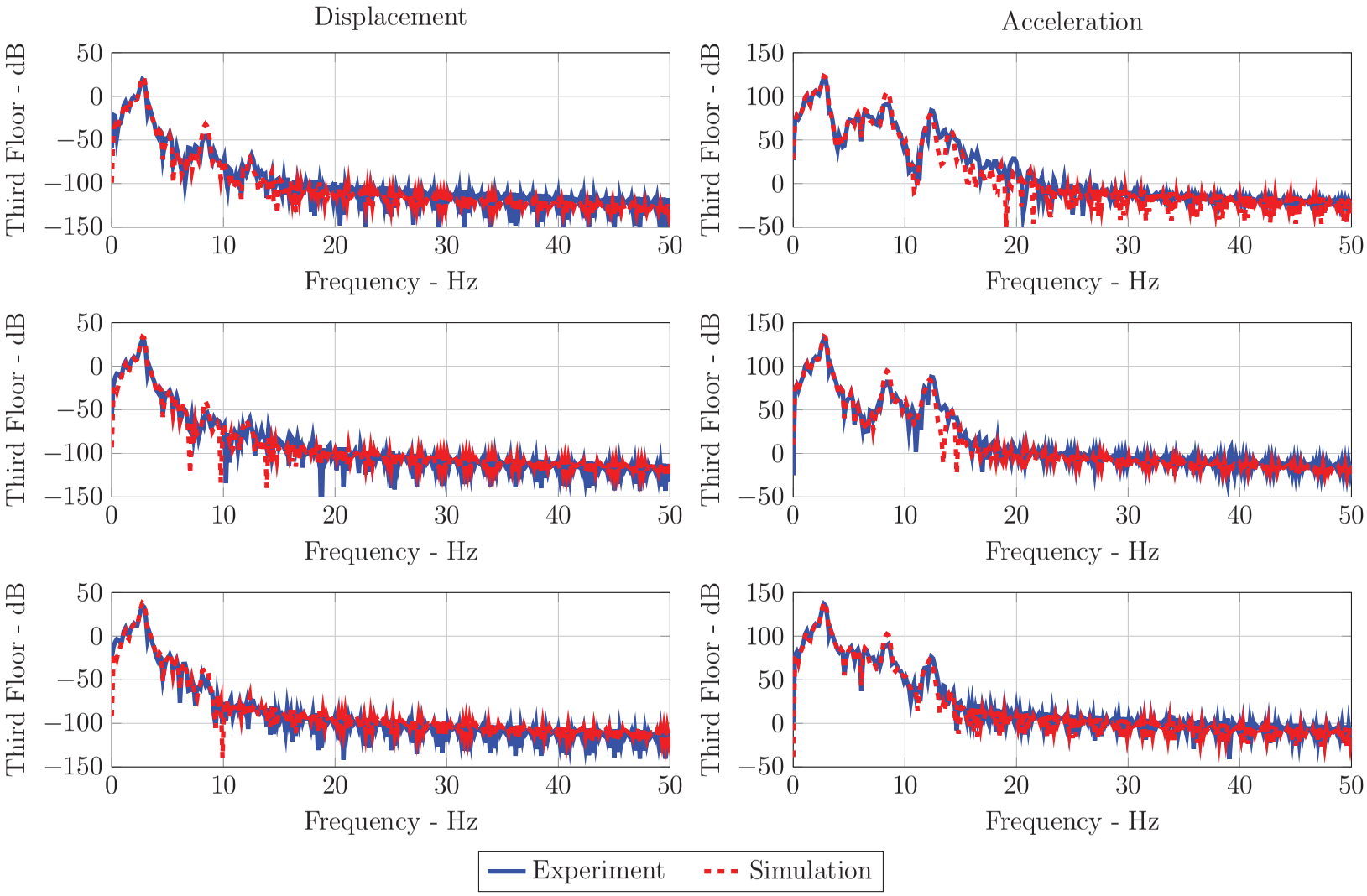


Figure 5.5: El Centro earthquake response comparison in frequency domain for ST–AS POFF case

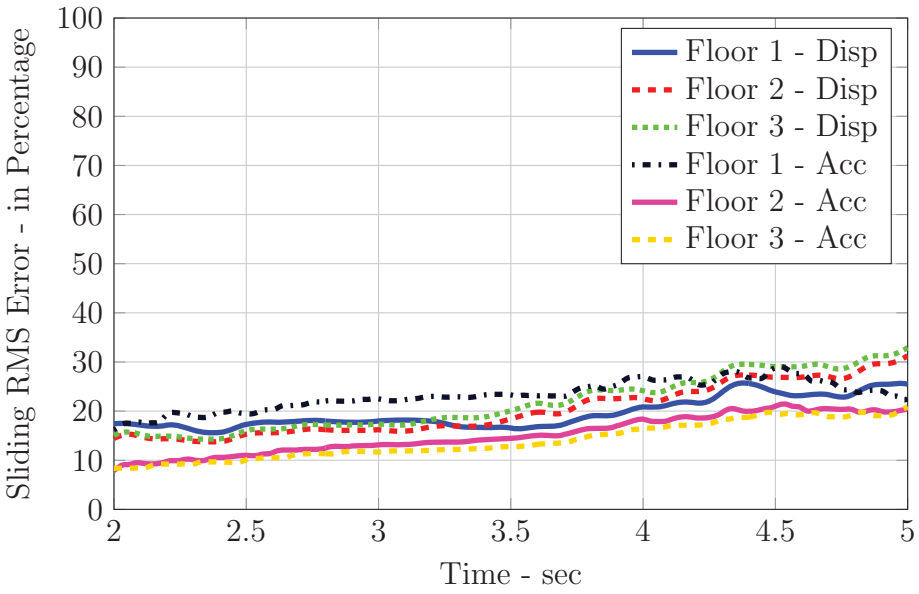


Figure 5.6: Moving RMS error for El Centro earthquake ST–AS POFF case

RMS and peak response errors for floor accelerations and displacements are ranging from 4 % to 45 %. The criteria-averaged RMS error is varying from 15 % to 30 %. The elevated errors indicate that with increasing levels of MR damper forces, it is harder to match structural responses in time-domain.

Semi-active

The comparisons for SA case are given in Figures 5.10 to 5.12 and table 5.1.

RMS and peak response errors vary from 3 % to 25 %, while criteria-averaged RMS errors are reaching up to 15 %. Compared to PON case, the errors are much smaller since MR damper forces fall in between PON and POFF cases.

### 5.3.2 Kobe

In this section, results between shake table and pure simulations are compared for Kobe earthquake. POFF, PON and SA cases are considered for the comparisons.

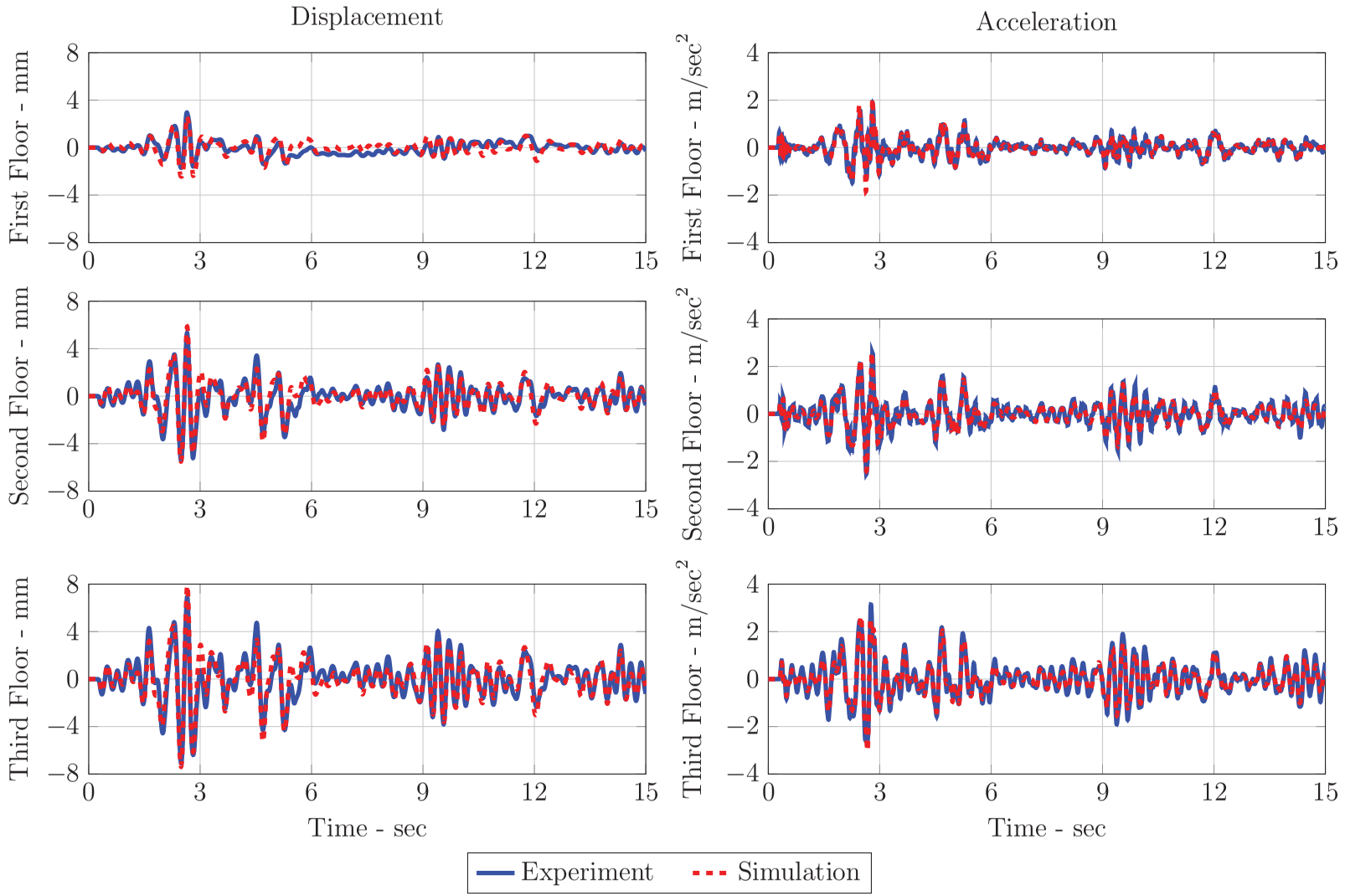


Figure 5.7: El Centro earthquake response comparison in time domain for ST–AS PON case

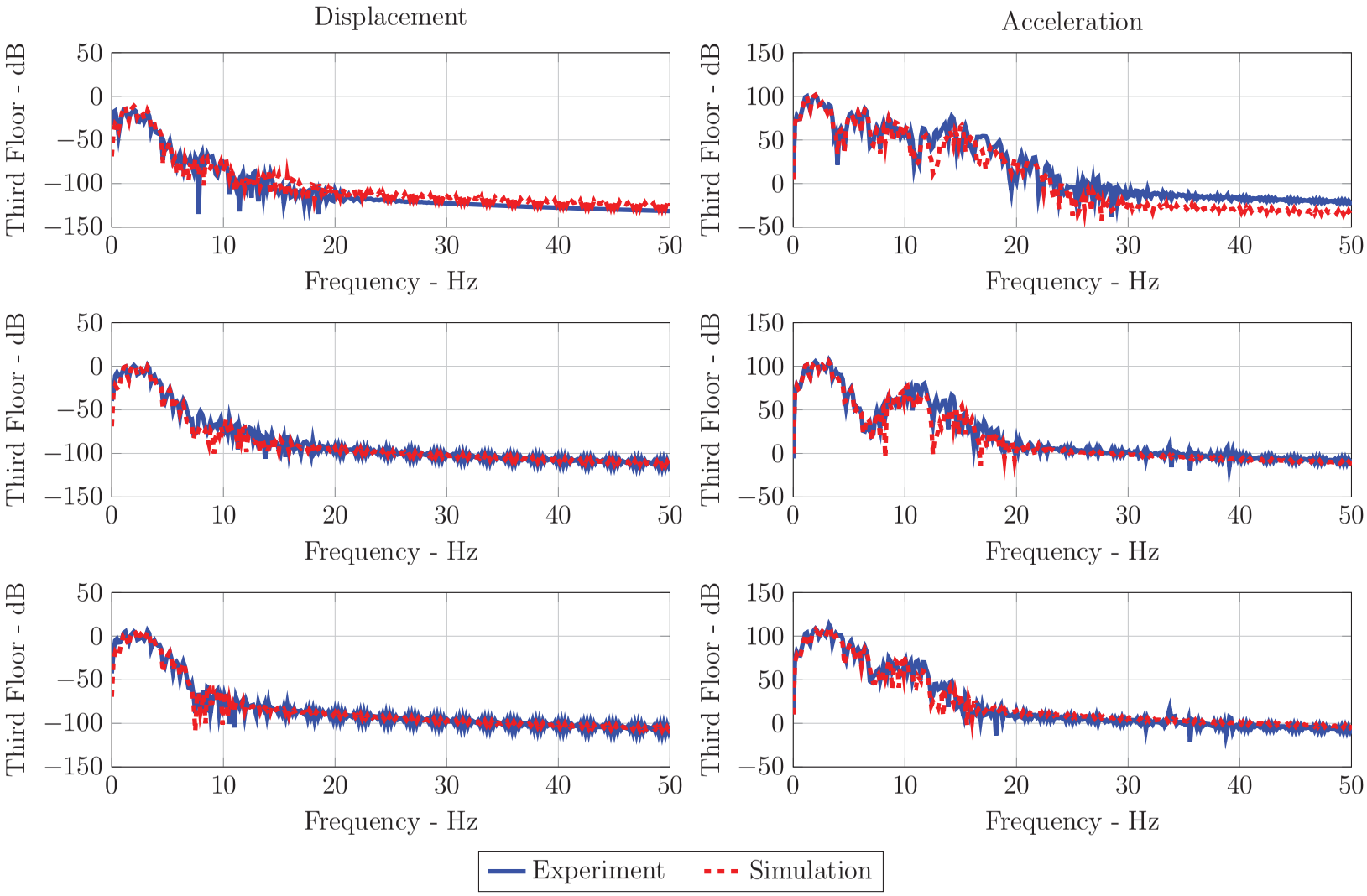


Figure 5.8: El Centro earthquake response comparison in frequency domain for ST–AS PON case

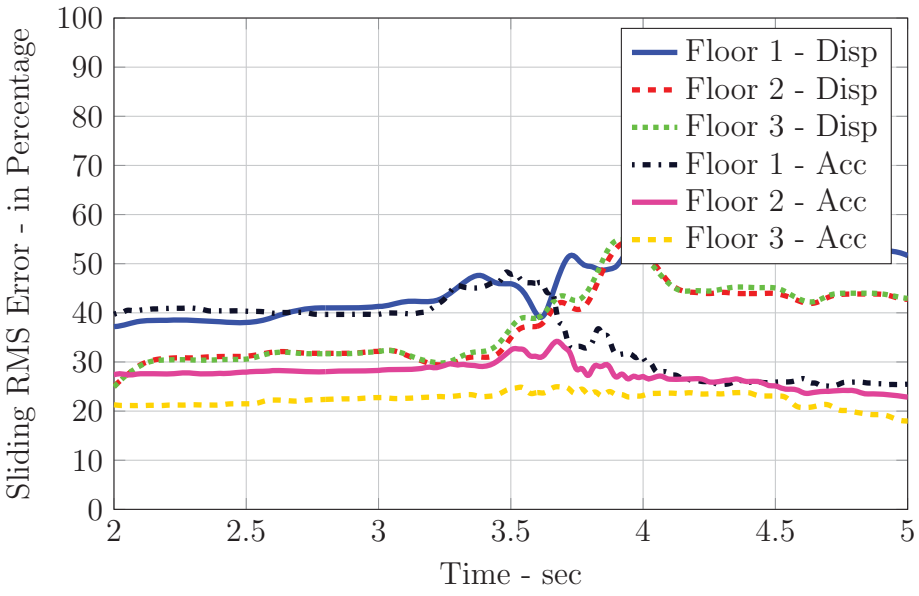


Figure 5.9: Moving RMS error for El Centro earthquake ST–AS PON case

Passive-off

Shake table vs. simulation response comparisons are given in Figures 5.13 and 5.14. This case has the smallest error among all cases including El Centro and Morgan Hill earthquakes.

Passive-on

PON case comparisons are given in Figures 5.16 and 5.17. In Figure 5.9 and table 5.1, error tables and moving RMS error plot are provided.

Although errors are similar to El Centro and Morgan Hill PON cases, discrepancy due to LVDT is most evident in this case. RMS and peak response errors range from 10 % to 60 %, while criteria-averaged errors are bounded to 30 % to 35 %.

Semi-active

In Figure 5.19 and Figure 5.20, SA case comparisons are presented.

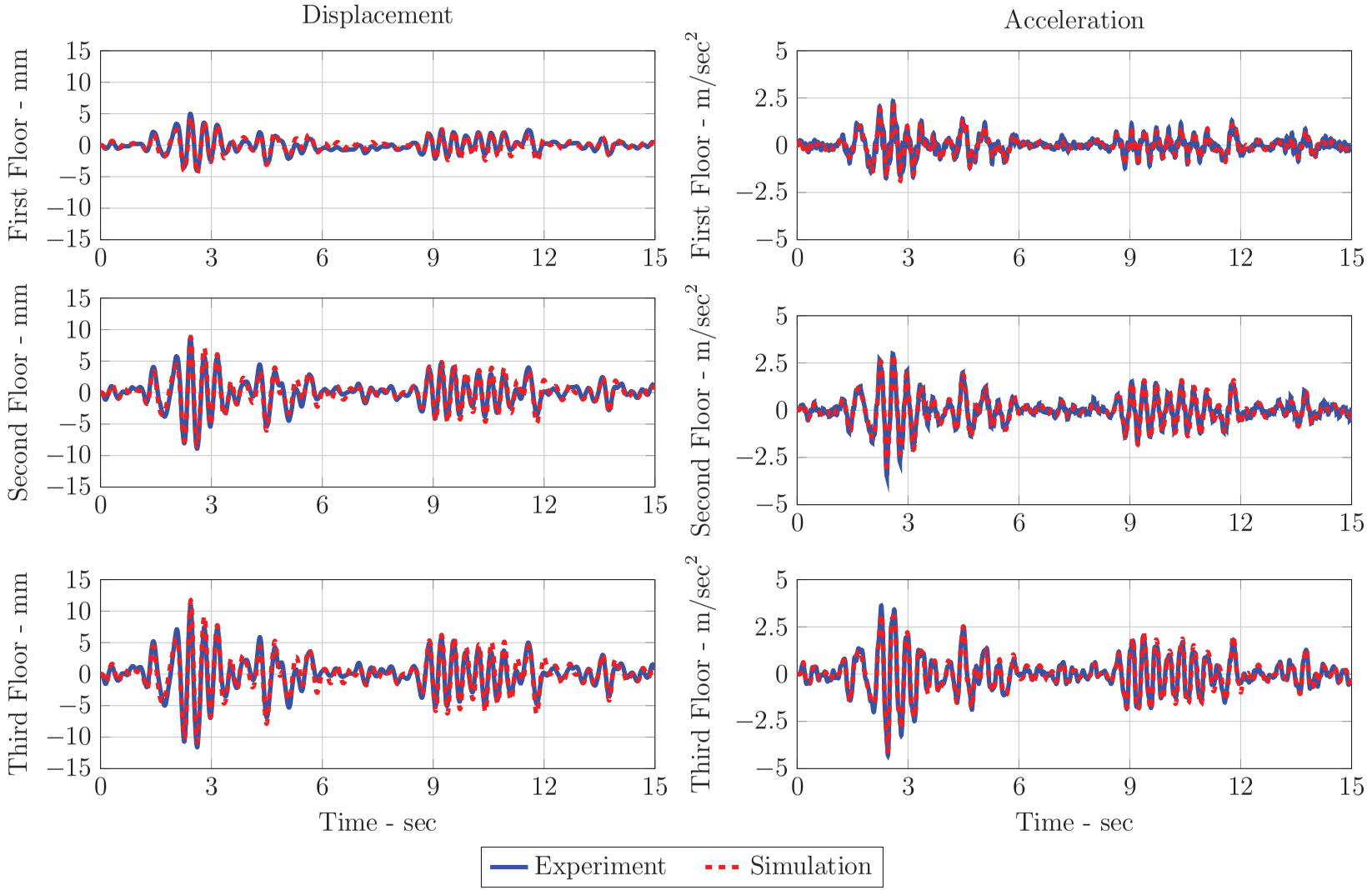


Figure 5.10: El Centro earthquake response comparison in time domain for ST–AS SA case

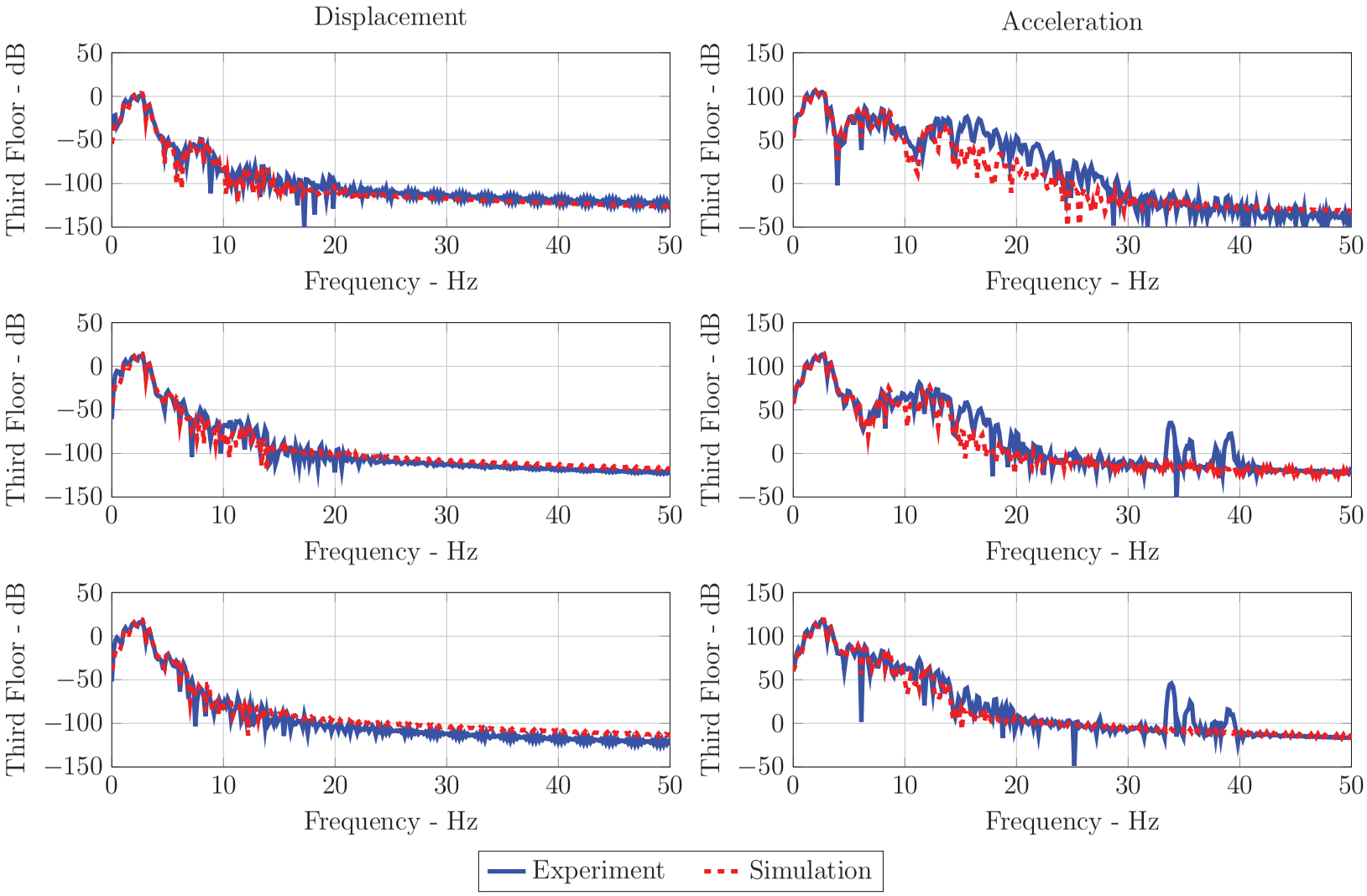


Figure 5.11: El Centro earthquake response comparison in frequency domain for ST–AS SA case

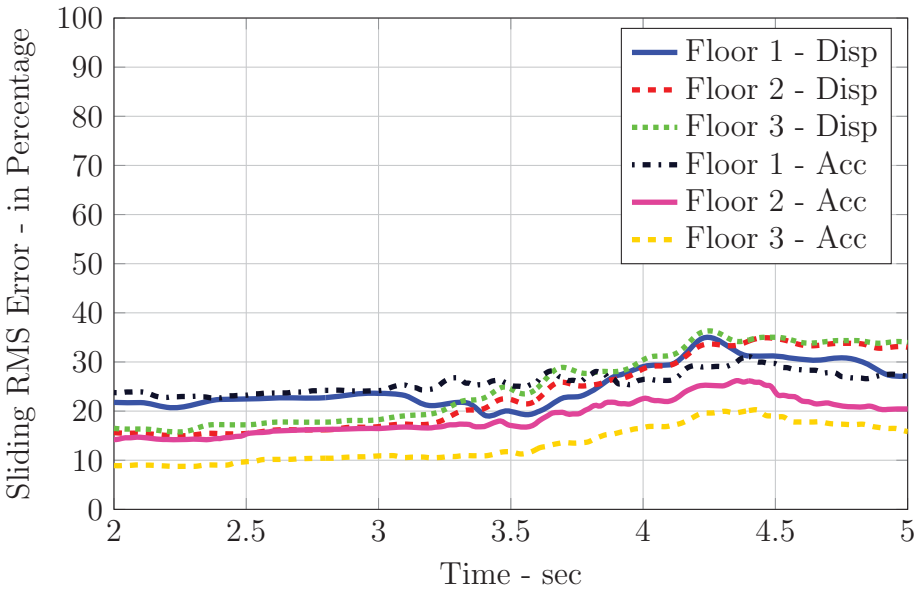


Figure 5.12: Moving RMS error for El Centro earthquake ST–AS SA case

Like in El Centro case, this SA case produced less errors compared PON case. The peak and RMS errors and criteria-averaged errors are in the range of 3 % to 30 % and 12 % to 16 %, respectively.

### 5.3.3 Morgan Hill

In this section, results between shake table and pure simulations are compared for Morgan Hill earthquake. POFF, PON and SA cases are considered for the comparisons.

Passive-off

Time- and frequency-domain comparisons for POFF case are provided in Figures 5.13 and 5.14. The reported errors are in the range of 5 % to 27 % and consistent with El Centro and Kobe cases. The averaged errors are as high as 9 %.

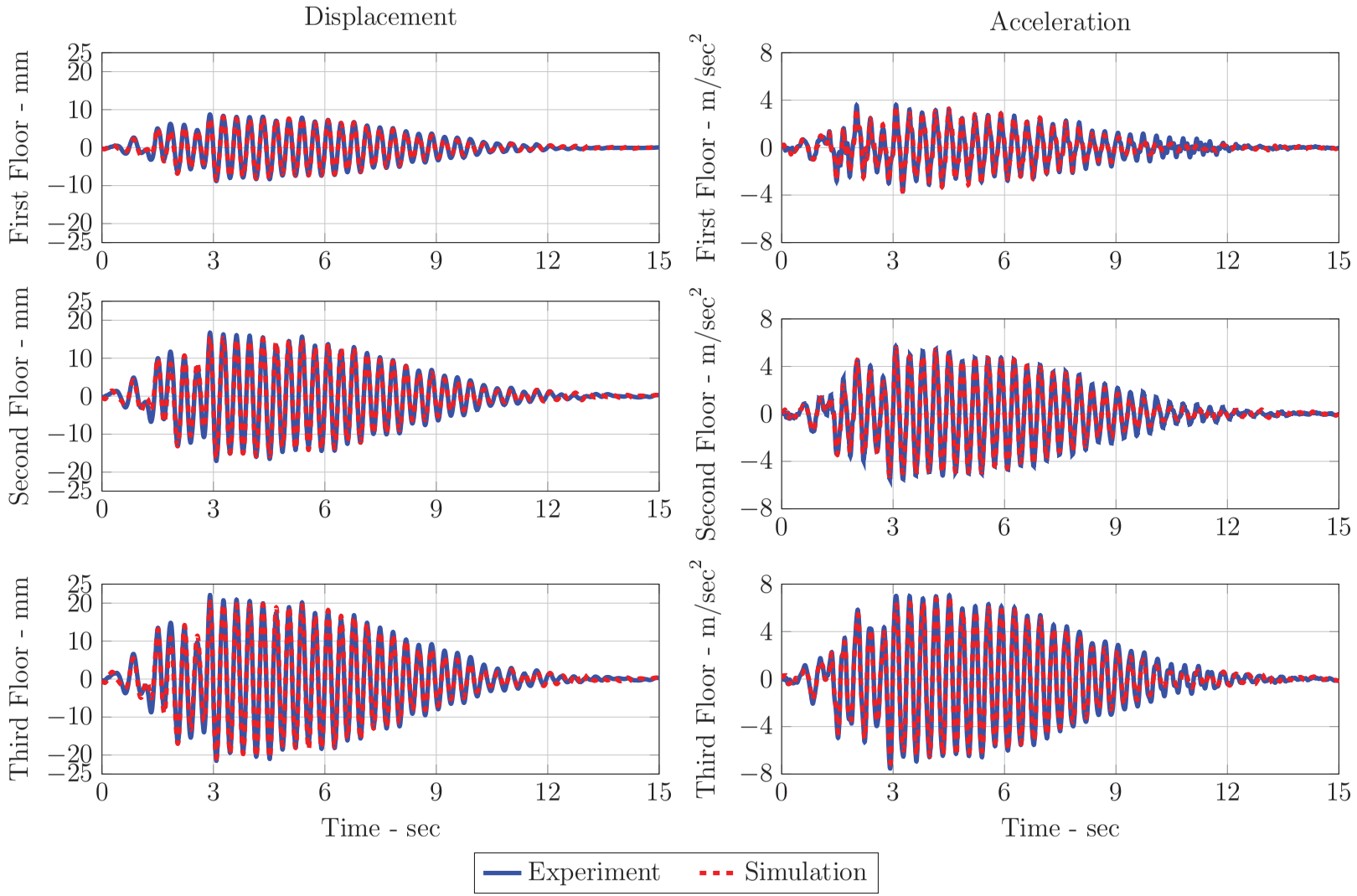


Figure 5.13: Kobe earthquake response comparison in time domain for ST–AS POFF case

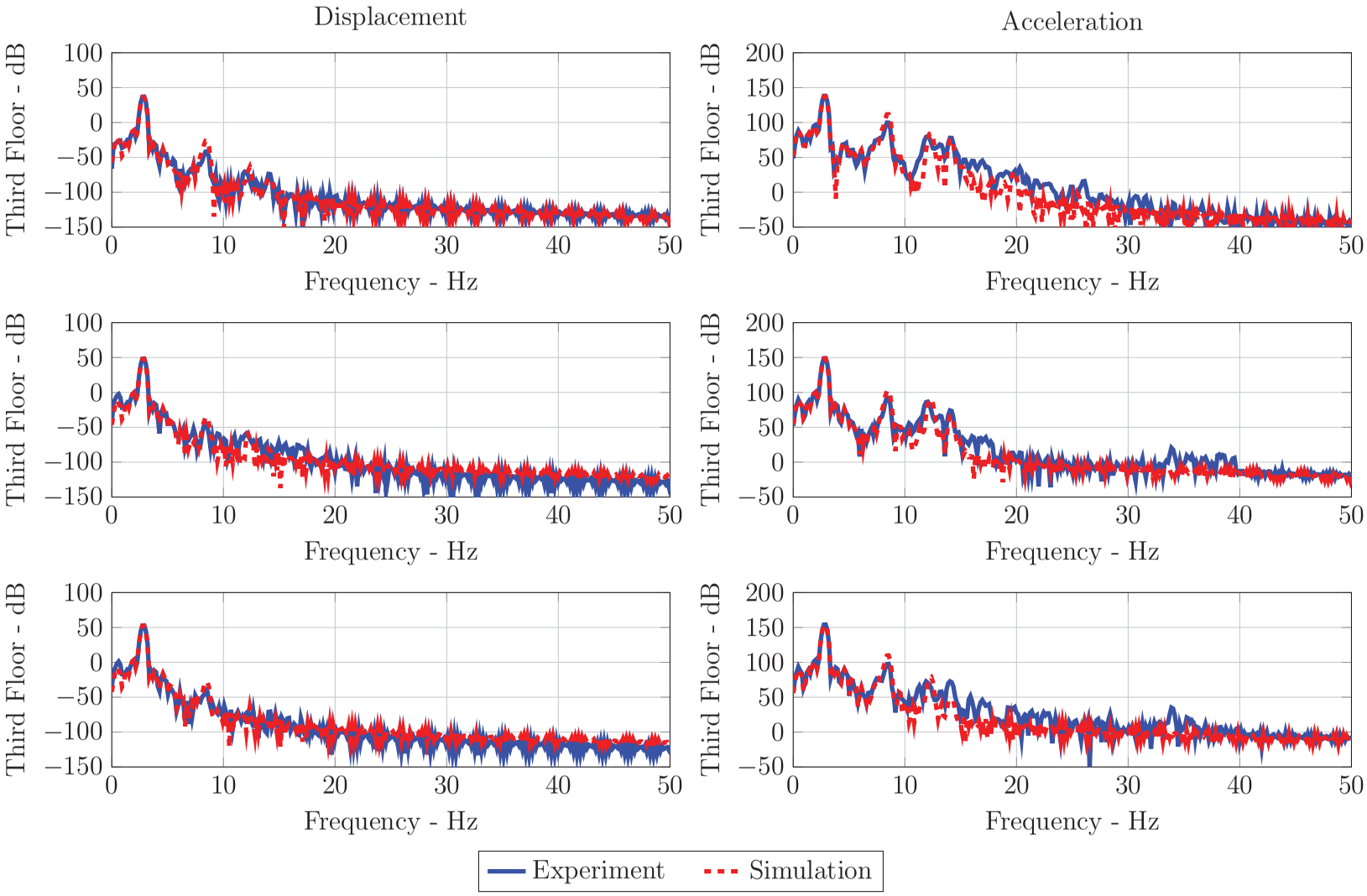


Figure 5.14: Kobe earthquake response comparison in frequency domain for ST–AS POFF case

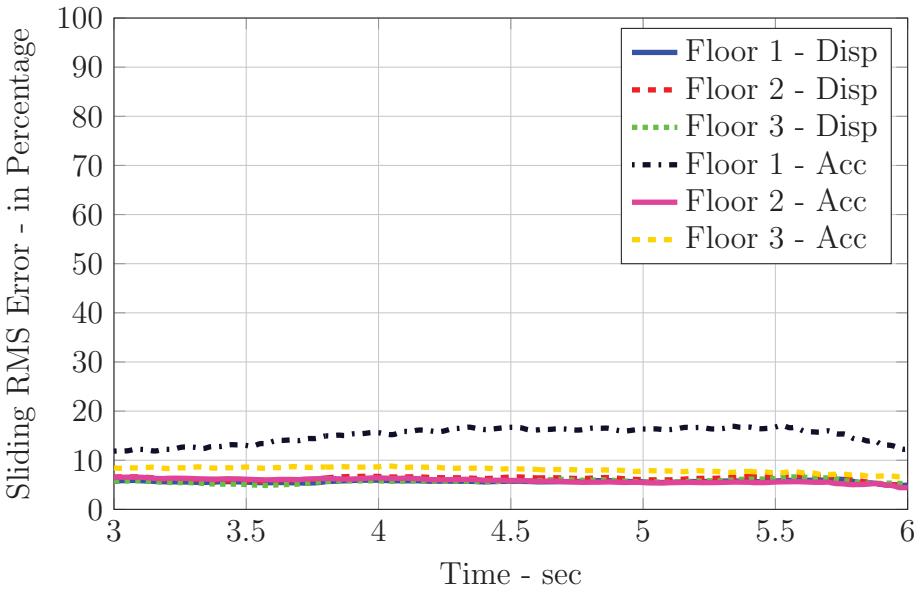


Figure 5.15: Moving RMS error for Kobe earthquake ST–AS POFF case

Passive-on

Displacement and acceleration comparisons are given in Figures 5.25 and 5.26. Although the time- and frequency-domain responses are in correlation, the errors are as high as the other two earthquake cases, closer to Kobe case.

RMS and peak response errors for accelerations and displacements are ranging from 6 % to 60 %. On the other hand, the criteria-averaged RMS error is varying from 19 % to 28 %.

Semi-active

SA case comparisons are presented in Figures 5.19 and 5.20. The RMS and peak response errors are confined within 3 % to 18 %. All criteria-averaged errors are concentrated near 10 %.

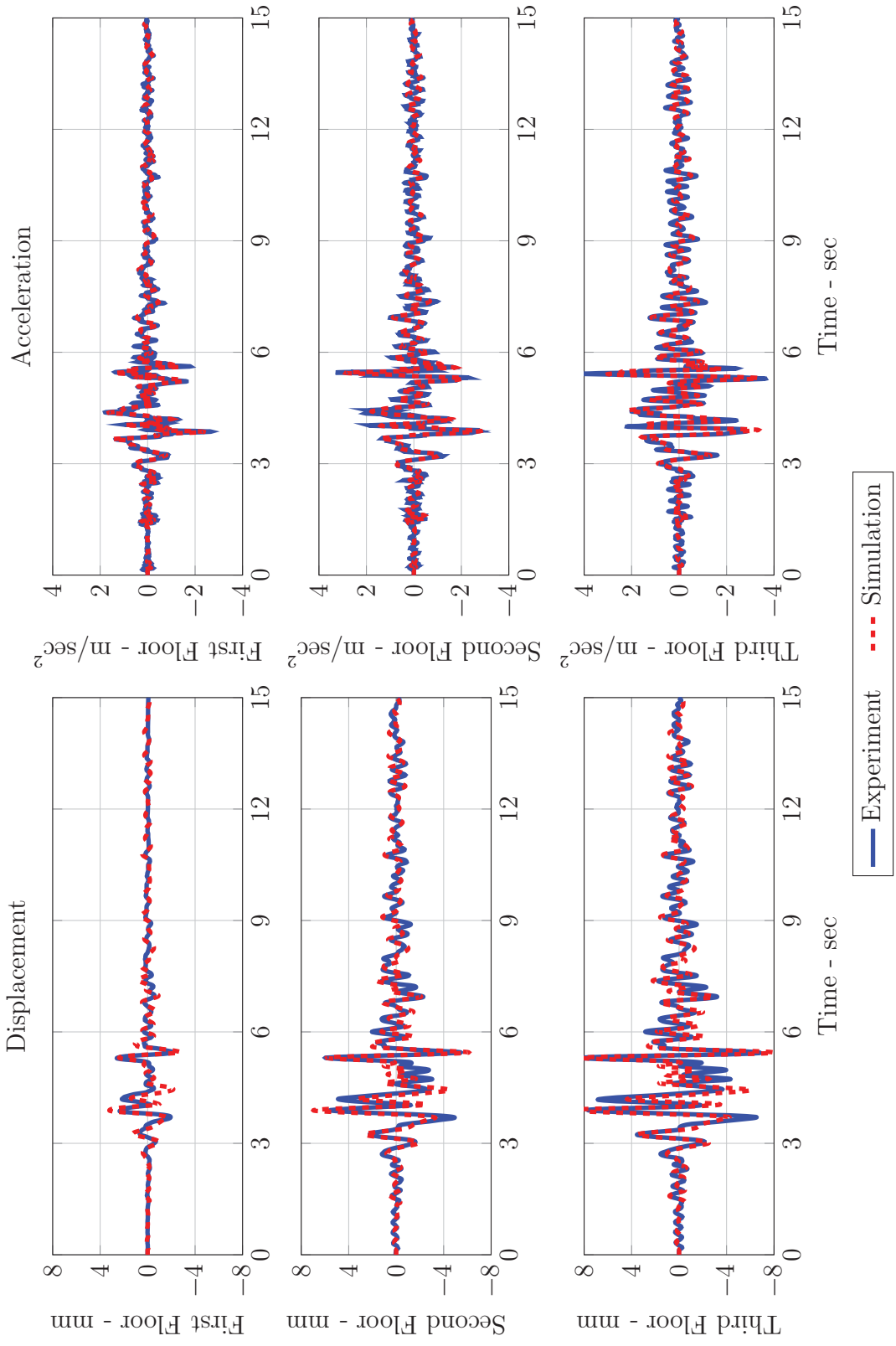


Figure 5.16: Kobe earthquake response comparison in time domain for ST–AS PON case

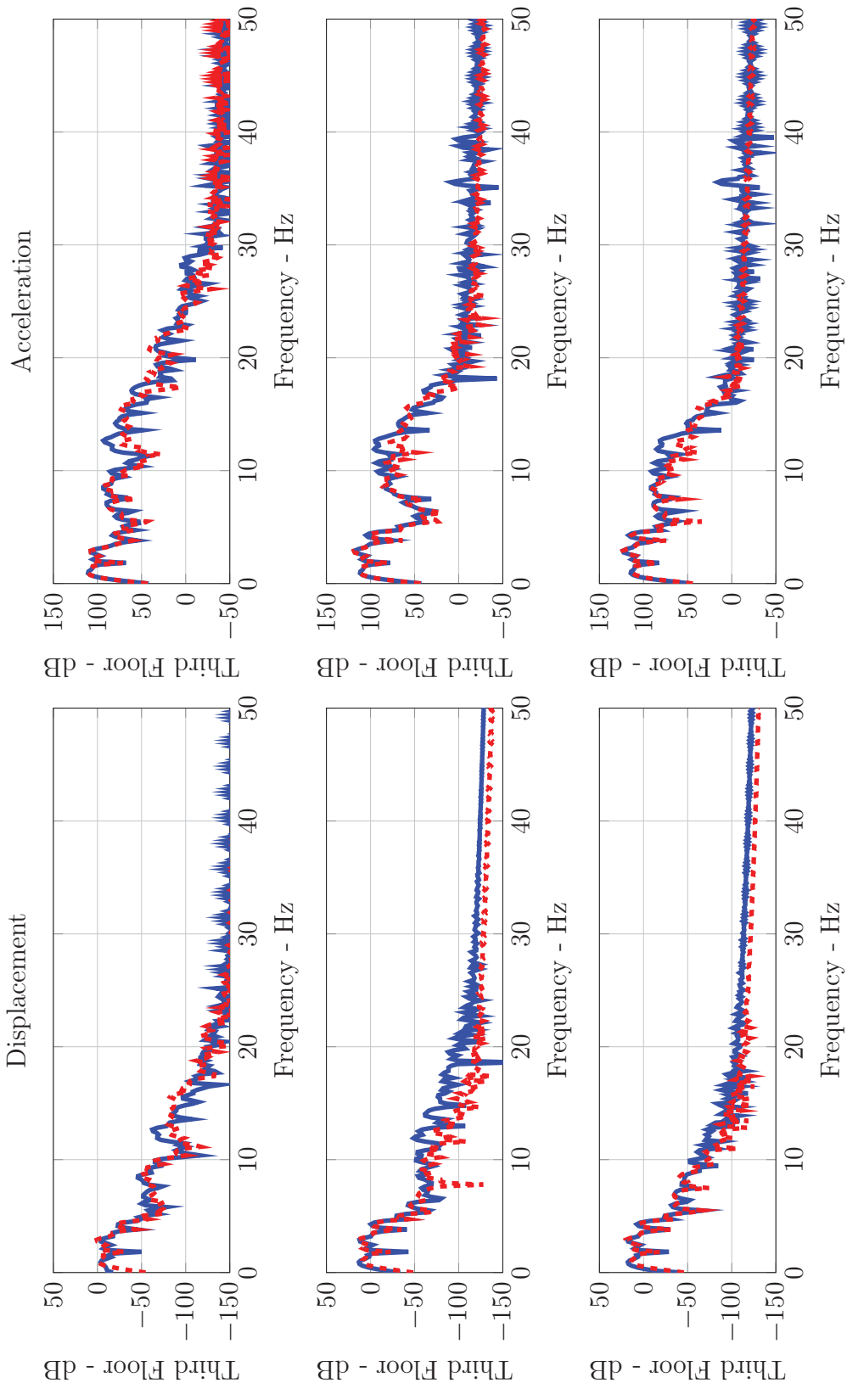


Figure 5.17: Kobe earthquake response comparison in frequency domain for ST–AS PON case

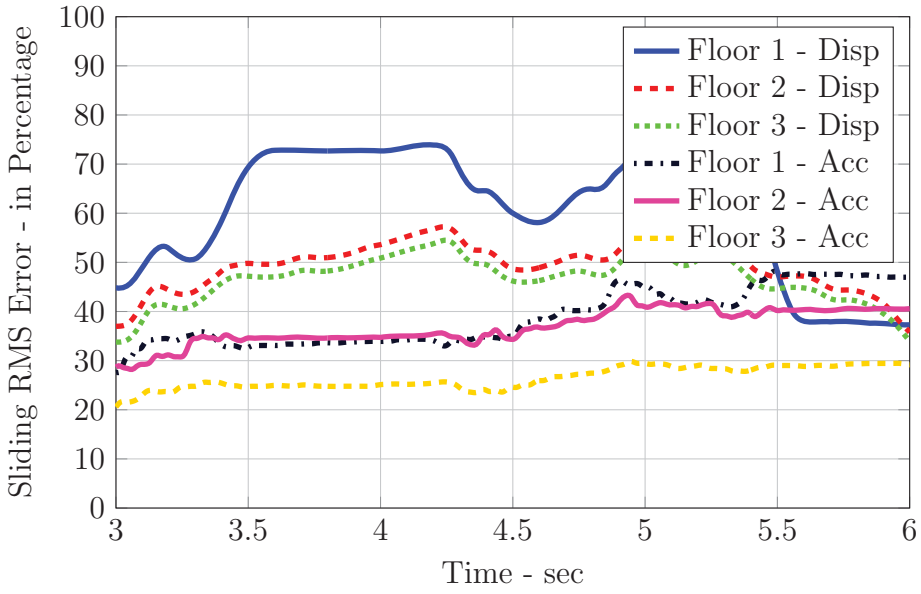


Figure 5.18: Moving RMS error for Kobe earthquake ST–AS PON case

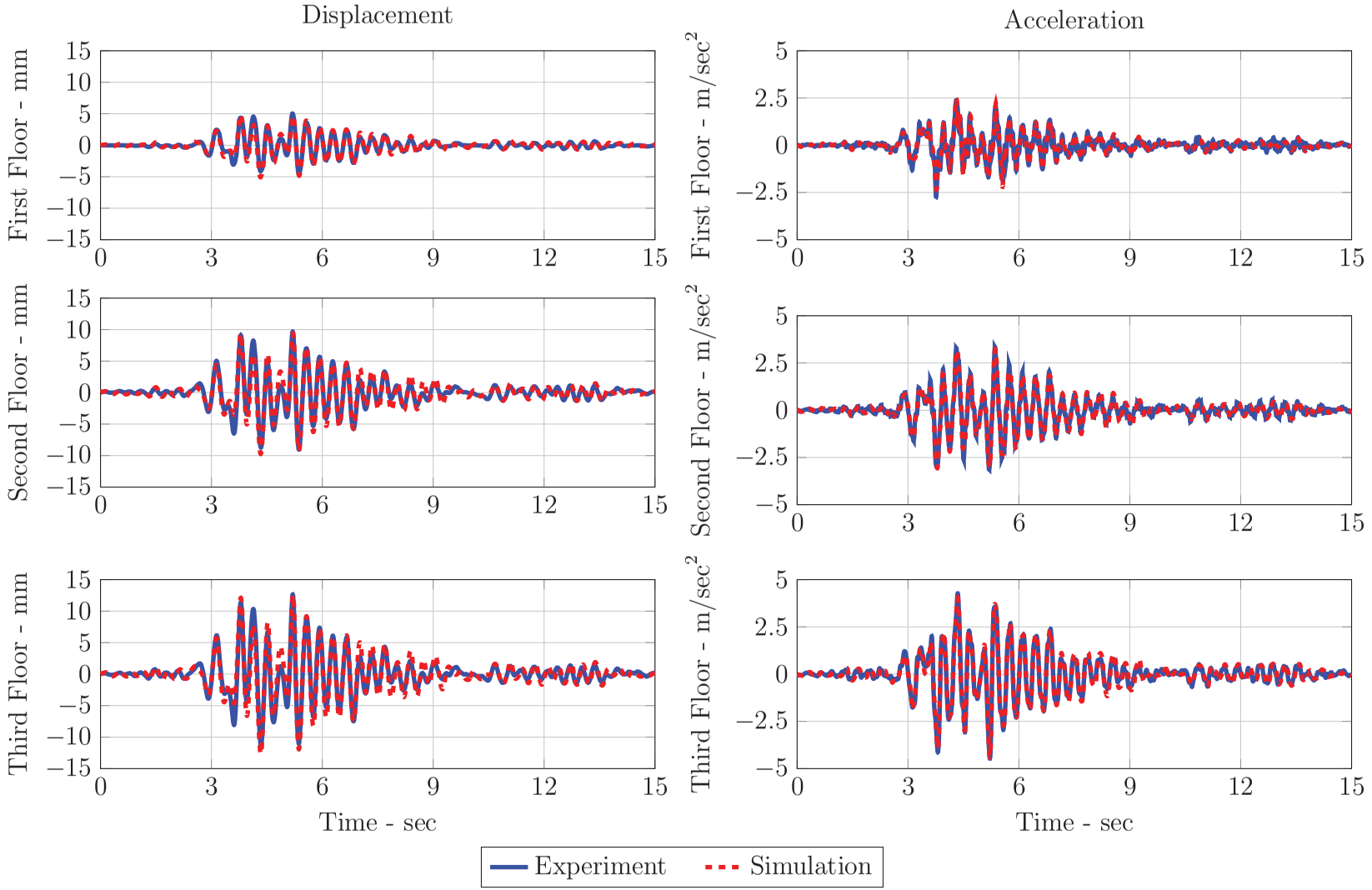


Figure 5.19: Kobe earthquake response comparison in time domain for ST–AS SA case

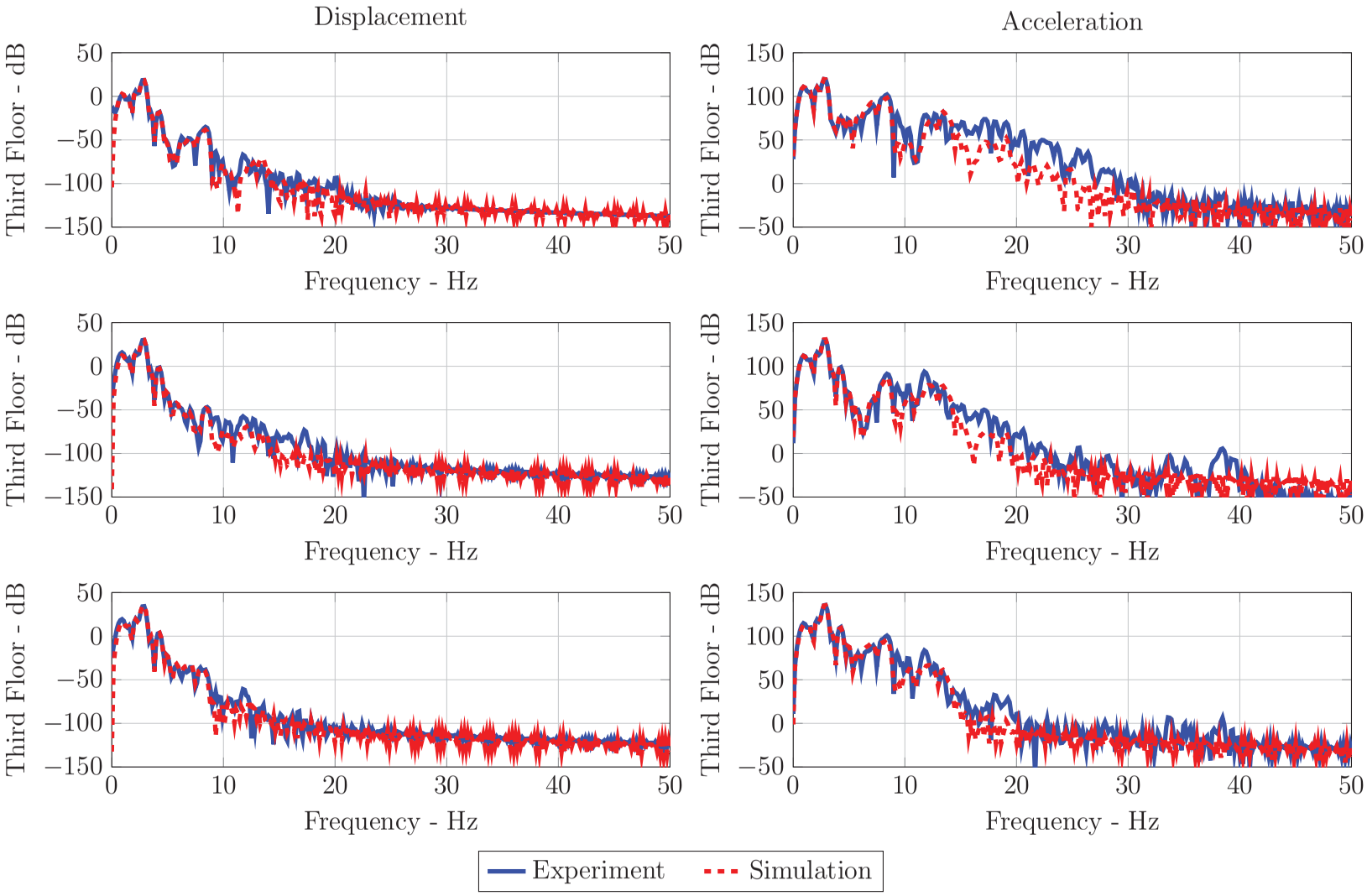


Figure 5.20: Kobe earthquake response comparison in frequency domain for ST–AS SA case

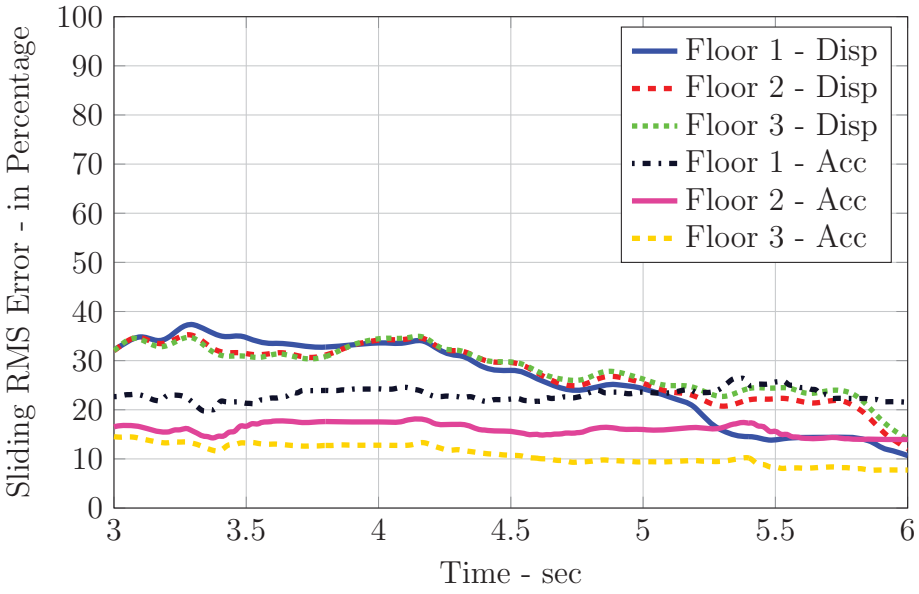


Figure 5.21: Moving RMS error for Kobe earthquake ST–AS SA case

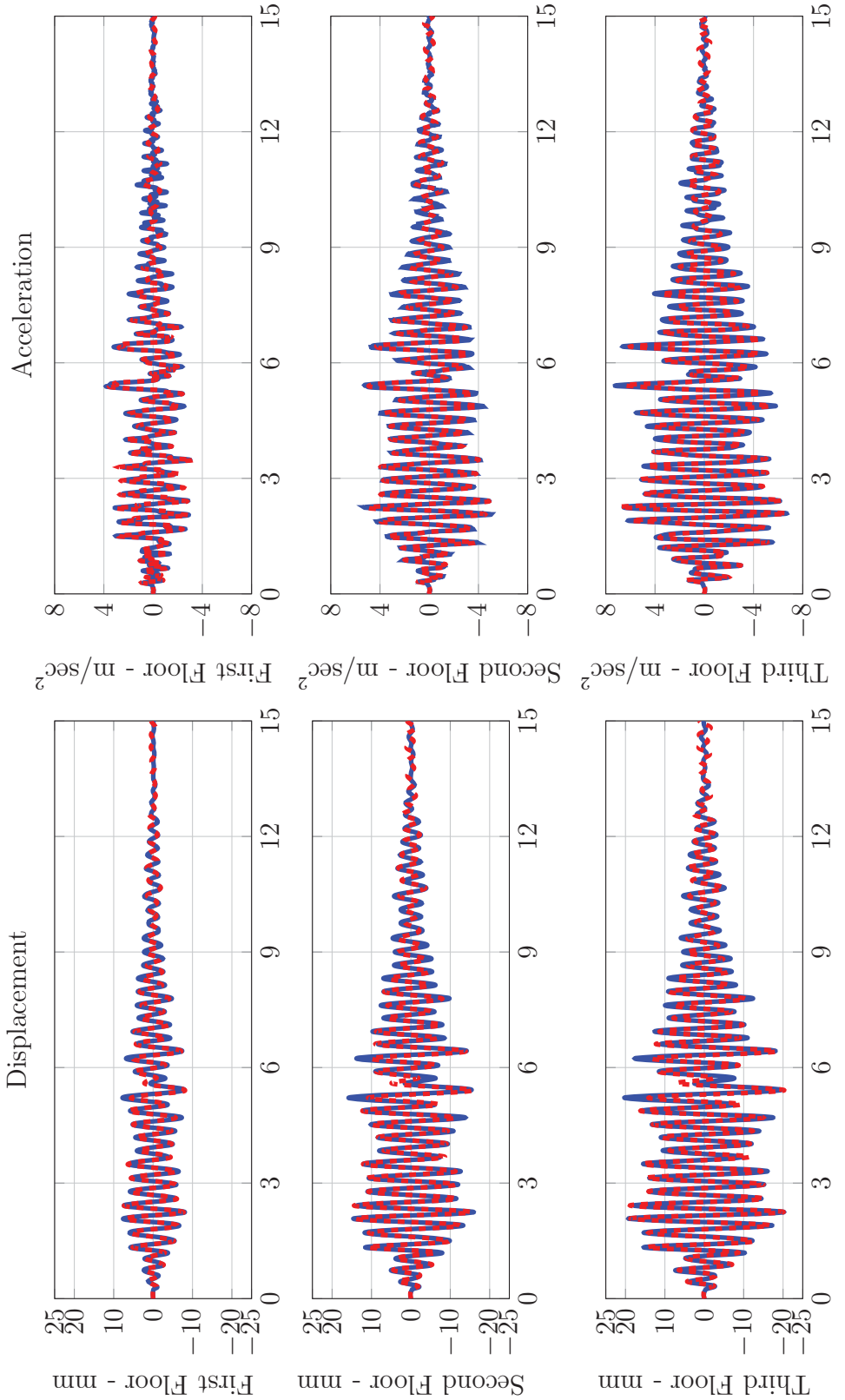


Figure 5.22: Morgan Hill earthquake response comparison in time domain for ST–AS POFF case

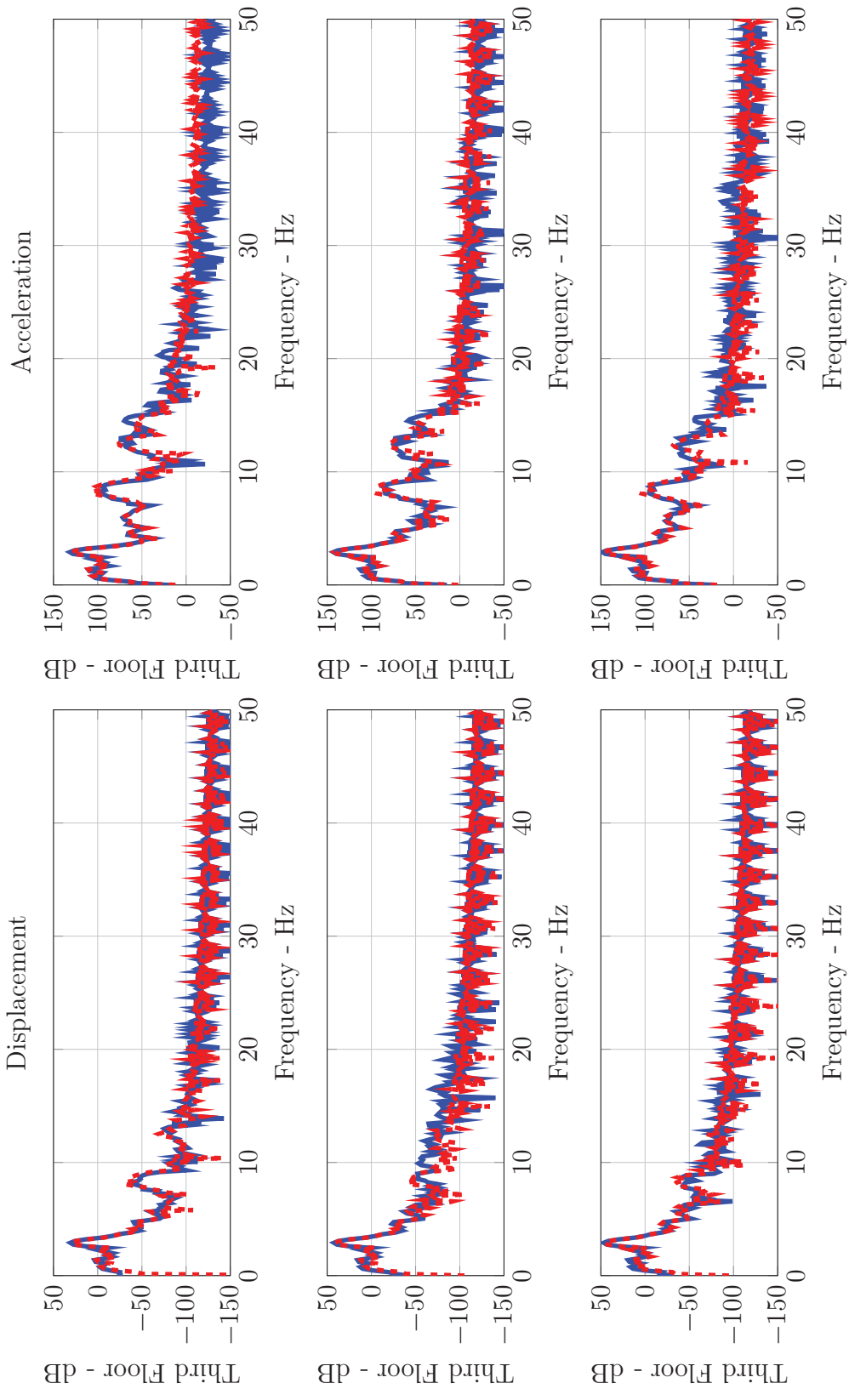


Figure 5.23: Morgan Hill earthquake response comparison in frequency domain for ST–AS POFF case

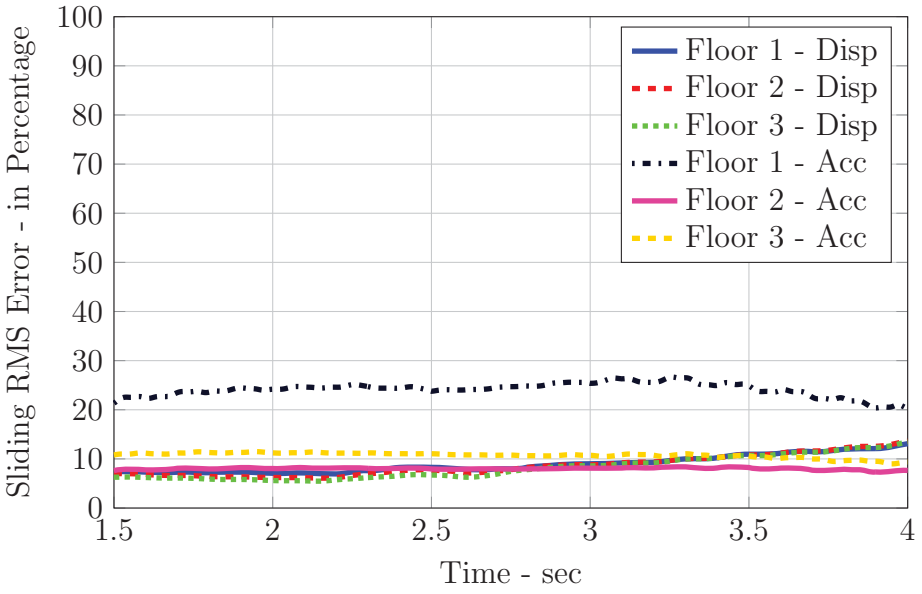


Figure 5.24: Moving RMS error for Morgan Hill earthquake ST–AS POFF case

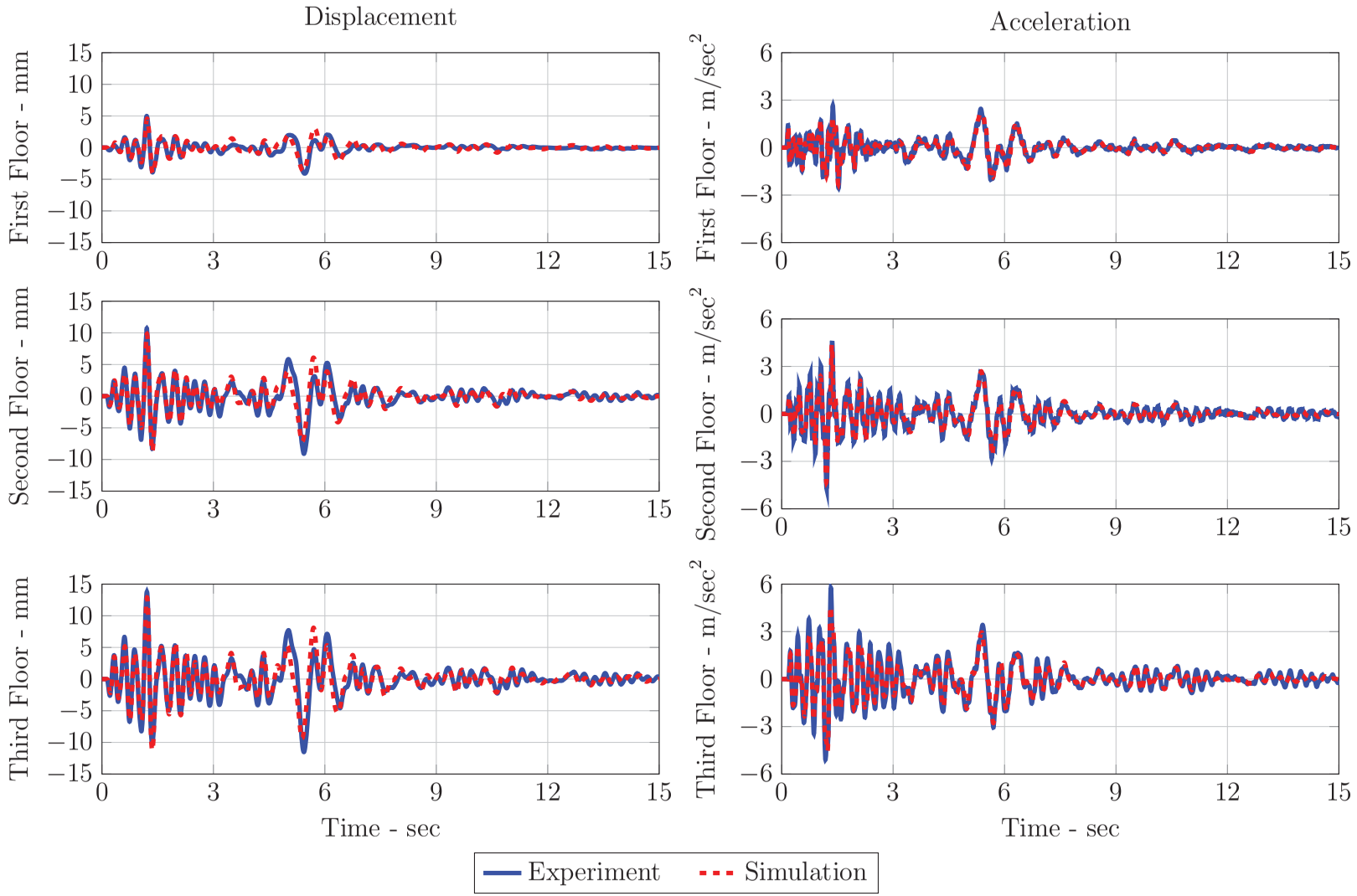


Figure 5.25: Morgan Hill earthquake response comparison in time domain for ST–AS PON case

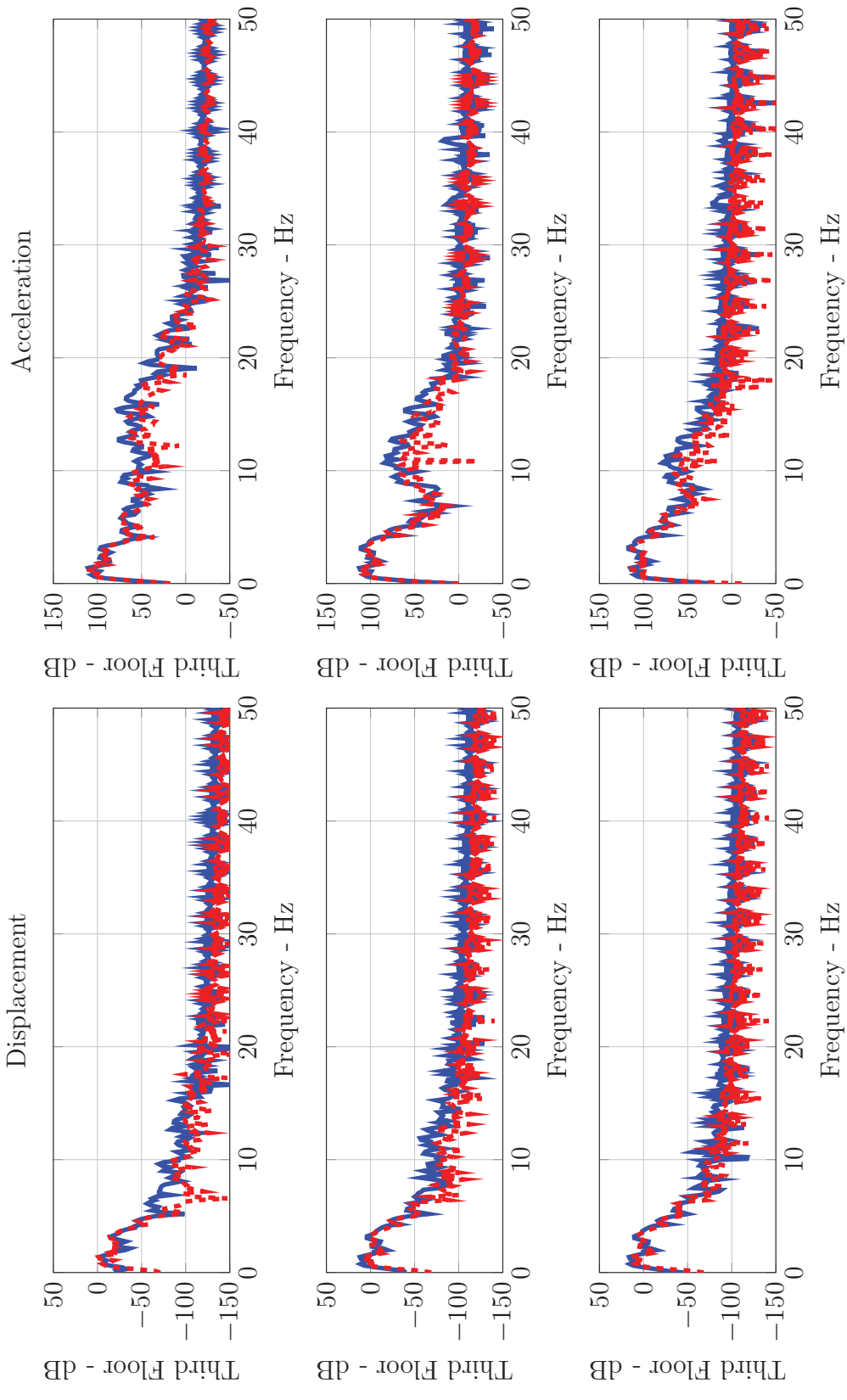


Figure 5.26: Morgan Hill earthquake response comparison in frequency domain for ST–AS PON case

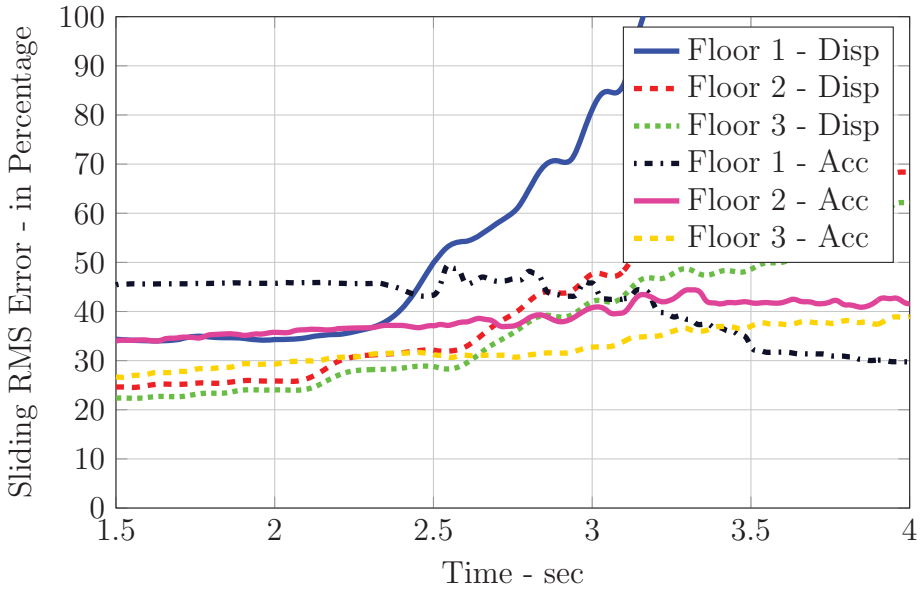


Figure 5.27: Moving RMS error for Morgan Hill earthquake ST–AS PON case

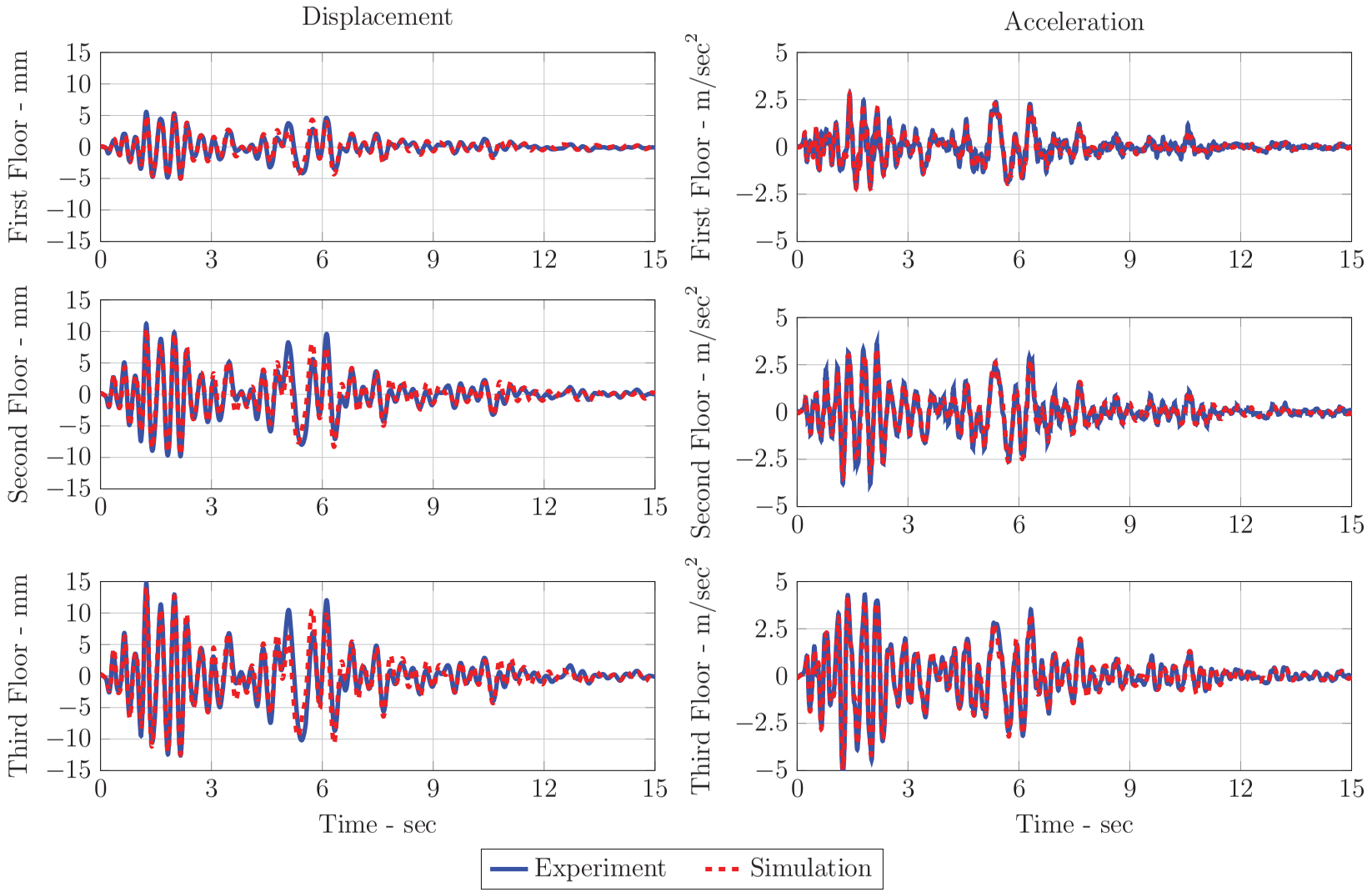


Figure 5.28: Morgan Hill earthquake response comparison in time domain for ST–AS SA case

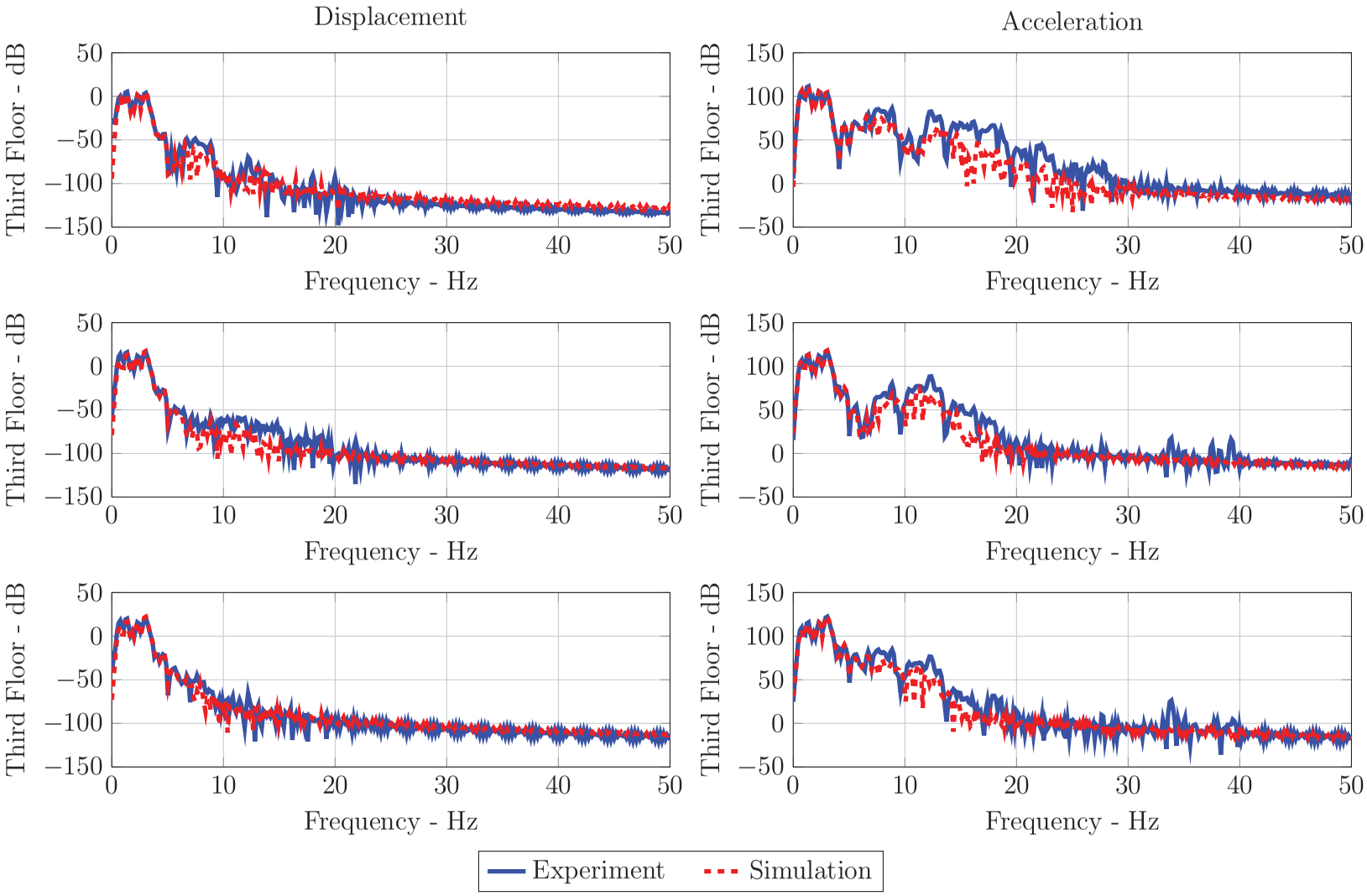


Figure 5.29: Morgan Hill earthquake response comparison in frequency domain for ST–AS SA case

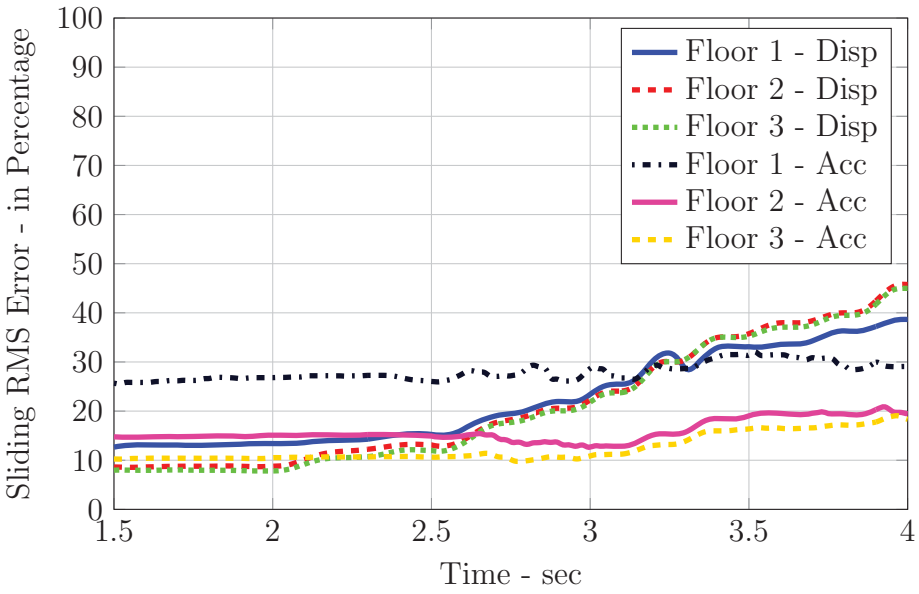


Figure 5.30: Moving RMS error for Morgan Hill earthquake ST–AS SA case

### 5.3.4 Discussions

Considering POFF cases for all earthquakes, the average errors are found below 20 %. However, for the PON cases, the errors elevated up to 60 % for the first floor and 50 % for the second and third floors. Three reasons can be related to the increased errors:

i. In Chapter 4, it has been stated that the MR damper model has up to 18 % of standard deviation error, both for POFF and PON cases. The force generated by the damper in POFF mode is small enough, it doesn't have a considerable impact in distorting structural responses. On the other hand, large PON forces are affecting structural responses notably. Consequently, it is justifiable to observe relatively large errors for PON case comparisons due to damper modeling error. Furthermore, the lessened error for SA case comparisons, where the level of force are between POFF and PON case, supports this claim.

ii. It is observable from PSD comparisons that around the third mode of the structure, the curves are deviating from each other. MR damper is characterized specifically with a sine wave displacement of an amplitude of 5 mm at 2.9 Hz. It is possible that the damper model may not be successful in capturing force levels at higher frequencies.

iii. In PON mode, the structural responses are reduced due to increased damping. However, it appears that for very small displacements, the first floor LVDT tends to stick, eventually causing faulty readings. This behavior is especially noticeable in the sliding RMS error plots.

The overall averaged errors reported in Table 5.1 are 7 % to 10 % and 10 % to 15 % for POFF and SA cases, respectively. For PON case, the first floor error is close to 30 %, whereas for second and third floors, it is about 20 %.

## 5.4 Conclusions

To compare and validate shake table responses with pure simulation results, the three story structure located at HIT with an MR damper attached to its first floor is tested. To perform the comparison successfully, system identification of the structure, characterization and modeling of the MR damper, integration of COC and selection of control parameters are carried out.

The global responses of the system to several ground motions such as relative displacements and absolute accelerations at each level are compared to pure simulation results for POFF, PON and SA cases. For the evaluation of the comparisons, peak, RMS, and sliding RMS errors are computed. In addition, PSD of the shake table and simulations responses are also presented.

In general, the pure simulations predicted shake table results. Further, in terms of displacements and accelerations, strong correlation is found between results. Tracking of the first floor displacements displayed elevated errors due to a sensor hardware error,

however, PSDs showed a good match in frequency domain. Overall, pure simulation results has proven to be successful in predicting shake table responses.

Table 5.1: Evaluation criteria for pure simulation verification

| Ground Motion | Controller | Location | Evaluation Criteria | | | | | | Criteria |
|---|---|---|---|---|---|---|---|---|---|
| | | | J1 | J2 | J3 | J4 | J5 | J6 | Average |
| El Centro | POFF | First Floor | 19.25 | 12.74 | 22.38 | 14.60 | 4.76 | 4.54 | 14.75 |
| | | Second Floor | 19.12 | 10.28 | 14.35 | 5.70 | 4.61 | 3.32 | 10.81 |
| | | Third Floor | 20.31 | 8.46 | 13.29 | 4.18 | 4.86 | 3.20 | 10.22 |
| | PON | First Floor | 43.25 | 43.35 | 37.19 | 24.62 | 8.44 | 6.39 | 31.37 |
| | | Second Floor | 34.47 | 9.92 | 27.31 | 4.78 | 6.66 | 4.49 | 16.63 |
| | | Third Floor | 34.51 | 13.61 | 21.89 | 16.02 | 6.77 | 4.23 | 18.56 |
| | SA | First Floor | 24.21 | 14.99 | 24.77 | 4.62 | 5.31 | 4.77 | 14.78 |
| | | Second Floor | 20.36 | 4.32 | 17.11 | 12.90 | 4.31 | 3.17 | 11.80 |
| | | Third Floor | 21.50 | 6.91 | 11.73 | 11.62 | 4.45 | 2.34 | 11.24 |
| Kobe | POFF | First Floor | 5.64 | 3.63 | 14.73 | 1.39 | 1.82 | 3.85 | 5.44 |
| | | Second Floor | 6.25 | 6.00 | 5.87 | 7.67 | 2.01 | 1.83 | 5.56 |
| | | Third Floor | 5.65 | 5.69 | 8.07 | 6.60 | 1.83 | 2.71 | 5.57 |
| | PON | First Floor | 62.47 | 27.22 | 38.44 | 10.18 | 13.25 | 6.12 | 30.31 |
| | | Second Floor | 48.68 | 17.33 | 37.04 | 12.08 | 10.37 | 6.22 | 25.10 |
| | | Third Floor | 46.17 | 16.36 | 26.86 | 25.98 | 10.13 | 4.64 | 25.10 |
| | SA | First Floor | 26.49 | 11.28 | 25.45 | 13.80 | 6.58 | 4.80 | 16.72 |
| | | Second Floor | 27.28 | 7.90 | 16.85 | 3.54 | 6.78 | 3.82 | 12.47 |
| | | Third Floor | 27.81 | 10.65 | 11.01 | 5.57 | 6.78 | 2.46 | 12.36 |
| Morgan Hill | POFF | First Floor | 9.26 | 3.38 | 23.24 | 7.14 | 2.59 | 5.98 | 9.12 |
| | | Second Floor | 9.05 | 4.31 | 8.00 | 5.63 | 2.50 | 2.14 | 5.90 |
| | | Third Floor | 8.69 | 1.96 | 10.73 | 4.40 | 2.38 | 2.98 | 5.63 |
| | PON | First Floor | 60.22 | 13.58 | 40.05 | 10.91 | 12.61 | 5.66 | 27.47 |
| | | Second Floor | 37.92 | 4.87 | 36.44 | 6.96 | 8.86 | 8.02 | 19.01 |
| | | Third Floor | 34.35 | 7.25 | 31.25 | 23.59 | 8.53 | 7.19 | 21.00 |
| | SA | First Floor | 18.46 | 6.07 | 25.16 | 5.35 | 4.03 | 4.90 | 11.81 |
| | | Second Floor | 17.76 | 1.99 | 14.91 | 15.38 | 3.96 | 2.88 | 10.80 |
| | | Third Floor | 17.26 | 2.15 | 11.52 | 7.25 | 3.75 | 2.51 | 8.39 |
| EQ Average | POFF | First Floor | 11.38 | 6.58 | 20.12 | 7.71 | 3.06 | 4.79 | 9.77 |
| | | Second Floor | 11.47 | 6.86 | 9.40 | 6.33 | 3.04 | 2.43 | 7.42 |
| | | Third Floor | 11.55 | 5.37 | 10.70 | 5.06 | 3.03 | 2.96 | 7.14 |
| | PON | First Floor | 55.31 | 28.05 | 38.56 | 15.23 | 11.43 | 6.06 | 29.72 |
| | | Second Floor | 40.35 | 10.71 | 33.60 | 7.94 | 8.63 | 6.24 | 20.25 |
| | | Third Floor | 38.35 | 12.41 | 26.67 | 21.86 | 8.48 | 5.35 | 21.55 |
| | SA | First Floor | 23.05 | 10.78 | 25.12 | 7.93 | 5.31 | 4.82 | 14.44 |
| | | Second Floor | 21.80 | 4.74 | 16.29 | 10.61 | 5.02 | 3.29 | 11.69 |
| | | Third Floor | 22.19 | 6.57 | 11.42 | 8.15 | 4.99 | 2.44 | 10.66 |

# CHAPTER 6
# VALIDATION OF RTHS WITH SHAKE TABLE TESTS

dRTHS platform inherits all features provided by RTHS configuration. It also means, any error related to RTHS will also appear in dRTHS. In this chapter, experimental study to validate RTHS with shake table test is given, to interpret the comparisons between dRTHS and RTHS, as well as shake table tests and to understand the source of discrepancies that may appear in the comparisons. First, an accurate dynamic model of the actuator and an efficient control algorithm to compensate actuator dynamics, both of which are essential elements of successful RTHS, are introduced in Section 6.1. In Section 6.2, a general implementation of the RTHS is discussed. Next, in Section 6.3, results of RTHS are compared to shake table results. For all cases, error in relative displacement, absolute acceleration in the global sense of the structure is examined including other evaluation criteria discussed in Section 3.5. Finally, a summary of the chapter that interprets and concludes main findings in the comparisons is given in Section 6.4.

A successful comparison between shake table experiments and RTHS, hence, dRTHS depends on the following tasks: (i) modeling of the existing test structure that will serve as the analytical substructure in the RTHS scheme, (ii) characterization of the MR damper which will be used as the physical substructure of RTHS, and (iii) actuator tracking controller design, particularly to ensure stable and high performance RTHS. Steps (i) and (ii) were already introduced in the previous chapters. In the following sections, system modeling and actuator tracking are also discussed. Later, in the subsequent sections, results of RTHS implemented based on these previously introduced concepts are studied.

## 6.1 Design of Tracking Controller to Compensate Actuator Dynamics

The transfer function system of a hydraulic actuator, $G_{x_m,x_c}$ can be idealized by servo-hydraulic system, including servo-valve and servo-valve controller, as well as the actuator and specimen. The system can be represented in block diagram as in Figure 6.1. In this diagram, $x_c$ is the command input, $x_m$ is the measured output and $f$ is the force applied by the actuator to the specimen. An inner loop PID control is often provided within the servo-valve controller that promises basic tracking of command. Although this inner loop control is adequate for slow-rate tests and non-real-time hybrid simulations, strict requirements of RTHS, such as low time delay between desired input and measured output, make the PID control meager. To improve the performance of the actuator control, actuator dynamics should be compensated via a proper control scheme.

In the following subsections, modeling of actuator and development of a novel *Robust Integrated Actuator Control* (RIAC) algorithm is briefly discussed.

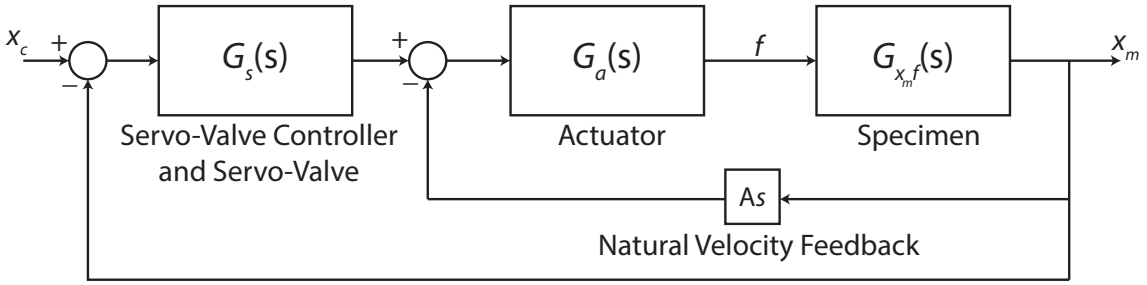


Figure 6.1: Servo-hydraulic system diagram

The performance of servo-hydraulic system can be extended by introducing an outer loop control algorithm that ensures tracking of desired response as simplified in Figure 6.2. In this diagram, $x_d$ is the desired input, and in a RTHS setting, it can be considered as a response of numerical substructure to be imparted to the physical substructure through actuator.

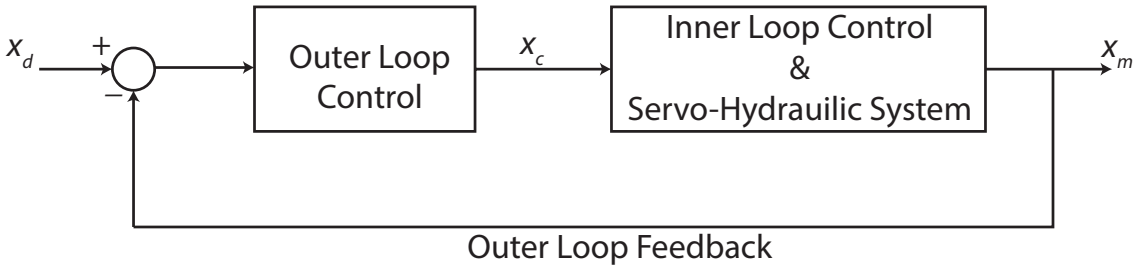


Figure 6.2: Introduction of outer loop control

### 6.1.1 Modeling of Servo-hydraulic Actuator

The actuator dynamics often manifest as a drop in frequency response magnitude and as lag in phase, undesirable for conducting successful RTHS. Developing an effective compensation control system depends on an accurate model that describes such dynamics over the operational frequency content of the target structure. For the purpose stated above, system identification for the HIT and Purdue setups are discussed.

HIT Setup

The hydraulic system at HIT is identified with MR damper attached using a 0–100 Hz band-limited white noise input signal in open loop control setting. The resulting response of the actuator system is stored as the measurement data. The time domain response of the system is shown in Figure 6.3.

Since the loading capacity of the actuator is very large compared to the MR damper maximum force, the resulting transfer functions for passive-off and -on control cases for the damper are assumed to be same. The plant model is determined using *invfreqz* command in MATLAB. The zero-pole system is written as a fourth order transfer function as given Equation (6.1):

$$G_{x_m,x_c,HIT} = \frac{1.5091 \times 10^8}{s^4 + 281.795s^3 + 6.6017 \times 10^4 s^2 + 6.0044 \times 10^6 s + 1.4966 \times 10^8} \quad (6.1)$$

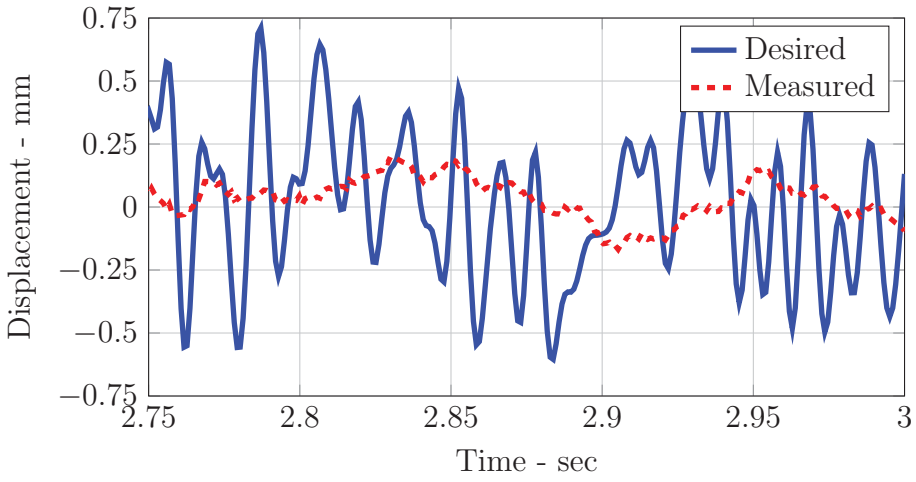


Figure 6.3: Open loop system input and output in time domain for HIT setup

The frequency domain response including identified transfer function of the open loop system is shown in Figure 6.4. It is observed that there is drop in gain ($\sim -0.5\,\mathrm{dB/Hz}$) and lag in the phase ($\sim -6.75\,\mathrm{dB/deg}$) as the frequencies increase.

Purdue Setup

Purdue actuator is identified with MR damper attached using a 0–100Hz band-limited white noise signal when damper is at passive-on and -off mode. The time domain response of the system is shown in Figure 6.5.

Two transfer functions are developed from desired input to measurement output for each case. Since the Purdue damper is relatively small, the effect of the damper mode on the transfer functions are noticeable. To minimize uncertainties due to this behavior, a new transfer function by averaging passive-on and -off results are taken as

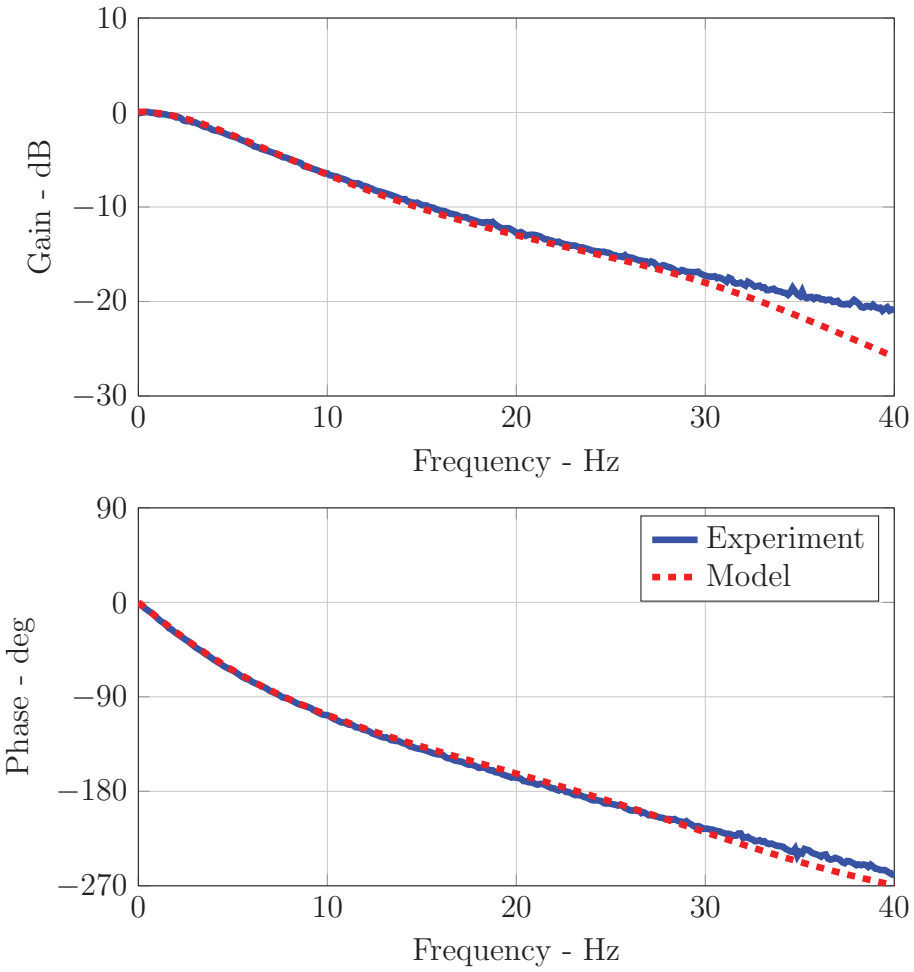


Figure 6.4: Frequency response and identified model of the open loop system for HIT setup

the final transfer function to be modeled. The resulting zero-pole systems are written as given in Equation (6.2):

$$G_{x_m,x_c,OFF,Purdue} = \frac{3.12 \times 10^9}{s^4 + 517.47s^3 + 3.008 \times 10^5 s^2 + 5.49 \times 10^7 s + 3.17 \times 10^9} \quad (6.2a)$$

$$G_{x_m,x_c,ON,Purdue} = \frac{4.70 \times 10^9}{s^4 + 639.55s^3 + 3.50 \times 10^5 s^2 + 7.51 \times 10^7 s + 4.79 \times 10^9} \quad (6.2b)$$

$$G_{x_m,x_c,AVG,Purdue} = \frac{3.91 \times 10^9}{s^4 + 578.51s^3 + 3.25 \times 10^5 s^2 + 6.50 \times 10^7 s + 3.98 \times 10^9} \quad (6.2c)$$

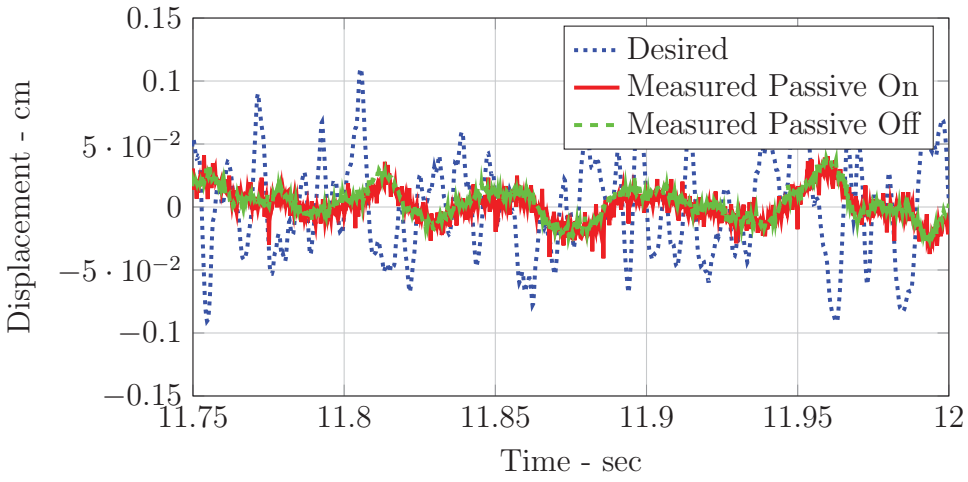


Figure 6.5: Open loop system input and output in time domain for Purdue setup

The frequency domain response including identified transfer functions of the open loop system is shown in Figure 6.6. The average transfer function shows a drop in gain ($\sim -0.3\,\mathrm{dB/Hz}$) and lag in the phase ($\sim -4.5\,\mathrm{dB/deg}$) for the actuator.

### 6.1.2 Control Scheme for Actuator Tracking

As stated before, a novel compensation method, RIAC is used as the outer loop control to track desired displacement. RIAC integrates three key components: (i) loop shaping feedback control based on $H_\infty$ optimization, (ii) a Linear Quadratic Estimator ($LQE$) block for minimizing noise effect and (iii) a feed-forward block for reducing small delay. The combination of these components provides flexibility in controller design to accommodate setup limits while preserving the stability. A block diagram of the controller is illustrated in Figure 6.7. RIAC is described in detail by Ou et al. (2014).

Loop shaping feedback control was first introduced by Gao et al. (2013). By nature, $H_\infty$ controller has a trade off between performance and sensitivity. The controller has limitations in performing perfect tracking while attenuating high frequency noise. A deterioration in performance can manifest when the noise/signal ratio in the system is

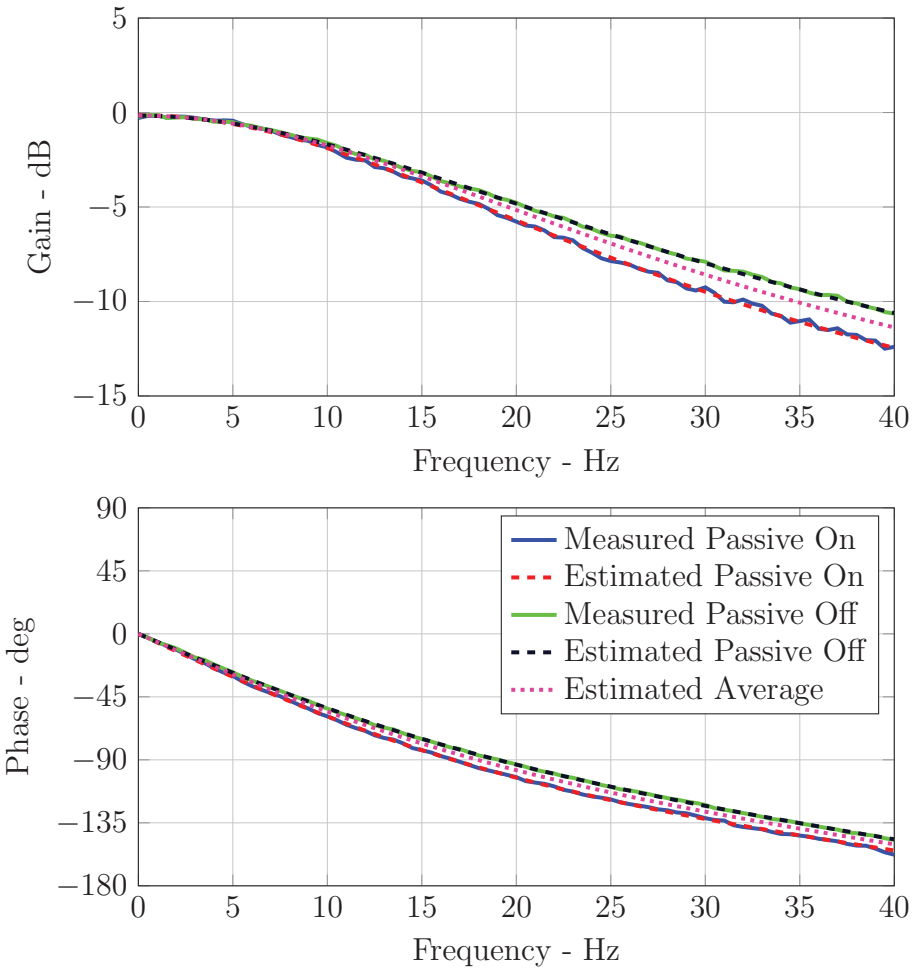


Figure 6.6: Frequency response and identified model of the open loop system for Purdue setup

high. To reduce the impact of noise and improve phase response efficiently, a Kalman filter is integrated into RIAC. Considering the small residual delay may still exist, to further enhance the efficiency of the RIAC, an inverse compensation algorithm proposed by Chen and Ricles (2009) is implemented.

RIAC can be applied to any servo-hydraulic system regardless the size or flow limitation of the actuator. In the following section, performance of the controller for HIT and Purdue setups is presented.

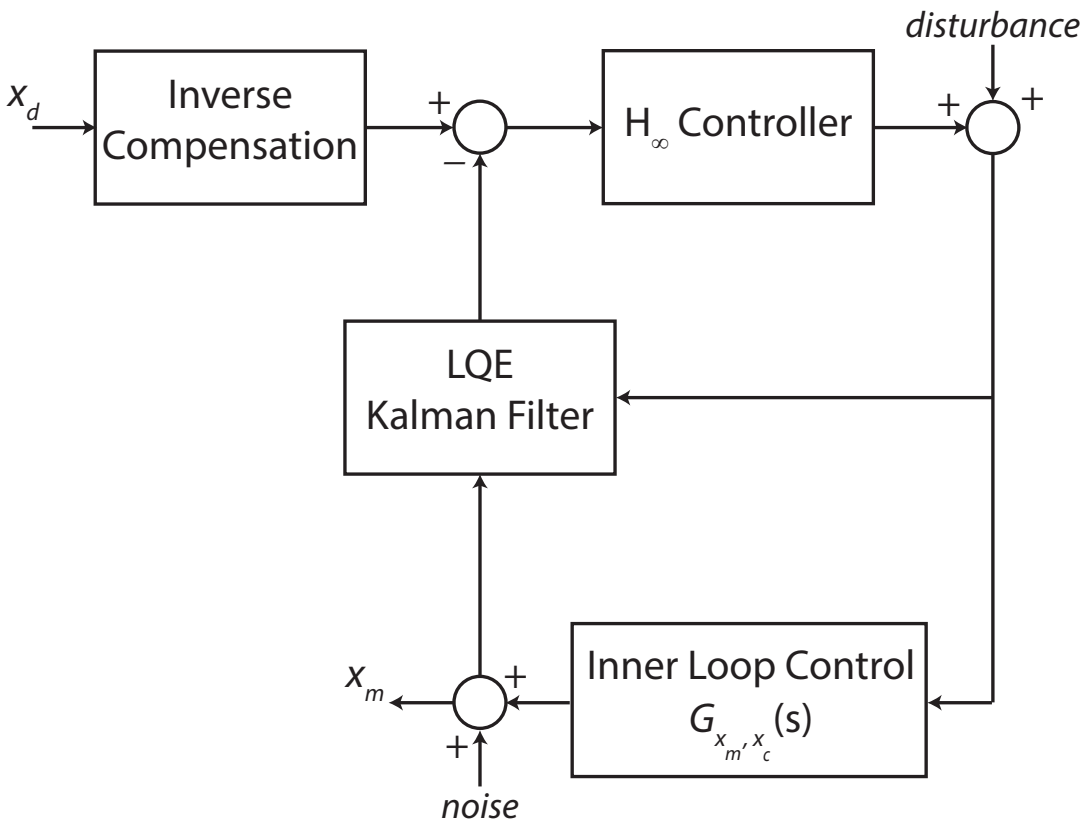


Figure 6.7: RIAC control block diagram

### 6.1.3 Verification of Controller

The performance of the actuator motion controller can be assessed by deriving the closed-loop system transfer function from desired and measured signals. Furthermore, the effect of the size and speed of the actuator on the controller efficiency, both large-size HIT and small-size Purdue actuators are tested. To obtain the transfer function, a band limited white noise bounded with 0-20 Hz is given to the actuators for 30 seconds in RIAC controlled closed loop setting. The transfer function is then compared to unity gain. In Figures 6.8 and 6.9, HIT and Purdue closed loop transfer functions are presented. For both actuators, an optimal performance close to unity gain is obtained. Ultimately, it is shown that RIAC can be used for two completely different actuators.

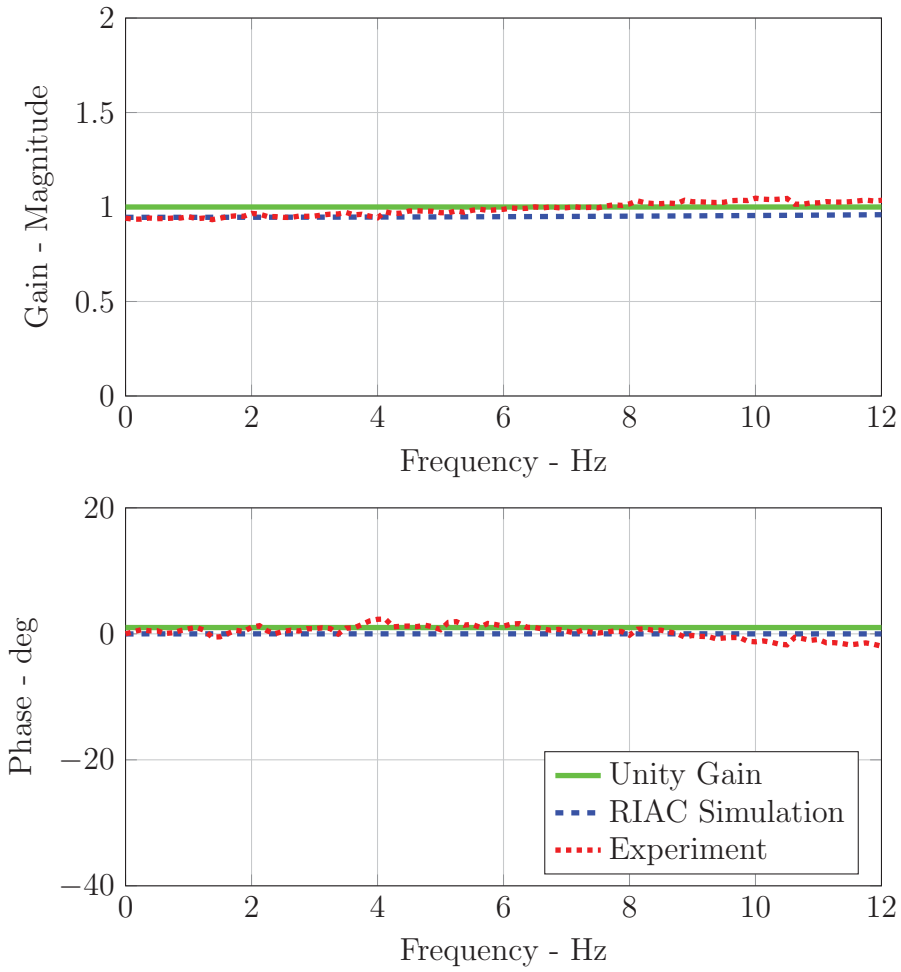


Figure 6.8: Performance of RIAC for HIT actuator

In time domain, RMS errors between desired and measured signals for both actuators varied in the range of 3 % to 10 %.

## 6.2 RTHS Implementation

Experimental RTHS setup at IISL has been previously discussed in Section 2.5. In this section, the RTHS implementations is explained thoroughly.

As shown in Figure 6.10, based on the given ground excitation, analytical substructure simulated in real-time by MATLAB/xPC generates global responses. Only

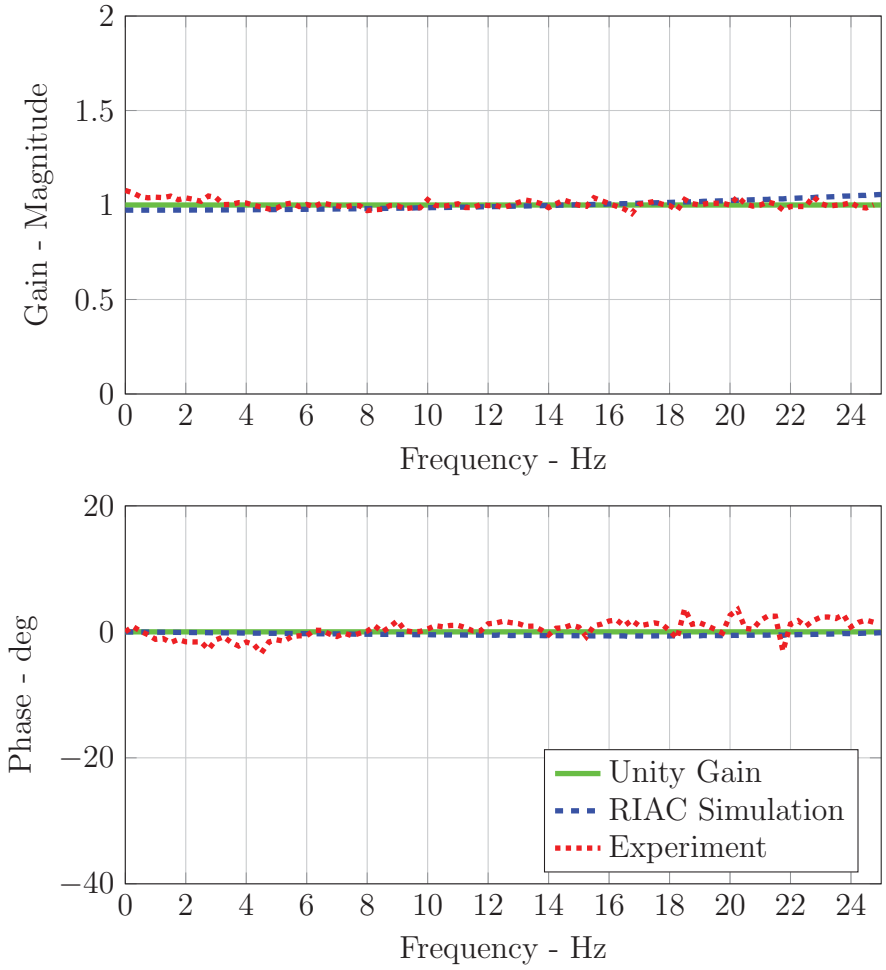


Figure 6.9: Performance of RIAC for Purdue actuator

the first floor displacement, which is compensated with RIAC, is sent to the actuator to engage the MR damper. Eventually, MR damper produces a force response to the given displacement which is fed back to the analytical substructure for the next time step.

A simplified implementation of RTHS configuration in MATLAB/Simulink is provided in Figure 6.11.

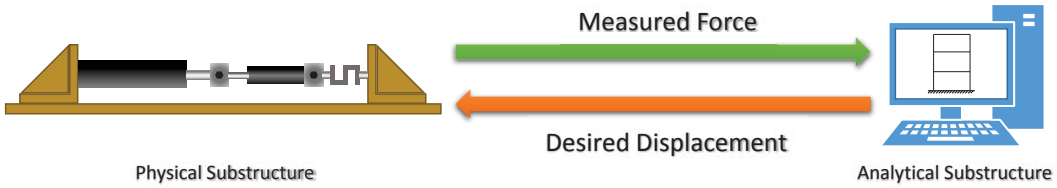


Figure 6.10: Communication between physical and anayltical substructure in a RTHS frame

## 6.3 Comparison of Shake Table Test Responses with RTHS Results

In this section, RTHS conducted at Purdue is compared to the shake table tests performed at HIT. The experimental plan for the validation of the RTHS is focused on simulating the seismically-excited three story structure while testing the damper device physically at passive on/off and semi-active control modes. Results obtained from RTHS are compared to shake table responses and accuracy of the RTHS configuration is assessed with evaluation criteria proposed in Chapter 3.

As in Chapter 5, passive on/off and semi-active control cases are considered for the comparison. Excitation input to the structure in RTHS setup is selected as El Centro, Kobe and Morgan Hill earthquakes measured by two accelerometers placed on the shake table. No filtering is applied to the ground accelerations. A sampling and integration rate of 5000 Hz is selected for the RTHS for a fair comparison.

### 6.3.1 El Centro

In this section, results between shake table and RTHS are compared for El Centro earthquake. Passive-off (POFF), -on (POFF) and semi-active (SA) cases are considered for the comparisons.

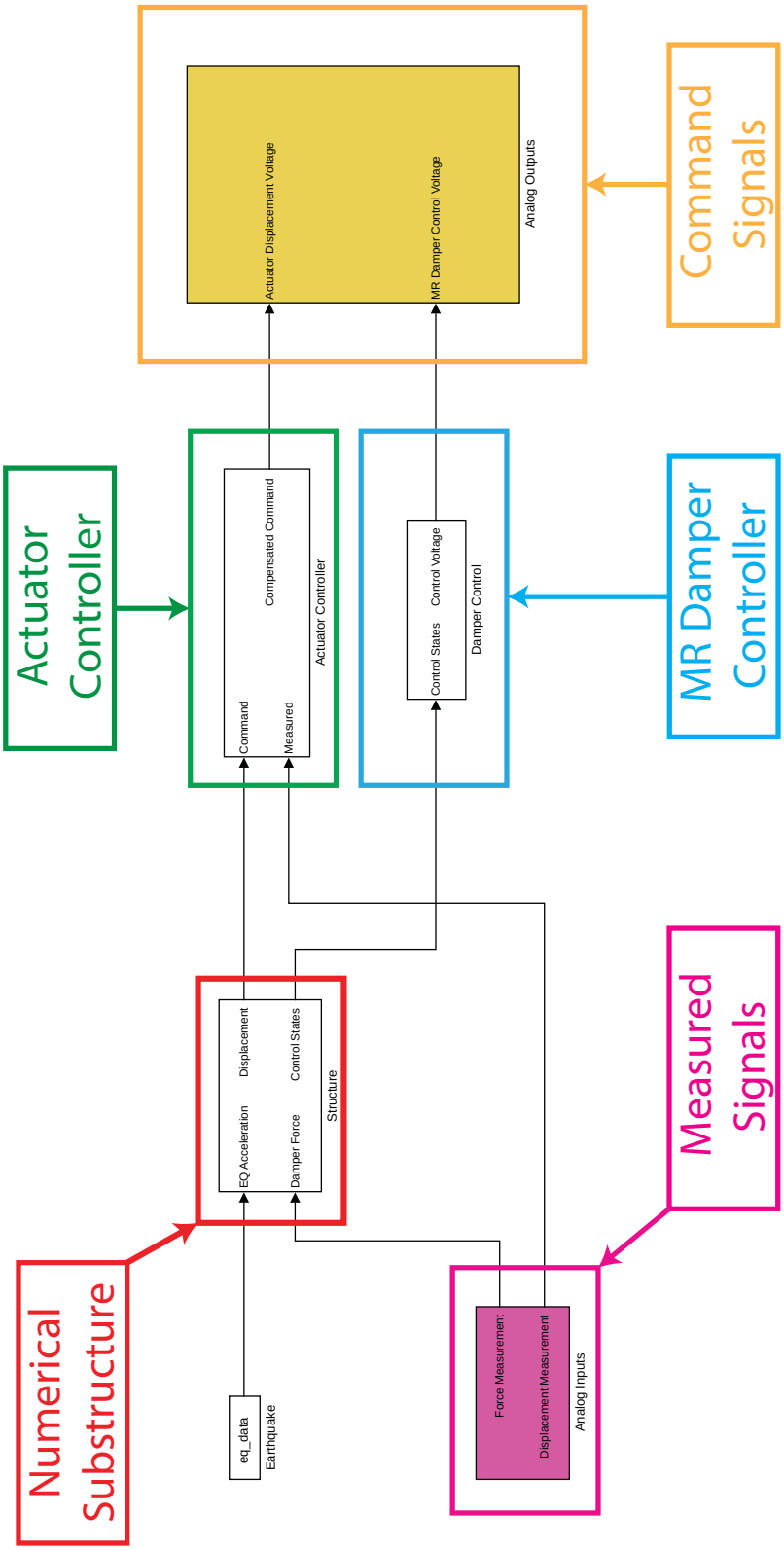


Figure 6.11: A representative Simulink model of the RTHS simulation

Passive-off

Displacement and acceleration comparisons are given in Figures 6.12 and 6.13. RMS and peak response errors are tabulated in Table 6.1 in percentage. In addition, moving RMS errors are illustrated in Figure 6.14.

Compared to shake table-pure simulation comparisons, the reported peak errors for floor accelerations and displacements are slightly large and ranging from 10 % to 30 %. On the other hand, the RMS error are lower and varying from 4 % to 15 %. Range-normalized RMS errors for RTHS and pure simulations are close to each other.

Passive-on

For PON case, displacement and acceleration comparisons are given in Figures 6.15 and 6.16. Related errors are tabulated in Figure 6.17 and Table 6.1.

As observed in shake table-pure simulation results, there is a deviation in the first floor displacement responses concentrated at around 6–9 seconds.

RMS and peak response errors for floor accelerations and displacements are lower than pure simulation errors and are ranging from 2 % to 35 %. The criteria-averaged RMS error is varying from 14 % to 20 %. It has been noted that the first floor errors are smaller than those of pure simulation case, possibly due to the fact that physical MR damper is showing better performance than its analytical model despite the difference in the force levels between HIT and Purdue dampers.

Semi-active

The comparisons for SA case are given in Figures 6.18 to 6.20 and Table 6.1.

As observed in the previous chapter, the reported averaged errors for SA case are between PON and POFF cases. RMS and peak response errors vary from 3 % to 238 % and the criteria-averaged RMS error is around 10 %.

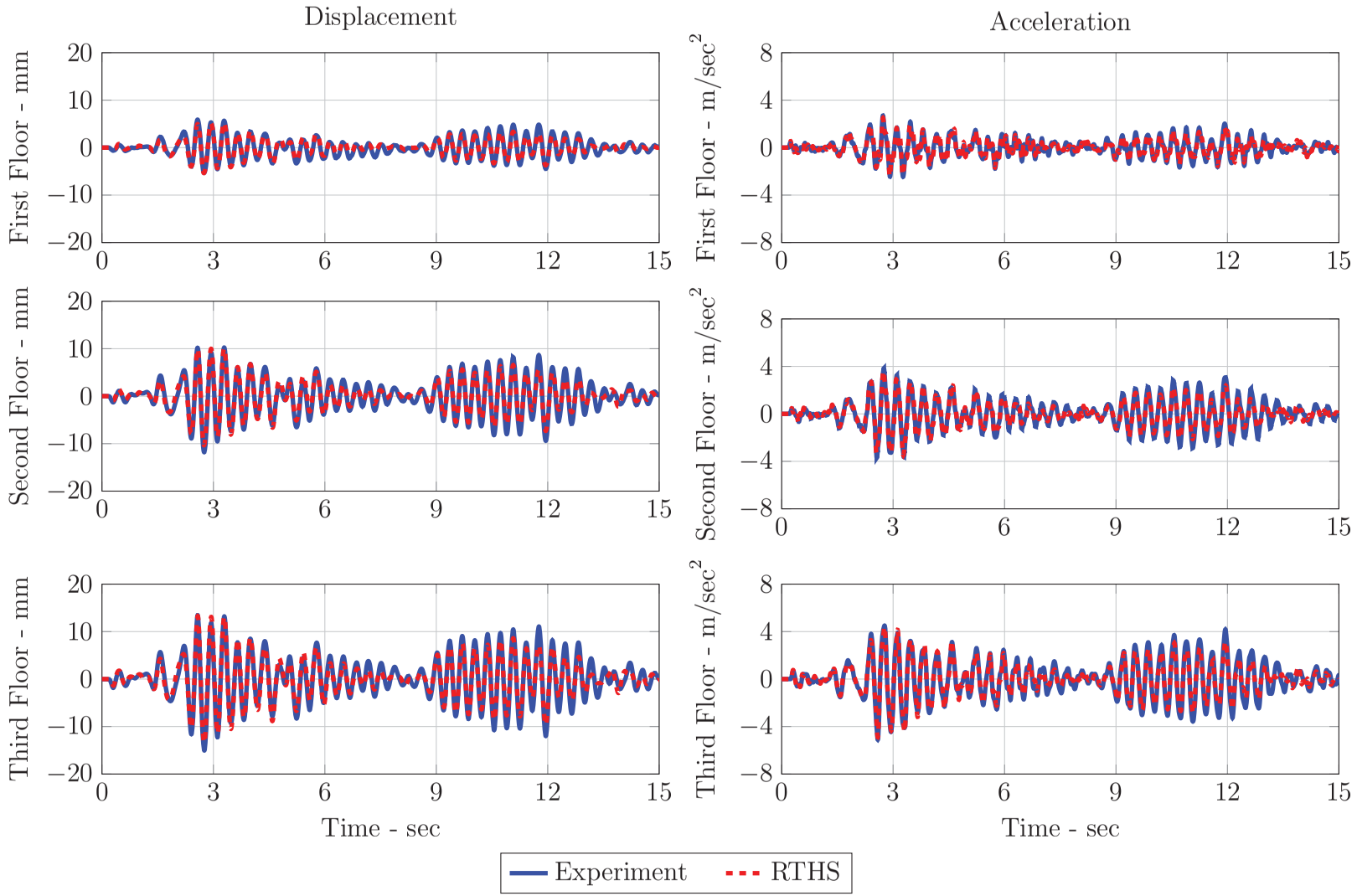


Figure 6.12: El Centro earthquake response comparison in time domain for ST–RTHS POFF case

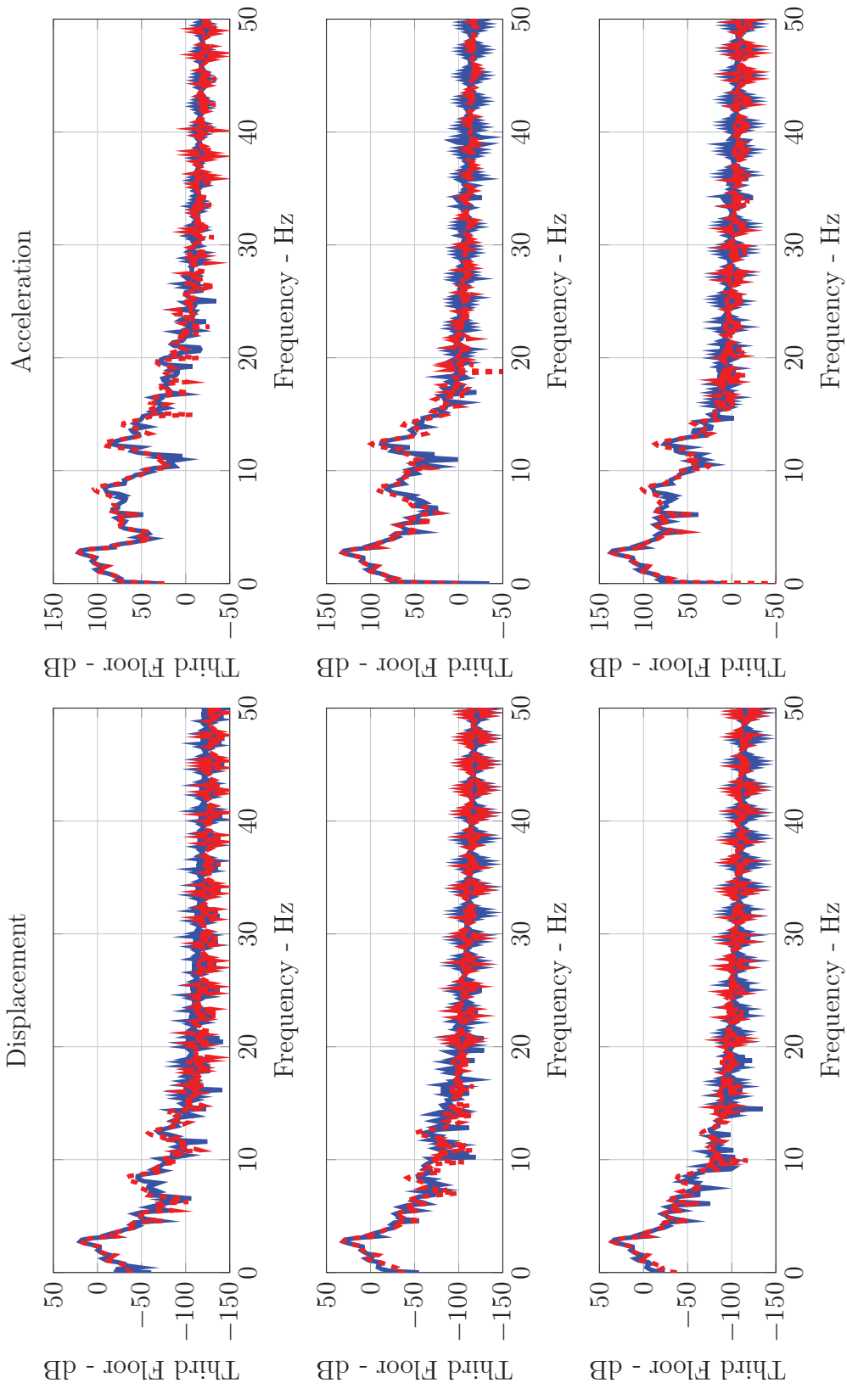


Figure 6.13: El Centro earthquake response comparison in frequency domain for ST–RTHS POFF case

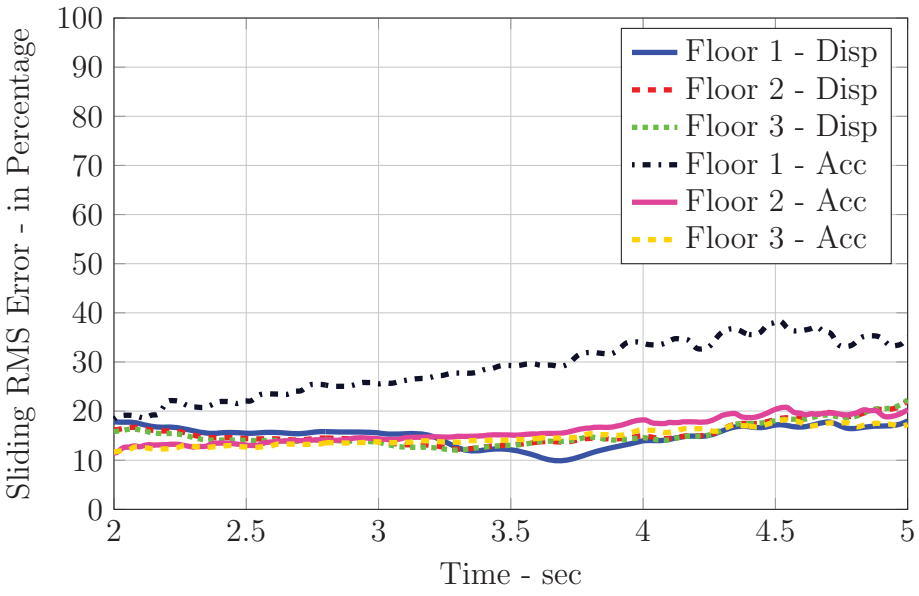


Figure 6.14: Moving RMS error for El Centro earthquake ST–RTHS POFF case

### 6.3.2 Kobe

In this section, results between shake table and pure simulations are compared for Kobe earthquake. POFF, PON and SA cases are considered for the comparisons.

#### Passive-off

The related response comparisons are given in Figures 6.21 and 6.22. The errors observed for this case are higher than pure-simulation results. The differences between Purdue and HIT damper POFF forces can be held accountable for this elevated disturbances.

#### Passive-on

PON case comparisons, error tables and moving RMS error plot are given in Figures 6.17, 6.24 and 6.25 and Table 6.1.

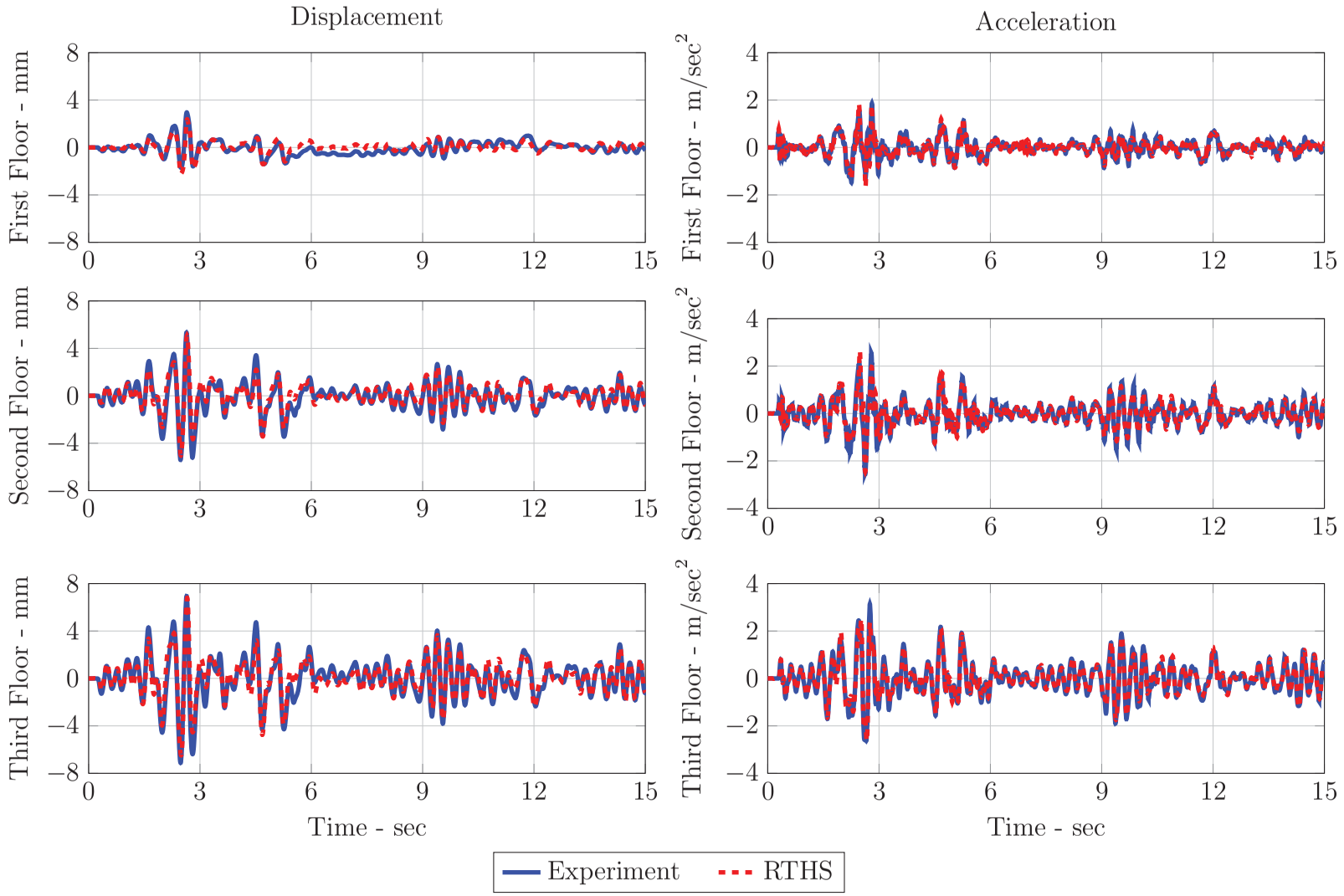


Figure 6.15: El Centro earthquake response comparison in time domain for ST–RTHS PON case

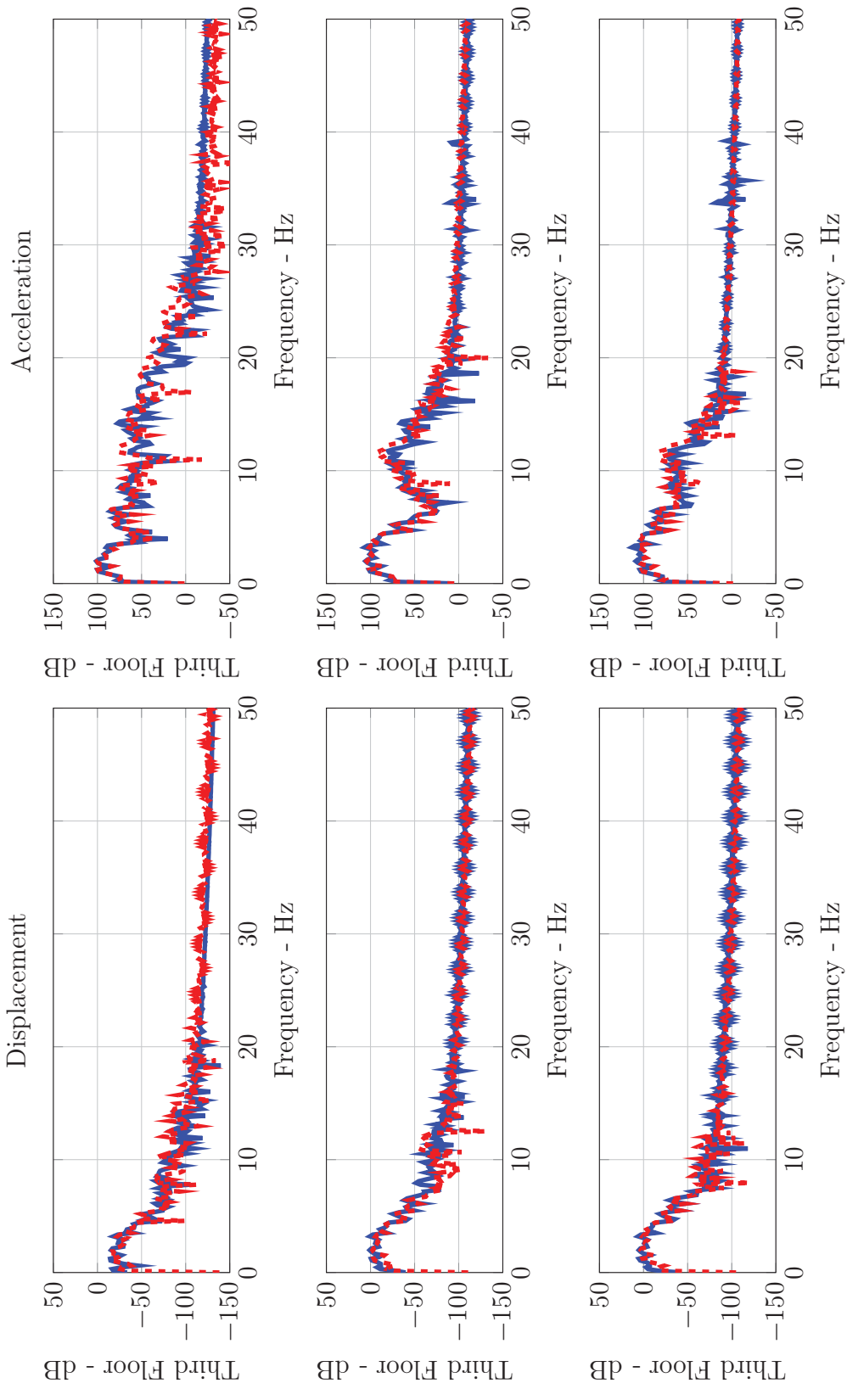


Figure 6.16: El Centro earthquake response comparison in frequency domain for ST–RTHS PON case

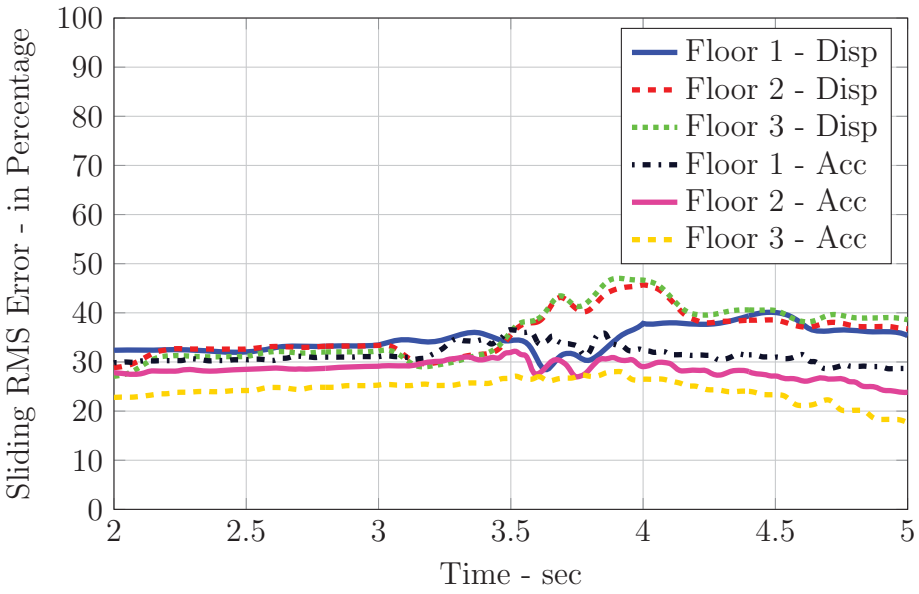


Figure 6.17: Moving RMS error for El Centro earthquake ST–RTHS PON case

For this case, RMS and peak response errors range from 5 % to 50 % which are lower than pure simulation comparisons. Likewise, the criteria-averaged errors are concentrated around 20 %, which are also smaller compered to pure simulation errors.

Semi-active

In Figure 6.27 and Figure 6.28, SA case comparisons are presented. The reported errors and criteria-averaged errors are similar to pure simulation comparisons and in the range 4 % to 27 % and 12 % to 16 %, respectively.

### 6.3.3 Morgan Hill

In this section, results between shake table and pure simulations are compared for Morgan Hill earthquake. POFF, PON and SA cases are considered for the comparisons.

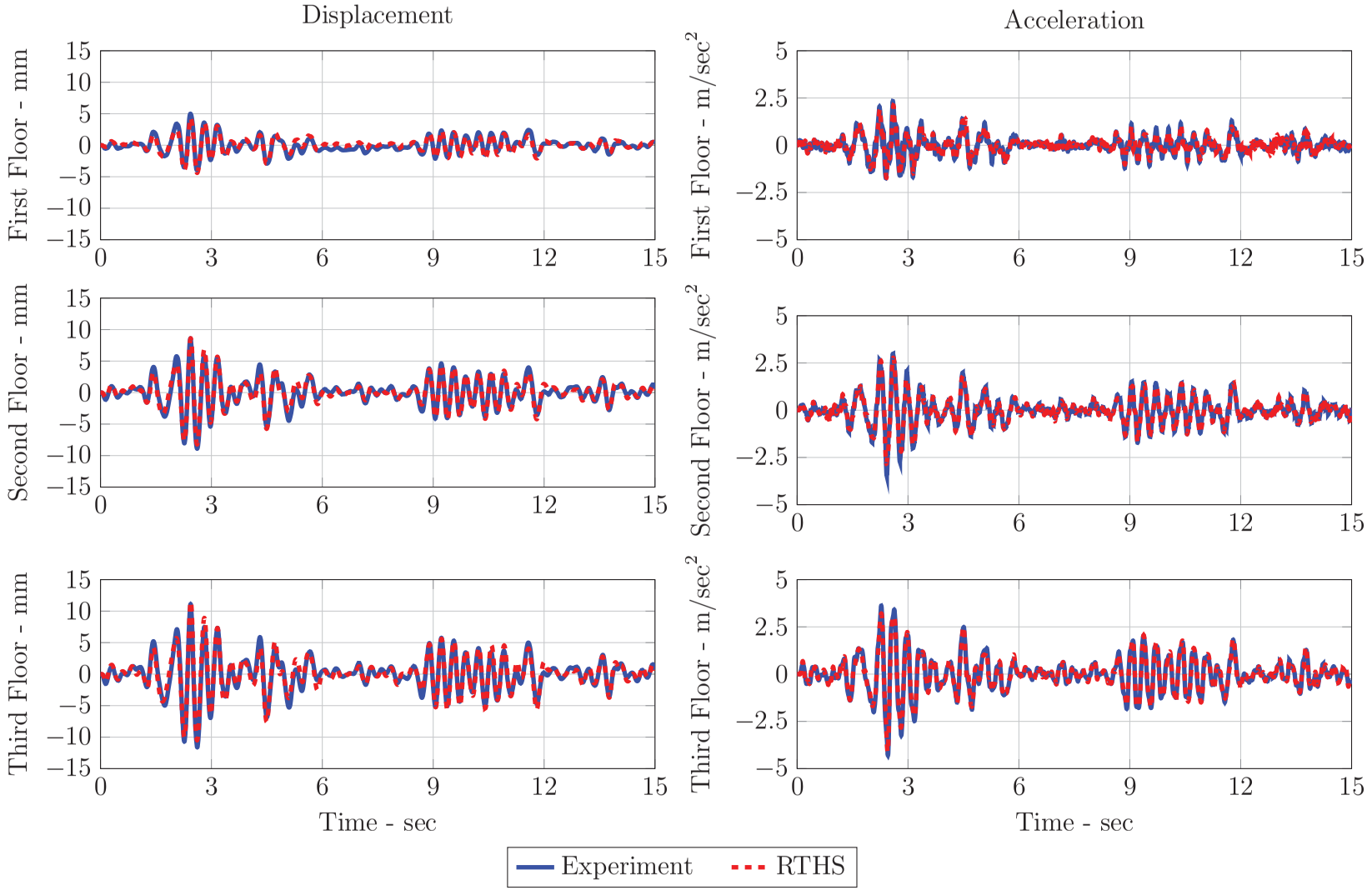


Figure 6.18: El Centro earthquake response comparison in time domain for ST–RTHS SA case

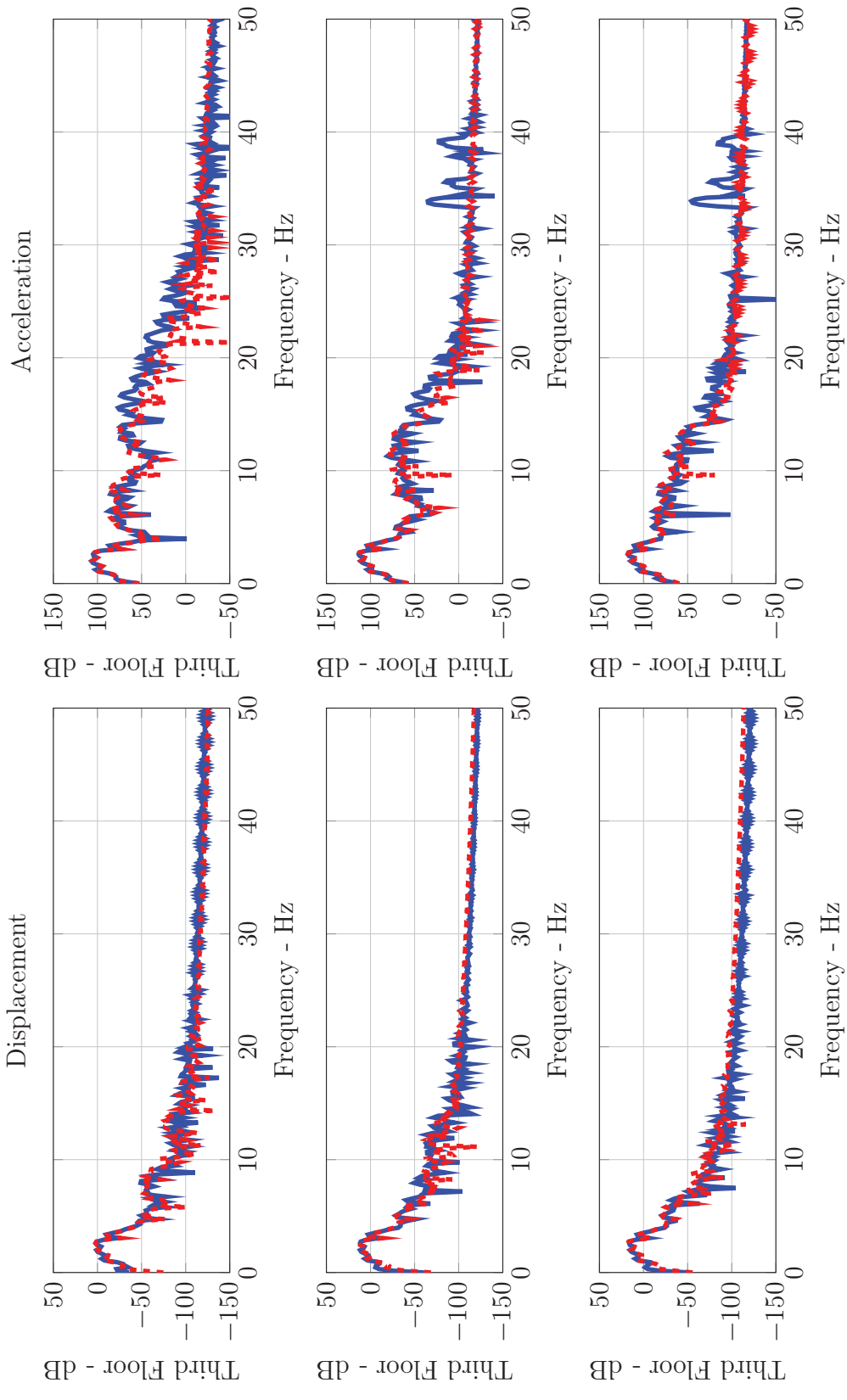


Figure 6.19: El Centro earthquake response comparison in frequency domain for ST–RTHS SA case

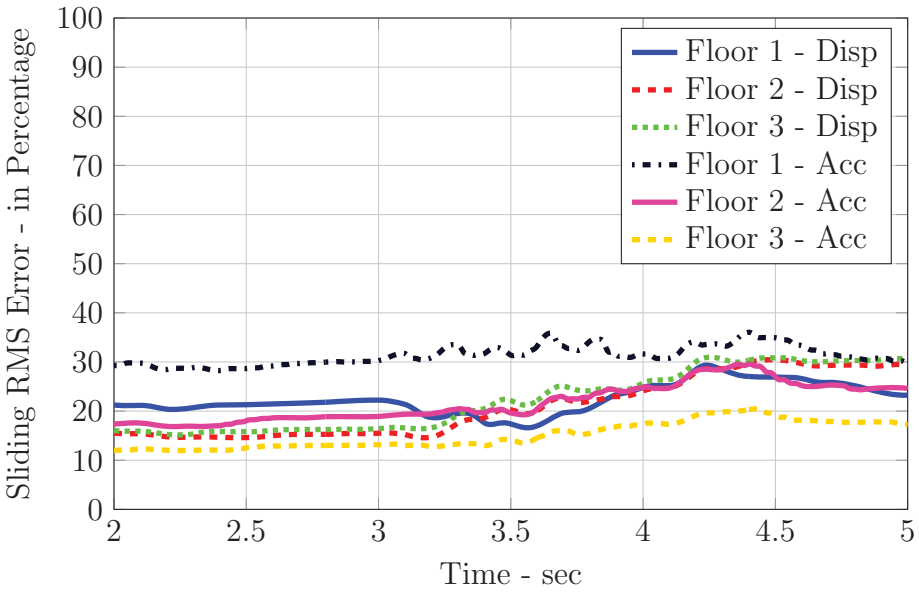


Figure 6.20: Moving RMS error for El Centro earthquake ST–RTHS SA case

Passive-off

Time- and frequency-domain comparisons for POFF case are provided in Figures 6.21 and 6.22. The reported errors and moving RMS errors are in the range of 5 % to 14 %. The averaged errors are nearly 10 % for all criteria.

Passive-on

Displacement and acceleration comparisons are given in Figures 6.33 and 6.34. RMS and peak response errors for accelerations and displacements are ranging from 7 % to 40 % and are lower than pure simulation errors. The criteria-averaged error is varying from 16 % to 21 %.

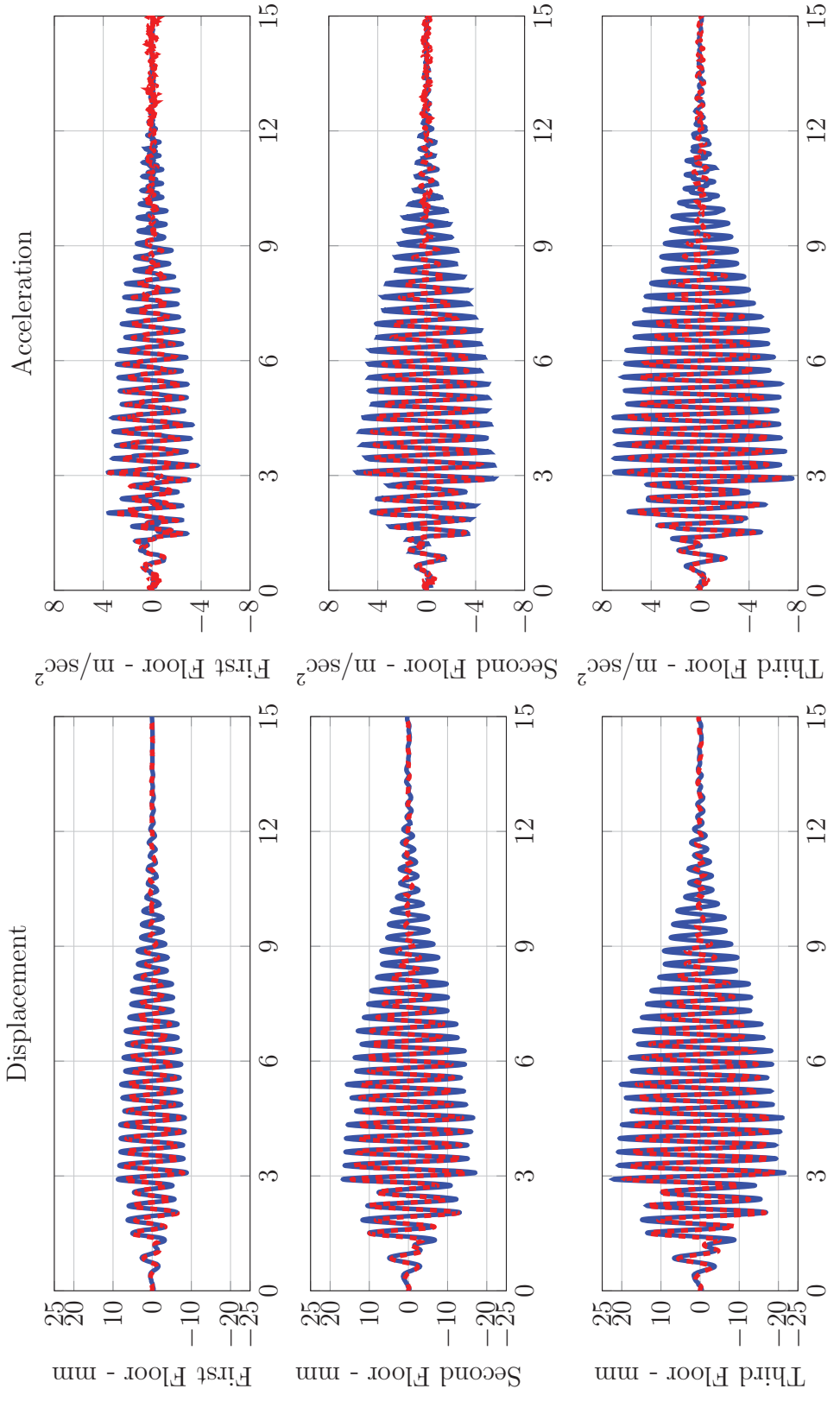


Figure 6.21: Kobe earthquake response comparison in time domain for ST–RTHS POFF case

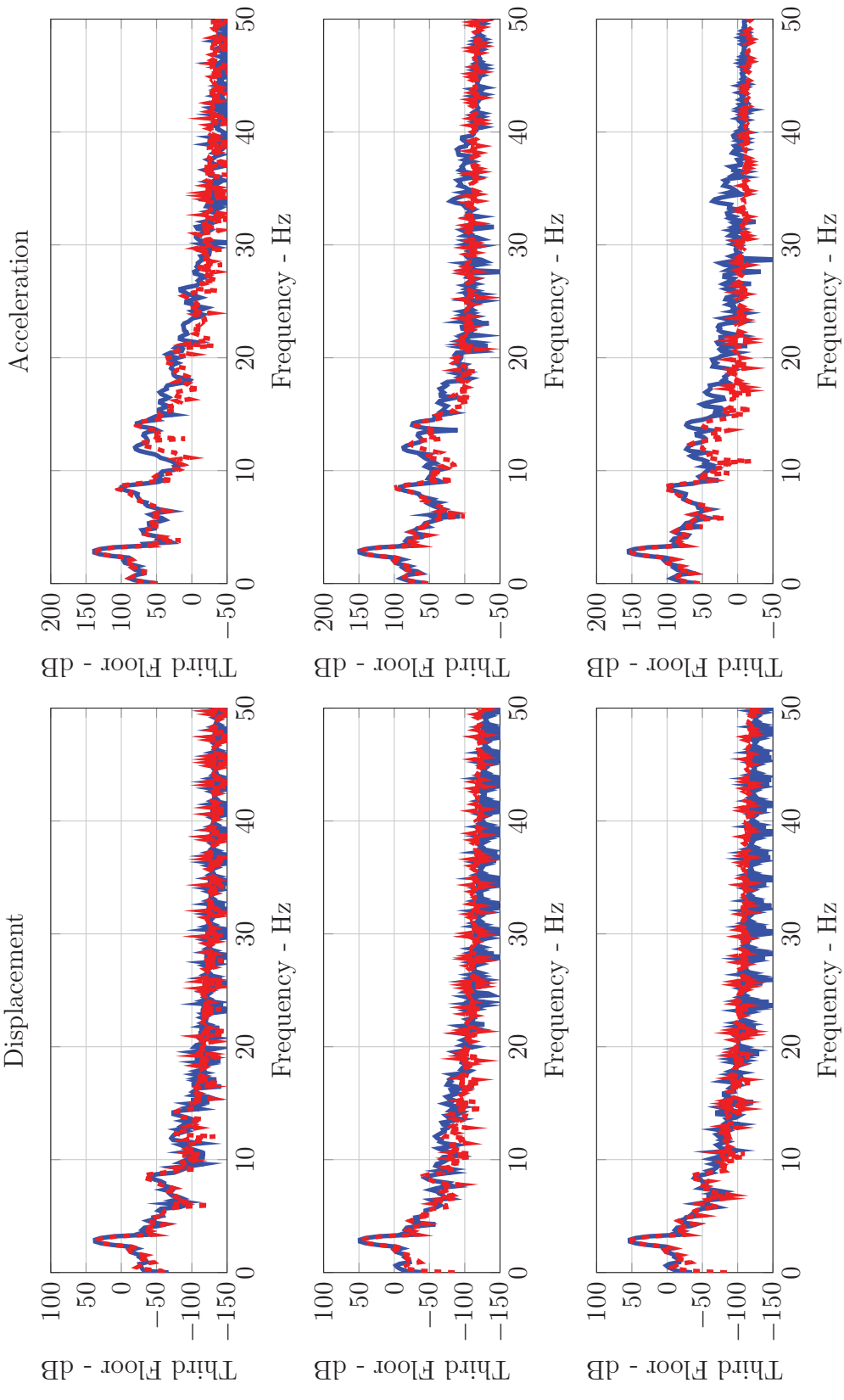


Figure 6.22: Kobe earthquake response comparison in frequency domain for ST–RTHS POFF case

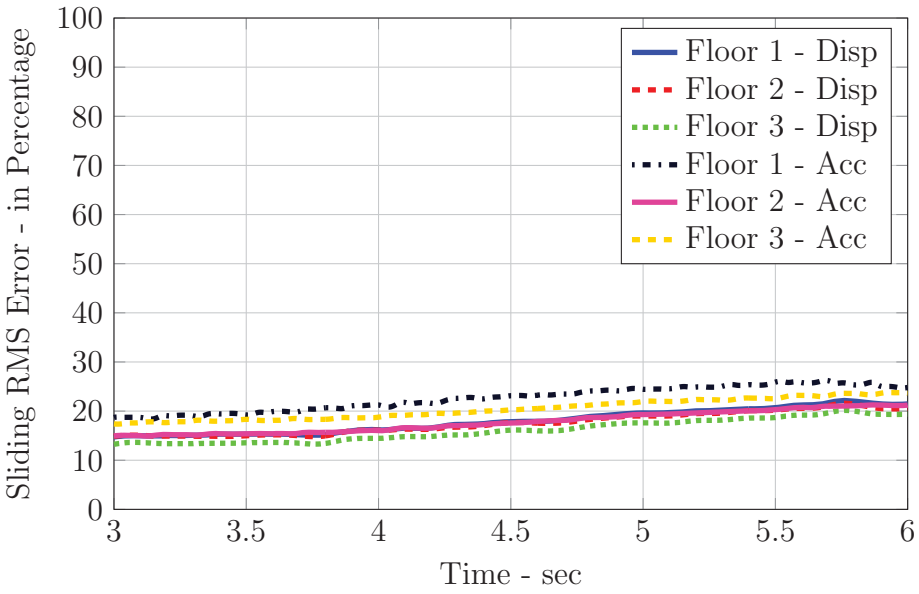


Figure 6.23: Moving RMS error for Kobe earthquake ST–RTHS POFF case

Semi-active

SA case comparisons are presented in Figures 6.27 and 6.28. The RMS and peak response errors are confined within 3 % to 18 %. The criteria-averaged errors are around 10 %.

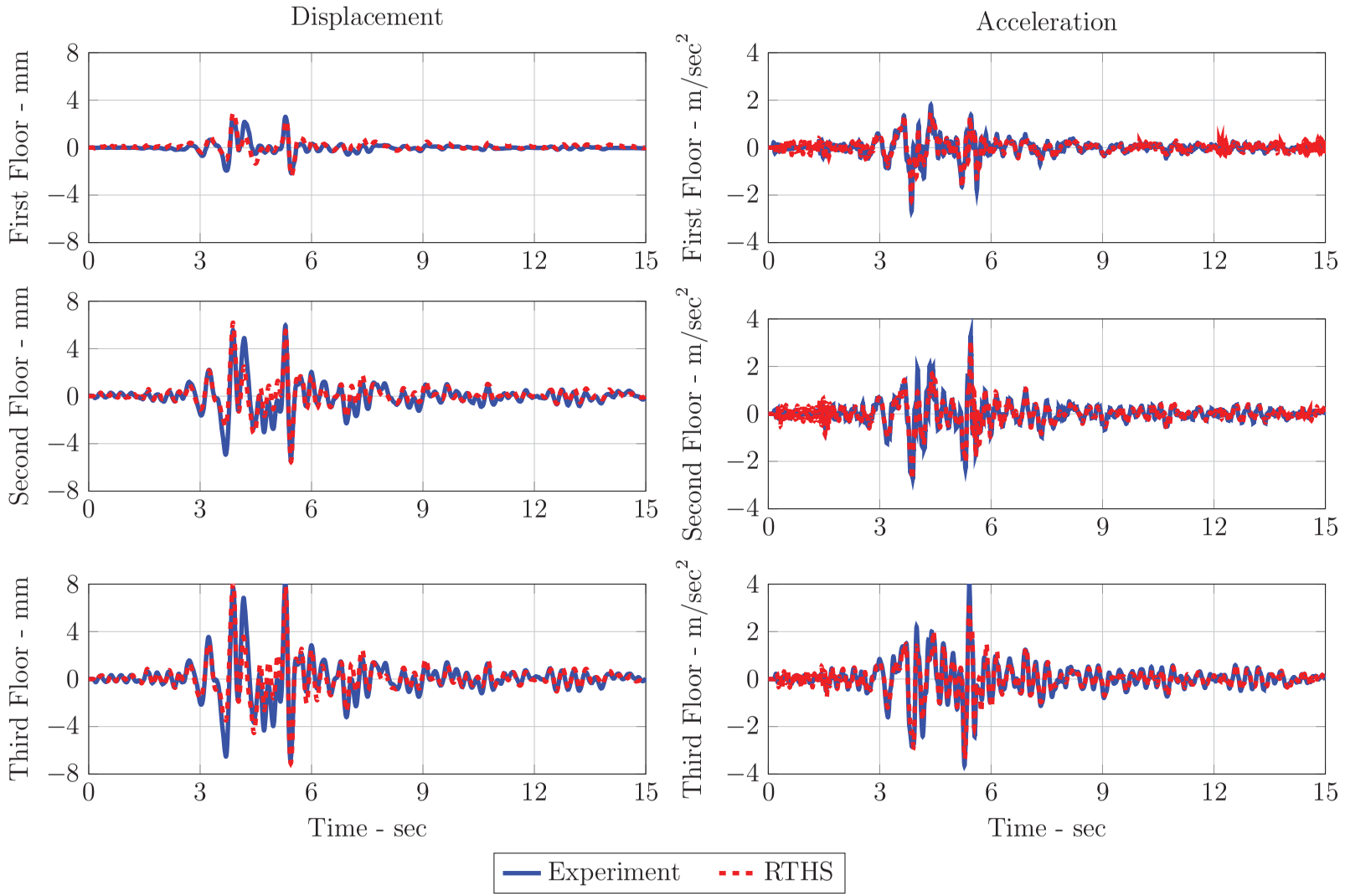


Figure 6.24: Kobe earthquake response comparison in time domain for ST–RTHS PON case

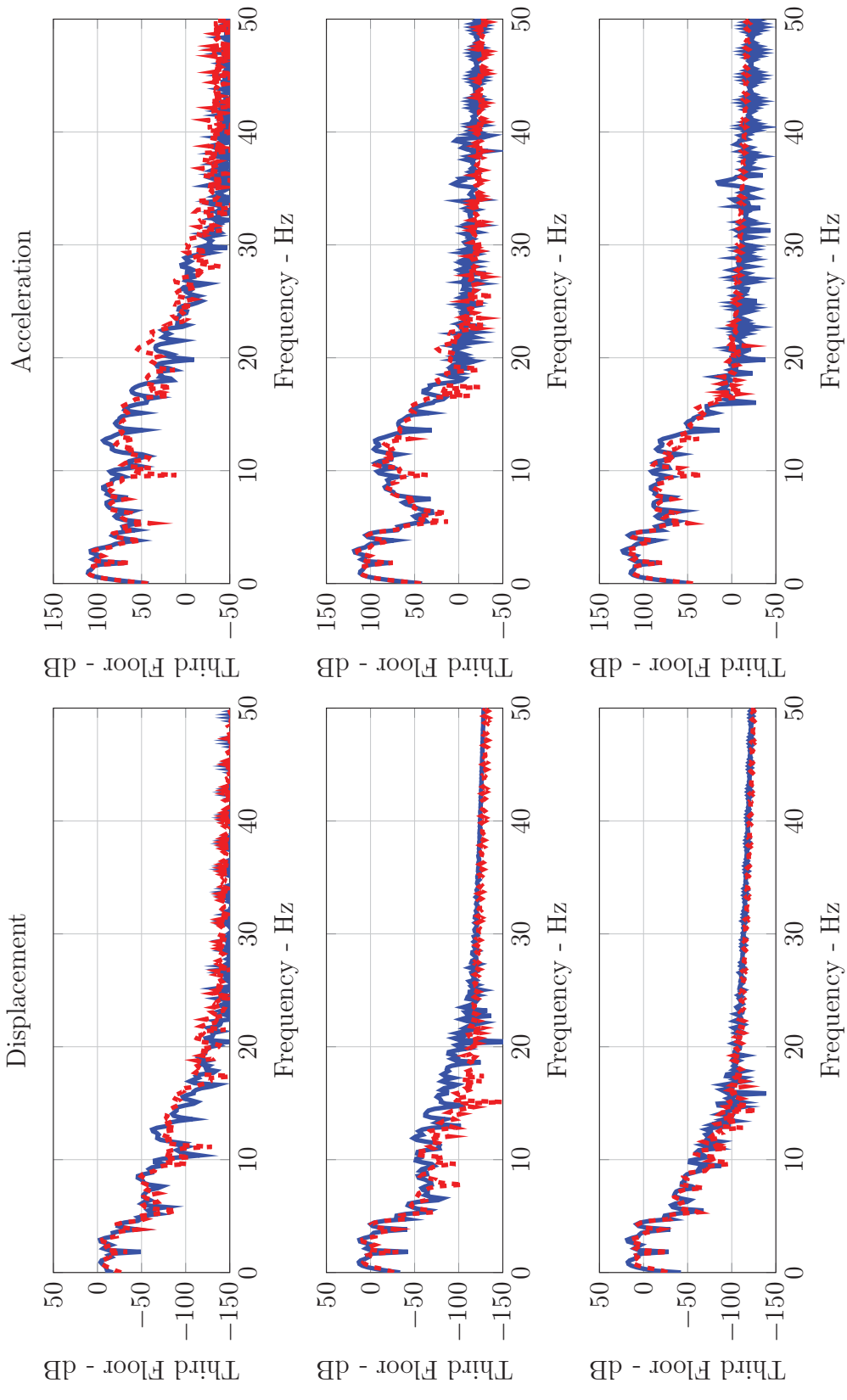


Figure 6.25: Kobe earthquake response comparison in frequency domain for ST–RTHS PON case

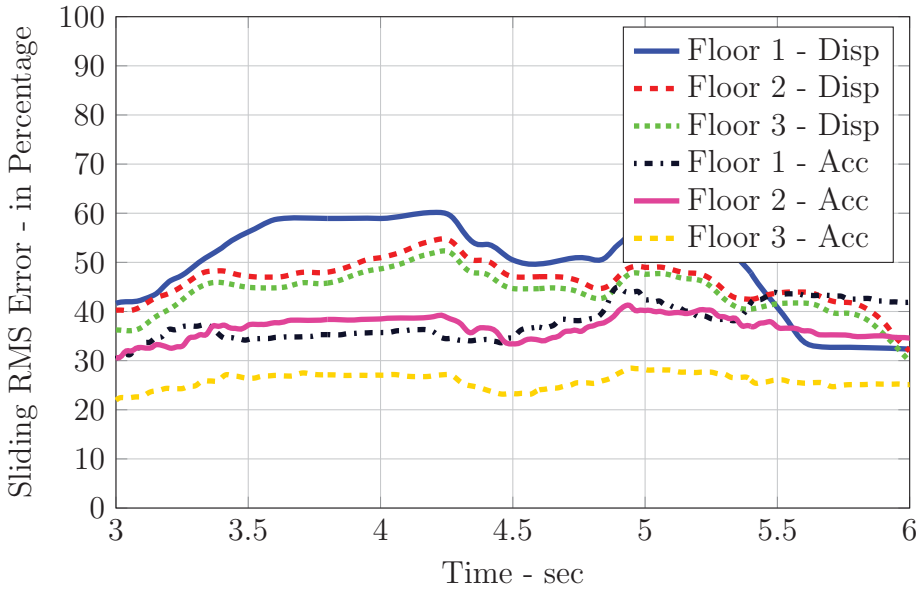


Figure 6.26: Moving RMS error for Kobe earthquake ST–RTHS PON case

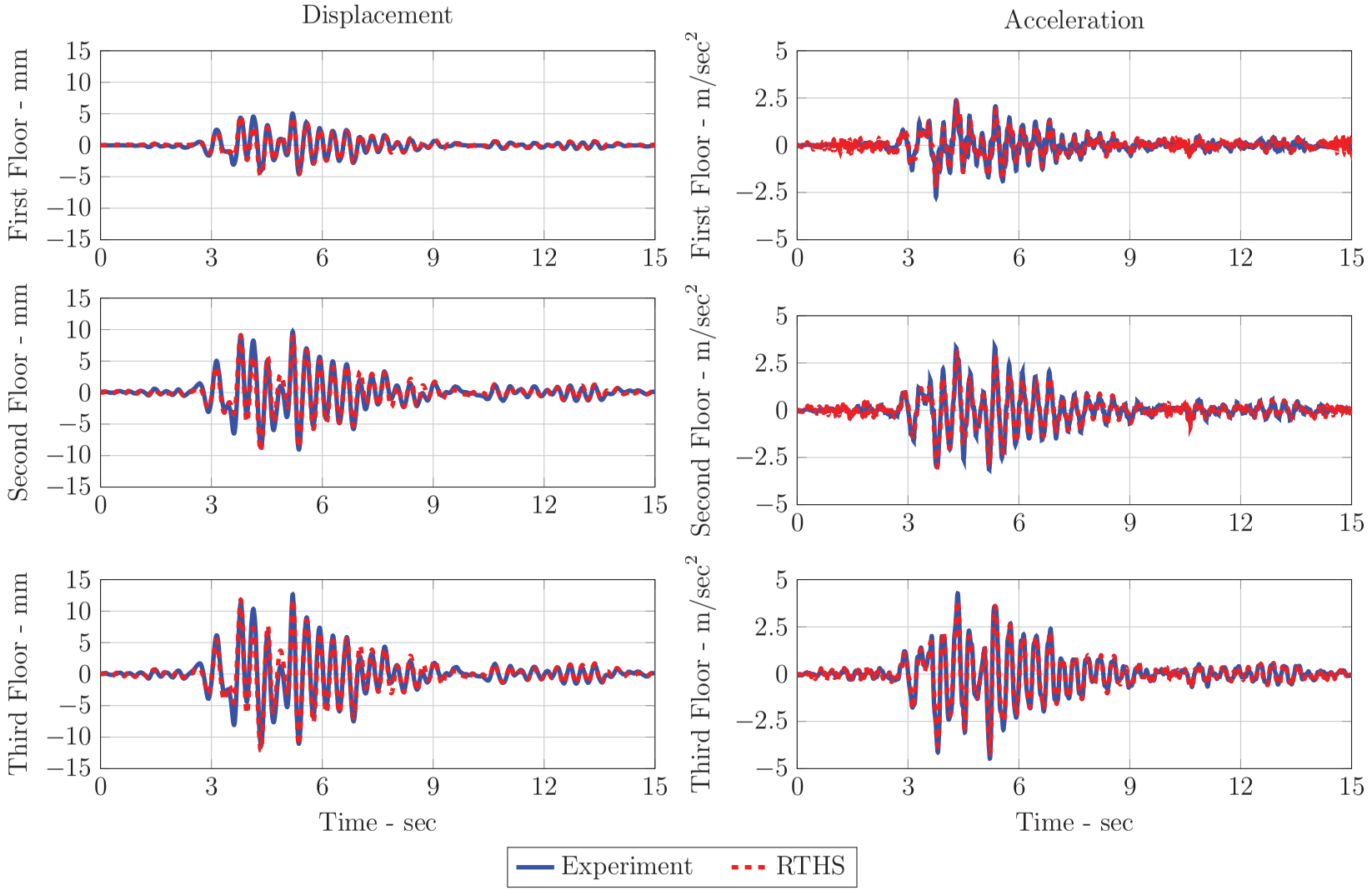


Figure 6.27: Kobe earthquake response comparison in time domain for ST–RTHS SA case

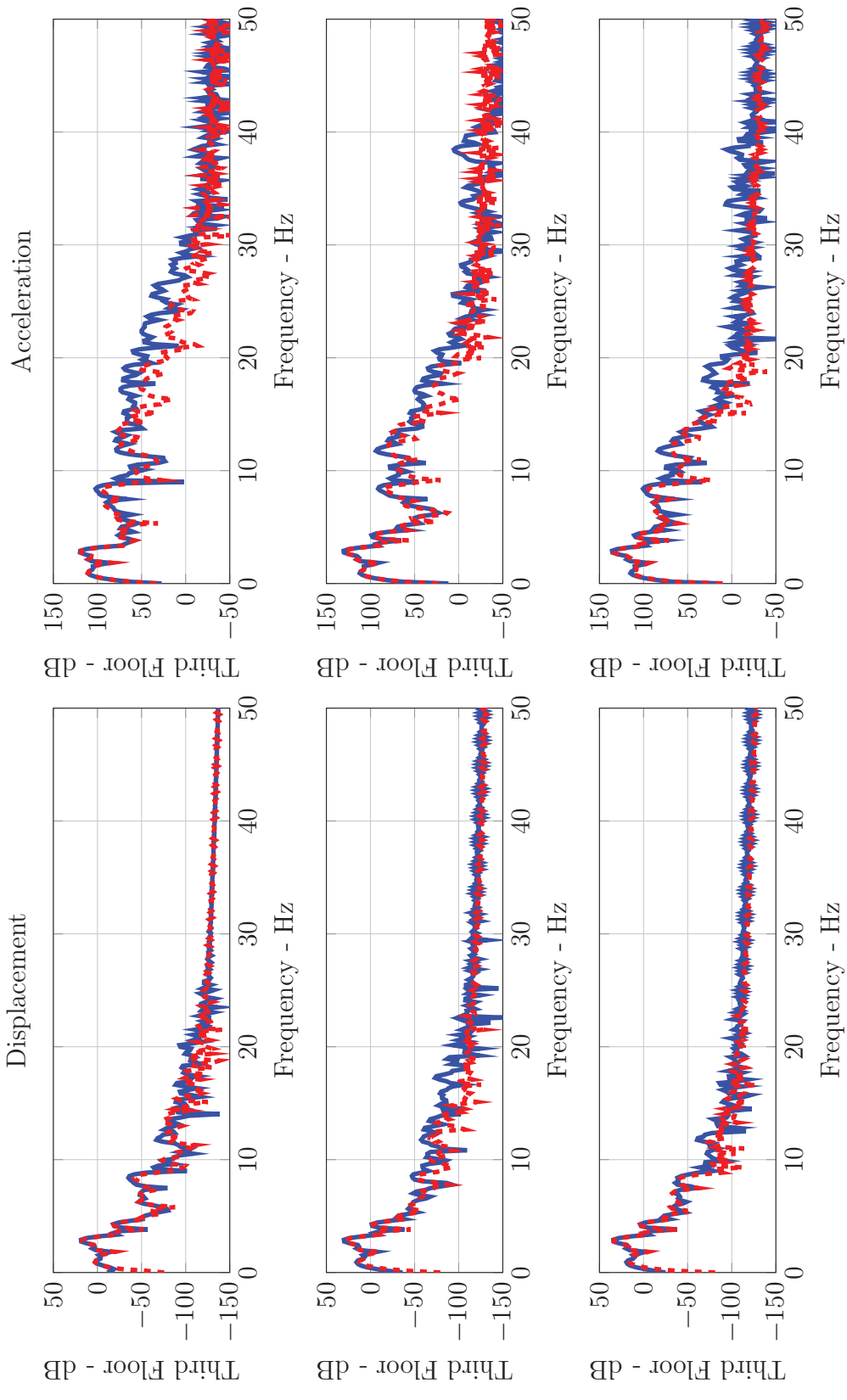


Figure 6.28: Kobe earthquake response comparison in frequency domain for ST–RTHS SA case

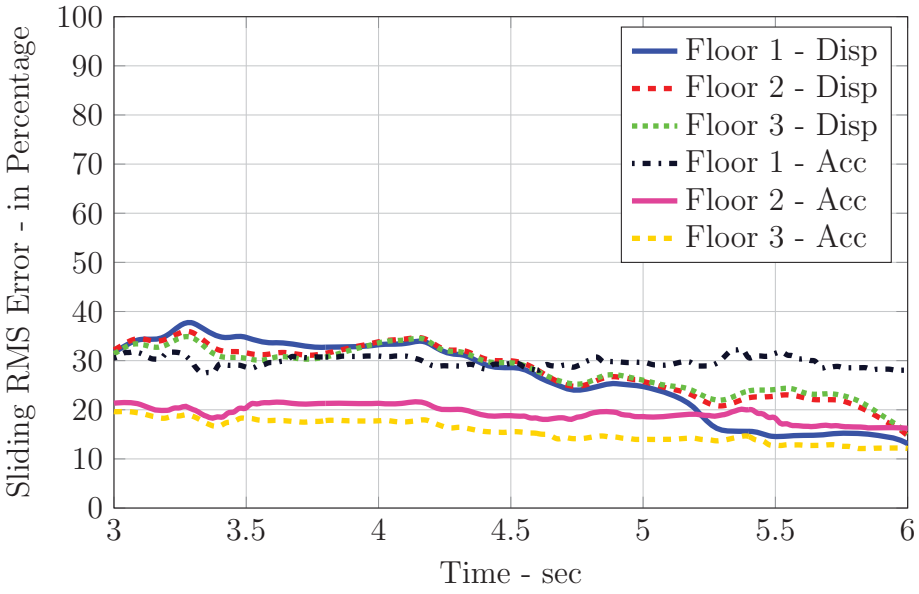


Figure 6.29: Moving RMS error for Kobe earthquake ST–RTHS SA case

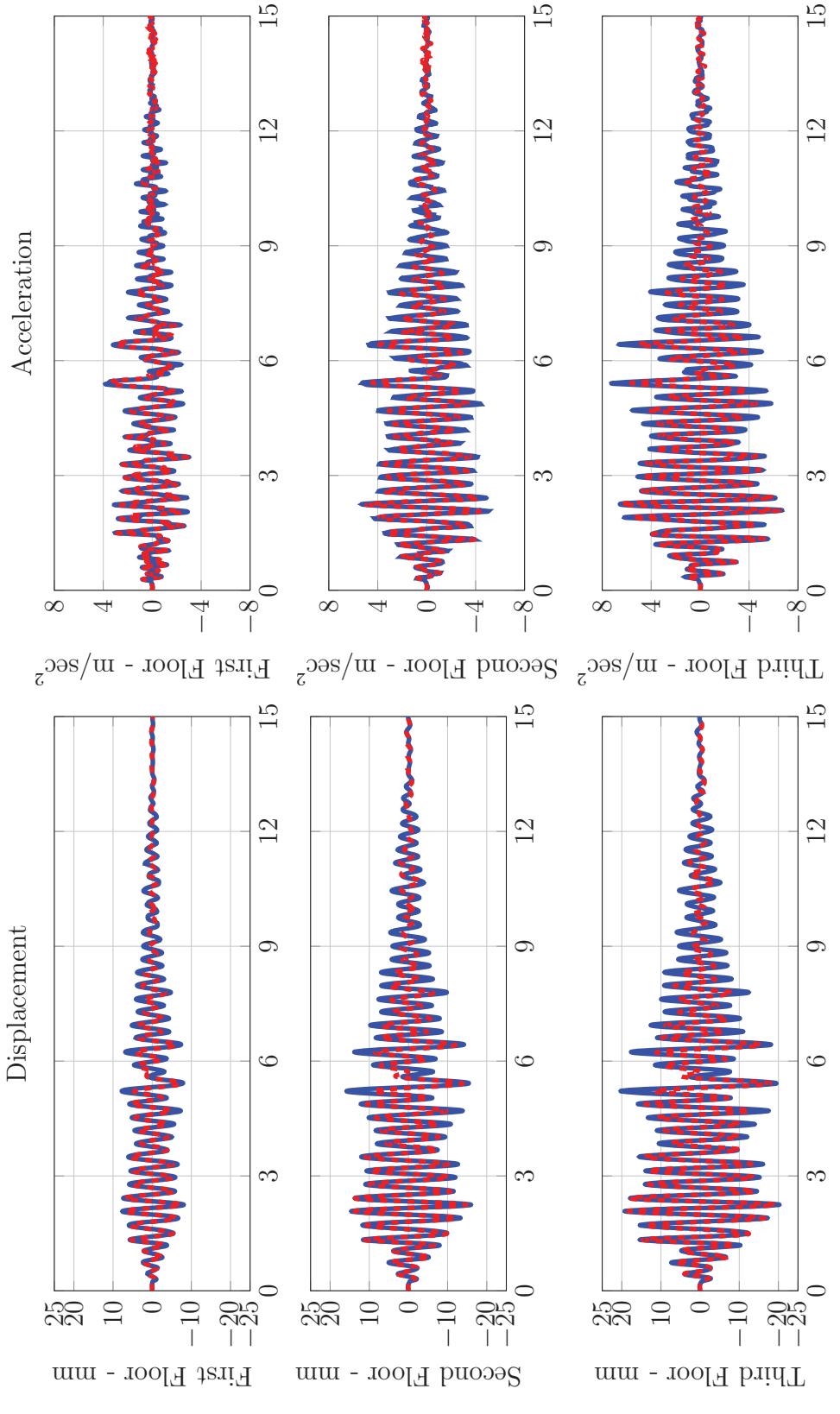


Figure 6.30: Morgan Hill earthquake response comparison in time domain for ST–RTHS POFF case

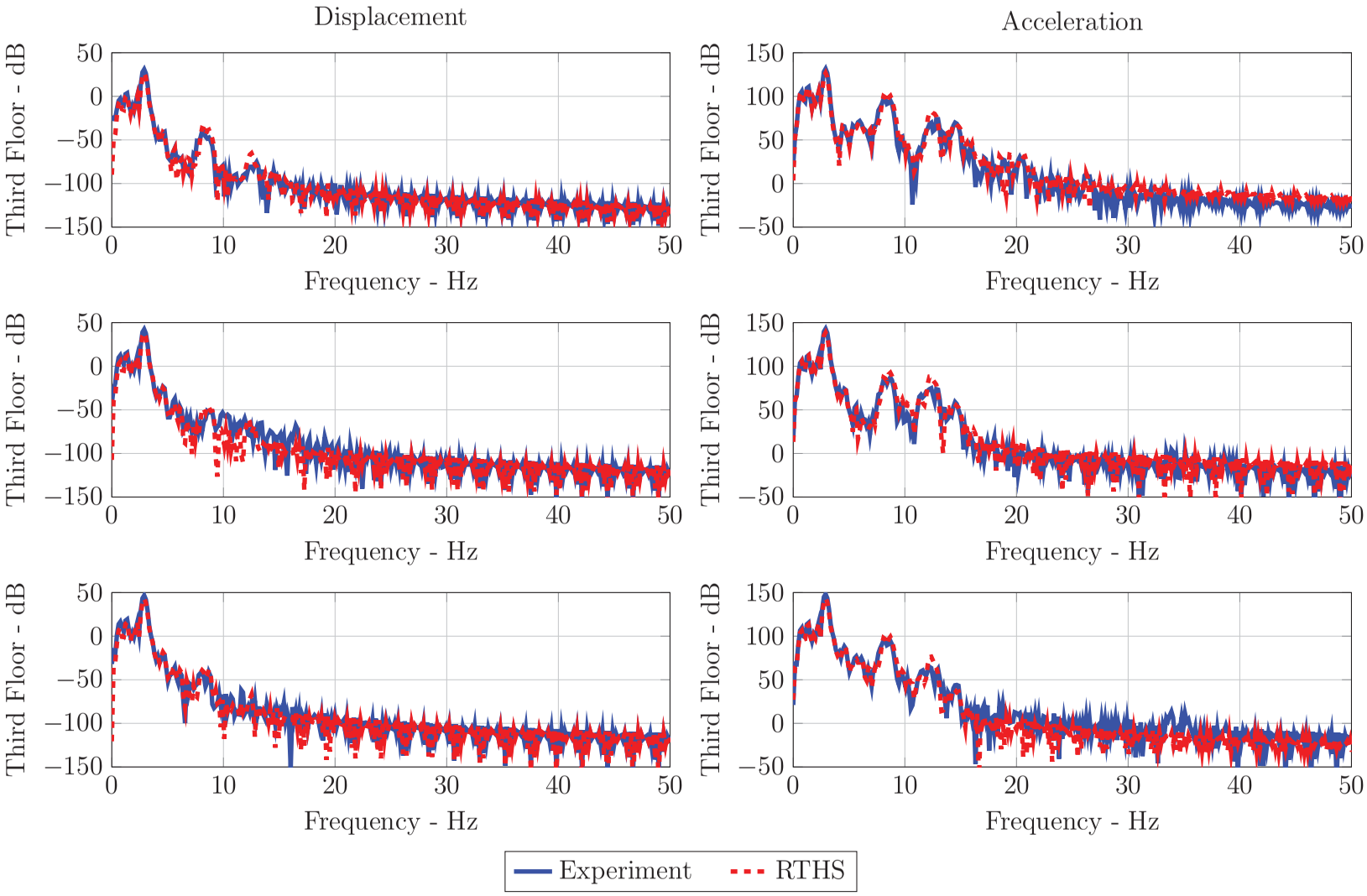


Figure 6.31: Morgan Hill earthquake response comparison in frequency domain for ST–RTHS POFF case

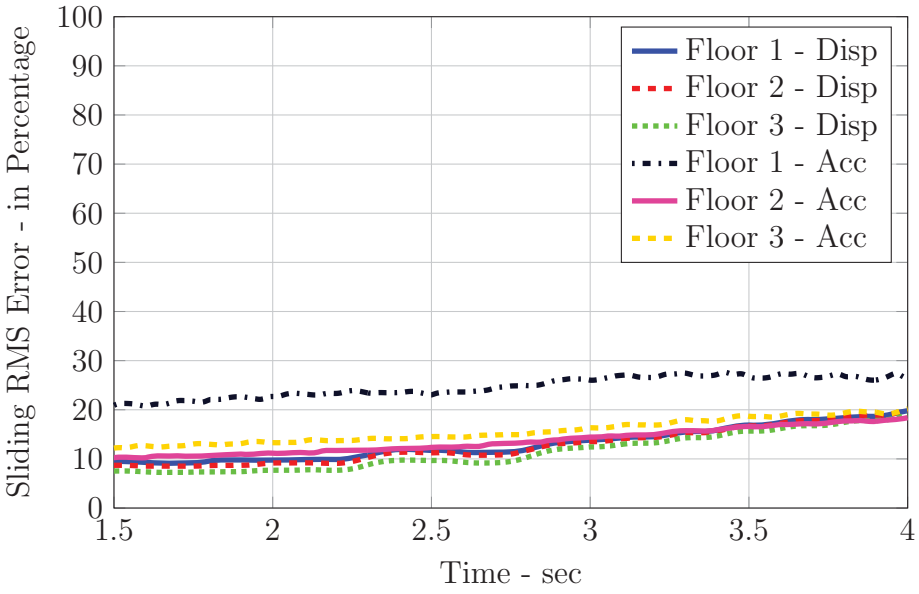


Figure 6.32: Moving RMS error for Morgan Hill earthquake ST–RTHS POFF case

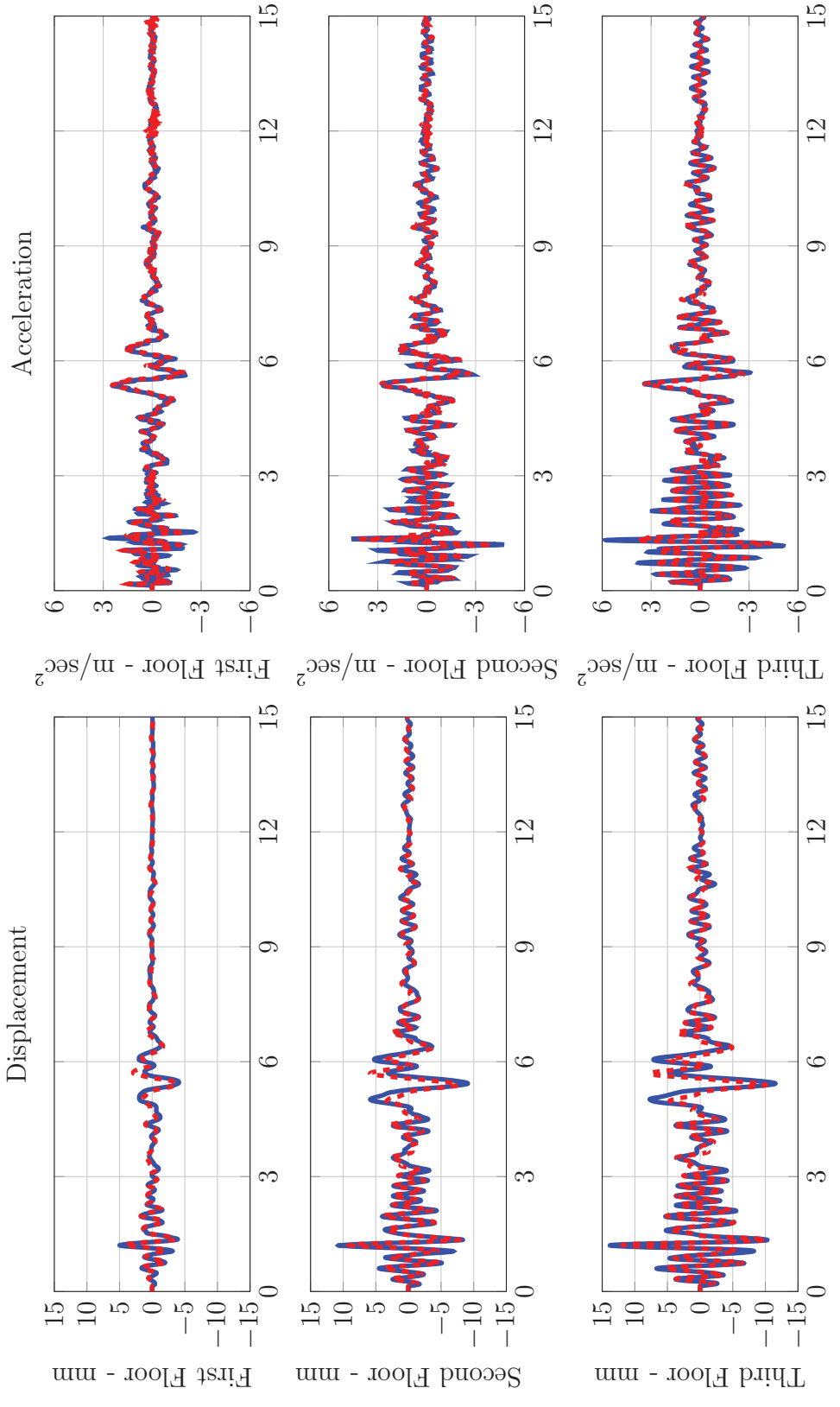


Figure 6.33: Morgan Hill earthquake response comparison in time domain for ST–RTHS PON case

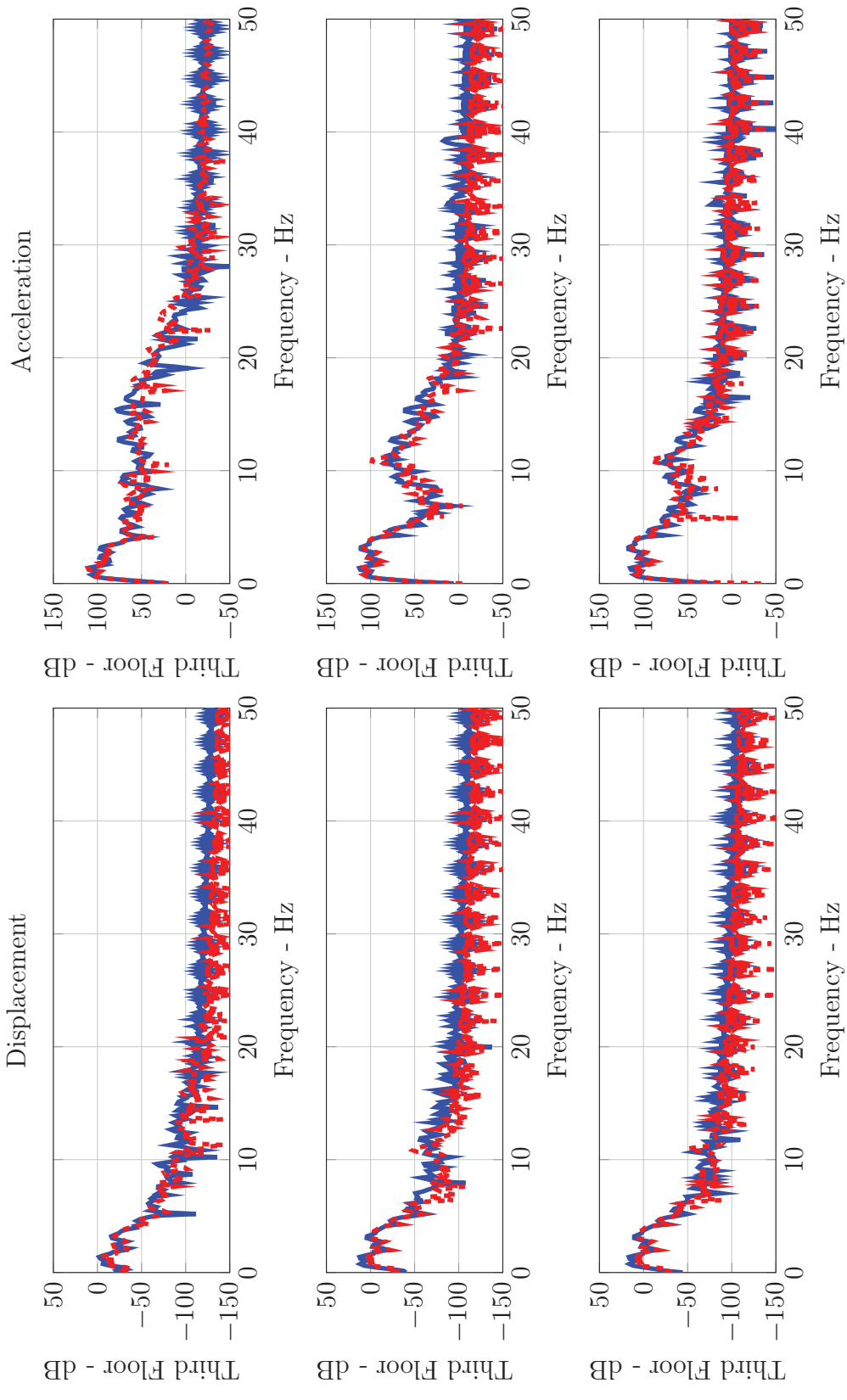


Figure 6.34: Morgan Hill earthquake response comparison in frequency domain for ST–RTHS PON case

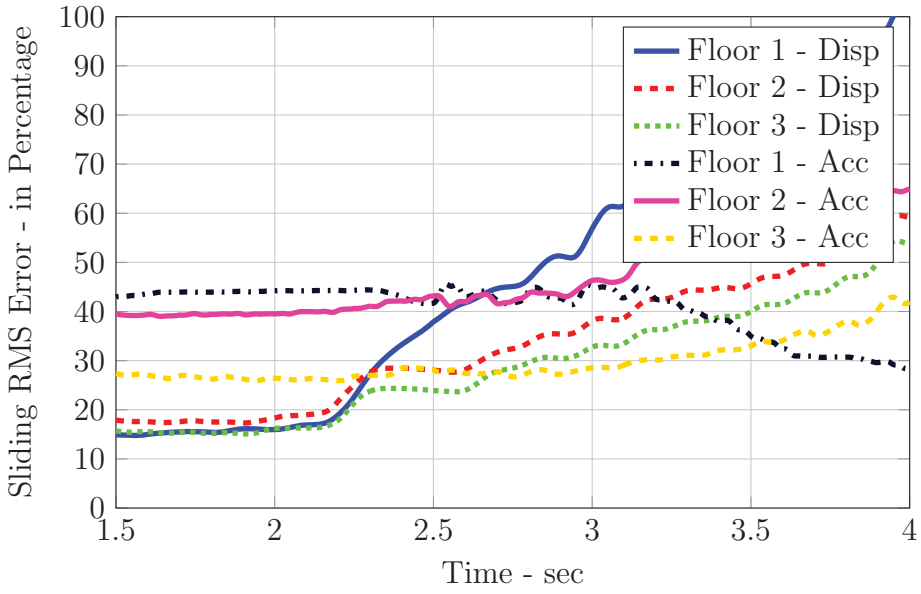


Figure 6.35: Moving RMS error for Morgan Hill earthquake ST–RTHS PON case

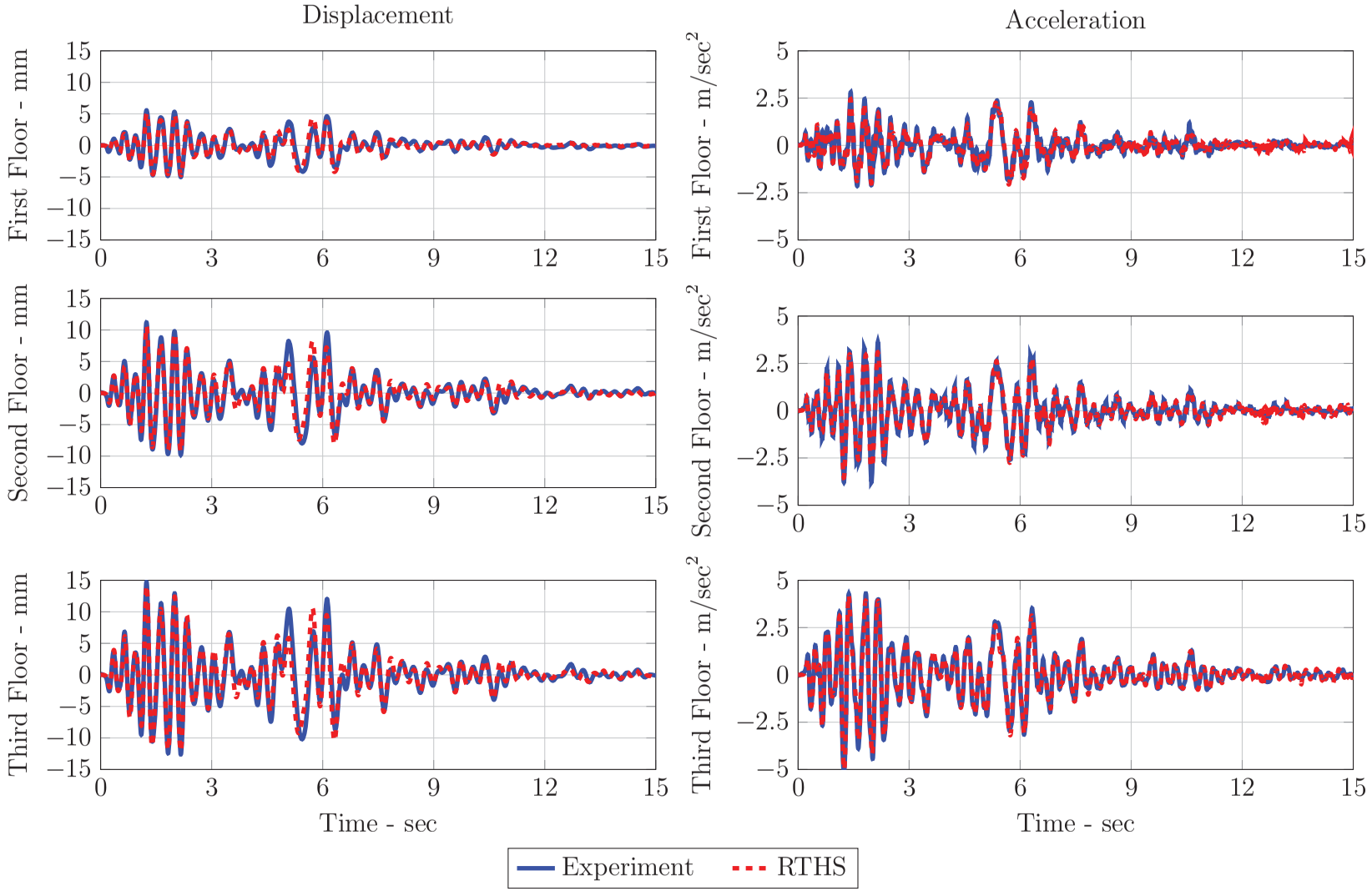


Figure 6.36: Morgan Hill earthquake response comparison in time domain for ST–RTHS SA case

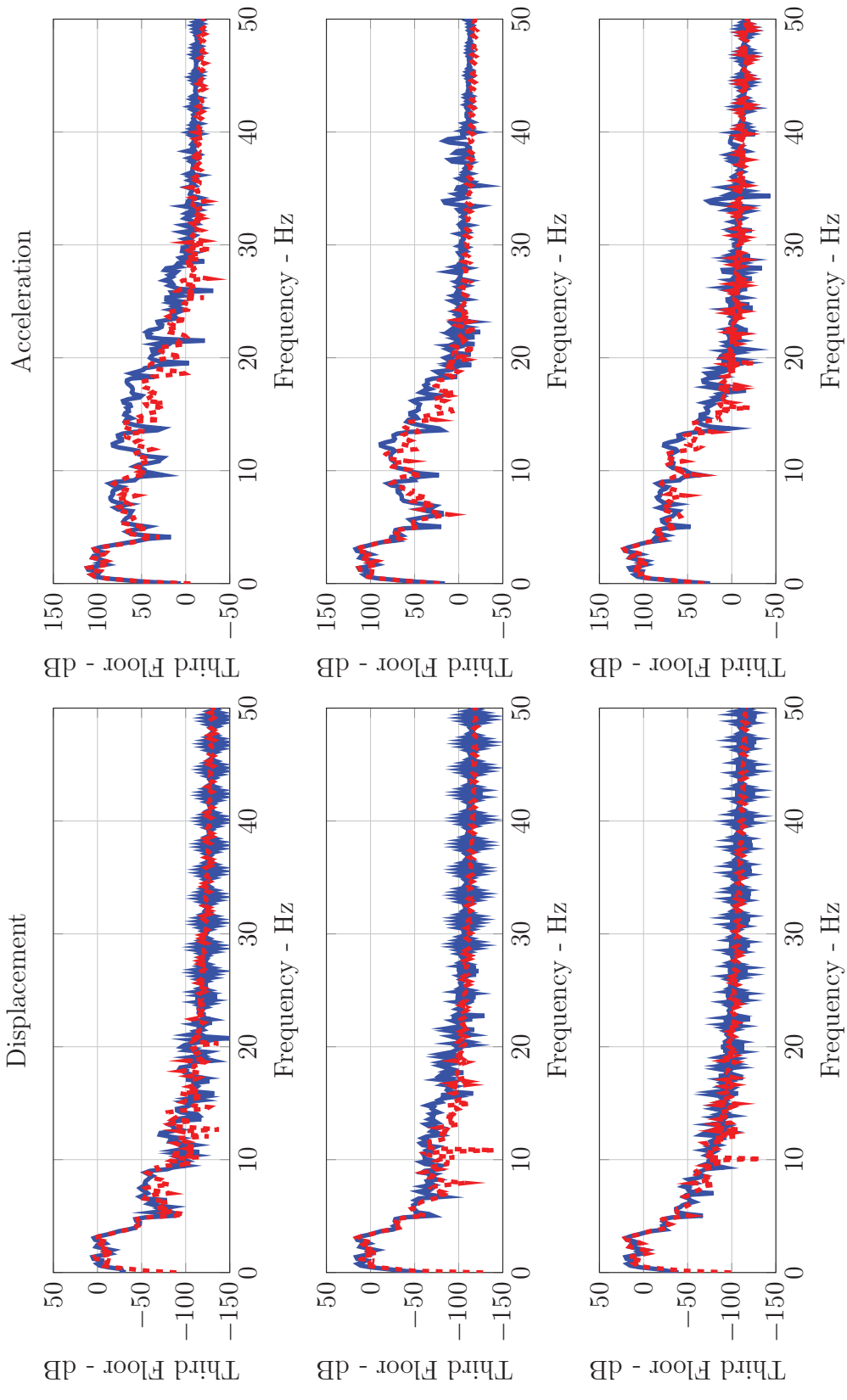


Figure 6.37: Morgan Hill earthquake response comparison in frequency domain for ST–RTHS SA case

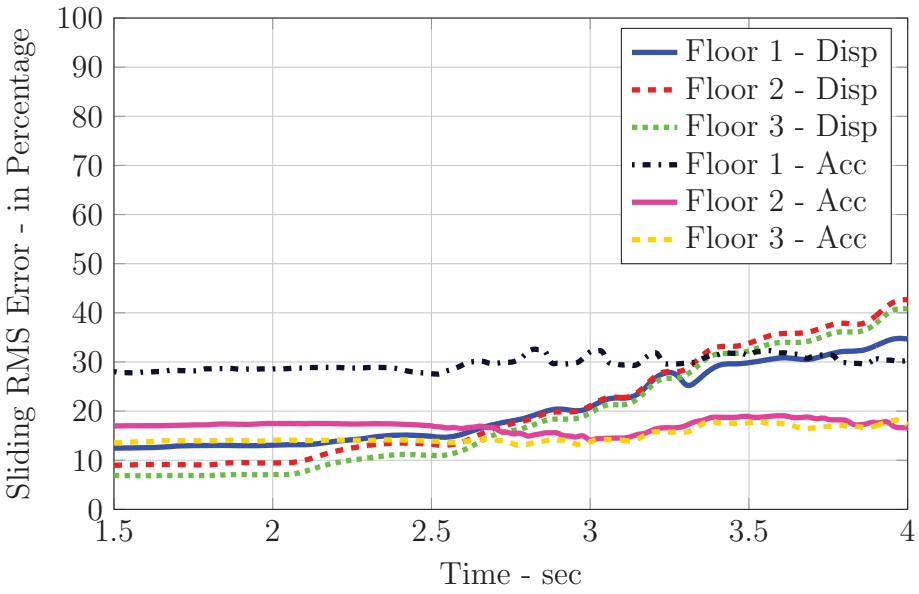


Figure 6.38: Moving RMS error for Morgan Hill earthquake ST–RTHS SA case

### 6.3.4 Discussions

Considering POFF cases, El Centro for RTHS case yielded a maximum average error of 16 % which is lower than the pure simulation comparison. On the other hand, RTHS errors for Kobe and Morgan Hill are around 15 %, relatively and slightly larger than the pure simulation errors. The differences between force-displacement behavior of Purdue and HIT dampers at POFF mode can be accounted for the elevated errors. Despite these discrepancies, PSDs of shake table and RTHS responses demonstrate strong correlation.

RTHS and pure simulation comparisons for SA cases present similar level of averaged errors. For the PON cases, the averaged errors, particularly, errors for the first floor responses are reduced.

The overall averaged errors reported in Table 6.1 are near 18 % and 20 % for POFF and SA cases, respectively. The PON case averaged errors are in the range of 24 % to 36 %.

Table 6.1: Evaluation criteria for for ST–RTHS comparison

| Ground Motion | Controller | Location | Evaluation Criteria | | | | | | Criteria |
|---|---|---|---|---|---|---|---|---|---|
| | | | J1 | J2 | J3 | J4 | J5 | J6 | Average |
| El Centro | POFF | First Floor | 15.95 | 11.62 | 27.59 | 7.31 | 3.94 | 5.59 | 12.00 |
| | | Second Floor | 15.56 | 12.34 | 15.43 | 5.78 | 3.75 | 3.57 | 9.41 |
| | | Third Floor | 15.22 | 10.96 | 14.28 | 3.88 | 3.64 | 3.44 | 8.57 |
| | PON | First Floor | 33.78 | 29.50 | 30.60 | 10.37 | 6.60 | 5.26 | 19.35 |
| | | Second Floor | 34.05 | 6.88 | 28.18 | 2.11 | 6.57 | 4.62 | 13.74 |
| | | Third Floor | 33.56 | 8.93 | 23.98 | 21.48 | 6.57 | 4.63 | 16.52 |
| | SA | First Floor | 22.40 | 13.36 | 30.13 | 10.37 | 4.91 | 5.80 | 14.50 |
| | | Second Floor | 18.51 | 7.67 | 19.88 | 17.29 | 3.92 | 3.69 | 11.83 |
| | | Third Floor | 19.36 | 9.54 | 13.84 | 11.30 | 4.01 | 2.77 | 10.14 |
| Kobe | POFF | First Floor | 17.96 | 11.19 | 22.35 | 7.90 | 5.79 | 5.84 | 11.84 |
| | | Second Floor | 17.56 | 13.84 | 17.78 | 16.68 | 5.65 | 5.55 | 12.84 |
| | | Third Floor | 16.13 | 13.71 | 20.39 | 16.93 | 5.23 | 6.85 | 13.21 |
| | PON | First Floor | 51.12 | 12.29 | 37.71 | 16.02 | 10.85 | 6.01 | 22.33 |
| | | Second Floor | 45.81 | 4.19 | 37.06 | 6.93 | 9.76 | 6.23 | 18.33 |
| | | Third Floor | 43.59 | 4.04 | 26.26 | 20.95 | 9.57 | 4.54 | 18.16 |
| | SA | First Floor | 26.68 | 7.38 | 29.93 | 17.59 | 6.63 | 5.67 | 15.65 |
| | | Second Floor | 27.59 | 6.32 | 19.34 | 9.01 | 6.86 | 4.37 | 12.25 |
| | | Third Floor | 27.45 | 6.23 | 15.54 | 8.87 | 6.69 | 3.47 | 11.37 |
| Morgan | POFF | First Floor | 13.53 | 9.01 | 23.89 | 9.81 | 3.78 | 6.15 | 11.03 |
| | | Second Floor | 13.19 | 7.83 | 13.72 | 14.06 | 3.65 | 3.67 | 9.35 |
| | | Third Floor | 12.14 | 5.28 | 15.69 | 4.23 | 3.33 | 4.36 | 7.50 |
| | PON | First Floor | 41.45 | 5.56 | 41.03 | 23.84 | 8.68 | 5.79 | 21.06 |
| | | Second Floor | 30.65 | 7.56 | 45.25 | 7.61 | 7.16 | 9.94 | 18.03 |
| | | Third Floor | 27.26 | 5.56 | 29.73 | 24.13 | 6.77 | 6.83 | 16.72 |
| | SA | First Floor | 17.25 | 9.89 | 28.86 | 9.31 | 3.76 | 5.61 | 12.45 |
| | | Second Floor | 17.13 | 5.89 | 17.36 | 21.10 | 3.82 | 3.35 | 11.44 |
| | | Third Floor | 15.64 | 4.23 | 14.44 | 8.42 | 3.39 | 3.14 | 8.21 |
| EQ Average | POFF | First Floor | 15.81 | 10.61 | 24.61 | 8.34 | 4.51 | 5.86 | 11.62 |
| | | Second Floor | 15.44 | 11.34 | 15.64 | 12.17 | 4.35 | 4.26 | 10.53 |
| | | Third Floor | 14.49 | 9.98 | 16.79 | 8.35 | 4.07 | 4.88 | 9.76 |
| | PON | First Floor | 42.12 | 15.78 | 36.45 | 16.74 | 8.71 | 5.68 | 20.91 |
| | | Second Floor | 36.84 | 6.21 | 36.83 | 5.55 | 7.83 | 6.93 | 16.70 |
| | | Third Floor | 34.81 | 6.18 | 26.66 | 22.19 | 7.64 | 5.33 | 17.13 |
| | SA | First Floor | 22.11 | 10.21 | 29.64 | 12.42 | 5.10 | 5.70 | 14.20 |
| | | Second Floor | 21.08 | 6.63 | 18.86 | 15.80 | 4.87 | 3.80 | 11.84 |
| | | Third Floor | 20.82 | 6.67 | 14.60 | 9.53 | 4.70 | 3.13 | 9.91 |

## 6.4 Conclusions

In this chapter, shake table responses of MR damper controlled three story structure located at HIT are compared to RTHS responses. In RTHS configuration, the system is partitioned into physical substructure represented by the Purdue MR damper, and analytical substructure simulated by the model of the test structure.

For the RTHS configuration, ground motions recorded by the accelerometers are used as the excitation input, while MR damper is driven in POFF, PON, and SA mode. Resulting relative displacements and absolute accelerations of each floor are compared to shake table responses. To assess the performance and validate feasibility of RTHS, peak, RMS, and sliding RMS errors are computed. PSDs of the shake table and RTHS responses are also supplemented to show the RTHS efficiency in frequency domain.

In summary, RTHS was able to predict shake table test responses successfully. The results of evaluation criteria also validated that RTHS can be a valid alternative to shake table tests.

# CHAPTER 7
# DEVELOPMENT AND EVALUATION OF DRTHS PLATFORM

Before considering the validation of dRTHS with shake table test results, it is imperative to explain what the Internet network is and how dRTHS architecture is implemented based on network communication. Since dRTHS architecture proposed here has not been tested before, it is best to start with a simple, focused example where the only source of error is delays in the Internet. Accordingly, the performance of the example test is assessed using an MR damper as the *numerically simulated* physical substructure and a two story structure as the numerical substructure in virtual distributed dRTHS (vdRTHS) configuration. The setup selected for the validation of the architecture is distributed between IISL at Purdue University and Smart Structures Technology Laboratory (SSTL) at University of Illinois in Urbana-Champaign.

This chapter begins with a brief discussion of the Internet topology as presented in Section 7.1. Following, in Section 7.2, MATLAB/xPC components used to conduct dRTHS are introduced. Section 7.3 outlines the architecture of dRTHS and describes how components fit to the large picture. In Section 7.4, the minimal working example is explained and methods to compensate the network time delays are discussed. Later, Section 7.5 introduces the proposed use of the estimator to determine initial network time delay that improves performance of compensation methods. In Section 7.6, a vdRTHS is conducted to validate the architecture and the delay estimator. Finally, main findings and observations are presented in Section 7.7.

## 7.1 Introduction

The Internet is a global system of networks and the procedure for the communication between each element on the net is standardized in seven layers such as link,

network, transport and higher application layers, also conceptualized as Open Systems Interconnection model (ISO, 1196). Each layer contains a number of communication protocols to handle certain Internetworking tasks as presented in Table 7.1. By definition of OSI, layers can function properly when the layers below are in operation.

Table 7.1: OSI model

| Model Layer | Description |
|---|---|
| Application Layer | User interface responsible for interpretation of the data |
| Presentation Layer | Syntactic representation and encryption of data |
| Session Layer | Management of connection sessions |
| Transport Layer | End-to-end communication services |
| Network Layer | Packet relay through intermediate routers |
| Data Link Layer | Low level transmission of data between adjacent networks |
| Physical Layer | Medium for physical transmission of raw bits |

For instance, distributed systems over the Internet mainly use Internet Protocol version 4 IPv4. Details on IPv4 are described by Postel (1981a), in depth. Hower, IPv4 by itself is not sufficient for transmitting data to the application layer where user interacts with the software. Consequently, an intermediate transport layer that can act as a middleman between application and Internet protocol is used. There are two main protocols called TCP and UDP. Basically, TCP is a connection-oriented protocol inheriting attributes such as flow, traffic, reliability and congestion control, and acknowledgment check (Postel, 1981b). These properties make TCP a perfect candidate for applications requiring reliability. On the other hand, TCP is heavy-weight and does not guarantee low network delays the due to time taking control checks.

Opposite to TCP, UDP is a connectionless protocol that doesn't have any connection quality control and therefore has less overhead (Postel, 1981b). This advantage

makes UDP suitable for real-time applications that requires minimal time delay such as VoIP or dRTHS. It should be considered that this lightweight protocol promises less network delays at the cost of possible data loss. However, considering the fact that network backbones are becoming more advanced in terms of technologies, data loss will be significantly less as compared to what might have occurred when UDP was first developed.

There are other such protocols that promise speed of UDP with reliability of TCP, such as Real-time Transfer Protocol (RTP) built on UDP, but they are designed for media streaming purposes (Schulzrinne et al., 2003), and are not the scope of this chapter.

## 7.2 Components of Real-time Communication

There are many real-time target platforms that might be used for performing RTHS. While the infrastructure described here can be applied to many of those, xPC is selected for this study, since MATLAB provides readily available network modules for distributed testing.

There are three main block libraries implemented in Simulink. Those are: (i) Ethernet-based, (ii) TCP-based and (iii) UDP-type data exchange blocks. As the Ethernet block uses link layer, each data packet is sent from a source MAC address to destination MAC address. This is an ideal mechanism for communication between nodes located under same Local Area Network (LAN). However for geographically distributed systems, data needs to be transmitted over a transport layer, i.e. IP.

The second option, data transport over TCP may not be a viable option since it may introduce significant transmission delays as mentioned before. Additionally, as TCP block implemented for xPC responsible for target-target communication, and host-target communication share the same resources over a single network interface card (NIC), a concurrency issue may arise and cause even further transmission delays.

The third option, UDP is forked into two branches. The first branch is similar to TCP in the sense that all communications are performed on the same NIC. The second branch, or the so-called Real-time UDP (RT-UDP) block, however, uses a dedicated NIC for target-target communication. Another nice feature of this block that is not implemented in other options, is the availability of buffering of the incoming data. Basically, buffer is a routine that compensates differences in data flow rate, by queuing incoming packets in first in-first out (FIFO) mechanism into a temporary medium, as illustrated in Figure 7.1. When the buffer is full and a buffered package is required, it is removed from the queue. Respectively, jittering in the transmission can be eliminated using this method. xPC block expects to get a data package at each time step. If a package doesn't arrive on time, xPC registers it as lost. This type of anticipation can be easily satisfied in locally distributed nodes with a low buffer size since almost no jitter will be observed, and low and deterministic network delay is still guaranteed. On the other hand, for dRTHS, in the case of degraded QoS, the flow rate may be interrupted. To take care of this problem, buffer size can be increased at the expense of delay.

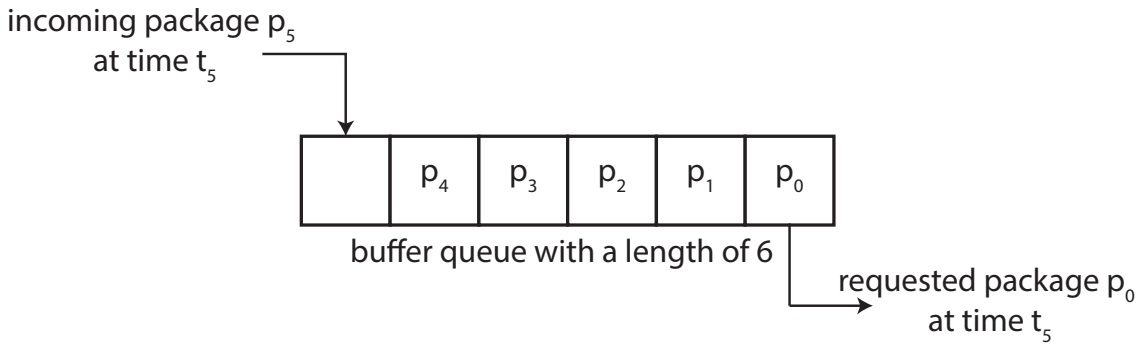


Figure 7.1: A generic buffering application

Each UDP packet sent over IPv4 layer contains 28 Bytes of overhead. A typical overhead is composed of at least 20 Bytes sized, IPv4 protocol dictated header including essential protocol requirements such as source and destination addresses, and of 8 Bytes sized UDP header encapsulating source and destination ports, length of

data and a checksum field, as given in Tables 7.2 and 7.3. When encapsulated with a double precision floating-point data with a size of 8 Bytes, the total packet size will be 36 Bytes. As observed, only a quarter of the packet is real data, while the rest of the package is header data. In addition, if an IP packet is transmitted over the Ethernet frame, a header of 18 Bytes for Ethernet should be added to the total size. It should be also noted that there is a minimum size requirement of 64 Bytes for an Ethernet packet.

Table 7.2: IP header structure

| Bit | 0 | 1 | 2 | 3 | 4 | 5 | 6 | 7 | 8 | 9 | 10 | 11 | 12 | 13 | 14 | 15 | 16 | 17 | 18 | 19 | 20 | 21 | 22 | 23 | 24 | 25 | 26 | 27 | 28 | 29 | 30 | 31 |
|---|---|---|---|---|---|---|---|---|---|---|---|---|---|---|---|---|---|---|---|---|---|---|---|---|---|---|---|---|---|---|---|---|
| 0 | Version | | | | Length | | | | Service Options | | | | | | | | Total Length | | | | | | | | | | | | | | | |
| 32 | Identification | | | | | | | | | | | | | | | | Flag | | | Fragment Offset | | | | | | | | | | | |
| 64 | Time to Live | | | | | | | | Protocol | | | | | | | | Checksum | | | | | | | | | | | | | | | |
| 96 | Source IP | | | | | | | | | | | | | | | | | | | | | | | | | | | | | | | |
| 128 | Destination IP | | | | | | | | | | | | | | | | | | | | | | | | | | | | | | | |
| 160 | Options (not required unless Service Options indicate) | | | | | | | | | | | | | | | | | | | | | | | | | | | | | | | |

Table 7.3: UDP header structure

| Bit | 0 | 1 | 2 | 3 | 4 | 5 | 6 | 7 | 8 | 9 | 10 | 11 | 12 | 13 | 14 | 15 | 16 | 17 | 18 | 19 | 20 | 21 | 22 | 23 | 24 | 25 | 26 | 27 | 28 | 29 | 30 | 31 |
|---|---|---|---|---|---|---|---|---|---|---|---|---|---|---|---|---|---|---|---|---|---|---|---|---|---|---|---|---|---|---|---|---|
| 0 | Source Port | | | | | | | | | | | | | | | | Destination Port | | | | | | | | | | | | | | | |
| 32 | Length | | | | | | | | | | | | | | | | Checksum | | | | | | | | | | | | | | | |

For geographically distributed systems, Internet may not always sustain such inefficient high-rate real-time communication. Instead of transmitting small packets containing large overheads, by framing, multiple data blocks can be sent at once at lower rates encapsulated under a single overhead. For example, instead of sending one data package at a rate of 1000 Hz, four data can be transmitted in a single package at a rate of 250 Hz, which will eventually yield smaller package size per data block and therefore more efficient transmission. The concept of framing is illustrated Figure 7.2.

It should be noted that framing causes the transmission to be delayed by the number of framed packages, thus it will introduce another source of time delay within the closed loop constituting the dRTHS. .

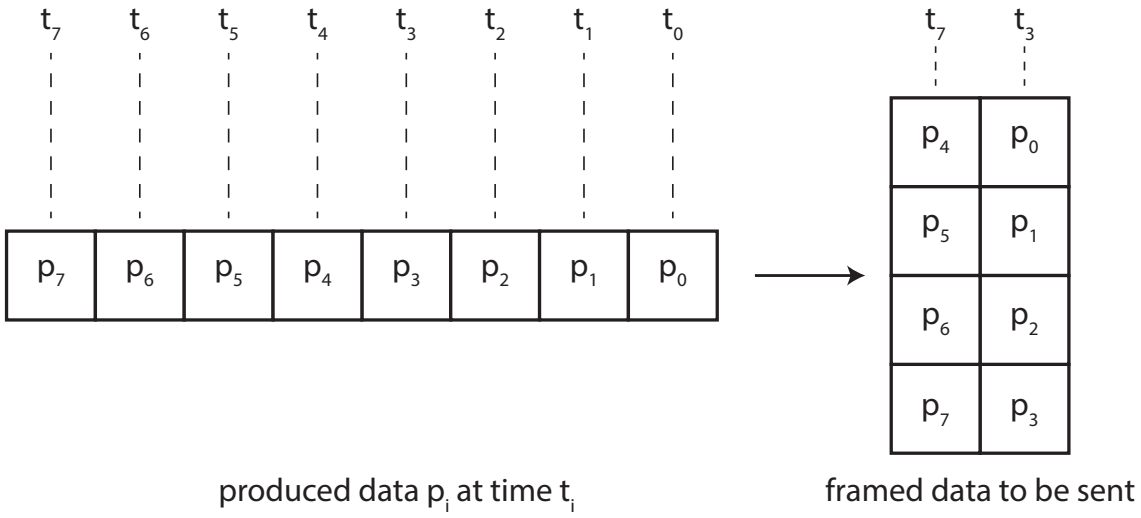


Figure 7.2: A generic framing application

In addition, both buffering and framing do not ensure data integrity, i.e. the incoming data may be corrupted on its way, get rejected by the RT-UDP Simulink block and lost forever. Ultimately, UDP is not designed to correct such issues. Still, in a healthy network, including the advantages aforementioned, RT-UDP remains an ideal candidate for dRTHS.

In MATLAB, the RT-UDP protocol is accompanied with several blocks, including a Network Configuration, Receive and Send blocks, given in Figure 7.3. The network configuration block determines several properties such as IP, subnet mask and gateway addresses, and type of the dedicated NIC. Send and Record blocks regulate destination address and port to send to and source address and port to receive from.


Figure 7.3: xPC RT-UDP blocks

## 7.3 dRTHS Architecture

An overview of the proposed architecture is shown in Figure 7.4. The xPC target computer node, realizing actuator control and measuring physical substructure responses is located in Intelligent Infrastructural Systems Laboratory (IISL) at Purdue University. The numerical substructure is simulated at Smart Structures Technology Laboratory (SSTL) at University of Illinois, Urbana-Champaign (UIUC). The host computer responsible for compiling and downloading xPC code to the nodes is also located at IISL.

The RT target node at IISL (xPC1) is a SpeedGoat system (model # 1474) running on xPC that acts as a digital controller. It employs the following tasks; (i) exchange data with the RT target node at SSTL, (ii) compensates actuator dynamics to realize the received desired signal coming from SSTL node, and (iii) collects the measured force from the physical substructure selected as LORD MR damper (model # RD-8041-1) and sends to remote node.

As for the SSTL site, the RT node configured on a Dell Optiplex 780 (xPC2) performs the following: (i) simulates the numerical model, (ii) generates the desired displacement and sends to IISL, and (iii) receives the feedback force from IISL, and finally (iv) compensates for the network time delays using Smith predictor. The design for the Smith predictor will be explained in the next section.

The host computer running on a Dell Optiplex 960 is tasked (i) to compile simulation files into a special form with the file extension, `*.dlm` that can be executed by xPCs, (ii) download `*.dlm` files to related nodes, and (iii) download binary formatted simulation results after a test is conducted.

All host, SSTL and IISL systems are equipped with Intel 82559 NICs compatible with MATLAB/xPC.

### 7.3.1 Connection Map

A connection map of dRTHS architecture shown above is illustrated in Figure 7.5.

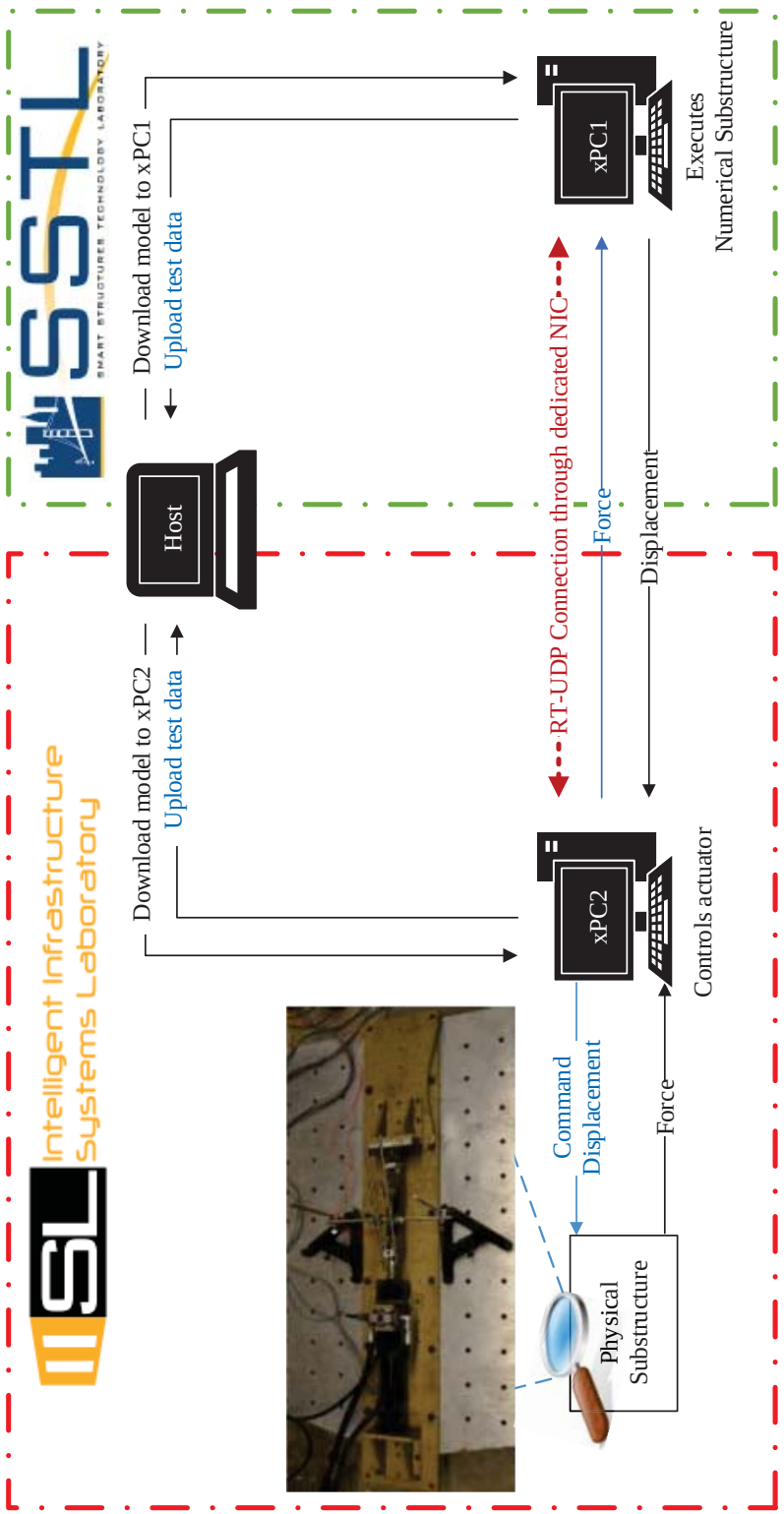


Figure 7.4: dRTHS system architecture

The two RT nodes are away from each other at a bird-eye distance of 70 miles or 110 km. An ICMP (ping) packet reached from IISL to SSTL about 9–12 msec. Route trace analysis showed that ping trails on 14 hops before reaching its destination. Although ping is a good way to quantify QoS, it does not guarantee data integrity or stable network time delays.

The host at IISL is located at a Local Area Network (LAN) behind Bowen Laboratory gateway (`10.3.3.1`) and addressed as `10.3.3.50`. The gateway is a low-end Dell GX260 running on Unix-like operating system FreeBDS.

As mentioned earlier, each RT target system has two NICs, each compatible with MATLAB/xPC and assigned a unique IP address. xPC1 has IP addresses, `10.3.3.100` and `128.46.160.50`, on its first and second NICs, respectively. IP address of the first NIC is also located behind the Bowen Laboratory router.

Bowen Lab router creates a Network Address Translation (NAT) enabled private network, known as subnet. NAT allows nodes on the same subnet to have unique private IP addresses while they share same public address. NAT can be also used as a primitive network security layout where all inbound connections can be rejected according to firewall restrictions. All target-host communications for XPC2 are designed, by choice, to be conducted inside Bowen Lab subnet, so that xPC2 is minimally exposed to the Internet. On the other hand, the second NIC of xPC2 is directly connected to Bowen Laboratory Gateway (`128.46.160.1`) set by the Engineering Computer Network (ECN) to bypass router rules and reduce the number of network hops, and hence, the delay. The gateway is an enterprise grade Cisco Catalyst 3750-E series switch.

For SSTL site, first and second NICs of xPC2 are assigned `130.126.240.42` and `130.126.240.38`. Both IPs are behind Newmark Laboratory Gateway (`130.126.240.38`) and firewalled strictly by Campus Information Technologies and Education Services (CITES). However, very few ports including `TCP/UDP-3283` used by Apple Remote Desktop service are open.

The host downloads simulation codes or sends command execution commands always through the first NIC of RT nodes. Such communication are processed through local source port `TCP-22222` as defined by MATLAB, by default. However, the remote destination ports may be different according to the network structure of the system. In this case, for SSTL site, destination source is selected as `TCP-3283` due to firewall restrictions.

The second NIC of xPC1 and xPC2 is dedicated to RT target-target communication and only active when a simulation is executed. Although the destination and source ports can be selected arbitrarily, xPC1 is located behind CITES firewall, and therefore, all inbound transmission to `130.126.240.38` should be processed through `UDP-3283`.

## 7.4 Validation System

Since dRTHS architecture proposed here is not tested before, it is best to start with a minimal working example where the only source of error is going to be the Internet. To examine the performance of the architecture, a vdRTHS configuration is prepared, where arbitrarily selected physical and numerical substructures are simulated numerically and data is exchanged between the xPC computer through Internet connection.

For the numerical substructure, representation of a two floor structure developed by Kim et al. (2012) is used, as given in Equation (7.1). The frequencies of the analytical model are determined as 1.00 Hz and 2.61 Hz.

$$[M] = \begin{bmatrix} 2.7 & 0 \\ 0 & 2.7 \end{bmatrix} \text{ tonne} \tag{7.1a}$$

$$[C] = \begin{bmatrix} 588 & -280 \\ -280 & 280 \end{bmatrix} \frac{\text{N}}{\text{mm}} \tag{7.1b}$$

$$[K] = \begin{bmatrix} 3.68 & -1.23 \\ -1.23 & 2.46 \end{bmatrix} \text{N}\frac{\text{sec}}{\text{mm}} \tag{7.1c}$$

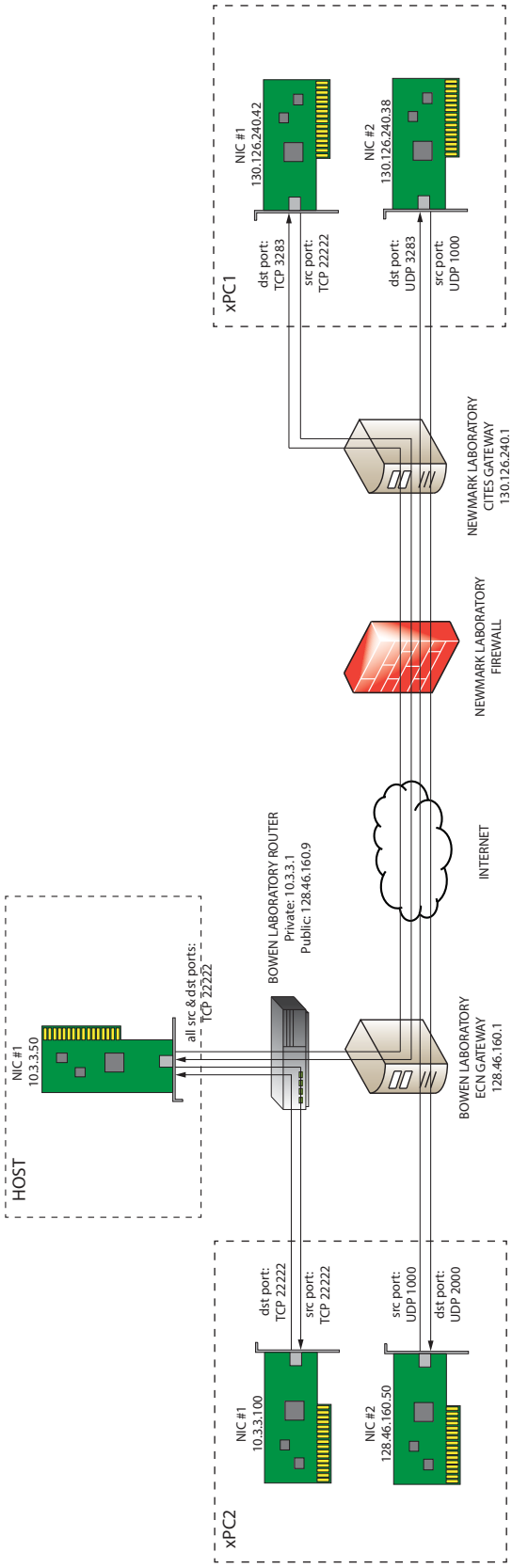


Figure 7.5: dRTHS connection map

$A$, $B$, $C$ and $D$ state matrices are generated to produce relative displacements and velocities to the ground and absolute accelerations, as prescribed in Equations (3.6) and (3.7). Ground motion is used as the excitation input to the system. The measured MR damper force responding to the first floor displacement is applied again to the first floor of the structure as an external feedback force. The damper is numerically modeled after the Bouc-Wen hysteresis model developed for Purdue damper, given in Table 7.4.

Table 7.4: Identified Bouc-Wen model parameters for Purdue damper

| Parameter | Value | Unit |
|---|---|---|
| $\alpha_a$ | 2740.734 | $\mathrm{N\,m^{-1}}$ |
| $\alpha_b$ | 10010.25 | $\mathrm{N\,m^{-1}\,V^{-1}}$ |
| $c_{0a}$ | 175.13 | $\mathrm{N\,sec\,m^{-1}}$ |
| $c_{0b}$ | 1709.24 | $\mathrm{N\,sec\,m^{-1}\,V^{-1}}$ |
| $c_{1a}$ | 3353.68 | $\mathrm{N\,sec\,m^{-1}}$ |
| $c_{1b}$ | 175.13 | $\mathrm{N\,sec\,m^{-1}\,V^{-1}}$ |
| $k_0$ | 1940.41 | $\mathrm{N\,m^{-1}}$ |
| $k_1$ | 1.58 | $\mathrm{N\,m^{-1}}$ |
| $\gamma$ | 36332.07 | $\mathrm{m^{-2}}$ |
| $\beta$ | 36332.07 | $\mathrm{m^{-2}}$ |
| $A$ | 155.32 | - |
| $x_0$ | 0 | m |
| $n$ | 2 | - |
| $\eta$ | 60 | sec |

### 7.4.1 Design of the Smith Predictor

Arguably, one of the trickiest challenge for real-time network applications is compensation of the dead time, which is basically the network time delay between the targets. The network time delays in the dRTHS platform can be idealized as given in Figure 7.6. Here, $\tau_1$ and $\tau_2$ are the transmission delays due to Internet for the inbound and outbound packets between SSTL and IISL sites, respectively. These transmission delays can be regarded as dead time, hence, can be treated with Smith predictor (Smith, 1959).

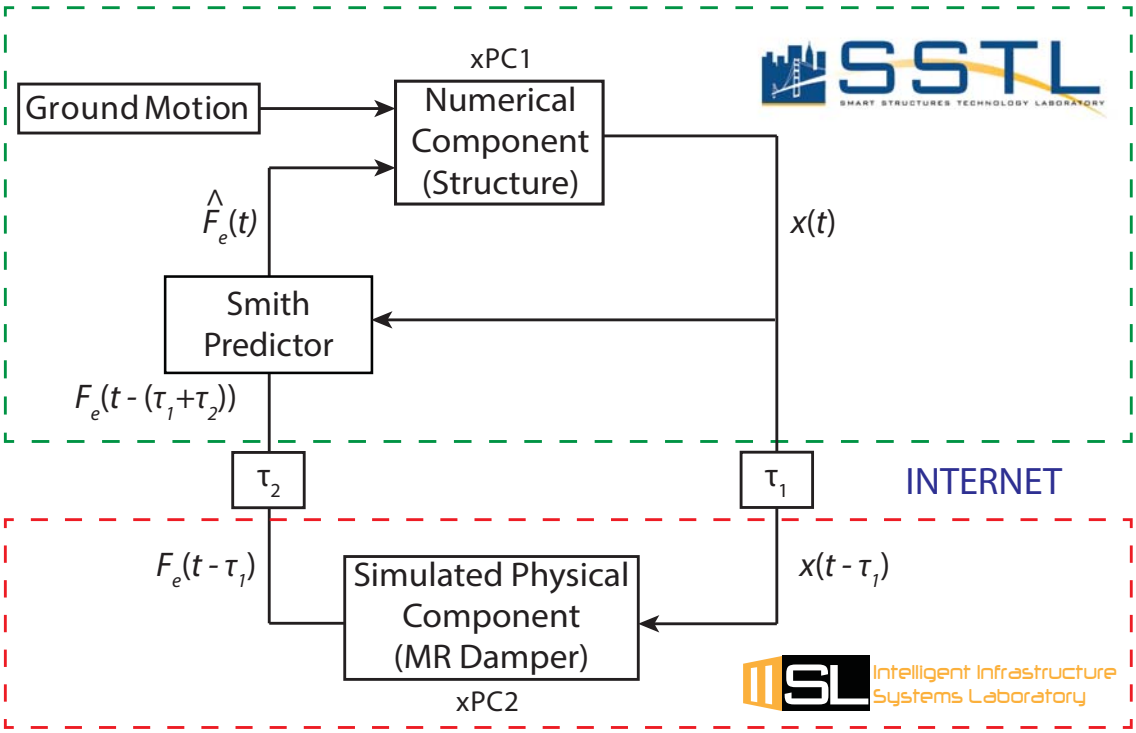


Figure 7.6: vdRTHS architecture including network time delays

The Smith predictor control structure proposed by Kim et al. (2012) is illustrated in Figure 7.7. The Smith predictor uses an internal model of the MR damper to predict the delay-free and delayed model responses, $F_a(t)$ and $F_a(t - (\hat{\tau}_1 + \hat{\tau}_2))$, respectively. $\hat{\tau}_1 + \hat{\tau}_2$ is the estimated round-trip delay prior to the testing. To compensate network

time delay, the delay-free response is fed to the numerical substructure while delayed model response cancels the delayed physical substructure response. The control structure can be formulated as given in Equation (7.2).

$$\hat{F}_e(t) = F_a(t) + [F_e(t - (\tau_1 + \tau_2) - F_a(t - (\hat{\tau}_1 + \hat{\tau}_2))] \tag{7.2}$$

where $F_e(t)$ is MR damper plant force and $\hat{F}_e(t)$ is the delay-compensated plant force.

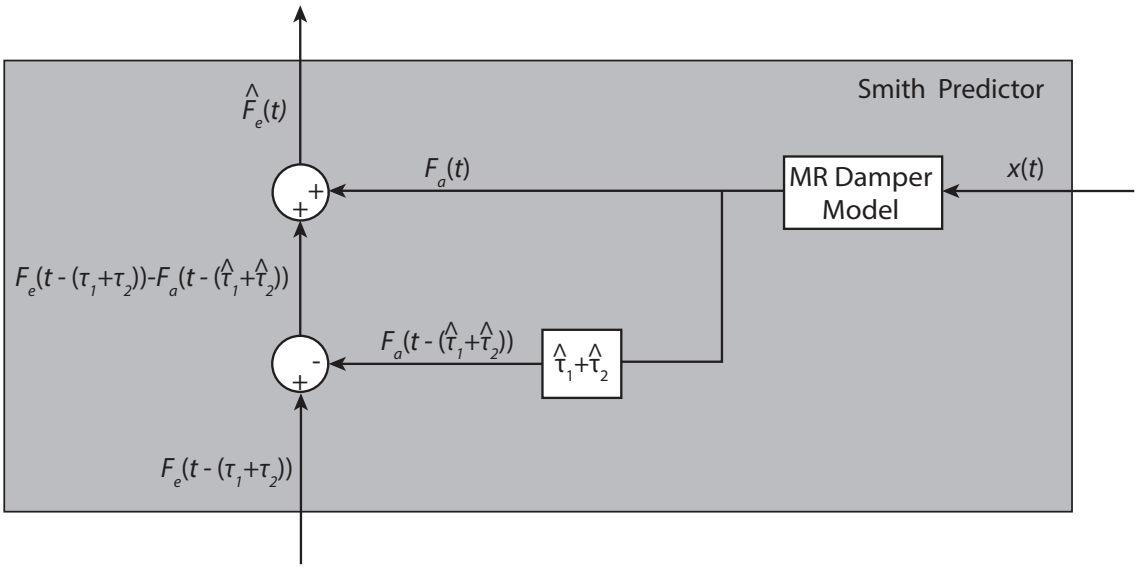


Figure 7.7: Implementation of Smith predictor

## 7.5 Initial Network Time Delay Estimator

The Smith predictor requires the dead time to be known prior to testing for the optimal operation and it may not always be possible to estimate the network time delay accurately since network conditions change continuously. The performance of the Smith predictor could be enhanced if network time delay could be determined just at the start of each test. In order to fulfill this objective, a network time delay estimator is developed. Essentially, this estimator calculates the time delay between

the distributed nodes using the relationship between first transmitting and receiving signals only for one time at the beginning of the test.

RT-UDP Receive block provides two output ports for processing incoming data. The first port contains received data in bytes. Respectively, the second port outputs size of the incoming packet. At a certain time step, zero from the second port indicates that the data has not arrived on time. Using the outputs from this port, arrival of packet can be checked during simulation time. This feature provides the basis of the delay estimator. An algorithmic flowchart of the estimator is given in Figure 7.8.

Fundamentally, this algorithm checks if some data is coming from the remote computer and whether the incoming data is a real data. As soon as a real data drops, it starts a timestep counter. While this counter runs, the real data is looped back intentionally. Eventually, the timestep difference between the real data and looped-back data is determined. This timestep difference is in fact the dead time required by the Smith predictor.

Procedurally, the algorithm first initialize an arrival flag (`arv_flag`) and time delay (`delay`) variables. For the first time step, the algorithm will check if the size of the packet is zero (`arv_check`) until data arrives. When first packet is received (`arv_check` = 1), `arv_flag` will be raised and delay will be fixed to the number of the current time step produced by a counter. Once `arv_flag` is raised, delay will persistently contain the already estimated time step number until the end of simulation.

This algorithm is applied at numerical simulation site to the inbound feedback force coming from physical substructure, before compensated by Smith predictor control structure block. The output of this algorithm, which is the estimated time delay (in fact, it is now the true time delay), is fed to the Smith predictor. An implementation in Simulink is given in Figure 8.2

One main disadvantage of this algorithm manifest itself, when data losses occur. Since the proposed algorithm doesn't account for corrupted or unbuffered data, such packages may cause additional delays that cannot estimated by the estimator correctly.

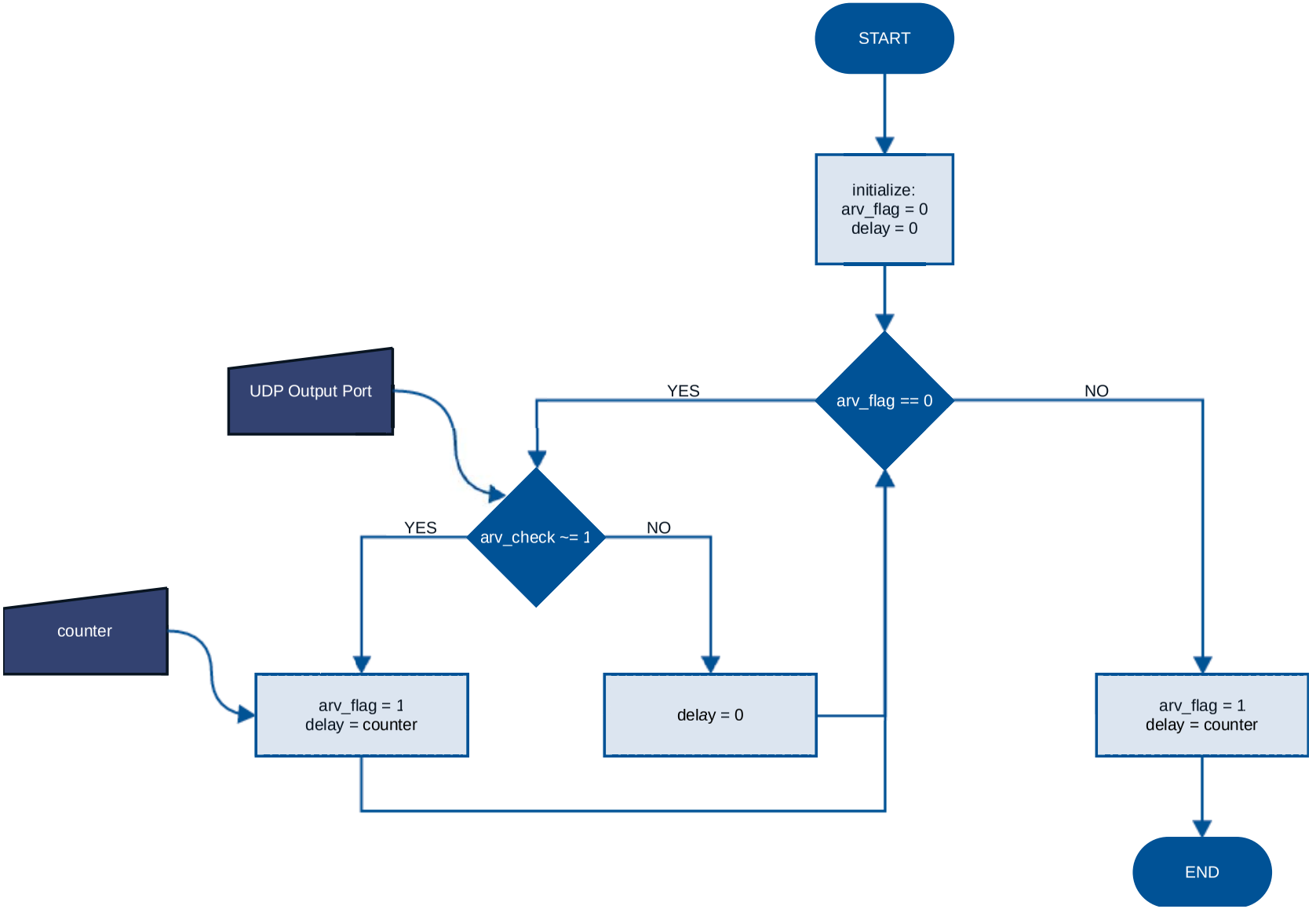


Figure 7.8: Implementation of initial time delay estimator

As another drawback of the estimator, still an initial assumption of the time delay should be guessed until a signal is received from remote computer and estimator starts to calculate the initial time delay based on the incoming signal. However, unless the assumed time delay and estimated time delay are far away from each other ($\sim$100 msec), it should not impose any considerable error.

## 7.6 Validation of dRTHS Architecture

To demonstrate effectiveness of the dRTHS when exposed to Internet communication, a series of virtual RTHS experiments are conducted. All components of those experiments, excluding Internet are numerically simulated in real-time including the virtual physical MR damper. Responses from three RTHS cases are compared: (i) single site virtual RTHS (vRTHS); (ii) multi-site virtual distributed RTHS (vdRTHS); and (iii) multi-site virtual distributed RTHS with framed packages (vdRTHS (Framed)).

A sampling rate of 1000 Hz is selected for both IISL and SSTL sites. Transmission is achieved at 1000 Hz for the non-framed simulation and at 200 Hz for the 5 packet-framed data. MR damper is kept in semi-active mode and the command voltage produced at SSTL is sent to remote target at IISL. The same command voltage is also used in Smith predictor MR damper plant in the SSTL simulation. El Centro earthquake is selected as the ground motion. The duration of experiment is 18 sec.

A buffer size of 10 and 80 in RT-UDP blocks is chosen for SSTL and IISL sites, respectively, to minimize data loss between the sites, when unframed data test is employed. For the framed data test, the buffer size for IISL site is decreased to 20. The initial network time delay estimator determined network delay as 90–110 time steps or 90 msec–110 msec for repeated number of trials. While small buffer size for SSTL node was sufficient for receiving the incoming data, IISL node was having difficulty to obtain the incoming transmission on time. Since the dedicated network card of IISL node is not behind a firewall, it is possible that the undesired and unrejected traffic is disrupting the communication, thus creating unbalanced network.

A comparison of responses from vRTHS, vdRTHS, and vdRTHS (Framed), is given in Figures 7.9 and 7.10. For the given comparisons, all three cases have the identical numerical models of the structure and MR damper. In addition, vdRTHS and vdRTHS (Framed) has the same estimated network time delay. Smith predictor is able to compensate the delayed MR damper force perfectly. Since the source of errors due to network delay and imperfect models in these experiments are nullified, exact responses are expected for all three cases. As a result, comparisons yield 0.0 % error.

## 7.7 Conclusion

In this chapter, a platform to conduct geographically distributed RTHS over UDP is presented. Since MATLAB/xPC is selected as the development environment, this platform provides versatility for researchers to integrate their own applications compared to some of the previous dRTHS middleware. Using this flexible platform, a network time delay predictor is used in conjunction with a Smith predictor, and introduced to handle network indeterminacy. The performance of the platform along with the predictor has been demonstrated through a series of virtual dRTHS considering a numerical two story structure equipped with a physical MR damper on its first floor. The analytical model of the structure is simulated at SSTL whereas the physical damper is simulated via a Bouc-Wen model at IISL. Excellent agreement is found between vRTHS and vdRTHS tests.

Although RT-UDP opens new venues to expand capabilities of RTHS, it should be noted that this protocol may not be suitable for all types of distributed applications. For example, UDP does not guarantee data integrity. Hence, experiments that require high fidelity data transmission, cannot rely on UDP. However, MATLAB/Simulink is flexible enough for a possible data integrity control implementation without much overhead.

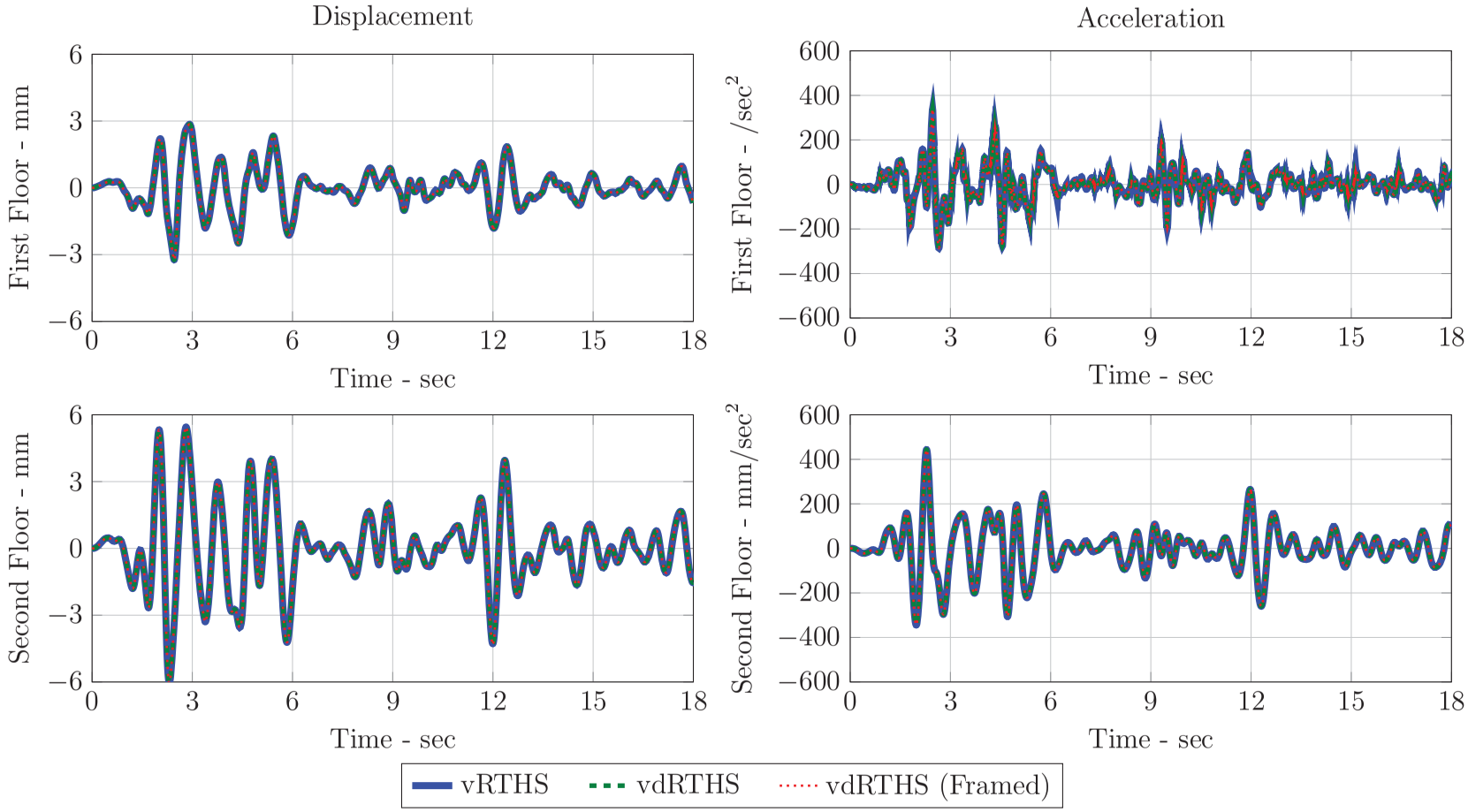


Figure 7.9: El Centro earthquake comparison in time domain for POFF case

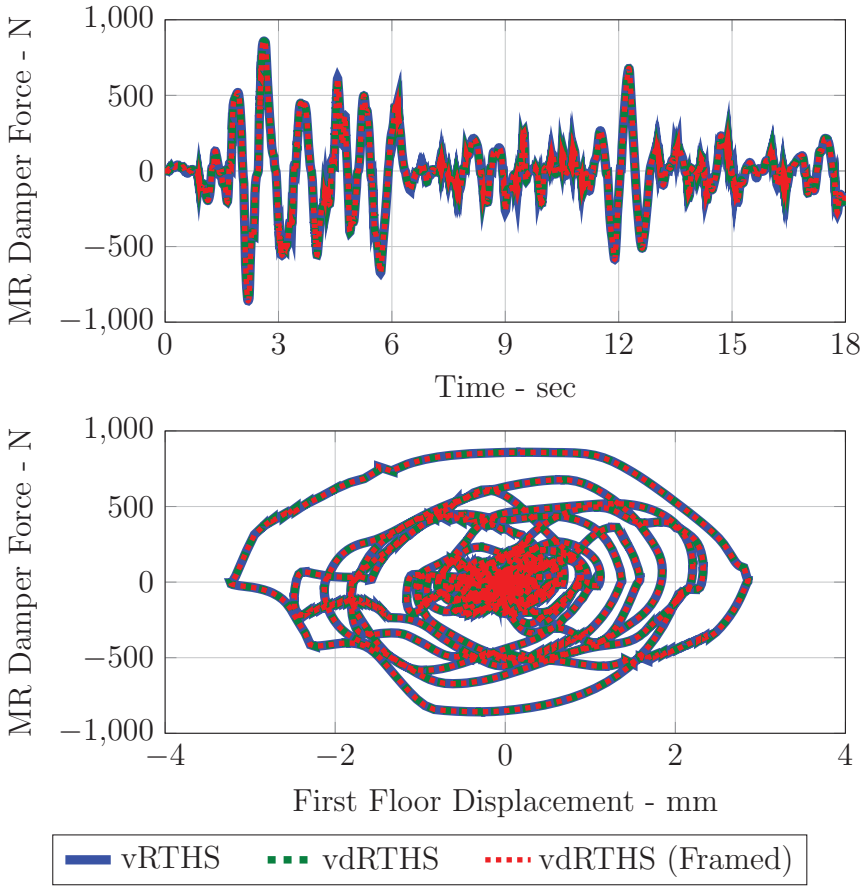


Figure 7.10: Numerical MR damper force response comparison in time domain for POFF case

As mention before, UDP is not a secure protocol and is vulnerable to cybersecurity attacks such as spoofing and data modifications. Even for well protected networks, such attacks may cause total loss of test setup and human life. To protect data transmission, at least the exchanged data should be hashed with a secure hash algorithm. Further actions can be taken by taking the whole communication system behind virtual private networks.

# CHAPTER 8
# VALIDATION OF DRTHS WITH SINGLE SITE RTHS AND SHAKE TABLE TESTS

In previous chapters, modeling of the analytical substructure, characteristics of the physical substructure, actuator tracking controller, and conceptual setup of geographically distributed RTHS were discussed. In this chapter, to validate dRTHS to its full extent, a setup similar to the single site RTHS, where MR damper and 3-DOF test structure are used as the physical and numerical respective substructures, is studied, and communication between substructures is carried out through Internet.

First, a general implementation of dRTHS is discussed in Section 8.1. Towards validation of dRTHS, responses of dRTHS are compared to single site RTHS in Section 8.2. In Section 8.3, the effect of incorrect delay estimation on the dRTHS responses are investigated experimentally, to demonstrate the efficiency of the network time delay estimator. Results of dRTHS are compared to shake table responses in Section 8.4. Finally, a summary of the chapter concluding the main findings is given in Section 8.5.

## 8.1 Implementation

The system architecture proposed in Section 7.3 is used with minimal modification for validation tests of dRTHS. For the physical portion of the test, the numerically simulated device is replaced with the physical MR damper used in comparisons presented in Chapter 6. The Simulink implementation for SSTL and IISL nodes is given in Figures 8.1 and 8.2 for unframed case. For the framed case, the implementation is provided in Figures 8.3 and 8.4.

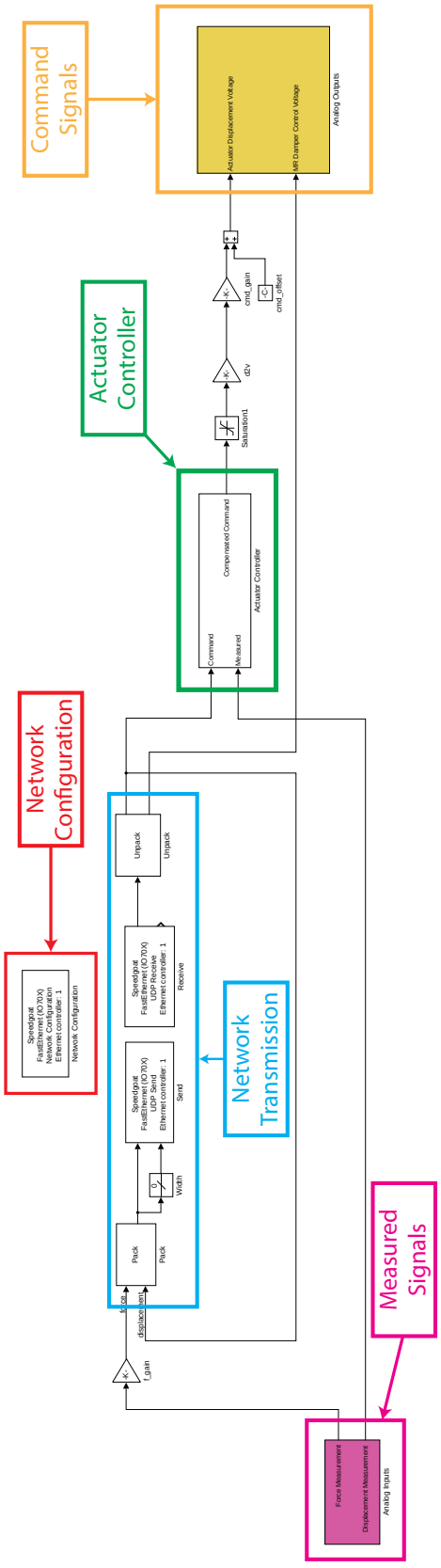


Figure 8.1: A representative Simulink model of the dRTHS for IISL node

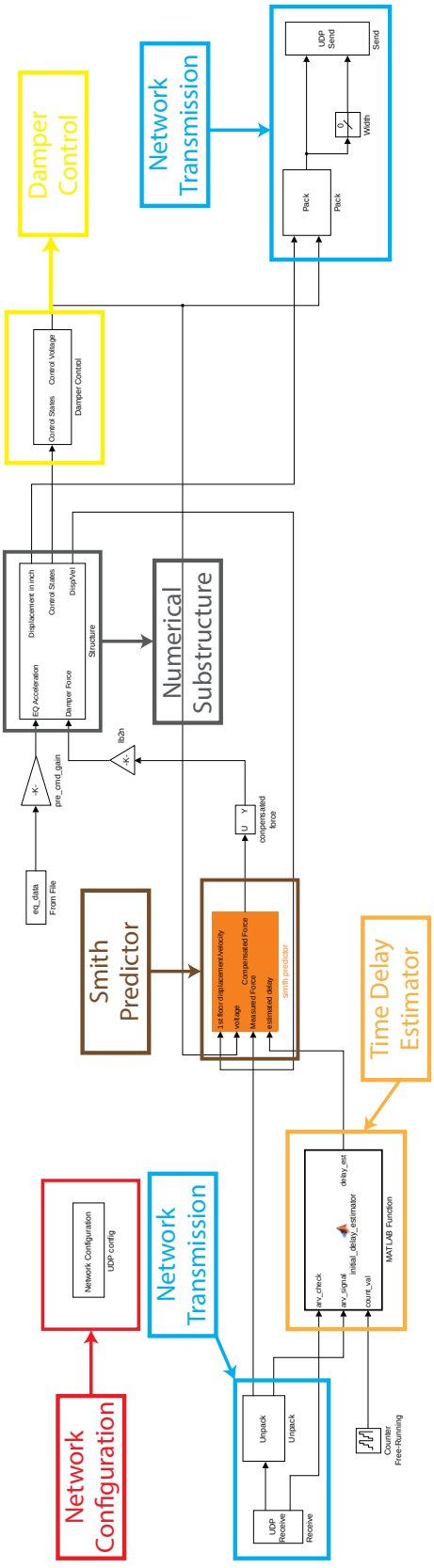


Figure 8.2: A representative Simulink model of the dRTHS for SSTL node

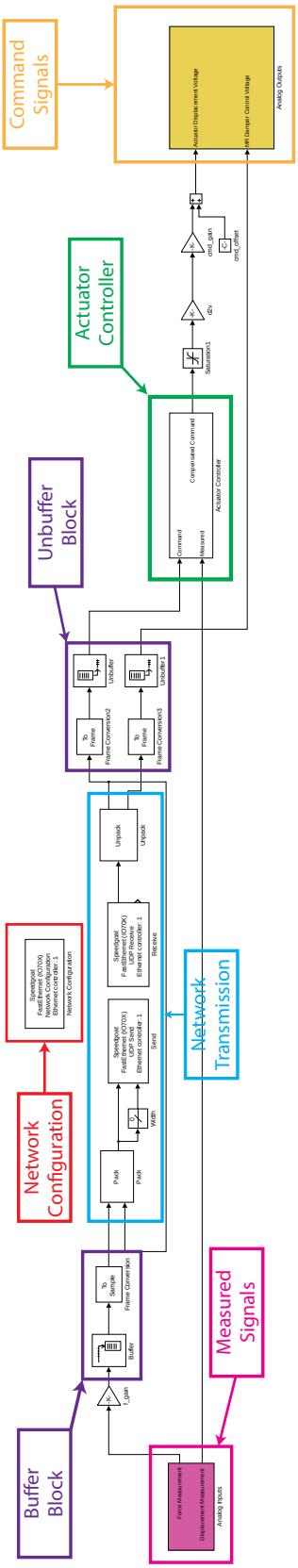


Figure 8.3: A representative Simulink model of the dRTHS for SSTL node

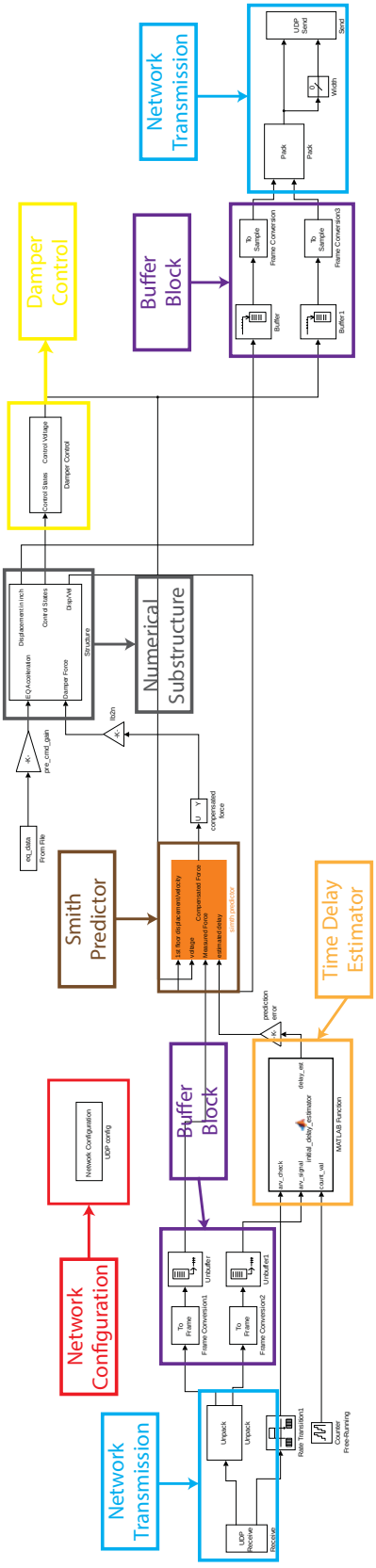


Figure 8.4: A representative Simulink model of the dRTHS for SSTL node

The sampling rate for the simulation is chosen as 5000 Hz at both sites. Two cases are considered for the communication speed between sites, where 5000 Hz, for the unframed transmission and 500 Hz, for the 10 package framed transmission are selected. First floor displacement and command voltage for the MR damper is transmitted from SSTL to IISL, and MR damper force and the loopback first floor displacement is sent from IISL to SSTL. All signals are considered as double precision data.

The transmission speed is estimated to be 1.67 Mbps for the unframed case and 0.72 Mbps for the framed case. The difference between transmission rates is due to packet overheads included for each packet in unframed case. To sustain a lossless transmission for the test duration (at least 14 sec) between the sites, a buffer of 300 and 30 time steps are selected for the unframed and framed data, respectively for the IISL node. For SSTL node, a buffer of 10 time steps for the unframed and framed data are sufficient for uninterrupted transmission. The delay is estimated by the initial network time delay block as $\sim$ 400 time steps or $\sim$80 msec for both the unframed and framed transmissions. It has been observed that the estimated delay is very close to the one in the validation setup discussed in Chapter 7. The Smith predictor used to estimate delayed MR damper forces using the estimated delay is modeled after Purdue damper.

## 8.2 Comparison of RTHS Responses with dRTHS Results

In this section, the dRTHS results are compared to the RTHS responses. The semi-actively controlled El Centro earthquake case is selected as the basis of comparison. Time domain comparisons, as well as RMS and peak displacement, acceleration and force errors are shown to quantify the performance of dRTHS.

In Figures 8.5 and 8.9, the acceleration and displacement responses of RTHS and dRTHS are compared in the time domain for unframed and framed cases. Likewise, in Figures 8.6 and 8.10, MR damper force comparisons are given. The frequency domain

Table 8.1: Evaluation criteria for RTHS–dRTHS comparisons

| Case | Location | Evaluation Criteria | | | | | | Criteria |
|---|---|---|---|---|---|---|---|---|
| | | J1 | J2 | J3 | J4 | J5 | J6 | Average |
| dRTHS Unframed | First Floor | 9.03 | 0.66 | 27.73 | 28.75 | 1.95 | 5.53 | 12.27 |
| | Second Floor | 8.11 | 0.78 | 17.19 | 5.06 | 1.73 | 3.59 | 6.08 |
| | Third Floor | 8.30 | 0.60 | 15.45 | 1.24 | 1.75 | 3.12 | 5.08 |
| dRTHS Framed | First Floor | 7.78 | 2.26 | 23.91 | 10.33 | 1.68 | 4.77 | 8.45 |
| | Second Floor | 6.96 | 0.56 | 13.84 | 4.70 | 1.48 | 2.89 | 5.07 |
| | Third Floor | 7.02 | 0.70 | 11.89 | 0.71 | 1.48 | 2.40 | 4.03 |

comparisons are presented in Figures 8.7 and 8.11. Additionally, sliding RMS plots are shown in Figures 8.8 and 8.12. Finally, in Table 8.1, the errors are tabulated.

It is observed from time domain comparisons that, for either framed or unframed case, dRTHS captures the general behavior of RTHS responses. When examining at MR damper force comparisons, it is noted that the Smith predictor is able to simulate the damper forces with respect to the given first floor displacements. Performance criteria are varying between 0 % to 30 %. Most of the evaluation criteria are below 10 %. On the other hand, for the first floor responses, RMS and peak acceleration errors are largest (J3 and J4). This increase is due to the slight underestimation of RTHS acceleration around $t = 3\,\text{sec}$ in the simulation where the ground motion is strongest and the RTHS MR damper force overshoots the dRTHS damper force.

Overall, it can be concluded that the proposed dRTHS platform yields quite similar results as the single-site RTHS tests despite the network time delay for this particular structure. It is also shown that this delay can be compensated with the help of Smith predictor and network time delay estimator.

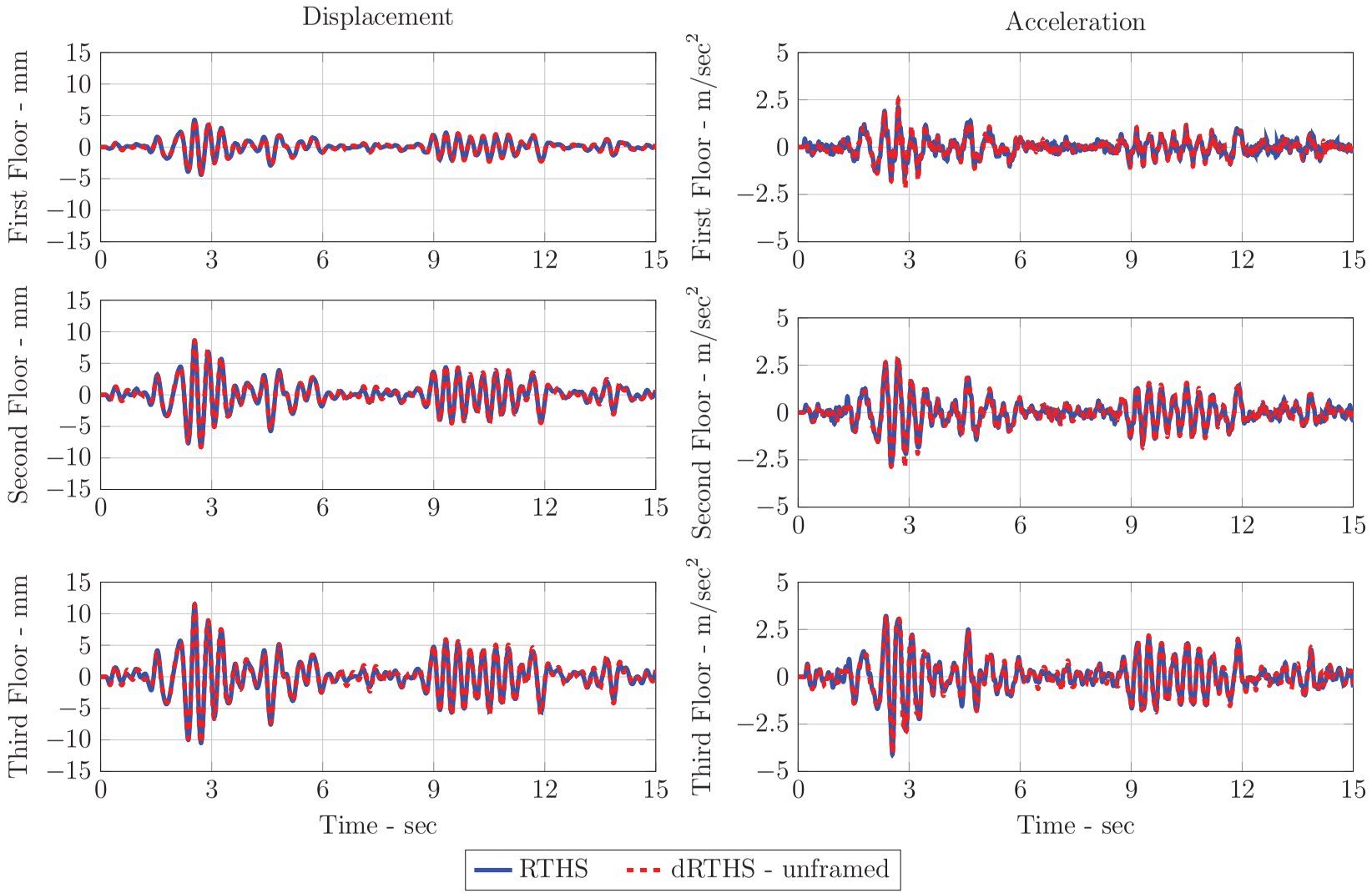


Figure 8.5: El Centro earthquake response comparison in time domain for RTHS–unframed dRTHS SA case

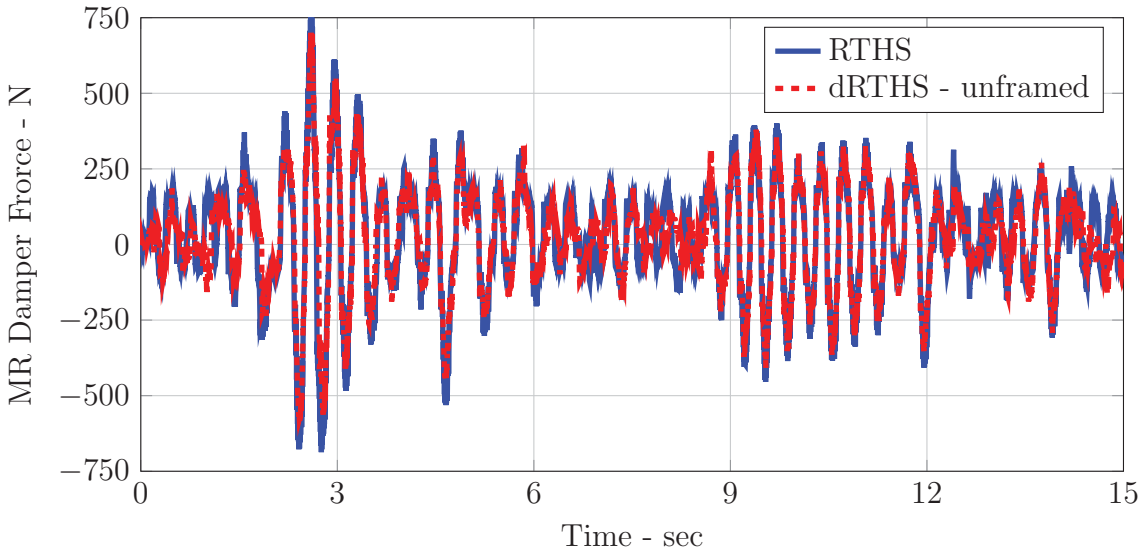


Figure 8.6: MR damper force response comparison in time domain for RTHS–unframed dRTHS SA case

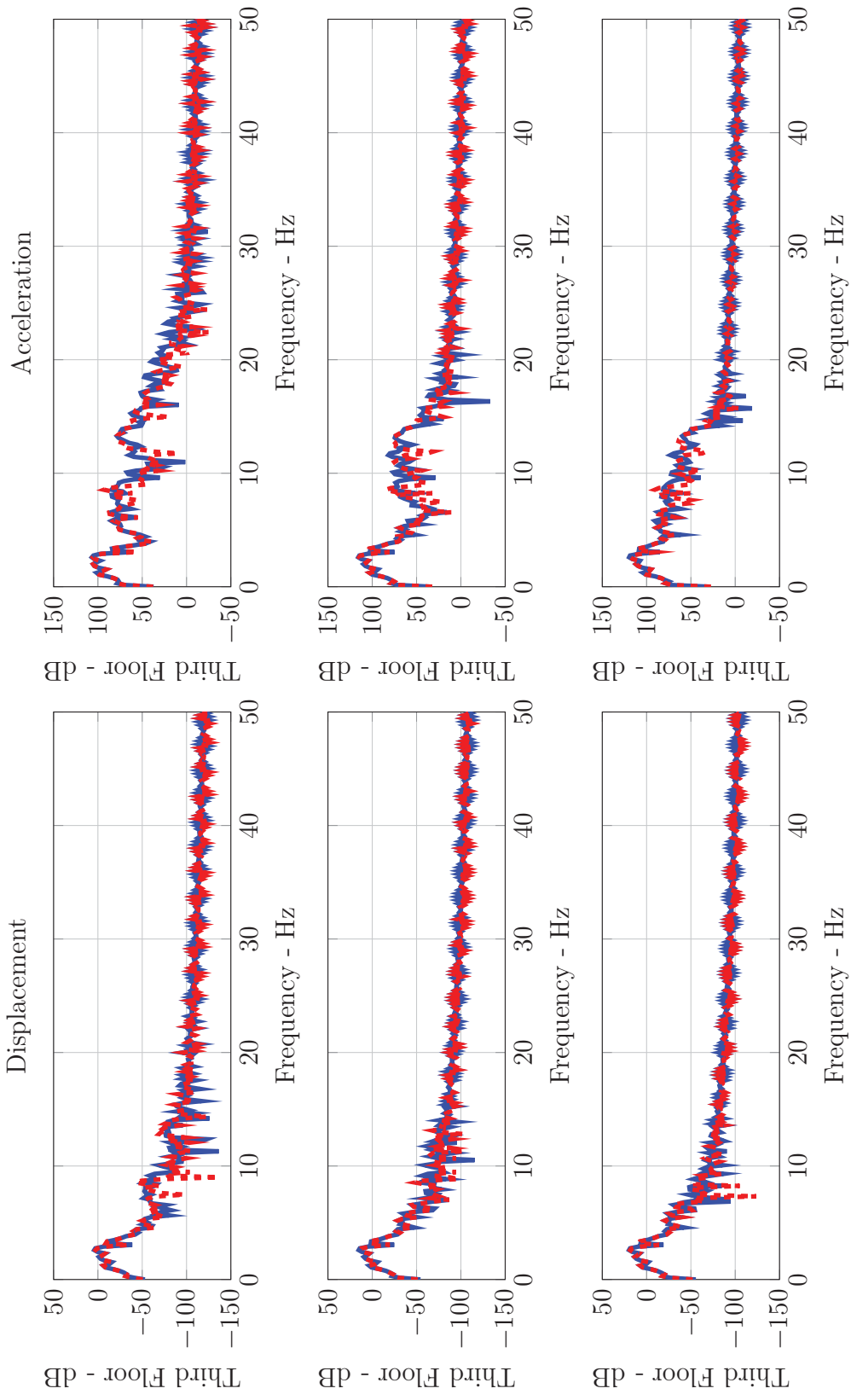


Figure 8.7: El Centro earthquake response comparison in frequency domain for RTHS–unframed dRTHS SA case

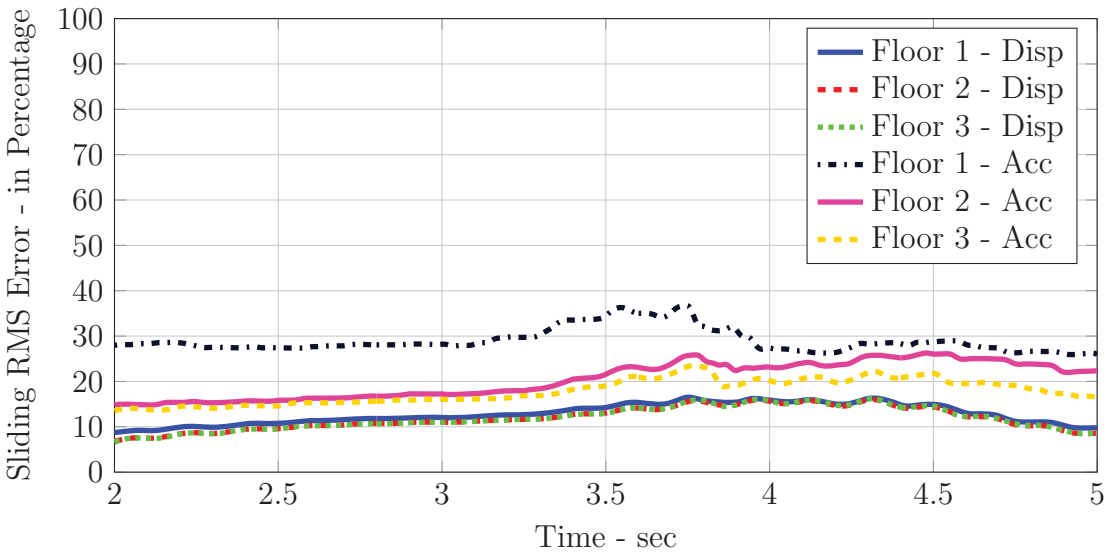


Figure 8.8: Moving RMS error for RTHS–unframed dRTHS SA case

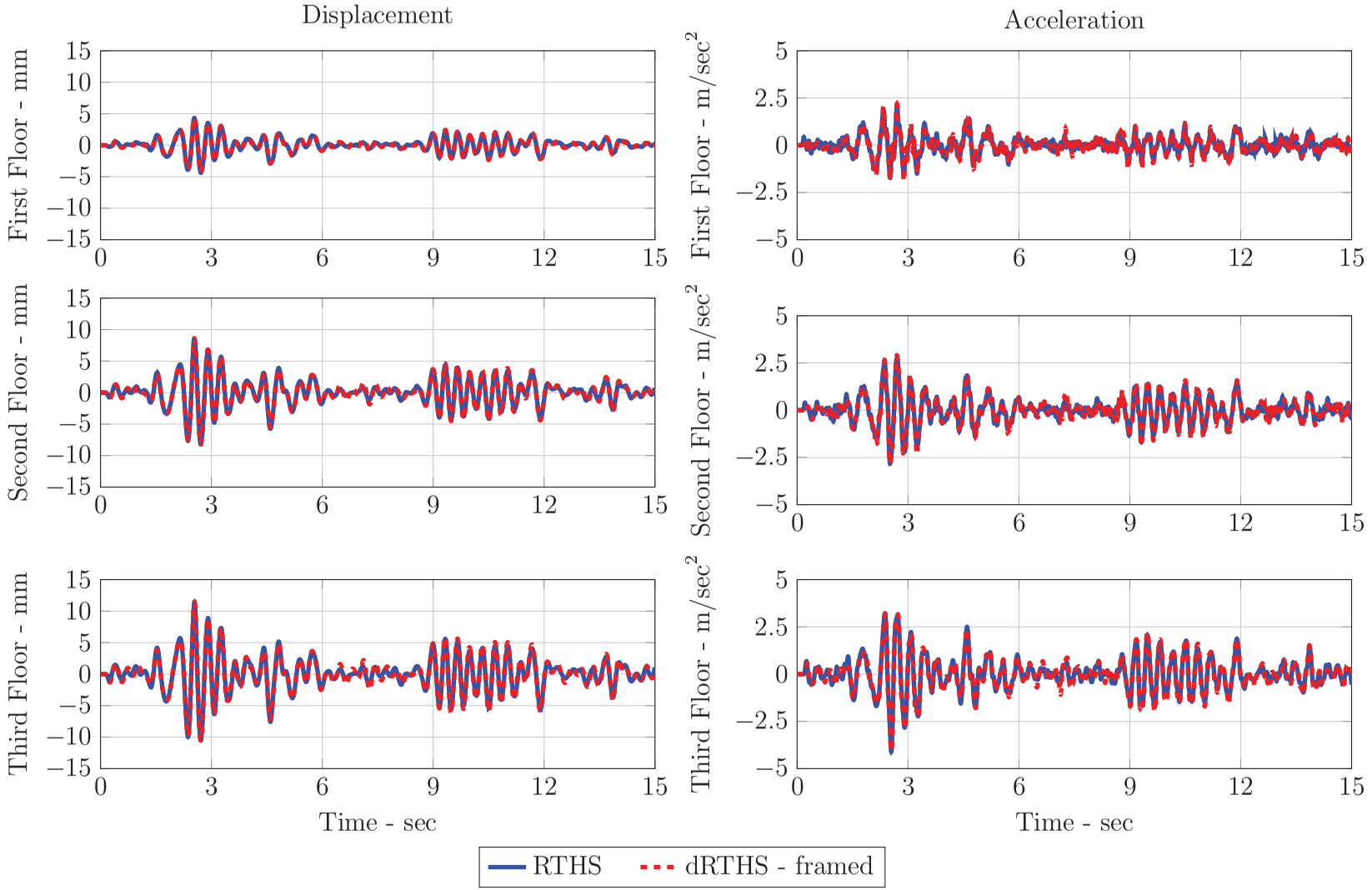


Figure 8.9: El Centro earthquake response comparison in time domain for RTHS–framed dRTHS SA case

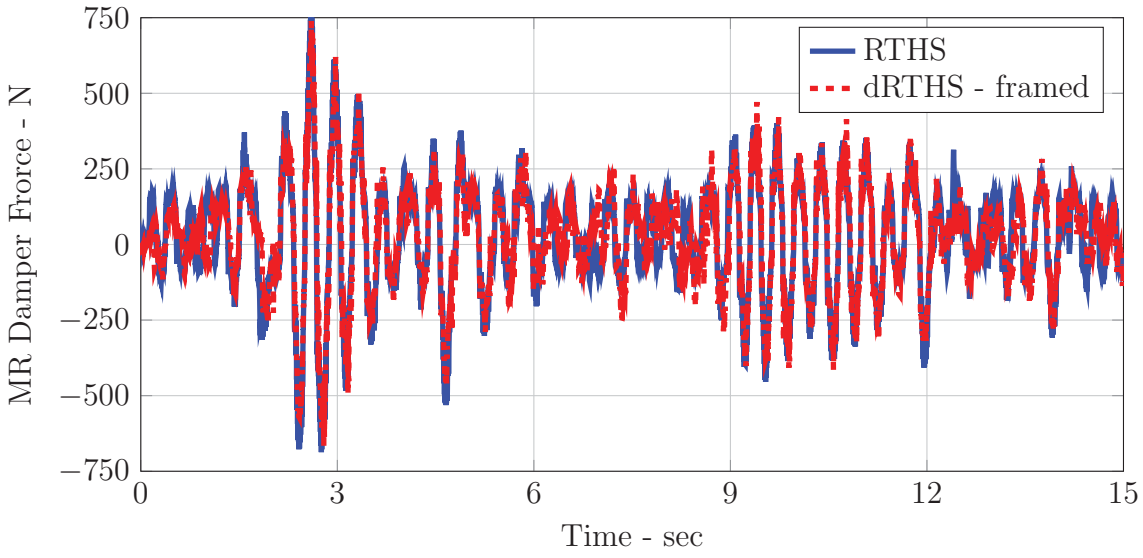


Figure 8.10: MR damper force response comparison in time domain for RTHS–framed dRTHS SA case

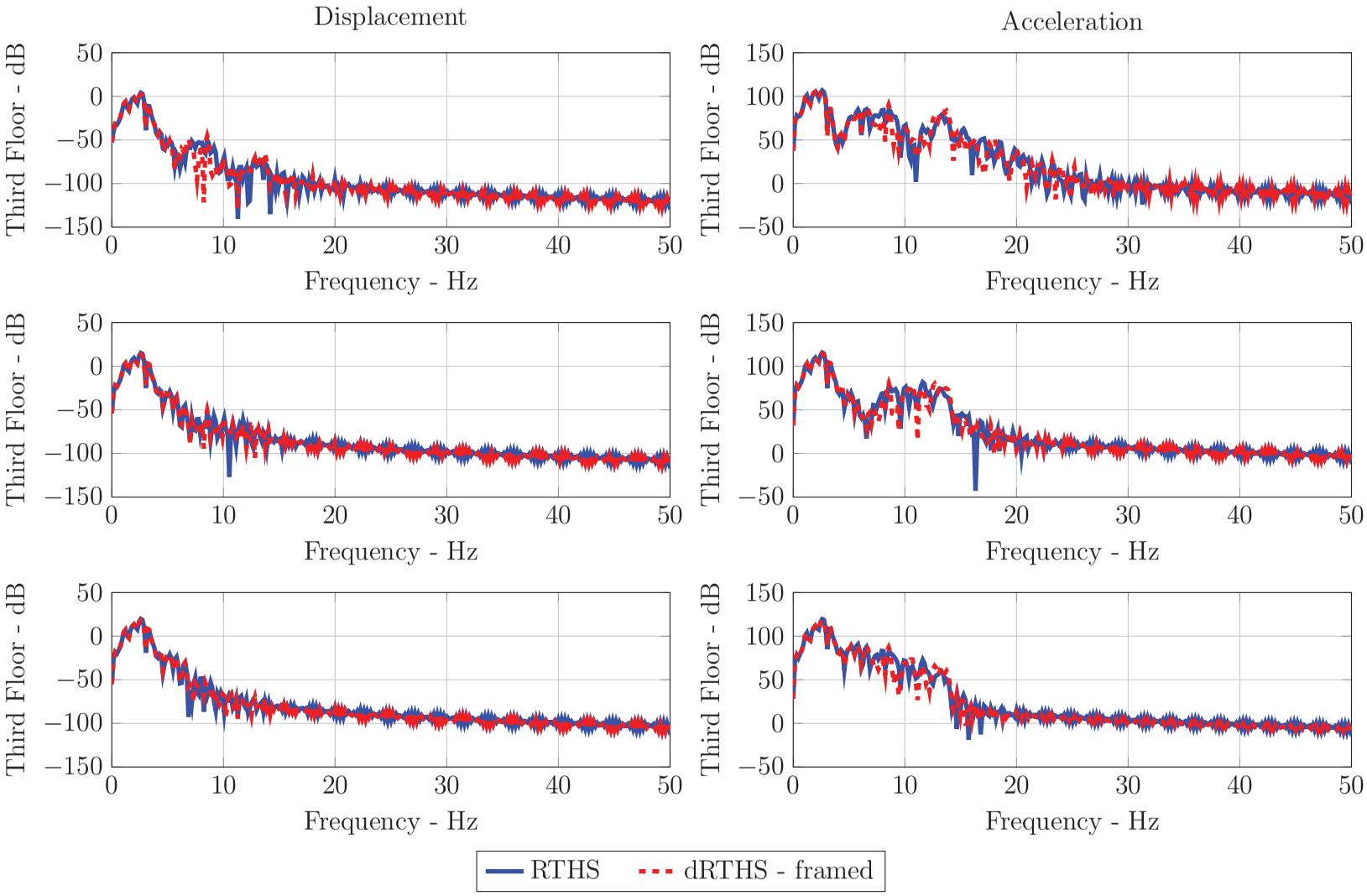


Figure 8.11: El Centro earthquake response comparison in frequency domain for RTHS–framed dRTHS SA case

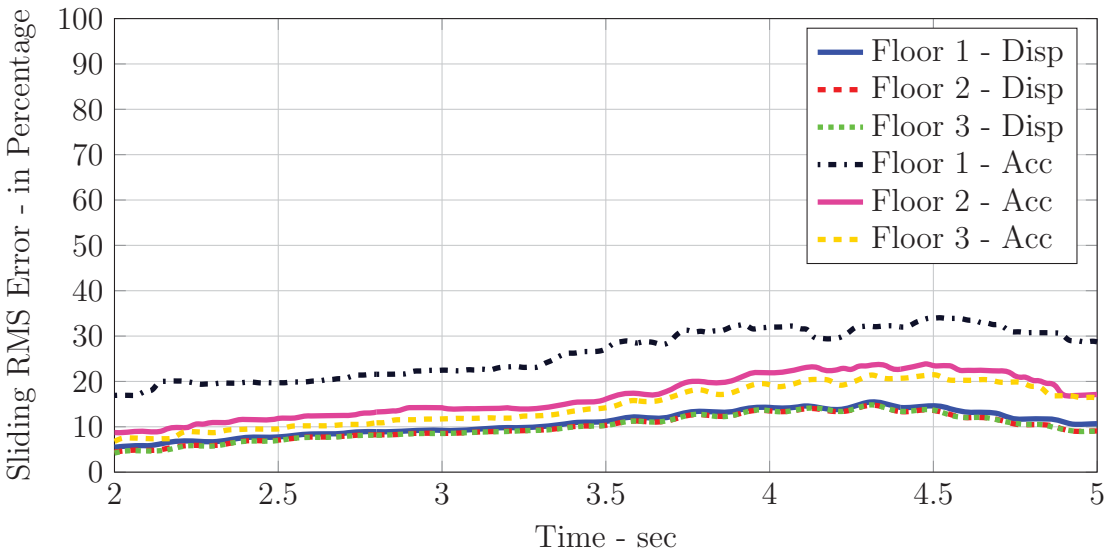


Figure 8.12: Moving RMS error for RTHS–framed dRTHS SA case

## 8.3 Quantifying the Effect of Network Time Delay on dRTHS Results

Assume that a network having a delay of $\Delta\tau_R$ is compensated with a predictor designed according to $\Delta\tau_P$. When $\Delta\tau_P$ is lower than $\Delta\tau_R$, in other words, the delay is underpredicted, the predicted force does not correspond to the measured displacement. Consequently, the error between predictor plant and actual plant behavior due to phase lag manifests as a pure time delay. This effect introduces additional energy to the system equivalent to negative damping and can lead to instability when overall damping of the system is smaller than the introduced negative damping. This phenomenon is discussed by Horiuchi et al. (1996) in detail. Similarly, for overpredicted delay, positive damping will be imposed on the system. Accordingly, system responses will be underestimated.

To understand the effects of prediction and to underline the usefulness of including the initial network time delay estimation block, incorrect estimation of network delay on the performance of dRTHS is investigated through a series of experiments. Here, estimated delays are over- and underpredicted by 10 % and 20 %, intentionally. The incorrectly predicted displacement and acceleration responses are compared to correctly estimated dRTHS results. The effect of delay on the first floor displacement responses is given in Figures 8.13 and 8.15 for unframed and framed cases. Additionally, first floor acceleration response comparisons are given in Figures 8.14 and 8.16. Errors are tabulated in Table 8.2. For all comparisons, the reference is taken as dRTHS with correctly predicted time delays.

For all unframed cases, under- and overpredicted delay estimations do not significantly alter overall dRTHS displacement responses. On the other hand, for acceleration responses, the effect of incorrect prediction is significantly more noticeable. The tabulated error for the unframed cases points that incorrect delay estimation causes deviations, especially for the first floors.

It is observed that the framed case responses are more sensitive to under- and overprediction in time domain. Specifically, for acceleration responses, underpredicted

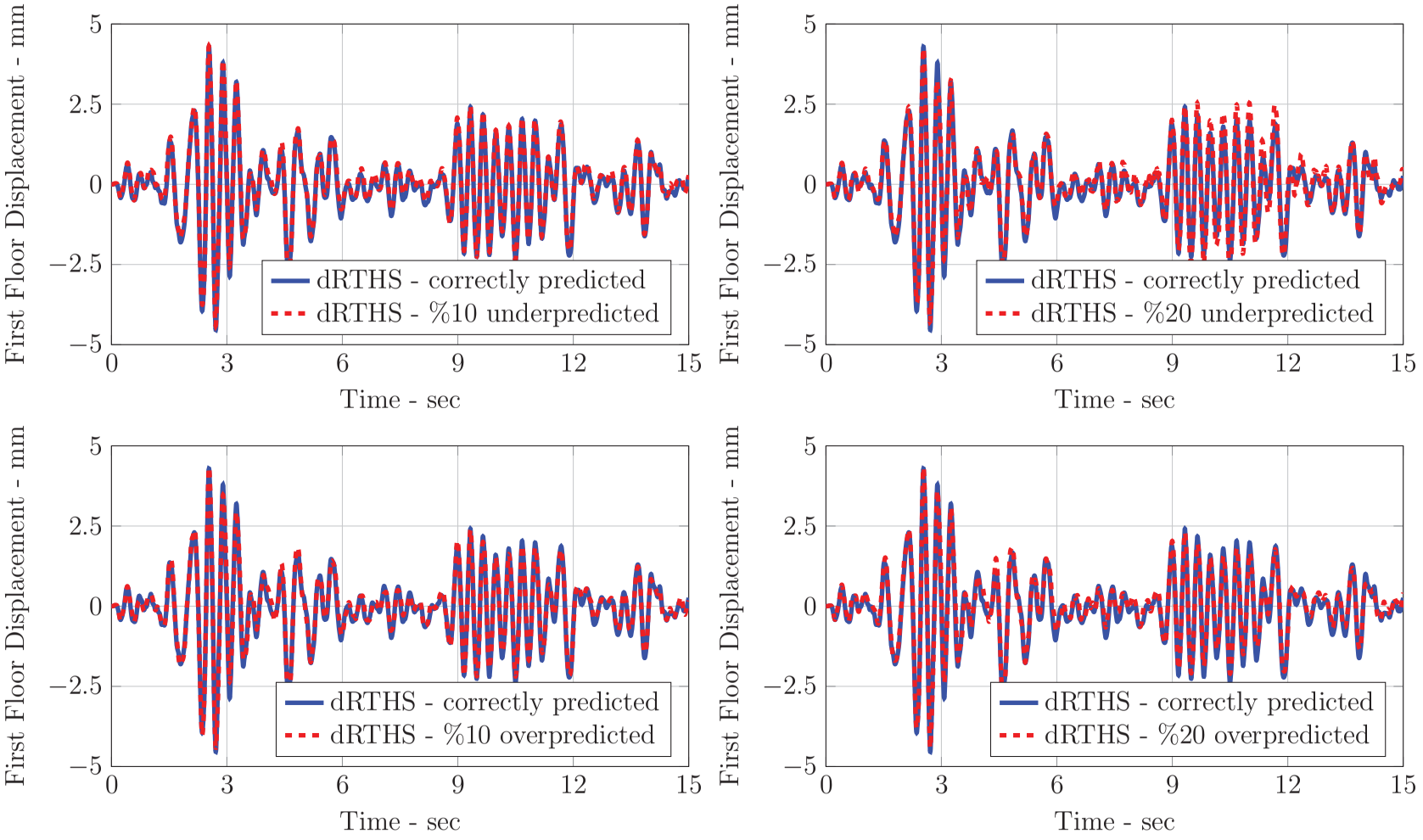


Figure 8.13: Delay estimation comparison for the first floor displacements - unframed

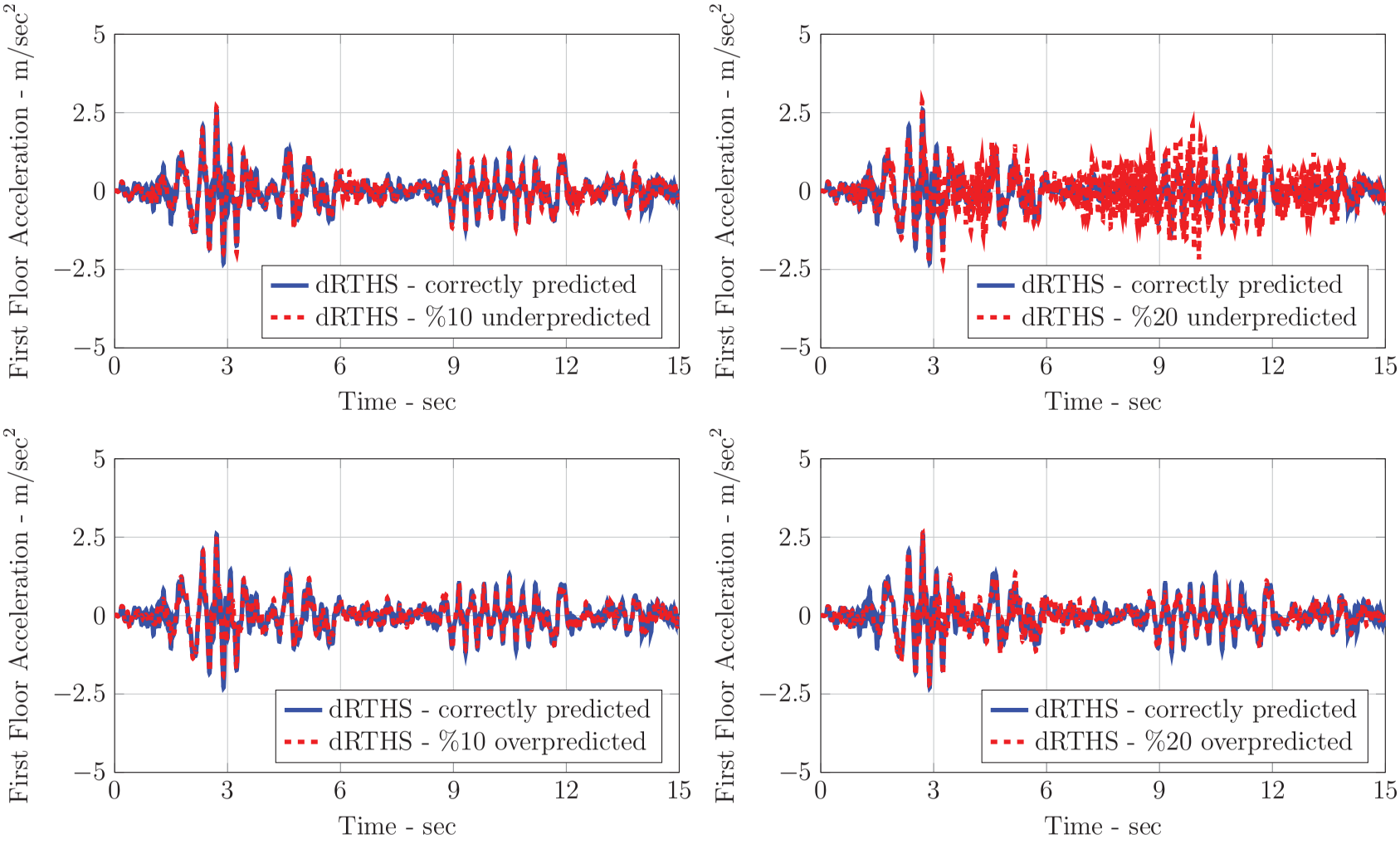


Figure 8.14: Delay estimation comparison for the first floor accelerations - unframed

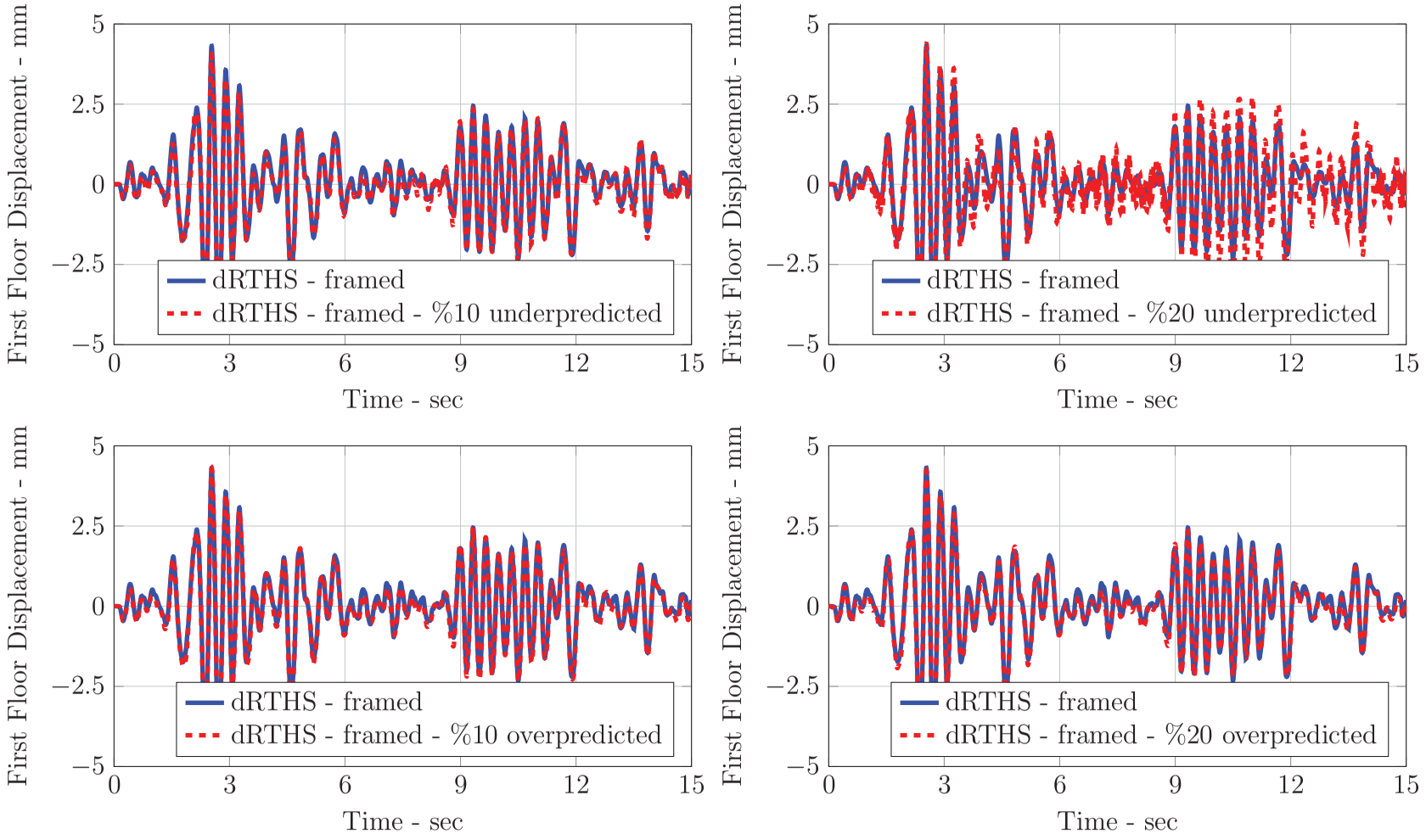


Figure 8.15: Delay estimation comparison for the first floor displacements - framed

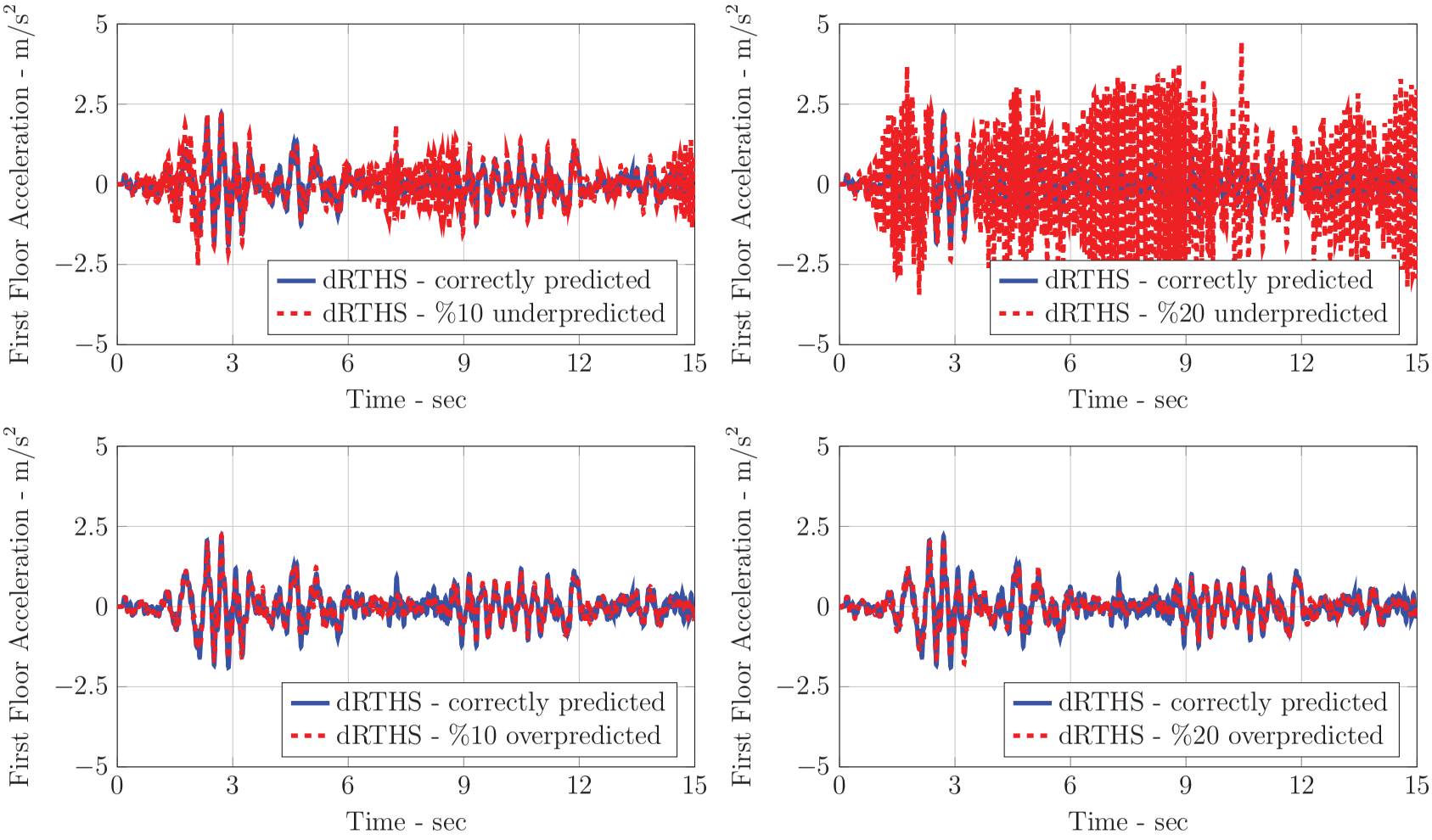


Figure 8.16: Delay estimation comparison for the first floor accelerations - framed

Table 8.2: Evaluation criteria for dRTHS induced network time delay estimations

| Case | Location | Evaluation Criteria | | | | | |
|---|---|---|---|---|---|---|---|
| | | J1 | J2 | J3 | J4 | J5 | J6 |
| Unframed | First Floor | 11.96 | 5.51 | 64.04 | 10.67 | 2.45 | 10.62 |
| Underpredicted | Second Floor | 7.88 | 2.38 | 26.72 | 10.45 | 1.64 | 5.18 |
| %20 | Third Floor | 7.89 | 0.48 | 22.53 | 6.62 | 1.66 | 4.76 |
| Unframed | First Floor | 7.79 | 2.86 | 29.98 | 13.66 | 1.60 | 4.97 |
| Underpredicted | Second Floor | 5.02 | 1.51 | 15.46 | 6.31 | 1.04 | 3.00 |
| %10 | Third Floor | 4.92 | 0.78 | 12.63 | 6.58 | 1.04 | 2.67 |
| Unframed | First Floor | 12.60 | 2.84 | 32.97 | 17.23 | 2.59 | 5.47 |
| Overpredicted | Second Floor | 10.87 | 1.99 | 18.21 | 8.43 | 2.26 | 3.53 |
| %10 | Third Floor | 10.77 | 0.34 | 17.20 | 2.25 | 2.26 | 3.63 |
| Unframed | First Floor | 13.45 | 2.60 | 35.85 | 4.95 | 2.76 | 5.94 |
| Overpredicted | Second Floor | 11.39 | 2.32 | 21.18 | 4.50 | 2.37 | 4.10 |
| %20 | Third Floor | 11.18 | 1.44 | 18.01 | 2.55 | 2.35 | 3.81 |
| Framed | First Floor | 27.95 | 10.02 | 138.40 | 81.80 | 5.93 | 26.11 |
| Underpredicted | Second Floor | 24.96 | 10.32 | 56.35 | 29.73 | 5.24 | 11.57 |
| %20 | Third Floor | 24.75 | 7.62 | 36.14 | 24.80 | 5.17 | 7.34 |
| Framed | First Floor | 9.56 | 6.21 | 45.11 | 33.48 | 2.03 | 8.51 |
| Underpredicted | Second Floor | 7.58 | 3.45 | 27.58 | 8.10 | 1.59 | 5.66 |
| %10 | Third Floor | 7.37 | 3.22 | 16.54 | 1.27 | 1.54 | 3.36 |
| Framed | First Floor | 6.65 | 3.59 | 25.20 | 12.74 | 1.41 | 4.75 |
| Overpredicted | Second Floor | 4.87 | 1.05 | 14.04 | 2.60 | 1.02 | 2.88 |
| %10 | Third Floor | 4.81 | 0.24 | 11.31 | 5.06 | 1.00 | 2.30 |
| Framed | First Floor | 6.94 | 3.49 | 29.85 | 6.23 | 1.47 | 5.63 |
| Overpredicted | Second Floor | 4.81 | 1.76 | 15.98 | 6.40 | 1.01 | 3.28 |
| %20 | Third Floor | 4.71 | 0.58 | 12.13 | 3.16 | 0.98 | 2.46 |

delay estimation causes large overshooting. Likewise, undershooting due to overprediction of delay is also evident in acceleration responses. Errors are slightly elevated for the underpredicted delay comparisons. For the unframed case, simulation integration and transmission rates are same. Hence, structure responds to the delayed force feedback at each time step and generates first floor displacement to be sent to the remote node, accordingly. That also means, at each time step, the Smith predictor can match the delayed force with the on-time displacement. However, for the framed case, 10 timestep data is transmitted at $1/10^{th}$ of the simulation rate, at once. Therefore, for each time step, the local and remote nodes receive 10 force measurements and 10 displacement measurements at once, respectively. When the delay is constant and is estimated correctly, the Smith predictor processes the incoming force without any problem. However if delay is incorrectly estimated for the framed case, the error between predictor plant and actual plant is accumulated through 10 timesteps. Consequently, it is expected that framed case is relatively sensitive to incorrect delay prediction, compared to unframed case.

Overall, the Smith predictor is generally stable as long as the error between model and actual plant is small. However, with increasing time delay prediction error, the Smith predictor starts to deviate from the physical MR damper. Likewise, framing of data amplifies the error in the event of incorrect prediction.

## 8.4 Comparison of Shake Table Test Responses with dRTHS Results

In this section, dRTHS conducted between IISL and SSTL sites is compared to the shake table test performed at HIT. Particularly, responses for semi-active control case for El Centro earthquakes are considered. dRTHS cases, where network time delays are under- and overpredicted, are ignored.

In Figures 8.17 and 8.20, the acceleration and displacement responses of shake table and dRTHS are compared in time domain for both the unframed and framed cases. The frequency domain comparisons are presented in Figures 8.18 and 8.21.

Table 8.3: Evaluation criteria for ST–dRTHS comparison

| Case | Location | Evaluation Criteria | | | | | | Criteria Average |
|---|---|---|---|---|---|---|---|---|
| | | J1 | J2 | J3 | J4 | J5 | J6 | |
| dRTHS Unframed | First Floor | 23.64 | 13.58 | 29.94 | 21.68 | 5.18 | 5.77 | 16.63 |
| | Second Floor | 20.45 | 6.93 | 19.55 | 15.57 | 4.33 | 3.63 | 11.74 |
| | Third Floor | 21.33 | 9.17 | 15.73 | 10.86 | 4.41 | 3.14 | 10.77 |
| dRTHS Framed | First Floor | 23.36 | 13.60 | 31.19 | 6.20 | 5.12 | 6.00 | 14.25 |
| | Second Floor | 19.90 | 7.85 | 22.23 | 18.02 | 4.21 | 4.12 | 12.72 |
| | Third Floor | 20.60 | 9.36 | 15.44 | 11.25 | 4.26 | 3.08 | 10.67 |

Additionally, sliding RMS plots are shown in Figures 8.19 and 8.22. Finally, in Table 8.3, the evaluation criteria are tabulated.

Comparisons for dRTHS vs shake table test in time domain presents similarity to RTHS vs shake table comparisons. Both unframed and framed cases yield similar power spectra, compared to shake table response spectra. It is observed that dRTHS captures the modes of the test structure obtained from shake table experiment reasonably well in the frequency domain. For the acceleration responses, spurious modes at 30 Hz–40 Hz range could not be tracked. A similar behavior was also observed for the RTHS vs shake table tests. As stated previously in Chapter 6, a possible reason for the discrepancy is the torsional and higher frequency modes of the structure that were excited by the vibration of the shake table and they were not included in the numerical model intentionally.

The reported errors for unframed and framed cases are varying from 3 % to 30 %. The largest errors are observed in first floor response RMS criteria for both cases. In addition, moving RMS errors demonstrate that all errors except first floor acceleration are trending at 20 %–25 % band. It should be noted that dRTHS configurations are using an MR damper different from the one used during the shake table tests. Addi-

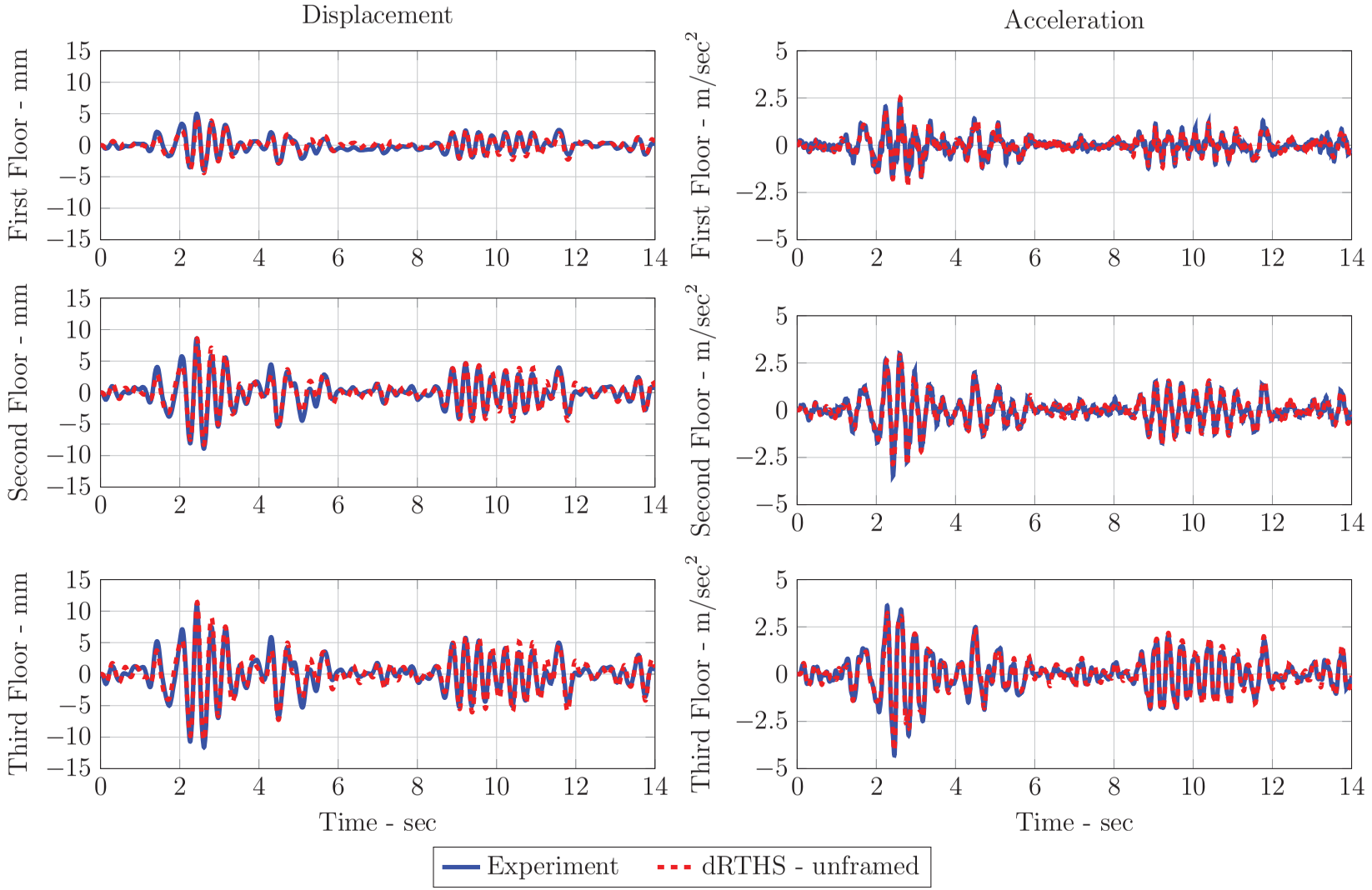


Figure 8.17: El Centro earthquake response comparison in time domain for ST–unframed dRTHS SA case

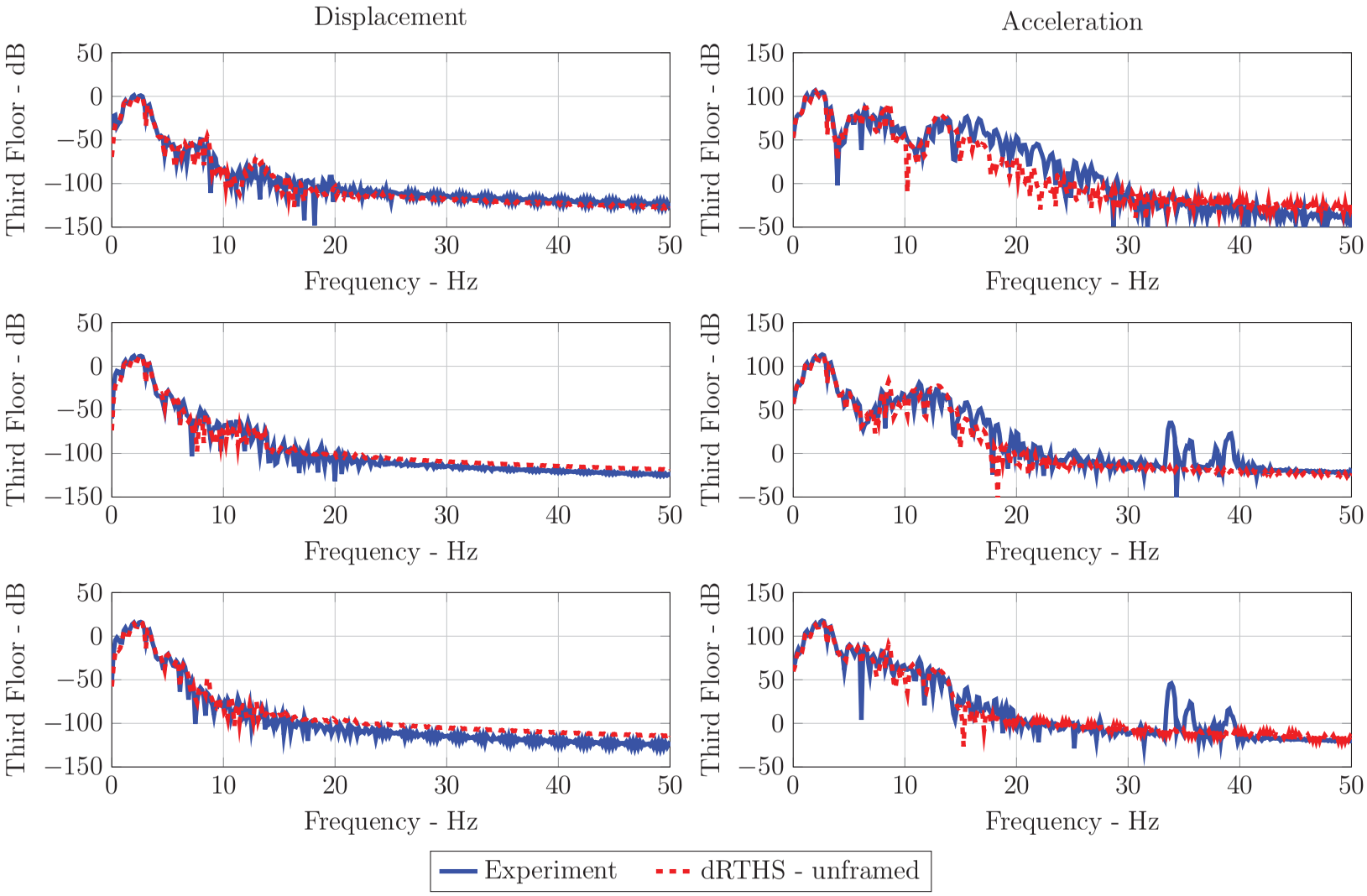


Figure 8.18: El Centro earthquake response comparison in frequency domain for ST–unframed dRTHS SA case

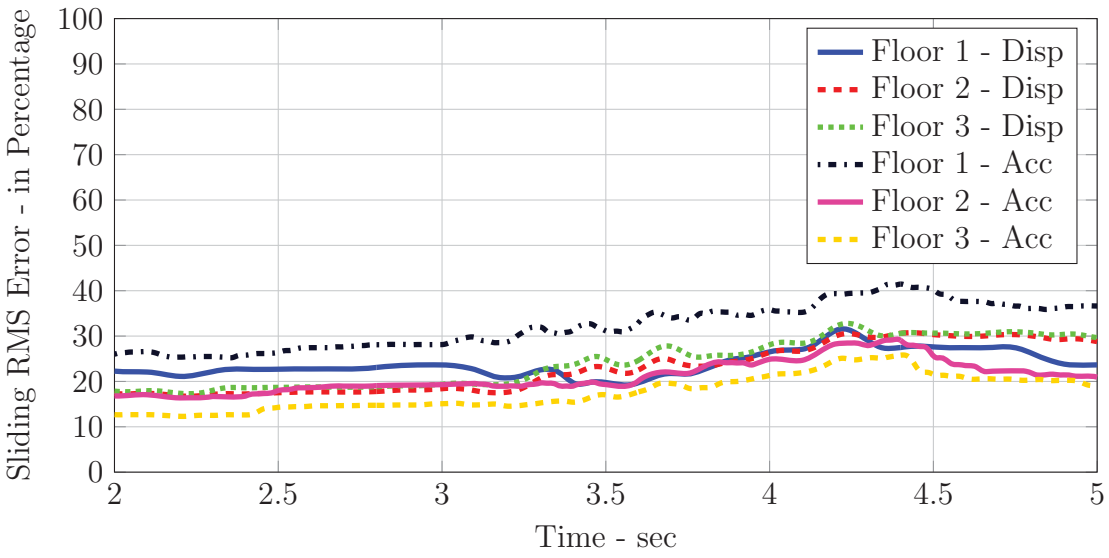


Figure 8.19: Moving RMS error for ST–unframed dRTHS SA case

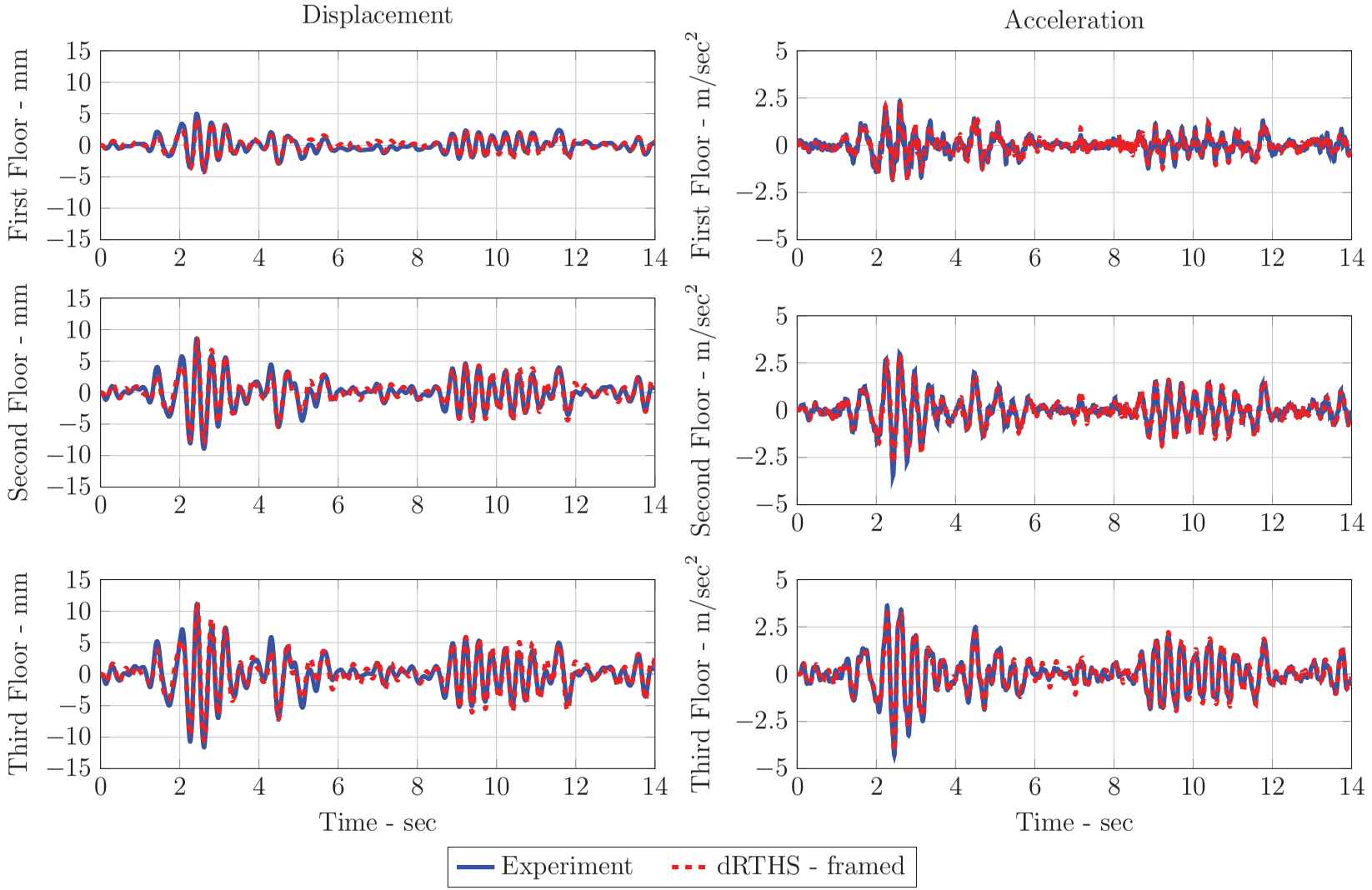


Figure 8.20: El Centro earthquake response comparison in time domain for ST–framed dRTHS SA case

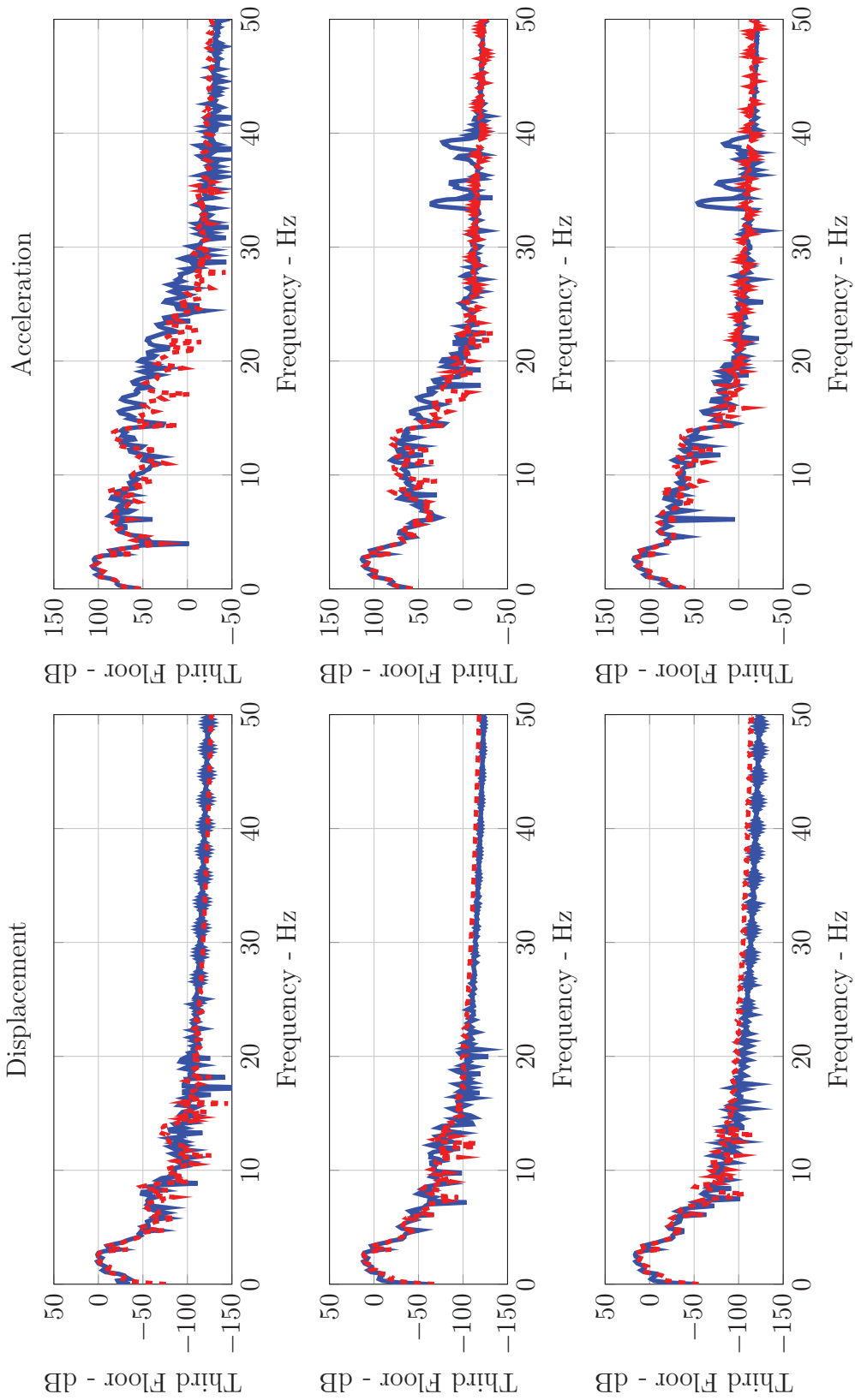


Figure 8.21: El Centro earthquake response comparison in frequency domain for ST–framed dRTHS SA case

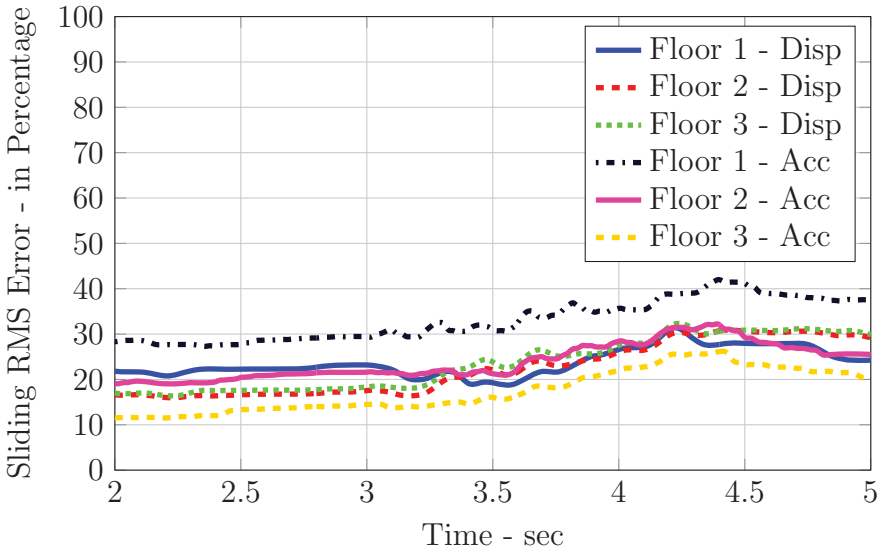


Figure 8.22: Moving RMS error for ST–framed dRTHS SA case

tionally, numerical substructure simulating the test structure has already a baseline line error when not controlled. Consequently, high errors in the comparisons are not predictable.

In Figure 8.23, the evaluation criteria, where unframed dRTHS, framed dRTHS and RTHS cases are compared to shake table tests, is represented as a bar chart. Here, almost all dRTHS and RTHS yield similar error level. The only main difference is observed at first floor J4. The variations in the errors can be attributed to the Internet QoS during the time of dRTHS testing. In addition, unlike RTHS, dRTHS uses a Bouc-Wen model simulating the MR damper within the Smith predictor to compensate network delays. Thus, the model may not capture the MR damper behavior perfectly.

In conclusion, it is shown that dRTHS can capture the response of shake table response of the test structure for El Centro ground motion when MR damper is controlled at semi-active mode. The error levels resulting in dRTHS are similar to those in RTHS when compared to shake table test. Overall, it can be concluded that the proposed dRTHS platform, along with the network time delay estimator provides a viable testing environment for geographically distributed labs having limited experimental resources.

## 8.5 Conclusion

In this chapter, dRTHS responses performed between Purdue University and University of Illinois at Urbana-Champaign are compared to RTHS and shake table responses of the MR damper controlled three story structure located at HIT.

In the dRTHS configuration, the physical substructure represented by the Purdue MR damper is tested at Purdue University, while the analytical substructure acting as the model of the test structure is simulated at UIUC. The signal transmission between two universities is performed over Internet using User Datagram Protocol.

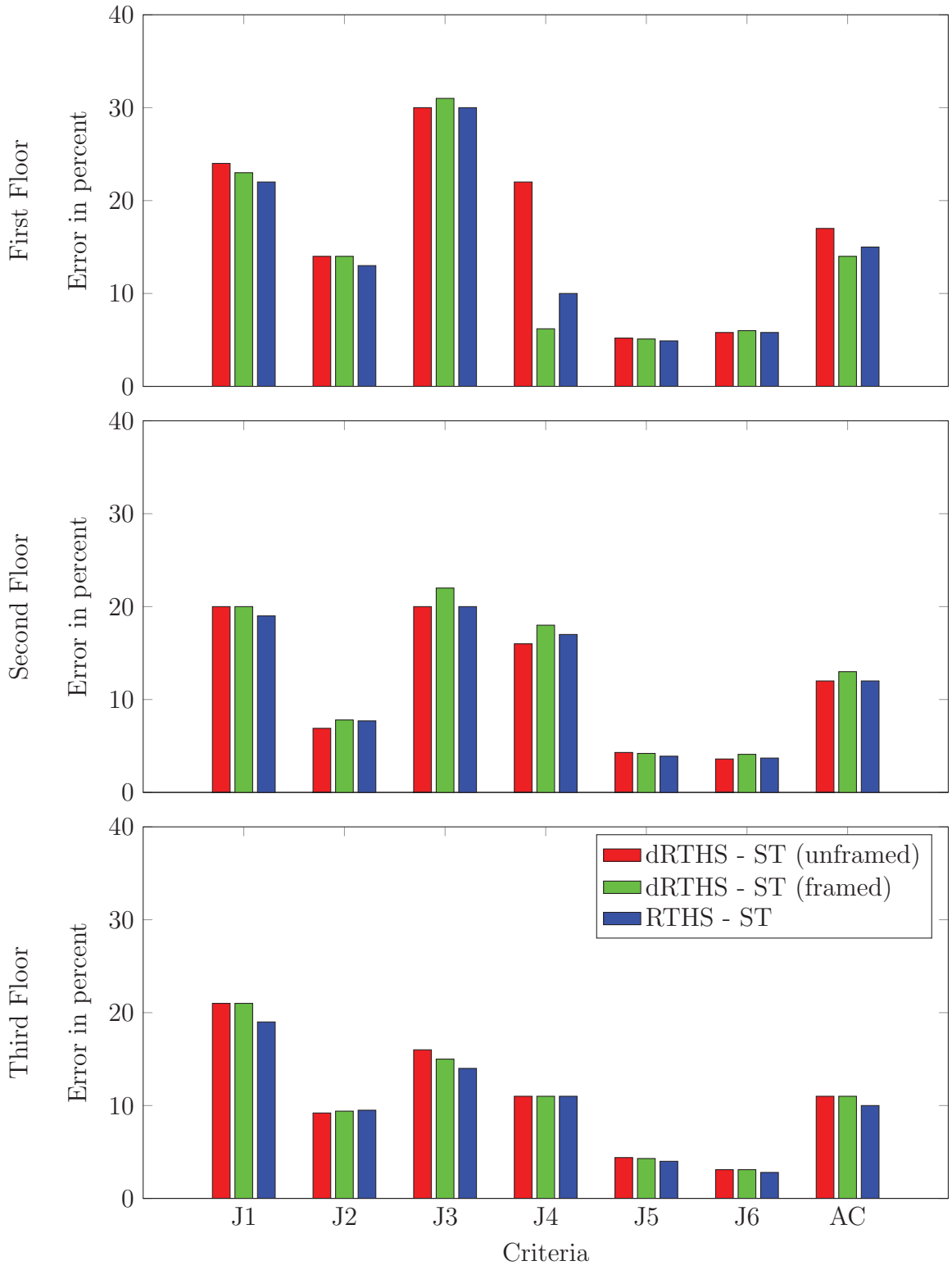


Figure 8.23: Bar chart error comparisons of dRTHS (unframed), dRTHS (framed) and RTHS to shake table test

For the dRTHS configuration, El Centro ground motion is used as the excitation input, while MR damper is driven in SA mode. Resulting relative displacements and absolute accelerations are compared to RTHS and shake table responses. To assess the performance and to validate feasibility of dRTHS, peak, RMS, and sliding RMS errors and PSDs are computed.

In addition to validation tests, to demonstrate the effectiveness of the network time delay estimator, estimated delays are intentionally over- and underpredicted. The resulting responses are compared to true dRTHS responses. The comparisons shows that especially for the framed case, correct estimation affects performance and quality of the test positively.

In summary, time and frequency domain comparisons, as well as evaluation criteria, showed that dRTHS can be considered as a valid testing environment for geographically distributed labs having limited experimental resources, alternative to RTHS and shake table testing.

# CHAPTER 9
# CONCLUSION AND FUTURE WORK

This dissertation discusses the development, implementation and validation of geographically distributed real-time hybrid simulation (dRTHS) platform. This platform is proposed in response to the lack of fully customizable environment with real-time execution, and information exchange capabilities to conduct distributed hybrid simulation. This chapter summarizes important research findings, observations and the capabilities of this proposed platform in Section 9.1. In addition, future work to advance the research is presented in Section 9.2.

## 9.1 Conclusions

To deliver the information in the most convenient way, first, a literature review emphasizing previous work on dRTHS is given. The shortcomings of previous studies were explored to build up and deliver a concrete motivation for the development of the new dRTHS platform. To explore the capabilities of the proposed dRTHS platform, a test scenario is established. According to the test plan, a three story test structure equipped with an MR damper is tested on the shake table located at Harbin Institute of Technology (HIT). The results are step-by-step compared to numerical simulations, RTHS conducted at Purdue University and finally dRTHS conducted between Purdue University and University of Illinois at Urbana-Champaign.

Before discussing the test results, an extensive review of the experimental setup, including the test structure, equipment, sensors and software for shake table tests is presented. Furthermore, the hardware to perform RTHS, including inner and outer loop controllers and servo-hydraulic systems are also discussed.

Next, a novel modeling and system updating technique based on system identification results of Eigensytem Realization Algorithm is introduced. This modeling method is focused on eliminating the drawbacks of its predecessors. Using this proposed tool, a *MCK* matrix of the test structure is derived. Later, the performance of this model is validated using shake table responses. This analytical model is also used as the basis of the numerical substructure of the dRTHS.

Since the MR damper used at HIT is similar but somewhat different than the one at Purdue, characterization of both dampers is required. By comparing force-displacement and force-velocity curves of those two dampers, equivalent voltage levels for the Purdue damper is determined to imitate necessary HIT damper force at passive-off and -on mode. In addition, an analytical model of both dampers based on Bouc-Wen hysteresis model is utilized. This model is also used in the pure simulation - shake table comparisons which will be discussed next.

To develop a baseline for dRTHS - shake table comparisons and understand main sources of error that may manifest during dRTHS validation tests, an integrated simulation including analytical models of the test structure and MR damper is conducted. The pure simulations predicted the global responses of the shake table tests accurately. The source of errors are explored and the possible reasons are described.

Conducting successful RTHS and dRTHS requires an actuator controller. Thus, a state-of-art controller, Robust Integrated Actuator Control to compensate actuator dynamics is introduced. Essentially, RIAC is a model based $H_\infty$ type controller that integrates a loop-shaping filter to handle delay and magnitude dynamics of the actuator and a Kalman filter to reject the noise in the measurements. To study the impact of the size and speed of the actuator on the tracking performance, the controller is verified by comparing desired and measured displacement of the actuator through band-limited white noises at HIT's large and Purdue's small actuators. To investigate the controller performance further, an RTHS test is employed at Purdue, where damper and test structure are selected as the physical and numerical substructures, respectively. The results of RTHS compared to shake table responses has shown that

the errors produced by RTHS are marginally lower than those of pure simulations. This observation leads to the conclusion that RIAC can be considered as a viable controller for this particular test case.

Prior to actual validation of dRTHS with shake table and RTHS responses, the distributed architecture for the data transmission is explained in detail, by introducing new concepts, for example, Internet and standard protocol suites such as UDP and TCP. Furthermore, a model based predictor to handle network time delays, known as the Smith predictor is described. Since the Smith predictor requires delay to be known prior to testing, a network time delay estimator is also implemented. Subsequently, to verify the dRTHS architecture, a two story structure with MR damper equipped at its first floor is tested. In this setup, both the analytical substructure representing the structure located at Smart Structures Technology Laboratory (SSTL) of UIUC and the physical substructure, MR damper located at Intelligent Infrastructure Systems Laboratory (IISL) of Purdue is simulated analytically, while communication between two laboratories is employed through the Internet. The single-site and multi-site test results show excellent correlation.

Finally, by testing the physical MR damper at IISL and simulating analytical model of three story HIT test structure at SSTL with the proposed architecture, dRTHS is performed and results are compared to RTHS and shake table responses. Additionally, the effectiveness of the network time delay estimator is investigated by comparing the dRTHS results with the wrong predicted delay cases.

Some key observations were drawn from the comparisons presented in this study:

- A new model updating methodology discussed in this dissertation captures the structural behavior in the frequency domain and offers more flexibility compared to its predecessor.

- A new control algorithm, *RIAC* presented here compensates the actuator dynamics robustly and is less prone to noise compared to previous *H*-inf type controller.

- Satisfying agreement between RTHS and shake table responses is achieved for each testing scenario.

- Flawless match in global responses is achieved for dRTHS, when all substructures are numerically simulated and the Internet infrastructure is used as the message passing interface between test sites.

- Comparisons between shake table and RTHS with dRTHS further validated the effectiveness of the platform.

- Since the force-displacement behavior of the MR damper used in shake table tests at HIT is different from the one utilized in RTHS/dRTHS tests at Purdue, errors are observed in ST-RTHS and ST-dRTHS comparisons, especially at the first floor level. Considering the fact that MR damper is attached to the test structure at the first floor, it is expected that most of the nonlinearities due the damper behavior will be observed at this floor level. As a result, the differences in the hysteresis loops of HIT and Purdue dampers will lead to different level of nonlinearity, and thus errors are introduced in the comparisons, mainly at the first floor. On the other hand, it has been also shown that, compared to RTHS, dRTHS platform does not introduce additional error in the comparisons.

The features of the proposed dRTHS platform can be summarized as follows:

- This platform is built for use in MATLAB/xPC. By relying only on MATLAB tools, the platform enables researchers to conduct dRTHS over UDP/Internet without any additional middleware. Additionally, since the platform provides a flexible built-in programming environment, researchers can execute customized scripts according to their own needs.

- The Internet Quality of Service (QoS) may not be always maintained during testing. Eventually, jittering during data transmission between sites may cause packets to be lost and experiment to fail. The platform gives user the option to

adjust a buffer for the incoming traffic to avoid jittering at the expense of time delay.

- The Smith predictor used as a common delay compensation mechanism, requires the delay to be known prior to the testing. By integrating a network time delay estimator to the dRTHS control loop, network delay can be determined on-the-fly and optimum operation for Smith predictor can be ensured.

## 9.2 Future Work

Some recommendations for future studies related to this work are:

- The model updating methodology proposed in Section 3.3 have been verified with comparison tests. Although this method provides more flexibility in modeling the system while still pertaining physical properties of the system, it fails to recreate the perfect damping and stiffness matrices given in Equations (3.2a) and (3.2b) like its predecessor. Section 3.4 discusses this issue in depth. A new search algorithm must be developed that induces error in the identified mode shapes and estimated seismic masses at the expense to be coherent with direct stiffness and damping matrices and, yet, trace the system behavior in time and frequency domain.

- Most of the compensation controllers for the actuators, for example $H_\infty$, are based on linearized model of the actuator while ignoring nonlinear behavior of the physical substructure. As mentioned by Carrion and Spencer (2007), a more adaptive controller should be implemented that can respond to changes in the nonlinear plant.

- Although $H_\infty$ actuator control promises an excellent tracking, noise in the load cell may cause performance loss since it will excite higher modes of the numerical model. Nonlinear Kalman filters of the MR damper to reject unwanted noise

should be developed. Some ideas on this aspect were explored by Song and Dyke (2013).

- The dRTHS experiments of this study are performed using only one physical and numerical substructure. Frameworks that involve multiple numerical and physical substructures should be investigated to validate dRTHS.

- For the sake of performance and stability, dRTHS systems, that are sensitive to network time delays, requires a plant predictor to estimate delayed response of the physical substructure. However, in the cases where modeling of physical portion is difficult, other approaches are needed. Use of adaptive and predictive plants for delayed real-time systems should be studied.

- The proposed dRTHS implementation is managed through insecure UDP, which is, by nature, vulnerable to cybersecurity attacks. Methods to improve the cyberinfrastructure should be investigated to prevent loss of test setup.

- Although the proposed platform is specifically designed for geographically distributed simulations, the infrastructure can be used as a low-cost alternative to SCRAMNet shared memory system for locally distributed RTHS applications (ldRTHS). The effectiveness of ldRTHS is studied in a multirate RTHS (mr-RTHS) application where a high degree-of-freedom finite element model running at low sampling frequency and a low degree-of-freedom lumped mass model utilized at higher sampling frequency are coupled (Maghareh et al., 2014c). In addition, another case is investigated where numerical model of a moment resisting frame is simulated along with a computationally intensive model updating algorithm, both running on two locally distributed real-time systems in parallel (Ou et al., 2015). Finally, a showcase for virtual RTHS (vRTHS) is based on this work (Hacker et al., 2013). Other applications should be sought that extends potential capabilities of the proposed dRTHS platform.

- It is possible that the use of impulsive dynamic loads may not fully exploit dRTHS platform. Especially, high frequency and short duration characteristics of such ground motions combined with the network delay and numerical infidelity regarding the plant model in Smith predictor will constrain performance of dRTHS.

- In order to asses performance and stability of future dRTHS applications, predictive performance indicator (PPI) and predictive stability indicator (PSI) can be used (Maghareh et al., 2014a,b). Eventually, with the help of PPI and PSI, tolerance of the system to the given network time delay can be determined and a delay compensation method best suited to the testing needs can be implemented.

# LIST OF REFERENCES

# LIST OF REFERENCES

Aktan, A. E. and Moon, F. L. (2005). *ASCE-SEI performance of structures track technical committee: Structural identification of constructed Systems*. Drexel University, Philadelphia, PA.

ASCE (2007). *Seismic Rehabilitation of Existing Buildings*. American Society of Civil Engineers, Reston, VA, asce/sei 41-06 edition.

Atkins, D. E., Droegemeier, K. K., Feldman, S. I., Garcia-Molina, H., Klein, M. L., Messerschmitt, D. G., Messina, P., Ostriker, J. P., and Wright, M. H. (2003). *Revolutionizing Science and Engineering through Cyberinfrastructure, Report of the National Science Foundation Blue-Ribbon Advisory Panel on Cyberinfrastructure*. National Science Foundation.

Bouc, R. (1971). Mathematical model of hysteresis: Application to systems with a degree of freedom. *Acustica*, 24:16–25.

Caicedo, J. M. (2011). Practical guidelines for the natural excitation technique (next) and the eigensystem realization algorithm (era) for modal identification using ambient vibration. *Experimental Techniques*, 35(4):52–58.

Caicedo, J. M., Dyke, S. J., and Johnson, E. A. (2004). Natural excitation technique and eigensystem realization algorithm for phase i of the iasc-asce benchmark problem: Simulated data. *Journal of Engineering Mechanics*, 130(1):49–60.

Carlson, J. D., Catanzarite, D. M., and Clair, K. A. S. (1996). Commercial magnetorheological fluid devices. *International journal of modern physics*, 10:2857–2866. 23/24.

Carlson, J. D. and Spencer, B. F. (1996). Magneto-rheological fluid dampers for semi-active seismic control. In *Proc. of the 3rd Int. Conf. on Motion and Vibr. Control*, volume II, pages 35–40.

Carrion, J. E. and Spencer, B. F. (2007). Model-based strategies for real-time hybrid testing.

Catbas, F. N., Kijewski-Correa, T. L., and Aktan, A. E. (2013). *Structural identification of constructed systems : approaches, methods, and technologies for effective practice of St-Id*. ASCE Publications.

Chang, C., Wang, Z., and Spencer, B. F. (2009). Application of active base isolation control. In *SPIE Smart Structures and Materials Nondestructive Evaluation and Health Monitoring*, pages 729239–729239. International Society for Optics and Photonics.

Chen, C. and Ricles, J. M. (2009). Analysis of actuator delay compensation methods for real-time testing. *Engineering Structures*, 31(11):2643–2655.

Chen, Z. Q., Wang, X. Y., Ko, J. M., Ni, Y. Q., Spencer, B. F., and Yang, G. (2003). Mr damping system on dongting lake cable-stayed bridge. In *Smart Structures and Materials*, pages 229–235. International Society for Optics and Photonics.

Chopra, A. K. (1995). *Dynamics of structures*, volume 3. Prentice Hall New Jersey.

Christenson, R., Dyke, S. J., Zhang, J., Mosqueda, G., Chen, C., Nakata, N., Laplace, P., Song, W., Y., C., A., M. G., , Ou, G., and Riascos, C. A. (2014). Hybrid simulation: A discussion of current assessment measures.

Christenson, R. E., Lin, Y. Z., Emmons, A., and Bass, B. (2008). Large-scale experimental verification of semiactive control through real-time hybrid simulation. *Journal of Structural Engineering*, 134:522–534.

Constantinou, M. C., Soong, T. T., and Dargush, G. F. (1998). *Passive energy dissipation systems for structural design and retrofit*. Multidisciplinary Center for Earthquake Engineering Research Buffalo, NY.

Coulouris, G. F., Dollimore, J., and Kindberg, T. (2005). *Distributed Systems: Concepts and Design (4th Edition)*. Addison-Wesley Longman Publishing Co., Inc., Boston, MA, USA.

Cowart, C., Hubbard, P., Miller, L., and Crawford, G. (2007). NHCP reference implementation and protocol reference guide. Technical report, University of California, San Diego.

Craig, R. R. and Kurdila, A. J. (2006). *Fundamentals of structural dynamics*. John Wiley & Sons.

Cyberinfrastructure Council (2007). *Cyberinfrastructure Vision for 21st Century Discovery*. National Science Foundation.

Deierlein, G., Arduino, P., Asimaki, D., Caicedo, J. M., Dyke, S. J., Hachem, M. M., Irfanoglu, A., McKenna, F., Lynett, P., Lowes, L. N., Mejia, L., Mazzoni, S., Mosqueda, G., Nakata, N., Zhang, J., and Rodgers, G. P. (2011). NEES vision report on computational and hybrid simulation.

Deierlein, G. G., Reinhorn, A. M., and Willford, M. R. (2010). Nonlinear structural analysis for seismic design. *NEHRP Seismic Design Technical Brief No*, 4.

Dyke, S. J. (1996). *Acceleration feedback control strategies for active and semi-active control systems : modeling, algorithm development, and experimental verification*. PhD thesis, University of Notre Dame.

Dyke, S. J., Spencer, B. F., Sain, M. K., and Carlson, J. D. (1996a). Experimental verification of semi-active structural control strategies using acceleration feedback. In *Proc. 3rd Int. Conf. on Motion and Vibration Control*, Chiba, Japan.

Dyke, S. J., Spencer, B. F., Sain, M. K., and Carlson, J. D. (1996b). Modeling and control of magnetorheological dampers for seismic response reduction. *Smart Materials and Structures*, 5:565. 5.

Friedman, A. J., Zhang, J., Phillips, B. M., Jiang, Z., Agrawal, A., Dyke, S. J., Ricles, J. M., Spencer, B. F., Sause, R., and Christenson, R. E. (2010). Accommodating MR damper dynamics for control of large scale structural systems. In *Proceedings of the Fifth World Conference on Structural Control and Monitoring*, volume 5WCSCM-10075.

Gao, X., Castaneda, N., and Dyke, S. J. (2013). Real time hybrid simulation: from dynamic system, motion control to experimental error. *Earthquake Engineering & Structural Dynamics*, 42(6):815–832.

Giraldo, D., Yoshida, O., Dyke, S. J., and Giacosa, L. (2004). Control-oriented system identification using ERA. *Structural Control and Health Monitoring*, 11:311–326. 4.

Hacker, S., Li, X., and Dyke, S. J. (2013). Virtual rths sample using xpc. *Network for Earthquake Engineering Simulation*.

Halvorsen, W. G. and Brown, D. L. (1977). Impulse technique for structural frequency response testing. *Journal of Basic Engineering*, 11(11):8–21.

Horiuchi, T., Nakagawa, M., Sugano, M., and Konno, T. (1996). Development of a real-time hybrid experimental system with actuator delay compensation. In *Proc. 11th World Conf. on Earthquake Engineering*, number 660.

Housner, G. W., Bergman, L. A., Caughey, T. K., Chassiakos, A. G., Claus, R. O., Masri, S. F., Skelton, R. E., Soong, T. T., Spencer, B. F., and Yao, J. T. P. (1997). Structural control: Past, present, and future. *Journal of Engineering Mechanics*, 123:897–971. 9.

ISO (1196). ISO/IEC 7498-1: 1994 information technology-open systems interconnection-basic reference model: The basic model. Technical report.

Jiang, Z. and Christenson, R. E. (2011). A comparison of 200 kN magneto-rheological damper models for use in real-time hybrid simulation pretesting. *Smart Materials and Structures*, 20:065011. 6.

Johnson, E. A., Ramallo, J. C., Spencer, B. F., and Sain, M. K. (1998). Intelligent base isolation systems. In *Proceedings of the Second World Conference on Structural Control*, volume 1, pages 367–76.

Juang, J. N. and Pappa, R. S. (1985). An eigensystem realization-algorithm for modal parameter-identification and model-reduction. *Journal of Guidance Control and Dynamics*, 8:620–627. 5.

Kalman, R. E. (1960). A new approach to linear filtering and prediction problems. *Journal of Basic Engineering*, 82(1):35–45. 10.1115/1.3662552.

Karkoub, M. A. and Zribi, M. (2006). Active/semi-active suspension control using magnetorheological actuators. *International Journal of Systems Science*, 37:35–44. 1.

Karnopp, D., Crosby, M. J., and Harwood, R. A. (1974). Vibration control using semi-active force generators. *Journal of Engineering for Industry*, 96:619–626. 2.

Kelly, J. M. and Konstantinidis, D. (2011). *Mechanics of rubber bearings for seismic and vibration isolation*. Wiley, Chichester, West Sussex, U.K.; [Hoboken, N.J.].

Kim, S. J., Christenson, R., Phillips, B., and Spencer, Jr., B. (2012). *Geographically Distributed Real-Time Hybrid Simulation of MR Dampers for Seismic Hazard Mitigation*, chapter 34, pages 382–393. asce.

Koodli, R. and Ravikanth, R. (2009). One-way loss pattern sample metrics. RFC 3357, RFC Editor.

Kwon, O. S., Nakata, N., Elnashai, A., and Spencer, B. F. (2005). A framework for multi-site distributed simulation and application to complex structural systems. *Journal of Earthquake Engineering*, 09(05):741–753.

Kwon, O. S., Nakata, N., Park, K. S., Elnashai, A., and Spencer, B. (2007). User manual and examples for UI-SIMCOR v2.6. Technical report.

Loh, C. H., Lynch, J. P., Lu, K. C., Wang, Y., Chang, C. M., Lin, P. Y., and Yeh, T. H. (2007). Experimental verification of a wireless sensing and control system for structural control using MR dampers. *Earthquake Engineering & Structural Dynamics*, 36(10):1303–1328.

Maghareh, A., Dyke, S. J., Prakash, A., and Bunting, G. B. (2014a). Establishing a predictive performance indicator for real-time hybrid simulation. *Earthquake Engineering & Structural Dynamics*, 43(15):2299–2318.

Maghareh, A., Dyke, S. J., Prakash, A., and Rhoads, J. (2014b). Establishing a stability switch criterion for effective implementation of real-time hybrid simulation. *Smart Structures and Systems*, 14(6):1221–1245.

Maghareh, A., Ozdagli, A. I., and Dyke, S. J. (2014c). Modeling and implementation of distributed real-time hybrid simulation. In *10th US National Conference on Earthquake Engineering*.

Mahin, S. and Shing, P. (1985). Pseudodynamic method for seismic testing. *Journal of Structural Engineering*, 111(7):1482–1503.

MATLAB (2011). *version 7.11.0 (R2011a)*. The MathWorks Inc., Natick, Massachusetts.

McConnell, K. G. and Varoto, P. S. (1995). *Vibration testing: theory and practice*. John Wiley & Sons Seoul.

Morton, A. and Claise, B. (2009). Packet delay variation applicability statement. RFC 5481, RFC Editor.

Mosqueda, G., Stojadinovic, B., Hanley, J., Sivaselvan, M., and Reinhorn, A. (2008). Hybrid seismic response simulation on a geographically distributed bridge model. *Journal of Structural Engineering*, 134(4):535–543.

Nakashima, M., Kato, H., and Takaoka, E. (1992). Development of real-time pseudo dynamic testing. *Earthquake Engineering & Structural Dynamics*, 21:79–92. 1.

Nakata, N. (2013). Effective force testing using a robust loop shaping controller. *Earthquake Engineering & Structural Dynamics*, 42(2):261–275.

Nakata, N., Dyke, S. J., Zhang, J., Mosqueda, G., Shao, X., Mahmoud, H., Head, M. H., Bletzinger, M., Marshall, G. A., Ou, G., and Song, C. (2014). Hybrid simulation primer and dictionary.

Nakata, N., Yang, G., and Spencer, B. F. (2004). System requirements for mini-most experiment. Technical report, NEESgrid.

NEESgrid (2003). The MOST experiment - whitepaper 1.0. Technical report.

NEESgrid (2004). The MOST experiment: Earthquake engineering on the grid - tr-2004-41. Technical report.

Oden, J. T., Belytschko, T., Fish, F., Hughes, T. J. R., Johnson, C., Keyes, D., Laub, A., Petzold, L., Srolovitz, D., Yip, S., and Bass, J. (2006). *Revolutionizing Engineering Science through Simulation, Report of the National Science Foundation Blue Ribbon Panel on Simulation-Based Engineering Science*. National Science Foundation.

Ojaghi, M., Williams, M. S., Dietz, M. S., Blakeborough, A., and Lamata Martnez, I. (2014). Real-time distributed hybrid testing: coupling geographically distributed scientific equipment across the internet to extend seismic testing capabilities. *Earthquake Engineering & Structural Dynamics*, 43(7):1023–1043.

Ou, G., Ozdagli, A., Dyke, S. J., and Wu, B. (2014). Robust integrated actuator control: experimental verification and real-time hybrid-simulation implementation. *Earthquake Engineering & Structural Dynamics*.

Ou, G., Ozdagli, A. I., Dyke, S. J., and Prakash, A. (2015). Novel rths with concurrent model updating on a distributed platform. In *11th International Workshop on Advanced Smart Materials and Smart Structures Technology*.

Ozdagli, A. I., Xi, W., Li, B., Dyke, S. J., Wu, B., and Zhang, J. (2013a). Actual hammer test on 3dof structure after structural modification. *Network for Earthquake Engineering Simulation*.

Ozdagli, A. I., Xi, W., Li, B., Dyke, S. J., Wu, B., Zhang, J., and Ding, Y. (2013b). Preliminary hammer test on 3dof structure after structural modification. *Network for Earthquake Engineering Simulation*.

Pan, P., Tomofuji, H., Wang, T., Nakashima, M., Ohsaki, M., and Mosalam, K. M. (2006). Development of peer-to-peer (p2p) internet online hybrid test system. *Earthquake Engineering & Structural Dynamics*, 35(7):867–890.

Panichacarn, V. (2006). *A Structural Health Monitoring Approach Using ERA, Real Numbered Mode Shape Transformation, and Basis Mode Screening*. ProQuest.

Pappa, R. S. (1994). *Eigensystem realization algorithm user's guide for VAX/VMS computers: Version 931216*. National Aeronautics and Space Administration, Langley Research Center, Hampton, VA.

Park, D. U., Yun, C. B., Lee, J. W., Nagata, K., Watanabe, E., and Sugiura, K. (2005). On-line pseudo-dynamic network testing on base-isolated bridges using internet and wireless internet. *Experimental Mechanics*, 45(4):331–343.

Pearlman, L., D'arcy, M., Johnson, E., Kesselman, C., and Plaszczak, P. (2004). NEESgrid teleoperation control protocol (ntcp) - tr-2004-23. Technical report.

Phillips, B. and Spencer, B. F. (2013). Model-based feedforward-feedback actuator control for real-time hybrid simulation. *Journal of Structural Engineering*, 139(7):1205–1214.

Postel, J. (1981a). Internet protocol. *ISI*.

Postel, J. (1981b). Transmission control protocol. *ISI*.

Sahin, I., Engin, T., and Cesmeci, S. (2010). Comparison of some existing parametric models for magnetorheological fluid dampers. *Smart Materials and Structures*, 19(3):035012.

Saouma, V. and Sivaselvan, M. (2008). *Hybrid Simulation: Theory, Implementation and Applications*. Taylor & Francis.

Schellenberg, A. H., Mahin, S. A., and Fenves, G. L. (2009). Advanced implementation of hybrid simulation - peer 2009/104. Technical report, University of California, Berkeley.

Schulzrinne, H., Casner, S., Frederick, R., and Jacobson, V. (2003). Rtp: A transport protocol for real-time applications. RFC 3350, RFC Editor.

Smith, O. J. (1959). A controller to overcome dead time. *ISA J.*, 6(2):28 – 33.

Song, W. and Dyke, S. J. (2013). Development of a cyber-physical experimental platform for real-time dynamic model updating. *Mechanical Systems and Signal Processing*, 37(12):388 – 402.

Soong, T. T. and Spencer, B. F. (2002). Supplemental energy dissipation: state-of-the-art and state-of-the-practice. *Engineering Structures*, 24:243–259. 3.

Spencer, B. F., Dyke, S. J., Sain, M. K., and Carlson, J. D. (1997). Phenomenological model for magnetorheological dampers. *Journal of Engineering Mechanics*, 123:230–238. 3.

Spencer, B. F., Finholt, T., Foster, I., Kesselman, C., Beldica, C., Futrelle, J., Gullapalli, S., Hubbard, P., Liming, L., Marcusiu, D., Pearlman, L., Severance, C., and Yang, G. (2004). NEESgrid: A distributed collaboratory for advanced earthquake engineering experiment and simulation. In *13th World Conference on Earthquake Engineering*.

Spencer, B. F. and Nagarajaiah, S. (2003). State of the art of structural control. *Journal of Structural Engineering*, 129:845–856. 7.

Stojadinovic, B., Mosqueda, G., and Mahin, S. (2006). Event-driven control system for geographically distributed hybrid simulation. *Journal of Structural Engineering*, 132(1):68–77.

Takahashi, Y. and Fenves, G. L. (2006). Software framework for distributed experimentalcomputational simulation of structural systems. *Earthquake Engineering & Structural Dynamics*, 35(3):267–291.

Takanashi, M., Udagawa, K., Seki, M., Okada, T., and Tanaka, H. (1975). Nonlinear earthquake response and analysis of structures by a computer-actuator on-line system. *Bulletin of Earthquake Resistant Structure Research Center*, 8.

Trethewey, M. W. and Cafeo, J. A. (1992). Tutorial: signal processing aspects of structural impact testing. *The International Journal of Analytical and Experimental Modal Analysis*, 7:129–149. 2.

Verma, D. C., Zhang, H., and Ferrari, D. (1991). Delay jitter control for real-time communication in a packet switching network. In *Communications Software, 1991, 'Communications for Distributed Applications and Systems', Proceedings of TRICOMM '91., IEEE Conference on*, pages 35–43.

Wang, K. J., Tsai, K. C., Wang, S. J., Cheng, W. C., and Yang, Y. S. (2007). Isee: Internet-based simulation for earthquake engineeringpart ii: The application protocol approach. *Earthquake Engineering & Structural Dynamics*, 36(15):2307–2323.

Wen, V. (1976). Method for random vibration of hysteretics systems. *Journal of the Engineering Mechanics Division*, 2:249–263.

Xiao, Y., Hu, Q., Guo, Y., Zhu, P., and Yi, W. (2004). Development of a network platform for remote hybrid dynamic testing. In *13th World Conference on Earthquake Engineering*.

Yang, Y. S., Hsieh, S. H., Tsai, K. C., Wang, S. J., Wang, K. J., Cheng, W. C., and Hsu, C. W. (2007). Isee: Internet-based simulation for earthquake engineering part i: Database approach. *Earthquake Engineering & Structural Dynamics*, 36(15):2291–2306.

Yao, J. T. P. (1972). Concept of structural control. *Journal of the Structural Division*, 98:1567–1574. 7.

Zapateiro de la Hoz, M. F. (2009). *Semiactive control strategies for vibration mitigation in adaptronic structures equipped with magnetorheological dampers*. PhD thesis, Universitat de Girona. Gi-976-2009.

VITA

# VITA

Ali Irmak Ozdagli was born in Istanbul, Turkey on December 15th, 1984. He received his B.S. in Civil Engineering from the Bogazici University, Turkey in 2007 and his M.S. in Civil Engineering from University of Notre Dame in 2009. In January 2010, Ali started his graduate studies at Purdue University and earned his Doctor of Philosophy degree in Civil Engineering in May 2015.